Searching for signals of photon-ALP mixing effects with gamma-ray spectra of AGNs

DISSERTATION
ZUR ERLANGUNG DES DOKTORGRADES
AN DER FAKULTÄT MIN
FACHBEREICH PHYSIK
DER UNIVERSITÄT HAMBURG

vorgelegt von

Qixin Yu
aus China

Hamburg
2023

Gutachter der Dissertation:	Prof. Dr. Dieter Horns
	Prof. Dr. Günter Sigl
Zusammensetzung der Prüfungskommission:	Prof. Dr. Dieter Horns
	Prof. Dr. Günter Sigl
	Prof. Dr. Michael Potthoff
	Prof. Dr. Manuel Meyer
	Prof. Dr. Marcus Brüggen
Vorsitzender der Prüfungskommission:	Prof. Dr. Michael Potthoff
Datum der Disputation:	01.12.2023
Vorsitzender Fach-Promotionsausschusses PHYSIK:	Prof. Dr. Günter Sigl
Leiter des Fachbereichs PHYSIK:	Prof. Dr. Wolfgang Parak
Dekan der Fakultät MIN:	Prof. Dr.-Ing. Norbert Ritter

"I'm smart enough to know that I'm dumb"

Richard P. Feynman

Abstract

Gamma-rays emitted by extragalactic sources propagating over cosmological distances has attracted growing interests and motivated a large variety of theoretical models as well as observational studies at GeV and TeV energies. However, the mean free path of these gamma-rays is limited above a certain energy (e.g. $\sim 100\,\mathrm{GeV}$) since they are attenuated due to pair-production process with extragalactic background light (EBL) photons. The resulted opacity of Universe can be reduced with gamma-ray photon mixing with a proposed hypothetical axion-like particle (ALP) in the presence of external magnetic field. This is known as the anomalous transparency of Universe towards TeV gamma-rays. Whereas at GeV energies, the photon-ALP mixing can also give rise to significant observable effects on the spectral energy distributions (SEDs) of gamma-rays, where the significance of such effects depends on the strength of photons coupling to ALPs ($g_{\gamma\gamma}$) as well as the ambient magnetic fields. Therefore, additional modulations shown on the observed SEDs in comparison to conventional physics are likely to result from the photon-ALP mixing effect. The significance of the irregularities on the SEDs can then be used to probe the existence of this hypothetical particle.

In this work, we use the energy spectra of 20 extragalactic gamma-ray sources of AGN recorded by *Fermi*-LAT in a 10-year observation. The propagation of the gamma-rays is divided approximately into three distinct regions, where different magnetic field profiles are configured and used for photon-ALP conversions. For the region in the vicinity of gamma-ray sources, we model the magnetic field with a large-scale homogeneous field (characterized with free parameters B for its field strength and s for its spatial scale) as little is known about its true nature. When photon/ALP beam continues to propagate in the intergalactic space, we take into account EBL absorption effect and neglect photon-ALP conversion here since the field strength is too weak to induce any prominent modulation on the final observed SEDs. Finally, as the beam enters Milky Way, the present Galactic magnetic field contributes another possible conversion region. After fully propagating the photon/ALP beam, we fit the observational spectral data points of each source to two models with and without the introduction of photon-ALP mixing effect respectively, namely, the H_0 (without photon-ALP mixing) and H_1

hypotheses (with photon-ALP mixing). Motivated from a possible ALP signal in a previous Galactic pulsar analysis we fix the ALP parameters at values of $g_{a\gamma\gamma} = 2.3 \times 10^{-10}\,\mathrm{GeV}^{-1}$ with $m_a = 3.6\,\mathrm{neV}$, while searching for best-fitting parameters of (B, s) on a grid map over large ranges of B ($1\,\mathrm{nG}$-$100\,\mu\mathrm{G}$) and s ($100\,\mathrm{pc}$-$10\,\mathrm{Mpc}$). We find for 18 of 20 sources a favorable fit, particularly for Markarian 421 and NGC 1275, under H_1 hypothesis in a likelihood fitting analysis. A significance level of $5.3\,\sigma$ is obtained from a combinatorial analysis of all 20 sources in hypotheses testing using bootstrapping method, where likelihood results of local maxima for 20 sources are chosen in the B-s planes. The local maximum of each source refers to the minimization of energy requirement that are used to sustain a magnetic field with energy density $\propto B^2 s^3$. In a similar way, a $6\,\sigma$ is also achieved when choosing all best-fitting parameters of (B, s) from the global maxima, instead of the local maxima.

It is important to note that the best-fitting parameters of (B, s) would still remain valid for different combinations of ALP parameters, due to the internal degeneracy of the parameters ($g_{a\gamma\gamma}$, m_a, B and s) that are used to describe spectral modulations on SEDs. The best-fitting values of (B, s) for 20 sources fall into ranges that are expected for large-scale magnetic fields present in relevant astrophysical environments in vicinity of the sources. A χ^2 analysis is also performed for the purposes of consistency check and possibly extending the analyzed LAT energy ($100\,\mathrm{MeV}$-$500\,\mathrm{GeV}$) to TeV range. We obtain consistent results from χ^2 analysis in terms of best-fitting parameter values and hypotheses testing.

Kurzfassung

Gammastrahlen von extragalaktischen Quellen breiten sich über kosmologische Distanzen aus haben wachsendes Interesse geweckt, sowie eine Vielzahl theoretischer Modelle und Beobachtungsstudien bei GeV- und TeV-Energien motiviert. Die mittlere freie Weglänge dieser Gammastrahlen ist jedoch oberhalb einer bestimmten Energie (z.B. $\sim 100\,\mathrm{GeV}$) begrenzt, da sie aufgrund des Paarbildungsprozesses mit Photonen vom extragalaktischen Hintergrundlichts (EBL) abgeschwächt werden. Die resultierende Opazität des Universums kann durch die Wechselwirkung von Gammastrahlen mit hypothetischen axionenähnlichen Teilchen (ALP) in Anwesenheit eines externen Magnetfeldes verringert werden. Dies wird als anomale Transparenz des Universums gegenüber TeV-Gammastrahlen bezeichnet. Bei GeV-Energien kann die Photonen-ALP-Mischung auch zu erheblichen beobachtbaren Effekten auf die spektralen Energieverteilungen (SEDs) von Gammastrahlen führen, wobei die Bedeutung solcher Effekte von der Stärke der Photonenkopplung an ALPs abhängt ($g_{a\gamma\gamma}$) sowie von den Umgebungsmagnetfelder. Daher sind zusätzliche Modulationen in den beobachteten SEDs im Vergleich zur konventionellen Physik wahrscheinlich auf den Photon-ALP-Effekt zurückzuführen. Die Signifikanz der Unregelmäßigkeiten in den SEDs kann dann dazu verwendet werden, die Existenz dieses hypothetischen Teilchens zu untersuchen.

In dieser Arbeit verwenden wir die Energiespektren von 20 extragalaktischen Gammastrahlenquellen von AGN, die von *Fermi*-LAT in 10 Jahren Beobachtungen aufgezeichnet wurden. Die Propagation der Gammastrahlen wird grob in drei verschiedene Regionen unterteilt, in denen unterschiedliche Magnetfeldprofile konfiguriert und für die Photon-ALP-Umwandlung verwendet werden. In der Region in der Nähe der Gammastrahlenquellen modellieren wir das Magnetfeld mit einem großskaligen homogenen Feld (charakterisiert durch die freien Parameter B für die Feldstärke und s für die räumliche Skala), da wenig über seine wahre Natur bekannt ist. Wenn der Photon/ALP-Strahl weiterhin im intergalaktischen Raum propagiert, berücksichtigen wir den Effekt der EBL-Absorption und vernachlässigen hier die Photon-ALP-Umwandlungen, da die Feldstärke zu schwach ist, um eine bedeutende Modulation auf der endgültig

beobachteten SED zu erzeugen. Schließlich, wenn der Strahl in die Milchstraße eintritt, trägt das dortige galaktische Magnetfeld zu einer weiteren möglichen Umwandlungsregion bei. Nach vollständiger Propagation des Photon/ALP-Strahls passen wir die beobachteten spektralen Datenpunkte jeder Quelle an zwei Modelle an, eines mit und eines ohne Einführung des Photon-ALP-Effekts, nämlich H_0 (ohne Photon-ALP-Effekt) und H_1-Hypothesen (mit Photon-ALP-Effekt). Motiviert durch ein mögliches ALP-Signal in einer früheren Analyse galaktischer Pulsare legen wir die ALP-Parameter auf Werte von $g_{a\gamma\gamma} = 2.3 \times 10^{-10}\,\mathrm{GeV}^{-1}$ fest $m_a = 3.6\,\mathrm{neV}$, während nach den am besten passenden Parametern von (B, s) auf einer Gitterkarte über große Bereiche von B ($1\,\mathrm{nG}$-$100\,\mu\mathrm{G}$) und s ($100\,\mathrm{pc}$-$10\,\mathrm{Mpc}$) gesucht wird. Wir finden, dass für 18 von 20 Quellen eine favorisierte Anpassung mit der Hypothese H_1 vorliegt, insbesondere für Markarian421 und NGC1275. Ein Signifikanzniveau von $5.3,\sigma$ wird durch eine kombinatorische Analyse aller 20 Quellen in Hypothesentests mit der Bootstrapping-Methode erzielt, bei der die Likelihood-Ergebnisse der lokalen Maxima für 20 Quellen in der B-s-Ebene ausgewählt werden. Das lokale Maximum jeder Quelle bezieht sich auf die Minimierung des Energiebedarfs, der zur Aufrechterhaltung eines Magnetfelds mit der Energiedichte $\propto B^2 s^3$ verwendet wird. In ähnlicher Weise wird auch ein $6\,\sigma$ erreicht, wenn alle am besten passenden Parameter von (B, s) aus den globalen Maxima anstelle der lokalen Maxima ausgewählt werden.

Es ist wichtig zu beachten, dass die am besten passenden Parameter von (B, s) für verschiedene Kombinationen an ALP Parametern gelten, aufgrund der internen Entartung der Parameter ($g_{a\gamma\gamma}$, m_a, B und s), die zur Beschreibung spektraler Modulationen auf SEDs verwendet werden. Die am besten passenden Werte von (B, s) für 20 Quellen liegen in Bereichen, die für die großräumigen Magnetfelder erwartet werden, die sich in den relevanten astrophysikalischen Umgebungen in der Nähe der Quellen befinden. Außerdem wird eine χ^2-Analyse durchgeführt, um die Konsistenz zu überprüfen und möglicherweise die analysierte LAT-Energie ($100\,\mathrm{MeV}$-$500\,\mathrm{GeV}$) auf den TeV-Bereich zu erweitern. Wir erhalten konsistente Ergebnisse aus der χ^2-Analyse in Bezug auf die am besten passenden Parameterwerte und das Testen von Hypothesen.

Contents

Dedicated to:
my grandparents and my Valeria

Chapter 1

Introduction

The standard model (SM) of strong, weak and electromagnetic interactions based on the gauge group $SU(3)_{color} \otimes SU(2)_{weak} \otimes U(1)_{\gamma}$ describes successfully all known processes for interactions of elementary particles and their properties. However, extension of SM is necessary as it cannot account for some of the evidence both in observational and theoretical aspects. For example, neutrinos, which are predicted to be massless particles by SM, was reported that they do have masses in the neutrino oscillation experiments by Super-Kamiokande Observatory [1] and the Sudbury Neutrino Observatories [2]. Such inability of SM is also seen in the baryon-antibaryon asymmetry problem. No solution to the imbalance between baryonic and antibaryonic matter in observable Universe can be provided within the framework of SM or other theories (such as General Relativity). Moreover, a violation of charge-parity-symmetry (CP-symmetry) [3], in relation to the baryonic asymmetry problem, should occur in the strong interaction sector based on current formulation of quantum chromodynamics (QCD). However, no such violation of CP-symmetry has been observed in experiments involving only strong interaction. This is then later referred as *the Strong CP problem*. Therefore, it is fair to view the SM as a low-energy effective manifestation of a more fundamental and complete theory that can describe the Universe well.

Consequently, this calls for explanation going beyond the SM. Several remarkable attempts have been made to address these issues and make modifications based on the current knowledge. This includes supersymmetric (SUSY) models [4–6], multidimensional Kaluza-Klein theories [7, 8], String theory [9] and Peccei-Quinn (PQ) mechanism [10]. These extended models of SM predict existence of weakly interacting massive particles (WIMPs) and weakly interacting subelectronvolt particles (WISPs), which are proposed as dark matter (DM) candidates, responsible for phenomena unexplained by fundamental particles of SM. However, no conclusive detection of signal has been observed for WIMPs in direct experimental searches [11–13], which makes WIMP a less promising candidate for the DM puzzle in the past years [14]. Therefore, more attention has been given to another appealing DM candidate, the WISPs. Representative examples of such particles are axions and axion-like particles (ALPs), whereas hidden sector photons generically arose from string compactifications [15] are irrelevant for this work and will be not discussed further. Axions are resulted from the PQ mechanism, which was proposed initially to solve the Strong CP problem by introducing a new global symmetry $U(1)_{PQ}$, which makes the CP violating term in QCD Lagrangian negligible. When this global symmetry breaks down, the so-called particle axions, are therefore generated as pseudo-Nambu-Goldstone bosons [16]. The predicted axion mass is inversely proportional to its decay amplitude. ALPs, on the other hand, as a generalized form of axions, originally predicted by String theory and arise from the breaking of other global symmetries [9, 17].

In the PQ mechanism, the decay constant of axion is of the order of the electron weak scale ($\sim 246\,\mathrm{GeV}$), which is linked to its mass, at the order of $100\,\mathrm{keV}$ [10, 16, 18, 19], in an inversely proportional relation [19]. In this way, this rather heavy axion can lead to sizable couplings to the SM particles, but was quickly ruled out by constraints found in experiments [20]. Thereafter, two new models DFSZ [21, 22] and KSVZ [23, 24] emerged based on the core idea of PQ mechanism. In these two models the symmetry breaking scale was proposed to be at very high energies ($\sim 10^{15}\,\mathrm{GeV}$), which results a very light axion with its mass around neV. Axions predicted from these models are very weakly coupled to other particles, and together with their extremely light masses, making the experimental searches very difficult. In contrast to the strict relationship between coupling and mass of axions, such relation is missing in the case of generic ALPs, and because of that, the searches of ALPs cover much larger parameter space of coupling and mass. In terms of detectability, their mainly coupling to photons (through a two-photon vertex with coupling constant denoted by $g_{a\gamma\gamma}$) is the most well-known interaction and is widely used in experimental searches of ALPs. In the realization of the two-photon vertex coupling, the basic idea follows that one photon propagates and the other plays the role of magnetic field instead (see right panel of Fig. 2.3 for an illustration), such that a conversion of $\gamma \rightarrow a$ (a stands for the ALP) could occur. Similarly, a conversion of $a \rightarrow \gamma$ could also take place as long as the same magnetic field (or another magnetic field) is in presence. This process of $\gamma \rightarrow a \rightarrow \gamma$ is the so-called photon-ALP oscillation [25, 26].

ALPs can, thus, give rise to a rich phenomenology that could be observed in laboratory and in the Universe with their mixing to photons. While searches for axion/ALP have so far only provided exclusion limits, astrophysical effects induced by photon-ALP mixing can be considered as a promising approach to search for signatures of ALPs (see references [27–46] for various examples).

In particular, it has been realized that the coupling of ALPs to photons could produce modulations and leave imprint of detectable signatures on the observational spectra of distant active galactic nuclei (AGN), due to the reason that high energy (HE, $100\,\mathrm{MeV} \lesssim \mathrm{E} \lesssim 100\,\mathrm{GeV}$) and very high energy (VHE, $E \gtrsim 100\,\mathrm{GeV}$) gamma-ray photons emitted by these sources can mix with ALPs in the presence of various astrophysical magnetic environments along their propagation to Earth [19, 33, 47]. Observations of these spectra in the VHE range of spectra are mainly through the use of Imaging Atmospheric Cherenkov Telescopes (IACTs) [19], while spectra in energy band of MeV to several hundreds of GeV has been made accessible since the launch of *Fermi* Large Area Telescope (*Fermi*-LAT) [48]. The precise effect brought by photon-ALP mixing onto gamma-ray spectra can differ from case to case, depending on the astrophysical environments that could contribute possible conversion regions along the line of sight. Moreover, it is obvious that such mixing effect would cause a certain amount of losses on the photon flux as a fraction of gamma-ray photons can convert into ALPs and therefore become undetectable. This type of conversion can be referred as the *photon disappearance* channel. Specific examples for such modulations on photon spectra can be found in, for example, disappearance effects from extragalactic objects in a galaxy cluster [49], intergalactic space [50] and the Milky Way [40]. In contrast to the *photon disappearance* channel, the *photon appearance* channel describes the scenario in which the ALPs produced in stars or galaxy clusters convert into photons in the presence of an external magnetic field (e.g. searches of solar axions by CAST experiment [39]). A third channel, *photon reappearance*, combines the previous types of the photon-ALP mixings, where gamma-ray photons convert into ALPs in one magnetic environment and convert back into photons in another magnetized environment before being observed, which can then alter the level of attenuated photon flux by pair-production process [51]. The pair-production is another process that can lead to major spectra modulations besides photon-ALP mixing, especially at TeV energies. As gamma-ray photons propagate along the line of sight, they can be absorbed by background radiation fields, e.g. extragalactic background light (EBL) photons, through pair production process: $\gamma_{\mathrm{VHE}} + \gamma_{\mathrm{EBL}} \rightarrow e^{+}e^{-}$. Notably, the level of absorption can be reduced if gamma-ray photons convert into ALPs to evade the pair production, and convert back into photons in the vicinity of Earth. This would result a hardening feature on the spectrum in the VHE band comparing to conventional physics [33]. Indeed, such anomalous transparency of the Universe to VHE photons has been reported and studied in several references [35, 52, 53], and are explained by the emergence of ALPs [34, 35]. Another remarkable consequence of the photon-ALP coupling is the change of polarization state of photons in the presence of the magnetic field, which is, however, beyond the scope of this work, and we refer readers to [25, 54] for further details.

In all three channels of searching for signatures of ALPs, an interpretation of the observations has been put forward that singles out the mass range of neV and coupling constants $10^{-12}\,\mathrm{GeV}^{-1} < g_{a\gamma\gamma} < 10^{-10}\,\mathrm{GeV}^{-1}$ for ALPs [40, 43, 49, 50, 53, 55–58] (see [59] for an incomplete summary of various constraints from astrophysical observations), where uncertainties are mainly caused by the assumption of the magnetic field profiles presented along the line of sight for photon/ALP beam. A well-constrained value for the coupling constant $g_{a\gamma\gamma}$ would become possible with the upcoming light-shinning-through-the-wall experiment, Any Light Particle Search II (ALPS II) at DESY [60]. However, the upper range ($10^{-10}\,\mathrm{GeV}^{-1}$) mentioned above is in small tension with the upper limit provided by analysis of stars in globular clusters [61], and especially with the similar bound given by CERN Axion Solar Telescope (CAST) experiment: $g_{a\gamma\gamma} < 6.6 \times 10^{-11}\,\mathrm{GeV}^{-1}$ for $m_a < 0.02\,\mathrm{eV}$ (at 2σ level). The bound given by CAST may be, however, affected by conversions of ALPs into photons inside the Sun or by other environmental effects in dense stellar plasma, and thereafter, effectively suppressing the emitted ALP flux from the Sun [44] and leading to a relaxation of the upper limit on $g_{a\gamma\gamma}$.

In most cases, gamma-ray spectral analysis used for searching of signature of ALPs are done by applying the best-fit (with ALPs), conventional models to gamma-ray data, and significant deviations from conventional model with respect to this best-fit model can be considered as a signal for ALPs after taking into account all conventional sources of uncertainties. When such significant deviation is missing with respect to the baseline model (with ALPs), all realizations of ALP parameters that should have produced a measurable effect in the data can then be excluded from the parameter space, leading to limits or bounds set for $(g_{a\gamma}, m_a)$. However, constraints set on ALP parameters in this way are debatable and should be used with caution, since one the one hand, there is model dependence on the magnetic profiles used in the fitting and tests, and one the other hand, limited number of simulations for realizations of B-field or ALP parameters is not guaranteed to cover the scenario where a true signal of ALP locates. The key in ALP searches is the conversion probability of $a \leftrightarrow \gamma$ since it determines the deviations observed on spectra, and the calculation of the conversion probability depends crucially on the magnetic fields used along the line of sight. Therefore, instead of trying to probe the parameter space it is more important to provide some guidelines for modelling the astrophysical magnetic field, such as its strength and scale in relevant regions [46]. This is the main idea of this work.

Here we search for the signature of photon-ALP mixing in a spectra sample of 19 high frequency peaked BL Lac type objects and the radio galaxy NGC 1275 using gamma-ray data recorded by *Fermi*-LAT in 10-year observations. Different from previous studies of photon-ALP mixing where particular models of magnetic fields are assumed for each conversion region along the line of sight, we instead assume fixed values of coupling $g_{a\gamma\gamma} = 2.3 \times 10^{-10}\,\mathrm{GeV}^{-1}$ and mass $m_a = 3.6\,\mathrm{neV}$ motivated by ALP signal found in [40] and leave the constant magnetic field strength and its spatial extension as free parameters.

In this chapter, we first give introduction for high and very high energy gamma-rays emitted from AGN, where we discuss the structure of AGN and the production schemes for these gamma-rays, and how they are detected by *Fermi*-LAT and other ground based telescopes. The coupling of gamma-ray photons to axions/ALPs is also briefly discussed, as well as the corresponding constraints on $(g_{a\gamma\gamma}, m_a)$ from various searches. Then, in Chapter 2, indications from astrophysical observation of AGN spectral modulations are given. Such modulations are then accounted for with the photon-ALP mixing effect. Also. we show the simplified case for calculating photon-ALP conversion probability, and in particular, the conversion probability used later in this work for the case of AGNs. Various astrophysical magnetic environments along the propagation of photon/ALP beam are given in Chapter 3 case by case to show in detail how they would affect the photon-ALP conversion probabilities for distant sources. Where, in Chapter 4, we collect a sample of AGNs with 10-years observational data recorded by *Fermi-LAT*. Estimates for source-dependent magnetic field are done using likelihood (and χ^2) fitting to spectral data. Also, we use likelihood ratio (and $\Delta\chi^2$) test to perform hypotheses testing for a spectral model without vs. a model with photon-ALP coupling. Finally, we conclude this work with a short summary and outlook presented in Chapter 5.

Large fraction of the work presented in this thesis has been published in peer-reviewed journals of [46] and [44].

1.1 High and very high energy gamma-rays from active galactic nuclei

γ-rays, as the most energetic form of electromagnetic radiation, can be used to probe interesting phenomena for astrophysics and fundamental physics in extreme conditions. Indeed, they are closely related to all different sorts of cosmic messengers, such as cosmic rays, cosmic neutrinos and gravitational waves [62]. Moreover, γ-rays play an important role in guiding us to address some of the fundamental physics issues related to, for example, the violation of Lorentz invariance [63, 64], or the existence of exotic particles beyond SM (*e.g.*, ALPs) [17]. Therefore, understanding the production mechanism of γ-ray and its emission are very crucial in studying any related subjects. Galactic astrophysical objects associated with sources of γ-rays include supernova remnants (and plerions), pulsars, microquasars and so on. The extragalactic γ-ray regime, on the other hand, is mostly dominated by galaxies themselves: starburst galaxies, gamma-ray bursts and AGNs. Among these objects, AGNs are believed to be the most powerful sources of energy in the Universe and great candidates for studying gamma-ray related physics.

1.1.1 Active galactic nuclei

The general term active galactic nuclei refers to galaxies with supermassive black holes (SMBHs) of masses in range of $10^6\, M_\odot - 10^{10}\, M_\odot$ in their central regions [65], where the evolution of these SMBHs is currently in a phase of actively growing with enormous circumnuclear material as input [66]. As a consequence, the falling of these material onto the black hole by gravitational energies can be converted into radiation fields and/or kinetic energies of outflows [66] (also see Sec 3.1 in Chapter 3 for a related description of AGN jet formation). The outflow carries a significant amount of energies released during accretion and ultimately emitted as a form of radiation covering energy band of radio to γ-ray. As a matter of fact, these outflows may take the form as two strongly-collimated jet of plasma moving with ultra-relativistic speed, which can be observed in some AGNs [67, 68]. Depending on their radio-loudness (emission), width of emission lines, morphological differences and other considerations, ANGs can be empirically classified into the types illustrated in Fig. 1.1. Alternatively, these different types of AGNs might be

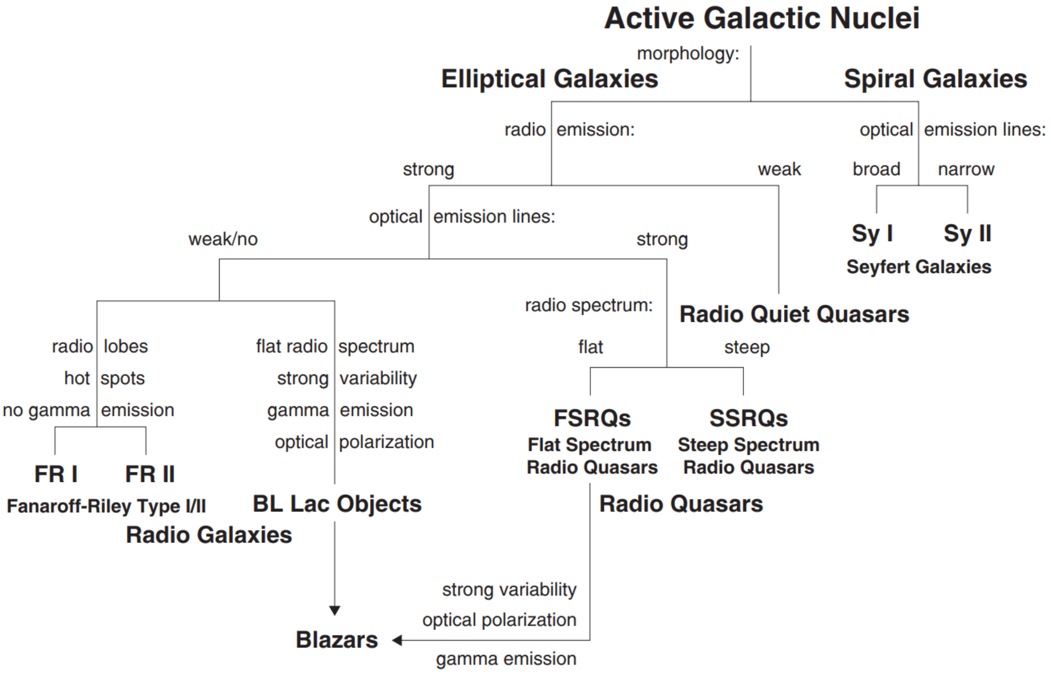

FIGURE 1.1: An empirical classification of AGNs (figure taken from [69]).

intrinsically the same class of objects seen at different viewing angles with respect to the line of sight [70]. The main idea is that, as summarized in [71], the emission is highly anisotropic in the inner regions of AGN. The general AGN paradigm (see Fig. 1.2), as stated above, consists of a SMBH in the center which is surrounded by an accretion disk and outflows with extreme-high velocities. The fast-moving outflow close to the center emits Doppler-broadened lines whereas distant outflow emits narrower lines [71]. In this way, when the circumnuclear material is absorbed in a flattened configuration under the influence of gravitational field, the central parts are obscured for the transverse line of sight due to the geometically and optically thick dust torus, such that only outflows emitting narrow lines are seen. This is, for example, the case for Seyfert II galaxies and Fanaroff-Riley Type galaxies. In contrast, AGN types (such as Lobe-dominated radio loud quasars, Seyfert 1 galaxies and broad line radio galaxies) of near-infrared to soft-X-ray continuum and broad lines are only visible when viewing at a larger angle with respect to the case of Seyfert 2 galaxies or narrow line radio galaxies. Under this circumstance, these different types of AGNs displayed in Fig. 1.1 can then be sorted in an alternative way based on their orientation effects and emission properties, as shown in Fig. 1.3.

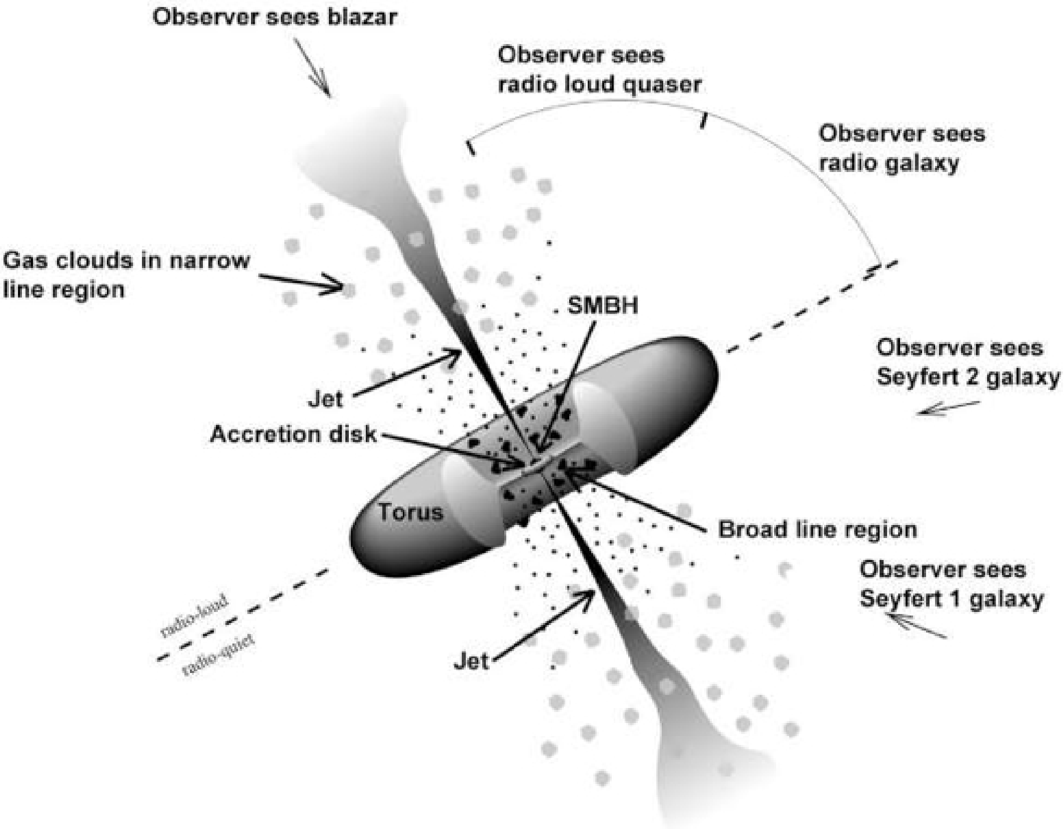

FIGURE 1.2: Impression for a model of AGN in the unified scheme [71]. Classification of AGNs based on different viewing angles are also presented. (figure taken from `https://fermi.gsfc.nasa.gov/science/eteu/agn/`).

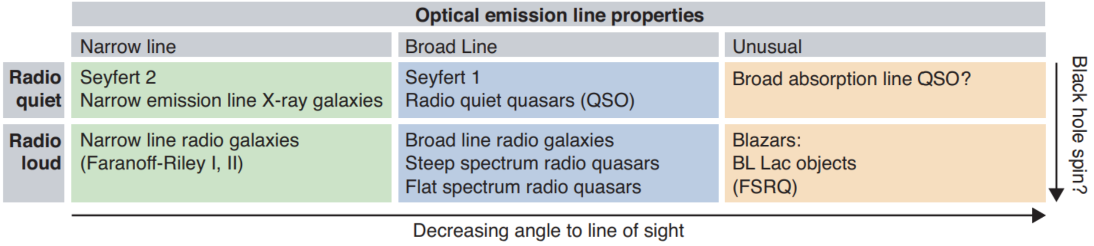

	Optical emission line properties		
	Narrow line	Broad Line	Unusual
Radio quiet	Seyfert 2 Narrow emission line X-ray galaxies	Seyfert 1 Radio quiet quasars (QSO)	Broad absorption line QSO?
Radio loud	Narrow line radio galaxies (Faranoff-Riley I, II)	Broad line radio galaxies Steep spectrum radio quasars Flat spectrum radio quasars	Blazars: BL Lac objects (FSRQ)

Figure 1.3: A simplified scheme for AGN taxonomy indicated by [70, 71], where phenomenological classification can be largely explained by the viewing angle (figure taken from [69]).

For radio-loud objects as displayed in Fig. 1.2 and 1.3 there appears to be a close relationship between the strong, non-thermal radio emissions (relativistic beaming effect) and the presence of a relativistic jet. Particularly, blazars, as a special class of radio-loud AGN with a close alignment between the jet axis and the line of sight for observers, produce strong amplification of emission over a very broad energy band from radio to γ-ray and thus can be detected at large distances. Furthermore, the significant total output of luminosity exhibited by blazars are in most cases dominated by γ-rays [71]. They are the main subjects of this section as ideal targets for studying AGNs with HE and VHE γ-ray emission.

Blazars in general consist of the AGN subclass of flat spectrum radio quasars (FSRQs) and BL Lacertae (BL Lac) type objects. The main difference between these two types of blazars comes from the emission lines [72], where FSRQs show strong, broad emission lines and BL Lacs show almost no emission lines. In addition to properties of exhibition of radio loudness and broad, non-thermal continuum emission, there are some other commonly observed features for blazars as summarized in [71]: rapid variability, variable polarization, compact flat-spectrum radio emission and superluminal motions. These properties in principle can all be attributed to the relativistic beaming effects and orientation effect of jets [71].

The study of jet-dominated AGNs naturally follows the train of thought: in order to obtain the emitted photon spectrum and other properties we have to take a step back and acquire a basic understanding of the radiative process, type of particles involved and their energy distributions, as well as speed and orientation of the jet. This would then lead us to possible mechanisms responsible for the acceleration of radiating particles where the specific mechanisms should give us additional information about the jet structure. In the end, this should all go back to the engine, the SMBH in the center, that drives all the dynamics within the AGN and its jet. Knowledge has to be established about how the gravitational energy coming from SMBH can be converted into kinetic energy of the jet, and ultimately to photons.

A key ingredient connecting all these processes is the magnetic field within the AGN environment, particularly in jet (see Chapter 3 for details). For example, in the description of magnetohydrodynamic (MHD) model for the AGN system [73], particle acceleration and collimation mechanism of jet are accounted for while operated within the framework of gravitational collapse and/or accretion paradigms. Plasma of jets is resulted from the rotating disk in the presence of the a magnetic field [74]. Fig. 1.4 shows an example of numerical simulation with the MHD model for a AGN jet.

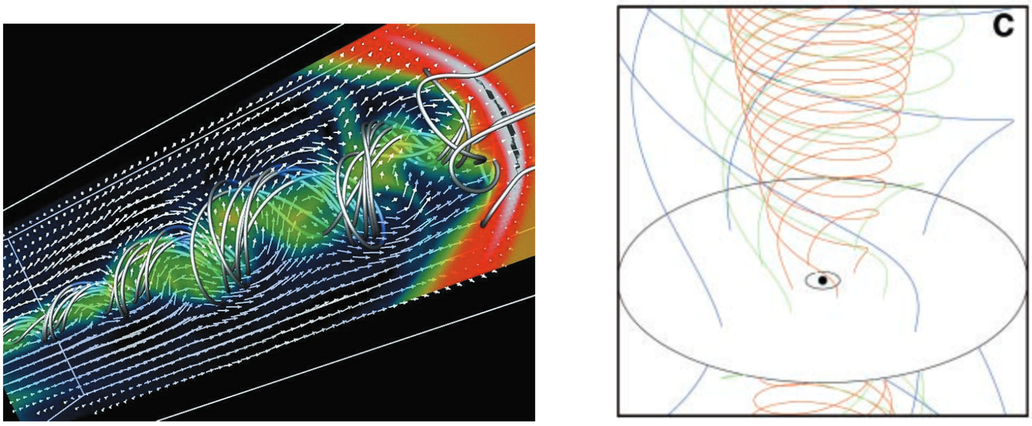

Figure 1.4: Left panel: A 3D MHD simulation of the propagation of a magnetized jet. The arrows indicate flow velocity. Plasma fields with high and low pressure are colored with white and blue respectively, and follow closely the field lines. Right panel: Schematic diagram of the scenario where a differential rotation of magnetic field generates relativistic jet outflow. The poloidal magnetic field lines (colored in blue) protruding from an accretion disk flings the coronal material outward in a wind, thus, the outflow. The rotation of the wind slows down as it goes outward due to angular momentum conservation and the outflow driven by the wind would coil the field lines (figures taken from [74]).

MHD model, as a very popular method of producing and collimating jets, has been widely used in describing the jet dynamics in many studies [74–77]. In these models, the magnetic field lines anchored and protruded from the rotating accretion disk play the role of constraining and guiding the plasmas in such a way that the plasmas are tied to it and are flung outward along these field lines, as shown in Fig. 1.4. Another important feature about these magnetic field lines is the fact that the parallel lines have a tendency to repel each other, such that a perpendicular pressure is imposed onto the plasma, and this further leads to an enhancement on the field compression and its energy density [74]. Thus, the collimation and acceleration of the jet with the magnetic field lines proceed with the following process: the circumnuclear material dragged via the gravitational energy of the SMBH are threaded by the poloidal field lines, and since these field lines are anchored into a differential rotating accretion disk, this would therefore produce a helix magnetic field around the rotating axis. The plasma trapped in the magnetic field is then driven by these coiled lines upward and outward as they tend to uncoil in this process.

Acceleration mechanisms of charged particles:

Particularly, the charged particles in plasma of jet, such as protons and electrons, can be accelerated to relativistic speeds via acceleration mechanisms. These accelerated charged particles are then later responsible for different forms of radiation, from radio to γ-rays. Several mechanisms have been proposed to account for the acceleration in jets.

- **Fermi acceleration**: Fermi acceleration [78], also known as Shock acceleration, in which shock waves are formed due to the interaction of jet plasma and surrounding medium. These shocks can generate regions of frequently changing magnetic fields and gas densities. Charged particles gain an energy proportional to the shock velocity when they repeatedly cross the shock fronts. As the charged particles go back and forth across these regions for many times, they eventually achieve relativistic velocities.
- **Magnetic reconnection**: Magnetic reconnection refers to situation when magnetic field lines break and reconnect in a highly dynamic and energetic process [79, 80]. For example in [81] the author proposed a mechanism responsible for initial acceleration of the plasma jet to relativistic speed in the case of GRS 1915+105, where a violet reconnection occurs between the magnetic field lines of the inner disk region and those anchored into the central black hole. In general, magnetic reconnection converts magnetic energy into heating and non-thermal acceleration of charged particles.
- **Stochastic acceleration**: This mechanism is very similar to the shock acceleration, proposed by E. Fermi in 1949 [78]. Originally, the stochastic acceleration refers to the scattering of cosmic-rays off randomly moving magnetized clouds [82], also known as the second-order Fermi acceleration [83]. This process later refers to the acceleration of charged particles by randomly changing magnetic field (such as turbulent magnetic field or MHD field) in AGN jet.

Given the complexity in AGN jet environment, multiple acceleration may be applied at the same time but at different regions of jet. Therefore, the observed spectral energy distribution (SED) should be a combined effects of these mechanisms.

1.1.2 Production of gamma-rays

Depending on whether the parent population is made of leptons or hadrons, production of γ-rays can be discussed respectively in leptonic and hadronic emission models. In leptonic model, the γ-ray flux is normally probed via the electron density and radiation fields, whereas in hadronic model, the production of γ-rays is related to the cosmic-ray density and the target gas density [62].

1.1.2.1 Leptonic models

The ejected energetic plasma of outflow consists of highly ionized gas composed of charged particles such as electrons/positrons and ions. These relativistic charged particles accelerated by magnetic fields (as described in the previous subsection) could radiate photons through synchrotron emission. The power loss of charged particles in this process depends on the particle mass and its charge, as well as the strength of the B-field in presence. Due to very significant mass difference between protons and electrons, the energy loss is much lower in the case of synchrotron emission by electrons. In this way, low energy synchrotron photons (from optical to X-ray band) are produced. In general, they are believed to characterize the broad, non-thermal component of the SED of AGNs in the low energies, and they play an important role in the production mechanism of X-ray and high-energy gamma-rays for reasons listed below.

These low-energy seed photons are then scattered off of the same population of relativistic electrons via the Inverse Compton (IC) scattering process, namely, the Synchrotron Self-Compton (SSC) process. Thus, emission of γ-ray and spectral energy distribution of AGN at higher energies are directly linked to the energy distribution of the relativistic electrons[1]. Moreover, depending on the energy of the seed photon, the IC process can take place in two different regimes [62, 84]. In the first regime, the Thomson regime, the low-energy photons are produced via synchrotron radiation of relativistic electrons and/or from a dusty torus around the central accretion flow (this way, resulted photons are in infrared band, then can further lead to External Compton (EC) scattering on dust-torus emission [84]), then IC scattering to GeV γ-ray photons. In the other regime, the Klein-Nishina regime [62, 84, 85], the seed photons that enter the IC scattering process later are originally from the Broad Line Region (BLR) in AGN, where the emission is dominated by optical to ultraviolet photons. These photons then undergo EC process on BLR emission, and IC scattering to GeV photons.

---

[1] Some of these high-energy photons can be absorbed by low-energy synchrotron photons inside the emitting region (internal absorption) and thus modify the SED to some extension. Such process should be considered in both the Leptonic and Hadronic emission models.

The GeV photons resulted from the IC process are then responsible for characterizing the Compton component of the SED of AGN in the higher energy band. An example of SED for AGN 3C 279 [86] is shown in Fig. 1.5, where different components dominate different energy bands. The GeV γ-rays (corresponds to $\nu \gtrsim 10^{21}$ Hz) are presented in the second "bump" of the SED arising mainly from EC and SSC processes, whereas the first "bump" (10^{11} Hz $\lesssim \nu \lesssim 10^{14}$ Hz) is mainly a result of synchrotron emission.

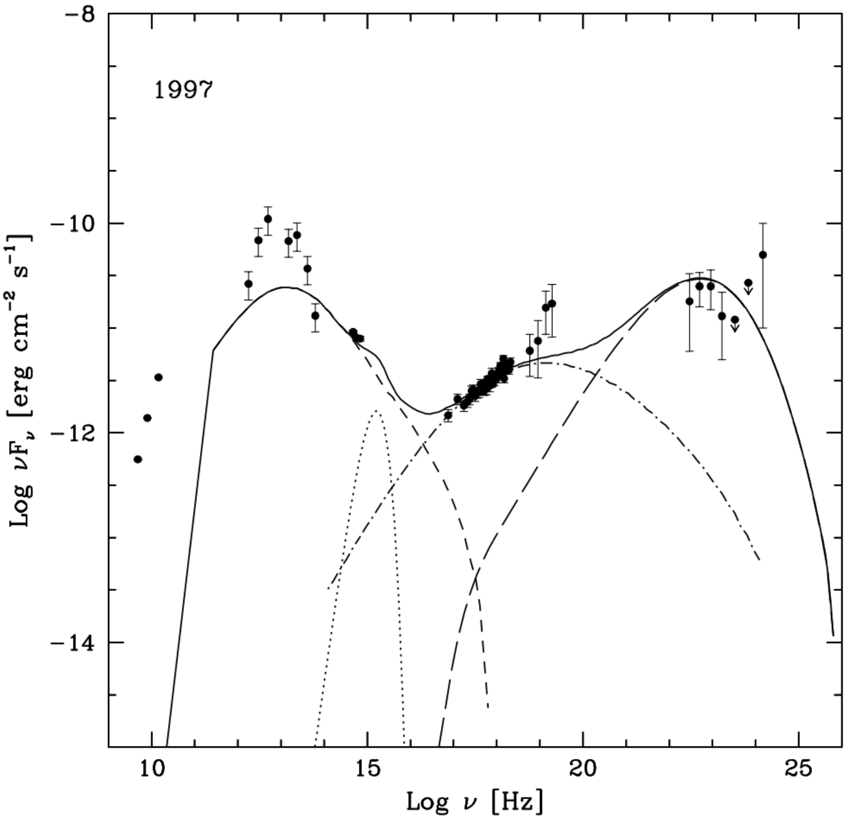

Figure 1.5: SED of 3C 279 with observations of BeppoSAX in 1997. The synchrotron component is presented as the short-dashed line, EC component the long-dashed line, SSC component the dot-short-dashed line and disk component the dotted line. The solid line is shown as a sum of all components (figure taken from [86]).

Combining the gamma-ray emission via Leptonic model with different emission components of AGN, we can see in general different components are responsible for emission of photons in different energy bands [71, 87]. The jet emits non-thermal radiation via synchrotron and IC (SSC) due to the energetic plasma (in form of relativistic electrons) contained within it, covering an emission band of optical to γ-ray. The accretion disk emits thermal radiation, occupying the band of optical to ultraviolet. The dust torus emits mainly infrared photons that further leads to EC process on dust-torus emission.

1.1.2.2 Hadronic models

Alternatively, γ-rays can be produced with hadronic models. The interaction of high-energy protons (from the plasma of jet) and the surrounding environment (radiation field, other particles within the jet) is the starting point for these models. In general, a hadronic (nucleonic) cascade process is first initiated by a hadron colliding with nucleons [62, 88, 89]. Charged ($\pi^{\pm}$) and neutral (π^0) pions are the end products of this hadronic process. The neutral pions have very short lifetime ($\approx 10^{-17}$ s), they thus decay immediately into two photons $\pi^0 \to \gamma + \gamma$ with a branching ratio of about 99%, and each of these two photons carry approximately half of the energy of π^0. The subsequent π^0-produced γ-rays can interact with electrons or other radiation fields and thus begin the electromagnetic cascade process. Whereas charged pions have slightly longer lifetime ($\approx 10^{-8}$ s), and they would first decay to muons before decaying into electrons, e.g., for π^+: $\pi^+ \to \mu^+\nu_\mu$, $\mu^+ \to e^+\nu_e\bar{\nu}_\mu$.

The high-energy bump (see e.g. in Fig. 1.5) in hadronic models is associated with the synchrotron radiation of ultrahigh energy protons [90, 91] and/or their interactions with surrounding photons. As described in the previous Subsection 1.1.1, protons are accelerated to ultrahigh energies together with electrons, but they suffer significantly more energy loss in the synchrotron process in comparison to electrons. These very high energy protons can collide with low-energy internal and/or external photons, where these photons could come from synchrotron radiation of the same population of the relativistic electrons [90, 92] or surrounding environment [91, 93]. This so-called *photonproduction* [62] can lead to two different end products via the Δ^+ resonance:

$$\begin{aligned} p + \gamma &\to \Delta^+ \to \pi^+ + n, \\ p + \gamma &\to \Delta^+ \to \pi^0 + p. \end{aligned} \tag{1.1}$$

However, the cross-section of the processes shown in Eq. (1.1) depends crucially on the ambient photon density of the environment. The decay products π^+ and π^0 (in Eq. (1.1)) then decay further following the previously stating processes. The energy of the γ-ray photons produced by π^0 depends naturally on the energy carried by π^0 itself, and gives rise to the high-energy bump in the SED of AGN. By comparing the masses of secondary p and π^0, we can estimate the energy of the γ-ray photons produced by π^0 is roughly about one tenth of the energy of the produced protons p.

In case of proton-proton interactions for hadronic collision, they are commonly neglected in (e.g.) blazar spectra for the reason that the particle density is too low for them to be prominent [94], although such process for hadronic models should be carefully taken into account in denser environments (see e.g. [95, 96]).

Although leptonic and hadronic models are employed accordingly in different scenarios, they may present and account for gamma-ray emission in different regions at the same time. For example, in Böttcher et al. [97], the authors described implementation of both leptonic and hadronic models for broadband emission of blazars detected by *Fermi*-LAT.

Alternatively, it has also been discussed that the observed γ-rays could be produced by exotic particles (see e.g. [62]). In particular, γ-rays could originate from the decay or annihilation of these exotic particles.

1.2 Detection of HE and VHE gamma-rays

Gamma-rays (emitted from AGN), with the shortest wavelength in the range of electromagnetic spectrum, is the most energetic radiation that has been detected by various astronomical instruments and observatories scattered in different locations. Direct detection of gamma-rays, however, can only be carried out from space platforms as the atmosphere is opaque to such high-energy photons. The *Fermi Gamma-ray Space Telescope* is one of the most prominent gamma-ray detection telescope operated in the space, originally known as the Gamma-ray Large Area Space Telescope (GLAST) (see [98] for an overview of the gamma-ray sky covered by *Fermi*). *Fermi*'s main instrument, the Large Area Telescope (thereafter, *Fermi*-LAT) surveys the entire sky once every three hours on a daily basis, and is sensitive to gamma-rays in an energy range of 20 MeV to $> 300\,\mathrm{GeV}$[2]. *Fermi*'s secondary instrument to augment the study of gamma-ray bursts, the Gamma-ray Burst Monitor (GBM), provides spectral coverage of gamma-ray bursts that extends to even lower limit than LAT. With *Fermi*-LAT and GBM, *Fermi* opens opportunities to explore various interesting phenomena of the Universe best studied in the gamma-rays: the supernova remnants, gamma-ray bursts, pulsar wind nebulae (PWN), AGN, EBL intensity, binary sources, pulsars and diffuse gamma-ray radiation (see Fig. 1.6 for an example of the gamma-ray sky recorded by *Fermi*-LAT). Among these, the AGN-dominated extragalactic γ-ray regime is the main subject of this work. *Fermi*-LAT has successfully detected 2295 AGNs by the time of writing (AGNs here are exclusively referring to 1456 BL Lac type blazars, 794 FSRQs and 45 radio galaxies, which are marked separately in Fig. 1.6). The very bright horizontal strip in Fig. 1.6 roughly outlines the Galactic plane, which is a source of diffuse emission resulted from interactions of cosmic-rays with interstellar gas and photons (see Appendix D for some relevant information) [98].

---

[2] `https://fermi.gsfc.nasa.gov/ssc/data/analysis/documentation/Cicerone/Cicerone_Introduction/LAT_overview.html`

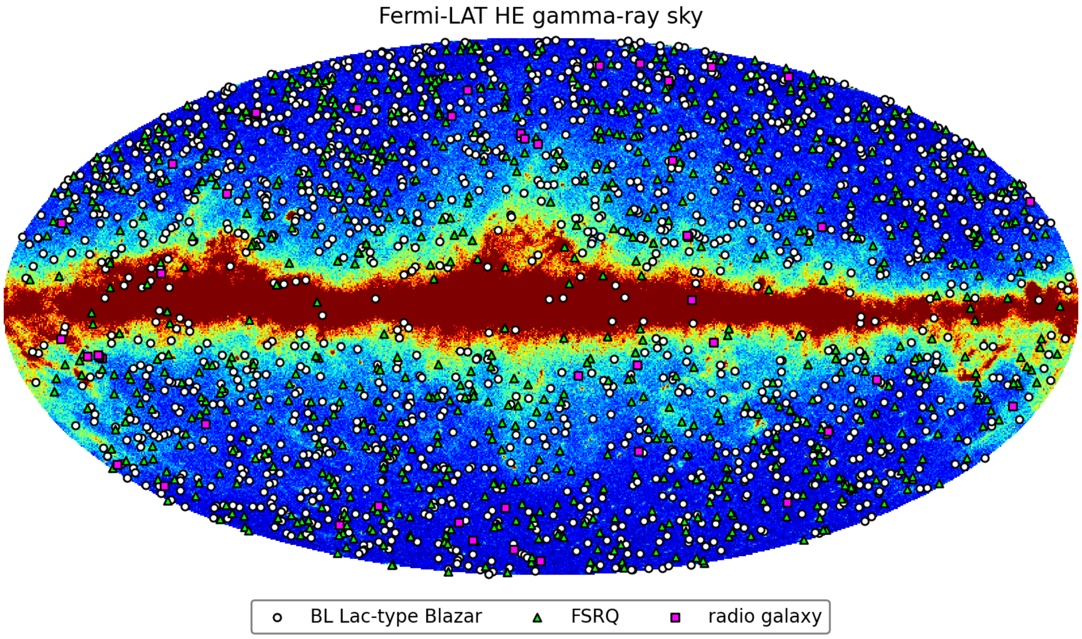

Figure 1.6: The gamma-ray sky recorded by *Fermi*-LAT from 2008 to 2022 with an energy cut in 1 GeV – 10 GeV, shown in Galactic coordinates in a Hammer-Aitoff projection. Brighter colors indicate higher γ-ray intensities. AGNs, such as BL Lac type blazars, FSRQs and radio galaxies are marked respectively with white circles, green triangles and magenta squares.

1.2.1 The *Fermi* Large Area Telescope

The γ-ray astronomy truly blossomed with the launch of the Compton Gamma-ray Observatory (CGRO) in 1991-2000, in particular with its main instrument, the Energetic Gamma-ray Experiment (EGERT), observing the 20 MeV $\sim$ 30 GeV gamma-ray sky [99]. EGRET detected about 60 γ-ray sources associated with AGNs, and almost all of them being blazars [100].

In 2008, with the launch of *Fermi*, a new chapter for the astrophysical gamma-ray investigation begun [48, 101]. The main instrument of *Fermi*, the imaging Large Area Telescope with a wide field of view (about one-fifth of the entire sky), has improved significantly in terms of effective area, solid angle, energy range coverage, angular resolution (at higher energies) in comparison to EGRET. *Fermi*-LAT is built to conduct long-term gamma-ray observation of celestial sources in the energy range $\sim$ 20 MeV to $>$ 300 GeV [48, 102]. *Fermi*-LAT can identify and observe sources accurately, it can measure locations of bright sources to within 1 arcminute. Also, the LAT has great capability of measuring bursts of gamma-rays over short time intervals. We summarize some of the other characteristics of *Fermi*-LAT in Table 1.1[3] (see detailed discussion of these characterized parameters in later text).

---

[3] `https://fermi.gsfc.nasa.gov/ssc/data/analysis/documentation/Cicerone/Cicerone_Introduction/LAT_overview.html`

TABLE 1.1: Characteristics of the LAT instrument performance (table adapted from the Fermi Science Support Center (FSSC), for more details see [48]).

Parameters	**Value or Range**
Energy Resolution	$< 15\%$ at energies $> 100\,\mathrm{MeV}$
Effective Area	$> 8000\,\mathrm{cm}^2$ maximum effective area at normal incidence
Single Photon Angular Resolution	$< 0.15^\circ$ for E $> 10\,\mathrm{GeV}$ $< 0.6^\circ$ for $1\,\mathrm{GeV} <$ E $< 10\,\mathrm{GeV}$ $< 3.5^\circ$ for E $= 100\,\mathrm{MeV}$
Source Location Determination	< 0.5 arcmin for high-latitude sources
Point Source Sensitivity	$< 6 \times 10^{-9}\,\mathrm{ph\,cm^{-2}\,s^{-1}}$ for E $> 100\,\mathrm{MeV}$
Time Accuracy	$< 10\,\mu$s, relative to spacecraft time
Background Rejection (after analysis)	$< 10\%$ residual contamination for $100\,\mathrm{MeV} <$ E $< 300\,\mathrm{GeV}$
Dead Time	$< 100\,\mu$s per event

The LAT has four main subsystems that work together to detect γ-rays and reject signals from the intense cosmic-rays: Tracker, Calorimeter, Anti-coincidence Detector (ACD), and Data Acquisition System (DAQ) (see Fig. 1.7) [102]. It shows more clearly in Fig. 1.8 of how the LAT detects gamma-rays. When a gamma-ray photon enters the LAT, it first goes into the ACD, and then continue to propagate to the trackers. The Tracker consists of an array of 4×4 tower modules, and each tower module consists of layers of silicon-strip particle tracking detectors interleaved with thin tungsten conversion foils. The gamma-ray photon then interacts in one of the 16 tungsten foils and converts into electrons and positrons (as shown in Fig. 1.8) via pair production. The silicon strips are used to track the moving paths of the e^+e^- pair, which are then used to determine the arrival direction of the gamma-ray photon. After the electron-positron pair are produced, they hit the Calorimeter, which is made of a material called cesium iodide and it measures the energies of the incoming particles by producing proportional intensity of flashes of light, and therefore, the energy of the gamma-rays that enter the LAT. Finally, the DAQ subsystem is comprised of specially designed electronics and microprocessors, it gathers information from the ACD, the Tracker, and the Calorimeter, then based on the collected information it can reject the unwanted signals (e.g. cosmic-rays) and record the real gamma-ray events.

If cosmic-rays enter the LAT, they would immediately induce a signal as they pass

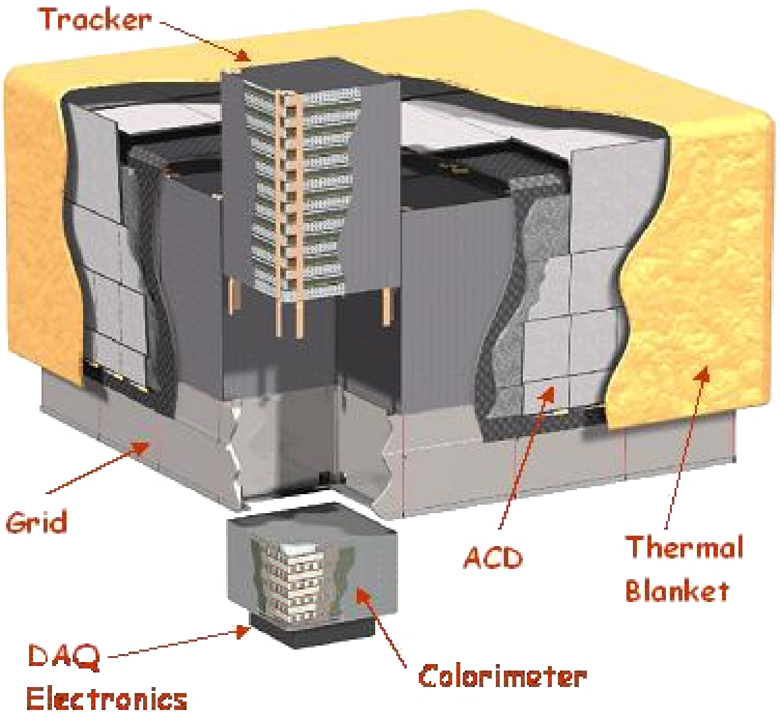

FIGURE 1.7: The *Fermi*-LAT structure (figure adapted from the FSSC).

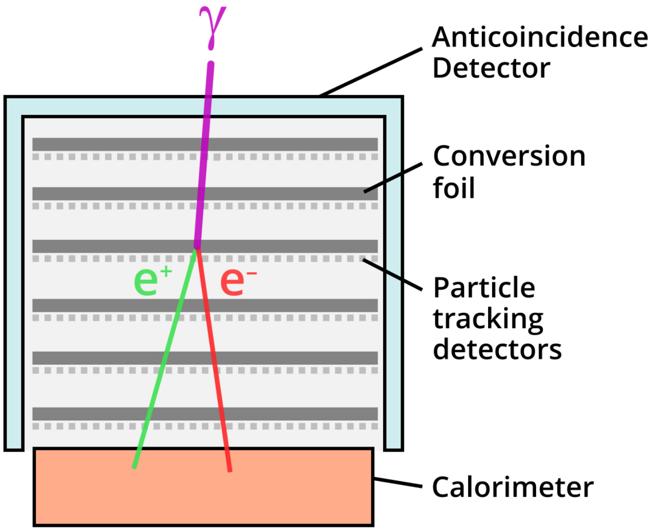

FIGURE 1.8: Illustration of the detection scheme in LAT (figure adapted from the FSSC).

through the ACD. According to the LAT team, the ACD rejects up to 99.97%[4] of signals produced by cosmic-rays that enter the LAT. The ACD produces flashed of light when hit by charged (cosmic-ray) particles. Furthermore, the pair-production signature

---

[4] See `https://www.nasa.gov/content/goddard/fermi-spacecraft-and-instruments` for more detailed description of the LAT subsystems.

found in the gamma-rays can also be used to help reject larger background of cosmic-rays when they enter the Tracker subsystem, Similarly, the Calorimeter also helps to reject cosmic-ray event since its pattern of energy deposition is quite different in comparison to that of gamma-ray event. The DAQ then combines information received from the other three subsystems and make the initial decision of whether or not this event is cosmic-ray.

***Fermi*-LAT Performance**:
Detection of the gamma-ray events not only depends on the LAT hardware but also the way how LAT is processing the observables and register the incoming event as a photon, i.e., estimating the probability of event being a photon and the mapping of photon flux to detected photon events. This part of event reconstruction is closely linked to the performance of the LAT. Because of this, in process of event reconstruction for the latest `Pass 8` data the LAT makes cuts and classifies the incoming events into the following generalized *standard* classes based on the likelihood of events as photons and quality of reconstruction [48]:

- TRANSIENT (`evclass=16, 64`): The TRANSIENT class is with the loosest selection criteria, but with a relatively high background contamination from isotropic diffuse gamma-ray emission [103]. Thus this class is particularly useful for short-period observation, such as gamma-ray bursts and relevant timing studies (as these types of analysis can benefit from an increased photon statistics while tolerating the background flux to some extension).

- SOURCE (`evclass=128`): The SOURCE class provides an intermediate selection with decent photon statistics and low background contamination. It is the most widely used event class for general analysis of e.g. point sources and extended sources over medium to long timescales. It is the event class used in this work.

- CLEAN (`evclass=256`): This class selects the same events as the SOURCE class below 3 GeV. However, it has about 1.3-2 times lower background and offers better photon statistics to hard spectrum sources at high galactic latitudes compared to SOURCE class.

- ULTRACLEAN (`evclass=512`)/ULTRACLEANVETO (`evclass=1024`): The ULTRACLEANVETO is the cleanest class with the most restrict selection for all energies in `Pass 8`. It is recommended by the LAT team for cosmic-ray induced gamma-ray emission and diffuse studies that need low background contamination of cosmic-ray. ULTRACLEAN class shares similar features for event selection and lower background level with ULTRACLEANVETO class: 15%-20% lower background rate below 10 GeV in comparison to SOURCE class, and 50% lower at 200 GeV.

- SOURCEVETO (`evclass=2048`): The SOURCEVETO is also one of the most restrictive event selection class in `Pass 8`, but not at all energies. Similarity is shared in terms of background flux level for SOURCEVETO and ULTRACLEANVETO in energies below 10 GeV and above 50 GeV.

These classes select and reconstruct events via different sets of instrument response functions (IRFs) of their own, characterizing importantly the LAT performance. Noticeably, the IRFs for each unique class are further divided based on the newly introduced *event types* in `Pass 8`. There are three different event types that partition and select events further within one class:

- Conversion event type: The events are divided depending on where the conversion of $\gamma \rightarrow e^+e^-$ takes place in the Tracker. Conversions that occur in the first 12 layers of conversion foils are the FRONT-converted events, while in the back 4 layers are the BACK-converted events.
- Point spread function (PSF) event type: Depending on the quality of the reconstructed direction, events are characterized as PSF0 (the worst), PSF1, PSF2 and PSF3 (the best) event types.
- Energy dispersion event type: Depending on the quality of the reconstructed energies, events are divided into EDISP0 (the worst), EDISP1, EDISP2 and EDISP3 (the best) event types.

These unique event classes and event types are a result of the LAT's changing sensitivity in different energies and different parts of the instrument. There are three factors that are taken into account when evaluating the performance of LAT: i) the hardware design, which has been briefly discussed in the introduction of LAT components; ii) the event reconstruction algorithms; iii) background subtractions and event quality selections. The performance of LAT (see also [104] for energy performance below 100 MeV) is summarized in the recently updated `Pass 8 Release 3 Version 3`[5] (known as `P8R3_V3`) IRFs. These IRFs provide information about the performance of LAT in terms of effective area, acceptance, point spread function (PSF), energy resolution as a function of photon energy, incidence angle θ, azimuthal angle ϕ and other parameters. Different IRFs should be used accordingly when dealing with different classes (and types) of

---

[5] `https://www.slac.stanford.edu/exp/glast/groups/canda/lat_Performance.htm`

events. For example, in Fig. 1.9 we present the effective area of the LAT instrument for SOURCE class of `Pass 8` data as functions of photon energy and incidence angle. The effective area is a measure of detector's efficiency in capturing gamma-ray photons, i.e., the probability of these photons interacting with tungsten foils in the Tracker. As we can see that the effective area for SOURCE class is mostly sensitive to photons with energy in range of 1 GeV to 100 GeV, where the LAT reaches the highest detection efficiency, but drops as the energy of incidence photon continues increasing. Such decrease of effective area at higher energies (above several hundreds of GeV) is because on the one hand, lower flux of incoming high-energy photons enters LAT, and on the other hand, the charged particles are deflected in magnetic fields many times and other complex interactions take place, causing losses of event reconstruction accuracy. In addition, the effective area shows a consistent decrease as the incidence angle of photon increases, as expected. Another LAT performance parameter, *acceptance*, is defined as the effective area integrated over the solid angle, and thus similar to what effective area presents in Fig. 1.9. However, it should be noted that the LAT field of view does have some dependence on energy since the secondary particles produced by higher energy gamma-rays have smaller opening angles, and thus more easily detected by LAT.

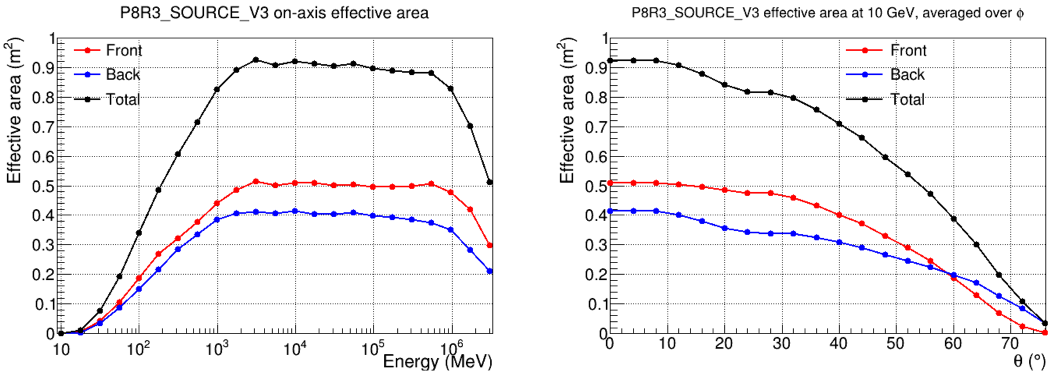

FIGURE 1.9: Left panel: The effective area of LAT as a function of energy for photons with $\theta = 0°$ for SOURCE class in `Pass 8` data. Right panel: The effective area as a function of incidence angle θ for photons at 10 GeV (figures taken from here[6]).

The point spread function of LAT is a probability distribution for reconstructed directions of incidence photons from a point source [48]. It is a function of photon energy and inclination angle, defined as a scaled-angular deviation (see here[7] for details of PSF):

$$\mathrm{PSF} = \frac{\delta p}{S_P(E)} = \frac{2\sin^{-1}\left(\frac{|p'-p|}{2}\right)}{S_P(E)}, \tag{1.2}$$

---

[6] `https://www.slac.stanford.edu/exp/glast/groups/canda/lat_Performance.htm`

[7] `https://fermi.gsfc.nasa.gov/ssc/data/analysis/documentation/Cicerone/Cicerone_LAT_IRFs/IRF_PSF.html`

where p' and p are respectively the reconstructed and true directions of the incidence photons. δp stands for the deviation and $S_P(E)$ is the scale factor. Parameters related to $S_P(E)$ and incidence directions are derived entirely through fitting and Monte-Carlo simulation in `P8R3` data. In the left panel of Fig. 1.10 we show an example of the (acceptance) weighted PSF performance for SOURCE class conversion-type events, where the containment angle shows the angular radius within which 68% (black solid line) and 95% (black dashed line) of the total incidence photons at different energies are detected and reconstructed by the instrument. As the name in left panel of Fig. 1.10 suggests, the containment angle parameter is tied to the LAT acceptance performance, where incidence photons with higher energies lead to spreading of point source with smaller angular radius, and therefore indicating a better angular resolution (e.g. $\lesssim 1^\circ$ for photons with energies greater than 1 GeV for both 68% and 95% containment, see also Table 1.1 for summarized LAT parameters). Conversely, the LAT instrument shows very poor single photon angular resolution for photons with energy below 100 MeV.

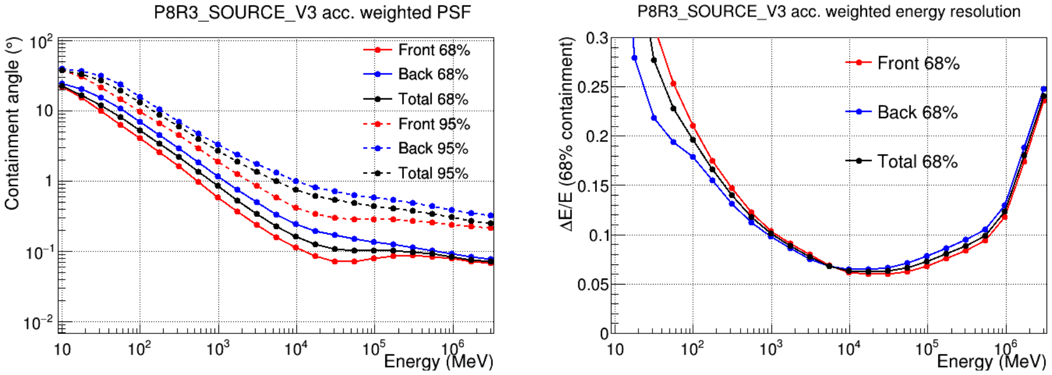

FIGURE 1.10: Left panel: The 68% and 95% containment angles of the acceptance weighted PSF for SOURCE class conversion-type events in `P8R3` data. Right panel: 68% containment half width of the measured (reconstructed) incidence photon as a function of energy (figures taken from here[8]).

The energy resolution of LAT, also known as the energy dispersion, is a probability distribution of measured energies, characterized by the energy dispersion response function of LAT[9]. *Fermi*-LAT internally expresses this response function as a product of energy dispersion matrix (see e.g. Fig. 4.4 in Chapter 4), which can be used to correct energies of photons as it demonstrates how true energies are redistributed with measured energies. The energy resolution can reach less than 10% (see right panel of Fig. 1.10) for energies in between 1 GeV and 100 GeV, which is sufficient to provide accepted systematic uncertainties in this energy range. Particularly, the energy resolution worsens for measuring energies below 100 MeV. Thus it becomes very important to implement the energy dispersion matrix for correcting energies when analyzed energy is around 100 MeV

---

[8] `https://www.slac.stanford.edu/exp/glast/groups/canda/lat_Performance.htm`

[9] `https://fermi.gsfc.nasa.gov/ssc/data/analysis/documentation/Pass8_edisp_usage.html`

or below. The reason for such bad resolution is due to the detector response. At low energies, the dominated interaction between gamma-rays and the Tracker is Compton scattering where electrons attain low energy depositions, leading to less distinguishable signals in comparison to interactions of Tracker with high-energy gamma-rays (via pair-production). In addition, when the energy of incoming gamma-ray flux increases, it also becomes challenging for LAT to distinguish different energies as high-energy incidence photons would induce more complex interactions and multiple scattering processes in the instrument, making it very difficult to reconstruct energies as well as directions of the incidence photons. This thus results in an upturn for the curves in right panel of Fig. 1.10.

Since the beginning of the *Fermi* mission the LAT collaboration has released: the bright γ-ray source list (0FGL) [105], the first full source catalogue (1FGL) [101], the second full source catalogue (2FGL) [106], the third full source catalogue (3FGL) [107], the fourth full source catalogue (4FGL) [108], the fourth source catalogue data release 2 (4FGL-DR2) [109] as well as the fourth source catalogue data release 3 (4FGL-DR3) [110]. With each release of the new catalogues or new observational data, analysis method and characteristic of sources (such as the spectral model, background templates) are updated and further optimized, in addition to the newly detected sources and improvement of statistics. Furthermore, in order to reduce contamination by diffuse γ-ray emission, the LAT team has also released special catalogues focusing on AGN sources with galactic latitude $|b| > 10^\circ$ (see e.g. [111]).

The most recent release (as time of writing) is the 4FGL-DR3 source catalogue [110], as an incremental version of the 4FGL catalogue. It is a collection of 6658 sources based on the first 12 years of observations (2008 to 2020) in the energy range of 50 MeV to 1 TeV. The major improvements in terms of characterizing sources comparing to previous catalogues are: i) more sources are fitted with curved spectra; ii) a more robust spectral parameterization is introduced especially for pulsars, and spectral points are extended to 1 TeV.

Fermi-LAT has successfully detected significantly more sources (especially γ-ray sources) than any previous γ-ray detection missions. This equips us with great opportunity and potential for the endeavor of studying the non-thermal γ-ray Universe.

1.2.2 Imaging Atmospheric Cherenkov Telescopes

While the MeV to GeV γ-ray observation is nicely performed by *Fermi*-LAT, higher energies, GeV to TeV gamma-rays are mainly measured by the ground-based Imaging Atmospheric Cherenkov Telescopes (IACTs). There have been several attempts to detect gamma-rays on the ground since 1950s [112], while the first meaningful detection started with the observation of Crab Nebula by the Whipple IACT since the operation in 1986 [113]. VHE γ-rays produced from specific environments of astrophysical objects, such as AGNs, starburst galaxies, GRBs, supernova remnants, pulsars, etc., if detected on the ground, can only be detected indirectly via secondary particles since these VHE γ-rays would interact with the air molecules when they enter the atmosphere of Earth. There are three main examples of the existing IACTs (see Fig. 1.11, and see footnote for images credits[10]): the High Energy Stereoscopic System (HESS) [114], the Major Atmospheric Gamma-ray Imaging Cherenkov Telescopes (MAGIC) [115] and the Very Energetic Radiation Imaging Telescope Array System (VERITAS) [116]. The energy range that these IACTs are sensitive to are roughly from $\sim 20\,\mathrm{GeV}$ to several tens of TeV, depending on the performance of the individual telescopes.

The HESS is a five-array IACT, consisting of four 12 m diameter and one 28 m diameter reflectors, located in Namibia at an altitude of 1.8 km. HESS started operating since 2004 with four array IACTs of each of the reflector at a diameter of 12 m. The fifth telescope with a reflector of 28 m was added and placed in the center of the array in 2012. The large mirror dishes make HESS capable of probing energies as low as $\sim 30\,\mathrm{GeV}$. MAGIC, located on the Canary Island of La Palma, consists of an array of two IACTs with a 17 m diameter for each reflector. It started operating since 2004 with only one telescope, and in order to achieve a better sensitivity and angular resolution, a second one was added in the year of 2009. The triggering threshold of gamma-ray energies is about 50 GeV [117]. VERITAS is a four-IACT array with each reflector at a diameter of 12 m, located at Whipple Observatory at an altitude of 1.3 km and started operating since 2007 in the energy range of roughly 100 GeV to several tens of TeV. Other operational IACT includes the First G-APD Cherenkov Telescope (FACT) [118], which is a single IACT with a 4 m diameter reflector located on the Canary Island of La Palma, operating since 2011.

Cherenkov Telescope Array[11] (CTA) is a planned project for the next-generation IACTs, intending to probe the γ-ray sky over a relatively larger energy range from 20 GeV to 300 TeV [119]. More than 60 telescopes will be used by the CTA team in two array sites located in northern and southern hemisphere (as rendered in Fig. 1.12). In the northern hemisphere (on Canary Islands of La Palma, Spain), the telescope array will aim at CTA's low- and mid-energy range from 20 GeV to 5 TeV, while in the southern site (Paranal, Chile), the telescope array will focus more on the mid- to high-energy

---

[10] HESS: `https://www.mpi-hd.mpg.de/hfm/HESS/pages/press/2012/HESS_II_first_light/images/Image_13.JPG`; MAGIC: `https://magic.mpp.mpg.de/gallery/pictures/tn/IMG_2576.JPG.html`; VERITAS: `https://veritas.sao.arizona.edu/images/stories/veritas_and_building.jpg`.

[11] `https://www.cta-observatory.org/`

[12] `https://www.cta-observatory.org/about/how-ctao-works/`

Figure 1.11: From top to bottom: the HESS (4+1) array of IACTs located in Namibia, consisting of four 12 m diameter and one 28 m diameter telescopes; the two 17m-diameter-dish array of MAGIC located on the Canary Island of La Palma; the four 12 m diameter IACT array of VERITAS located at Mt Hopkins, Arizona.

range of the CTA as it attains better sensitivity (see also Fig. 1.13) with the advantage of its Small-Sized Telescopes (SST), covering sky of gamma-ray energies from 150 GeV

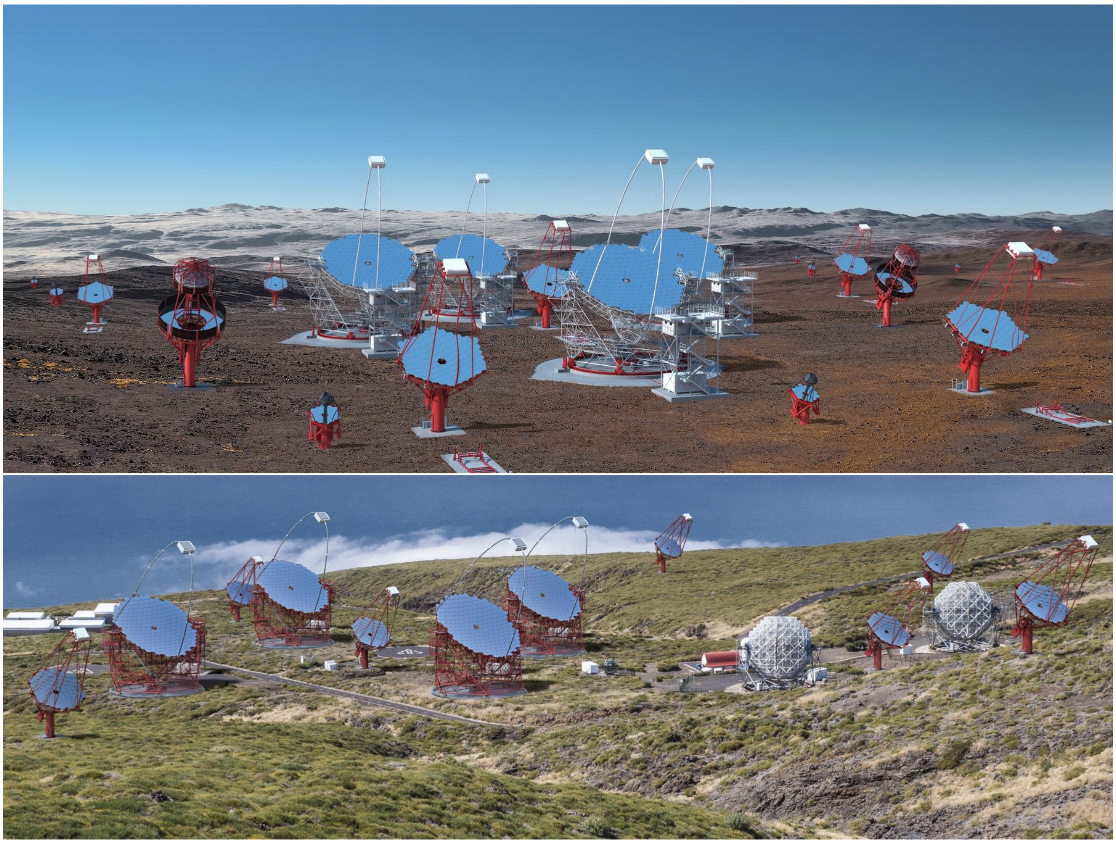

Figure 1.12: Artistic illustration of two CTA sites in southern (top) and northern (bottom) hemisphere. Image credits: Gabriel Pérez Diaz, CTAO ERIC[12].

to 300 TeV. Besides SSTs, two other types of telescopes will also be used in these two observation sites: the Large-Sized Telescope (LST), and Medium-Sized Telescope (MST). While SSTs are ideal for improving CTA's sensitivity at the highest energies, LSTs are responsible for optimizing sensitivity at low energies with their large reflectors. The MSTs will be deployed in both sites as they are probing CTA's core energy range. The CTA team has finalized the first configuration phase (the "Alpha Configuration"), which plans to distribute 4 LSTs and 9 MSTs in the northern site, and 14 MSTs and up to 37 SSTs in the southern site. CTA will be an international project for future VHE gamma-ray observation with Cherenkov telescopes, and will eventually become one of the leading gamma-ray observatories with potential synergies with other observational sites in other energy bands [117].

In Fig. 1.13 we show differential flux sensitivity of various instruments covering energy band from X-ray to gamma-ray[13] (the X-ray instruments are, however, of irrelevance to this study). This includes the past (e.g. EGRET) and current gamma-ray detectors (e.g.

---

[13] Noticing some of the sensitivity curves are not accurate enough as they were extracted from other plots by the authors of [62]. We remind readers to use these curves with caution.

Fermi-LAT, HESS), along with future instruments, such as CTA and e-ASTROGAM[14].

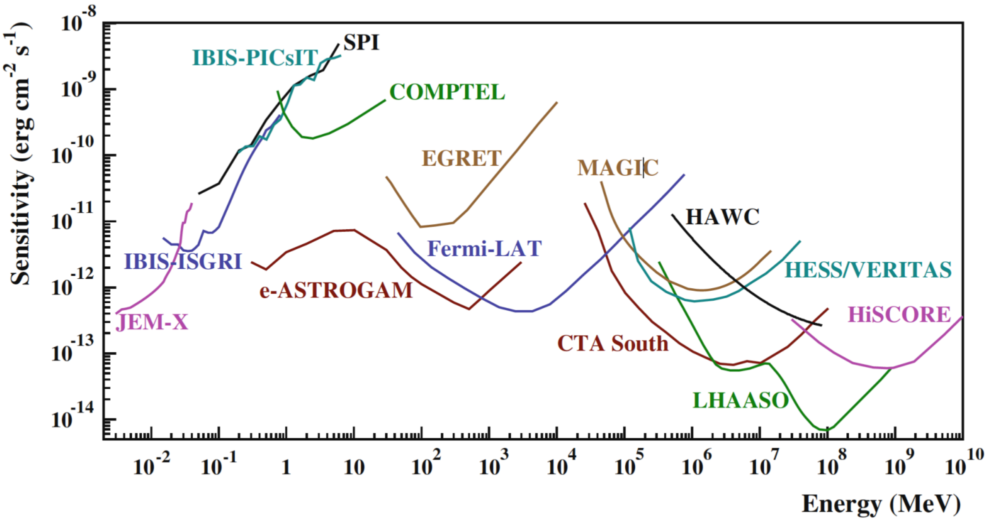

FIGURE 1.13: Point source continuum differential flux sensitivity of various instruments for X-ray and gamma-ray observations. The curves for JEM-X, IBIS-ISGRI, IBIS-PICsIT, and SPI are obtained with an effective observation time of 10^6 s. Sensitivities of COMPTEL and EGRET are calculated for observation time accumulated during 9 years of the CRGO mission. The *Fermi*-LAT sensitivity is derived for observing high Galactic latitude sources in a 10-year survey mode. Sensitivities of IACTs, including MAGIC, HESS, VERITAS, and CTA are given with a 50 hours of observation time. HAWC, LHAASO and HiSCORE are give with observation time of 5 years, 1 year and 1000 hours respectively. Sensitivity of future space mission is also shown with a 3σ confidence level for an effective expousre of 1 year for a high-Galactic latitude source (figure taken from [62]).

IACTs detect gamma-ray photons via indirect means (see Fig. 1.14 for an example of working principle of IACTs). When γ-rays enter the atmosphere of Earth they interact with the nucleus of air molecules in the atmosphere, producing a vast number of secondary particles such as electrons and positrons through pair-production process at high latitude. These high-energy electrons and positrons then radiate secondary gamma-ray photons mainly via *bremsstrahlung* process as they can be deflected by nucleus or other charged particles, after which the gamma-ray photon goes into the pair-production again and generate low-energy photons, and therefore, a shower of particles [62, 117]. These air shower charged particles reaching ground can be directly detected by the *Extensive Air Shower* technique [117]. Alternatively and more commonly adopted is the indirect observation of these shower particles, since they can emit Cherenkov radiation when they travel faster than the speed of the light in the same atmosphere medium. The very faint Cherenkov light are collected and focused by the highly reflective segmented mirrors on the telescopes, then pointed onto a camera placed in front of mirror dishes.

---

[14] e-ASTROGAM is a proposed space-based mission aiming at probing astrophiscal sources in energy range of 300 keV to a few GeV (see [120] for more details).

These cameras are composed of arrays of photomultiplier tubes (PMTs) or silicon photomultipliers (SiPMs) that can detect individual photons. The imaging intensity map by PMTs is related to the energy of the shower, and then to the primary gamma-rays, while the orientation of the map indicates the air shower direction (see Fig. 1.14).

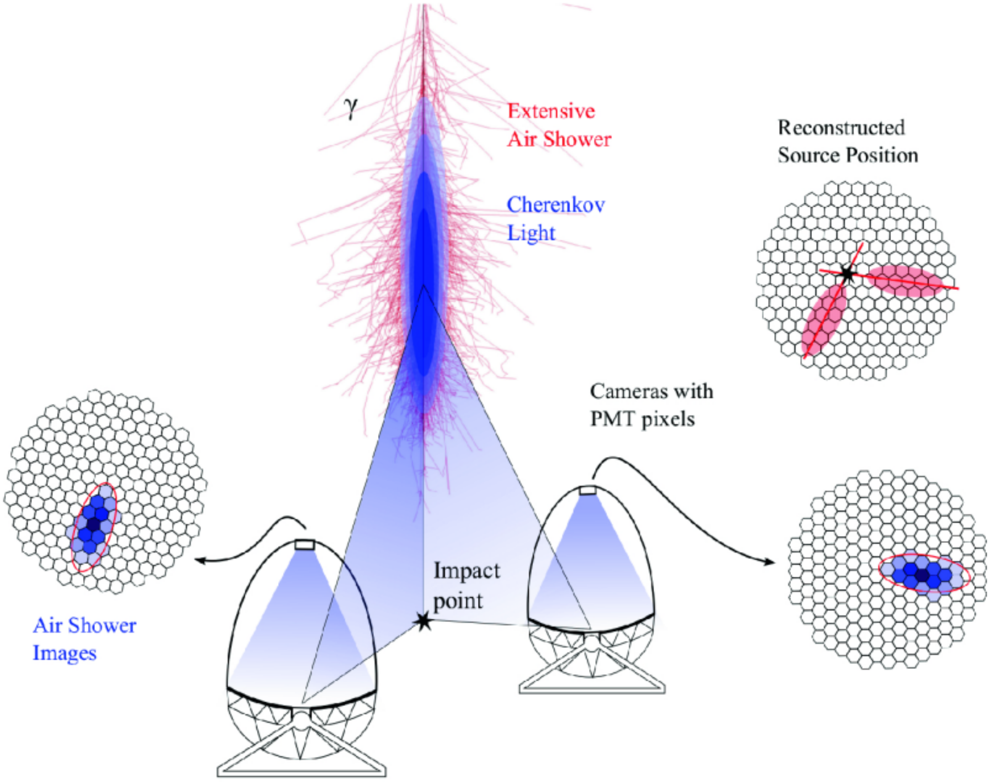

FIGURE 1.14: A schematic view of working principle for stereoscopic imaging telescopes. Primary gamma-rays initiate a cascade air shower (denoted with pink curves). The resulted secondary charged particles produce Cherenkov light (denoted with blue shaded area), collected by mirror dishes of telescopes and captured by PMTs on the central cameras. A reconstructed source position from two telescope images are also shown (figure taken from [117]).

Similar to *Fermi*-LAT, one of the main background contamination for IACTs is the cosmic-rays, and the other is the night sky background. Air shower induced by cosmic-rays are initiated by charged particles colliding with nucleus in the atmosphere (see Fig. 1 in [117]). Charged and neutral pions are produced by this collision. π^0 decays immediately into γ-ray photons, whereas $\pi^{\pm}$ decay into $\mu^{\pm}$ and their associated neutrinos. Charged particle products (such as electrons, muons) then emit Cherenkov light, the same process as described for gamma-ray initiated air shower. Due to the differences in the air shower development, muon compositions (fewer muons are produced in gamma-ray initiated shower), arrival time of Cherenkov photons (secondary particles in cosmic-ray initiated air shower take longer time to reach ground) as well as its distribution on the air shower image, the gamma-ray induced Cherenkov light can be separated from the the ones produced from cosmic-rays. On the other hand, the night sky background photon flux (order of $10^{12}/(\mathrm{cm}^2\,\mathrm{s}\,\mathrm{sr})$) is orders of magnitudes higher than the generated Cherenkov photons [117]. Given a photon of 100 GeV as the primary gamma-ray, only about 10 Cherenkov photons can be produced per square meter arrive at 2 km altitude above sea level. However, these night sky photons peak at different wavelengths in comparison to Cherenkov photons and therefore can be suppressed significantly by selecting specific PMTs for the telescope camera [117].

Thus, in order to obtain a gamma-ray spectrum or a light curve of a target source (as they are commonly used in the analysis for interpreting the characteristics of target sources), a complicated series of steps is needed to reconstruct the gamma-ray data emitted by a target source from recorded data of Cherenkov light. The energy of the detected gamma-ray photons are reconstructed based on the intensity and spatial distribution of the Cherenkov light with (e.g.) unfolding method. Unfolding method based on different algorithms (e.g. iterative method, Bayesian techniques) corrects the effects rising from the instrument's response function and resolution. The flux is then calculated with Monte-Carlo simulation of the so-called "OFF" data (background events recorded by the telescopes), taking into account the collection area of the telescopes and effective exposure time of the observation.

1.3 ALPs enter gamma-ray observation

Observations of HE and VHE gamma-rays opens a unique opportunity to study many interesting and the most extreme astrophysical phenomena in the Universe with the highest energies, serving as a complementary approach to the laboratory experiments of high energy physics. However, when γ-rays produced by AGNs, GRBs, PWNs, Supernova remnants or from a proposed DM annihilation/decay [62] start to propagate, they interact with the surrounding environment via different processes. Before being observed on Earth, gamma-ray photon beam is involved in all types of scattering processes with other particles [121–123], absorption by dust or particles (EBL absorption [124], internal photon absorption [125, 126]), and interactions with background magnetic fields. One prominent interaction is the gamma-ray photons coupling to axions/ALPs in the presence of the external magnetic fields, i.e., the photon-ALP mixing effect [25]. This effect offers great insight in re-viewing a wide range of astrophysical observations that can not be well described by conventional physics.

1.3.1 Axion as a motivator

The possibility of photon mixing with a light particle can alter the propagation of gamma-rays in different ways and was first realized in connection with the so-called pseudo-Nambu-Goldstone boson particle, the *axion*. The term "axion" was first introduced by Stephen Weinberg [16] in late 1970s where he discussed experimental implications of a neutral pseudoscalar boson, thereafter, axions. This hypothetical particle was famously known when it was proposed as a solution by Peccei and Quinn to solve the missing CP-symmetry violations in strong interactions (i.e., *the strong CP problem*) [10]. The Lagrangian term describing the CP violation can be written as [10, 19]:

$$\mathcal{L} = \theta_{QCD} \frac{g^2}{32\pi^2} G^c_{\mu\nu} \tilde{G}^{\mu\nu}_c, \tag{1.3}$$

where θ_{QCD} represents an effective true vacuum (tied to rotation of of the gluon field), $G^a_{\mu\nu}$ denotes the gluon field tensor where the subscription c is associated with $SU(3)$ color symmetry, and g is the QCD coupling constant.

The PQ mechanism solves the strong CP problem by introducing a global symmetry, $U(1)_{PQ}$, where all fermion masses have been made real via a suitable rotation of the fermion field, leading $\theta_{QCD} \rightarrow 0$ and thus a CP invariance of the strong interactions. Experimentally, this θ_{QCD} term is closely linked to the measurement of electric dipole moment (EDM) of neutron, d_n, for which an upper limit is set to be $d_n \leq 10^{-26} e\, cm$ [127], indicating a value of $< \mathcal{O}(10^{-10})$ for the θ_{QCD}.

Axion naturally arises as a pseudo-Nambu-Goldstone boson particle with the spontaneous breaking of $U(1)_{PQ}$. The axion mass is given by [128]:

$$m_a \simeq 6\,\mathrm{eV} \left(\frac{10^6\,\mathrm{GeV}}{f_a} \right), \tag{1.4}$$

where m_a is the axion mass, and f_a is its decay constant, indicating the scale (approximately at the order of electroweak scale, $E_{ew} \sim 246\,\mathrm{GeV}$) at which the $U(1)_{PQ}$ symmetry is broken. Axions have a characteristic two-photon vertex (inherited from their mixing with π^0 and η [129]), induced by a one-loop quark-axion Yukawa coupling, as shown in Fig. 1.15. The photon-axion coupling constant $g_{a\gamma\gamma}$ shown in Fig. 1.15 gives the strength of an axion coupling to two photons. The photon-ALP coupling is described by an effective Lagrangian: $\mathcal{L} \sim g_{a\gamma\gamma} F^{\mu\nu} \tilde{F}_{\mu\nu} a$ (where $F^{\mu\nu}$ is the electromagnetic field tensor, see also Eq. (2.1)), implying a dimension of the inverse of energy for $g_{a\gamma\gamma}$ and is given by [59]

$$g_{a\gamma\gamma} \simeq 8 \times 10^{-10}\, k^{-1} \left(\frac{10^6\,\mathrm{GeV}}{f_a} \right) \mathrm{GeV}^{-1}. \tag{1.5}$$

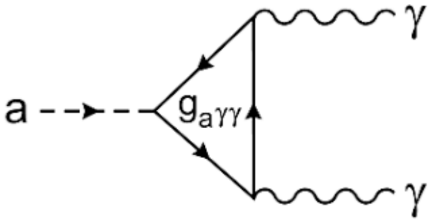

FIGURE 1.15: Feynman diagram of axion's two-photon vertex (figure from [19]), where the internal lines represent fermions.

The coupling constant is inversely proportional to f_a and independent of the mass of the fermions involved in the loop [47, 59]. The parameter k^{-1} implies the strength of coupling is model-dependent (see [130] for more details), which is resulted from the anomalous coupling of axions to gluons at energies below QCD confinement (see e.g. Sec. 90 in [129]). Representative examples for describing the relation of axion mass and coupling are the KSVZ [23, 24] and DFSZ [21, 22] models (see the highlighted orange band in Fig. 1.17). The relation $f_a \gg E_{ew}$ is typically seen in these models, as a result of axions evading almost all current experimental searches. While in KSVZ model axions arise with the breaking of a newly introduced chiral symmetry, where new heavy quarks (electrically neutral) carry $U(1)_{PQ}$ charges and couple to the axion field. Whereas in DFSZ model the ordinary quarks and leptons carry $U(1)_{PQ}$ charges, and axion field is introduced via the two-Higgs-doublet extension of the standard model [131]. In both models, the additional electroweak singlets used to generate the axion field acquire the vacuum expectation values by coupling to other particles and leading to a breaking of the PQ symmetry, and furthermore, the couplings of axions with quarks or leptons all eventually contribute to the axion-photon coupling.

In general, axion's two photon vertex is exploited in a way where the axion converts into a photon (or vice versa) in the presence of a strong external magnetic or electric field [132, 133] (see also Fig. 2.3). In a Coulomb field of charged particles, such conversion takes place in the form of a scattering process ($\gamma + Ze \to Ze + a$), i.e., the Primakoff process [23], where charged particles provide a photon via the magnetic field. On the other hand, a large-scale magnetic field can be used to generate a sea of virtual photons, with which axions can interact and to be converted to real photons (see Fig. 1.16). The latter is used as the main strategy for detection of axions in experiments (see later text for more details).

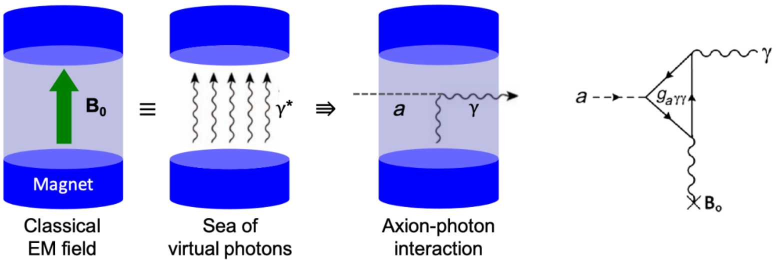

FIGURE 1.16: Illustration of principle of axion detection, along with the corresponding Feynman diagram, where axions convert into photons in the presence of external magnetic field (figure credit: [134]).

1.3.2 The hunt of ALPs

While axion enjoys a strict relationship between its mass and coupling (shown in Eqs. (1.4) and (1.5)) inherited from the corresponding π^0 properties ($m_a f_a \sim m_\pi f_\pi$), a generalized form of axions, namely axion-like particles, may be considered when relaxing the relation of m_a and $g_{a\gamma\gamma}$ is wanted. ALPs arise generically from several models through the extension of SM in addition to axions, including four-dimensional supersymmetric models [4–6], multidimensional Kaluza-Klein theories [7, 8, 135], and especially from the low-energy effective field theories of String theory [9, 17, 136–138]. ALP, as a very light pseudoscalar boson, shares many similar properties with axions. Particularly, their signature coupling to two photons and the inter-conversion of photon-ALP in the presence of external electromagnetic field, i.e., the photon-ALP mixing effect.

This mixing effect can result in two major consequences: 1) oscillation between photons and ALPs can induce a polarization change in the states of photons when they travel in the magnetic field (see e.g. [139]); 2) the $\gamma \leftrightarrow a$ process causes modulations on the photon beam intensity, which results in an attenuation [40] or hardening [33] (or both) of the flux depending on the external electromagnetic fields as well as photon energies.

1.3.2.1 Laboratory searches of ALPs

Searches of ALPs has really entered a blossomy age in the past years, taking place in both laboratories and astrophysical environments. Experimental searches of ALPs in laboratories are extremely challenging due to its significantly fragile coupling to normal matter or radiation fields. For axions/ALPs in the mass range of $\mathcal{O}(\mu\text{eV})$ the haloscope technique is regarded as a promising way to search for axions/ALPs from our Galactic halo with sufficient sensitivity. The axions in this mass range are considered to be plausible cold dark matter (CDM) candidates. The main setup for *haloscope* experiments involves a high-quality resonant cavity, where the frequency of the cavity can be tuned to resonate at a frequency matching the energies of converted photons approximately in the microwave energy band, such that the detecting axion signal is enhanced. This technique is widely used in a number of experiments, e.g., Axion Dark Matter eXperiment (ADMX) [140], Haloscope At Yale Sensitive To Axion CDM (HAYSTAC) [141, 142], Oscillating Resonant Group AxioN (ORGAN) [143], QUest for AXions (QUAX) [144], Magnetized Disc and Mirror Axion eXperiment (MADMAX) (not yet in operation) [145], and various cavity-based experiments in CAPP, Korea [146, 147].

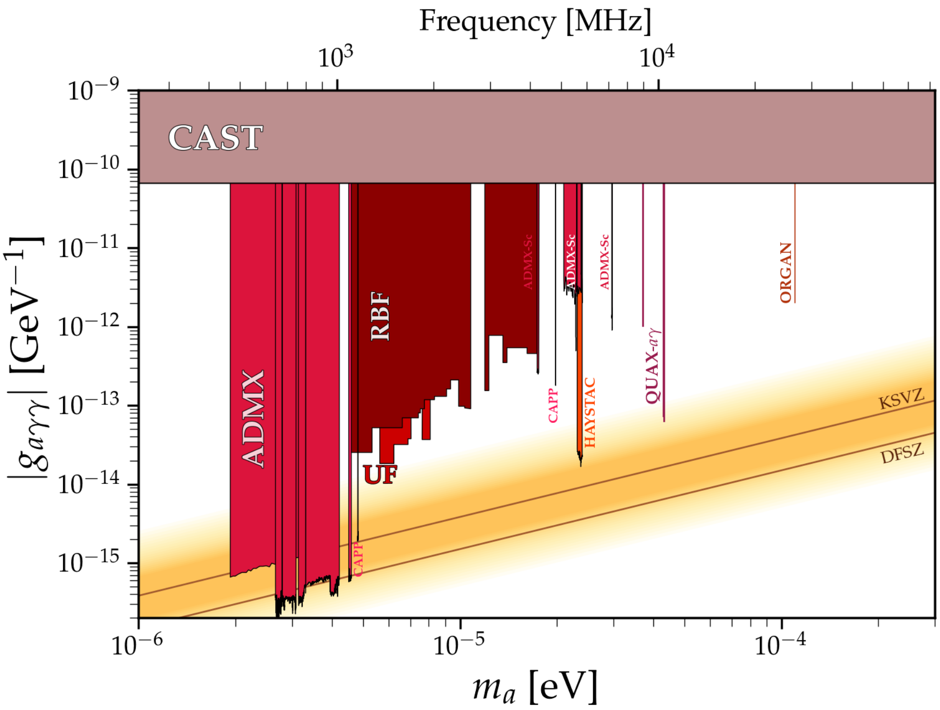

FIGURE 1.17: Updated (incomplete) Limits placed on ALP parameters by cavity-based experiments. This plot is produced using a collection of data from GitHub repository: https://cajohare.github.io/AxionLimits/docs/ap.html.

The cavity resonator based technique was employed in early experiments conducted at Rochester Brook haven Florida (RBF) and University of Florida (UF) with a small volume for sensitivity, placing limits over the mass range of $1.9 - 4.2\,\mu$eV [148–150] (see Fig. 1.17 for the corresponding exclusion regions of RBF and UF, together with all other haloscope experiments mentioned below). Representative example of modern experiments is the ADMX. With the most recent upgrade ADMX achieved a sensitivity to the DFSZ axions over the mass range $3.3-4.2\,\mu$eV [151]. Combined with previous reports over the mass range of $1.9-3.3\,\mu$eV [140, 152–154], ADMX has ruled out the KSVZ axions over the mass range of $1.9-4.2\,\mu$eV at a confidence level (CL) of 90%, whereas the exclusion ranges of mass for DFSZ axions are $2.6-3.3\,\mu$eV [153] and $3.9-4.1\,\mu$eV [151]. On top of that, ADMX has also made effort of conducting pathfinder experiments to probe higher masses, i.e. the so-called ADMX-Sidecar [155]. It placed limits on the ALP-photon coupling over three frequency bands within the range 4.2–7.2 GHz (see ADMX-Sc in Fig. 1.17). HAYSTAC showed a result excluding the two-photon coupling constant $|g_{a\gamma\gamma}| \gtrsim 2 \times 10^{-14}\,\text{GeV}^{-1}$ for axion mass $23.2\,\mu\text{eV} < m_a < 24.0\,\mu\text{eV}$ [142, 156], which is about a factor of 3 just above the KSVZ coupling benchmark. ORGAN is interested in probing the mass range of $60 - 207\,\mu\text{eV}$, where a limit is set on $|g_{a\gamma\gamma}| < 2 \times 10^{-12}\,\text{GeV}^{-1}$ for mass at $110\,\mu\text{eV}$, in a span of 2.5 neV, with a CL of 90% [143]. This narrow mass band is caused by the cavity configuration and design in the early stage, and therefore, untunable. Similar issue caused by the cavity design is also seen in the case of QUAX, where two narrow bands of mass ranges near $40\,\mu\text{eV}$ are reported, excluding $|g_{a\gamma\gamma}| \gtrsim 1 \times 10^{-12}\,\text{GeV}^{-1}$ (for $m_a \simeq 37\mu\text{eV}$) and $|g_{a\gamma\gamma}| \gtrsim 7 \times 10^{-12}\,\text{GeV}^{-1}$ (for $m_a \simeq 43\mu\text{eV}$) regions respectively [157, 158]. CAPP searches for axions across a relatively large range of mass compared to all other experiments. For example, the most recent CAPP-18TB experiment has reported a new upper bound for $|g_{a\gamma\gamma}|$ at a factor of 0.7 above the KSVZ coupling, over a narrow band near $19.9\,\mu\text{eV}$ in a span of $\sim 20\,\text{neV}$ [159]. At another narrow mass band around $4.5\,\mu\text{eV}$, the CAPP-12TB detector excluded the axion-photon coupling down to about $6.2 \times 10^{-16}\,\text{GeV}^{-1}$ at a CL of 90%. With the achieved experimental sensitivity, this excludes the DFSZ axions at the corresponding mass range [160] (see e.g. [147, 161] for more CAPP experiments). In addition to the conventional cavity-based haloscope experiments, there has also been development of probing axions/ALPs in the same mass range with other novel methods. For example, the Broadband Radiometric Axion/ALPs Search (BRASS) experiment uses a permanently magnetised conversion surface for generating an electromagnetic signal of axions/ALPs, which is then concentrated by a parabolic mirror onto a detector [162, 163]. However, BRASS and many other new experiments has not yet started operating as time of writing.

Axions/ALPs produced in the electromagnetic field of charged particles from the stars via Primakoff process are probed with the *helioscope* experiments. The representative experiment of this type is the CERN Axion Solar Telescope (CAST) experiment [39]. CAST, as the name suggests, it searches for solar axions, using a dipole magnet with a B-field strength of $\sim 9\,\text{T}$ and length of $\sim 9.3\,\text{m}$. The last constraint provided by CAST set the limit on photon-ALP coupling with $|g_{a\gamma\gamma}| < 6.6 \times 10^{-11}\,\text{GeV}^{-1}$ (for $m_a < 0.02\,\text{eV}$) at a CL of 95% [39]. The very large mass range covered by CAST is realized by filling the magnet bores with gas of varying pressure. In order to probe regions with smaller values of $g_{a\gamma\gamma}$, the next-generation helioscope, International Axion Observatory (IAXO) has been proposed, where its physics potential and conceptual design have been discussed explicitly [164, 165]. In the first stage of preparation, a test experiment named BabyIAXO is currently under construction at DESY, Germany [166].

Alternatively, ALPs can also be probed in a way where photons emitted from a laser beam are first converted into ALPs with the presence of a strong magnetic field, then an optical barrier is placed as a "wall" to only allow the propagation of ALPs. The produced ALPs can be converted back into photons when another magnet is placed in alignment with the first one, such that a photon signal can be detected [167, 168]. Such so-called Light-Shining-through-Walls (LSW) experiments are also quite challenging as the overall photon surviving probability is approximately proportional to $g^4_{a\gamma\gamma}$, leading to a feeble photon signal. This strategy was used in the Any Light Particle Search I (ALPS I) experiment, providing a limit of $|g_{a\gamma\gamma}| \lesssim 6 \times 10^{-8}\,\mathrm{GeV}^{-1}$ at a CL of 95% for $0.1\,\mathrm{meV} < \mathrm{m_a} < 0.6\,\mathrm{meV}$ [169]. A better sensitivity is achieved at a similar experiment, named OSQAR [170], excluding the region of $|g_{a\gamma\gamma}| > 3.5 \times 10^{-8}\,\mathrm{GeV}^{-1}$ for $m_a < 0.3\,\mathrm{meV}$. As an upgrade to the previous ALPS experiment, the proposed ALPS II experiment is currently under preparation and aims to offer a promising sensitivity that reaches into a parameter space much lower than the current laboratory bounds [60].

1.3.2.2 Astrophysical searches of ALPs

Although the endeavor made by laboratory experiments in present day has provided good results in terms of the exclusion region on the ALP parameter space, technical design of these experiments, substantial noise background, and other conditions have limited the laboratory searches of ALPs. Instead, astrophysical manifestation of ALPs emerges as a more promising way to probe their existence. The presence of large-scale magnetic field in the astrophysical environments can induce the photon-ALP mixing, and the resulting effects can be observed by inspecting the flux of detecting photons. The natural space magnets (see Chapter 3 for more details) typically have much smaller values of B in comparison to the B-field generated in laboratory, however, the effective conversion region length L for photon-ALP mixing is much larger than those of experiments mentioned in previous paragraphs. As a result, a sizeable photon-ALP conversion probability ($\propto g^2_{a\gamma\gamma} B^2 L^2$, see also Eq. (2.28)) can be achieved, in principle, for a wide range of ALP mass. However, meaningful sensitivities of astrophysical searches are usually constrained to very low masses of ALPs ($\mathcal{O}$(neV)), orders of magnitude lower than the searching range presented in Fig. 1.17.

Signatures of astrophysical searches of ALPs can be categorized in three types: 1) photon appearance: ALPs produced in the distant stars, galaxies or other objects convert into photons in e.g. Galactic magnetic field before being detected; 2) photon disappearance: photons emitted from various astrophysical objects oscillate into ALPs and result in an attenuation on their spectra; 3) photon reappearance: photons undergo the process of $\gamma \to a \to \gamma$ during their propagation in the presence of various astrophysical magnetic environments.

Constraints from photon appearance scenario:

One prominent example for the photon appearance is the the CAST experiment, where ALPs/axions produced in Sun can convert into X-ray photons in the presence of dipole magnetic field in the telescope [39]. Another one is the Galactic source, supernova 1987A (SN 1987A), similar to the case of solar axions a sizeable amount of ALPs are produced and emitted from the core of SN 1987A via Primakoff process. Then, a fraction of them would potentially convert into photons when they travel in the galactic magnetic field of Milky Way. However, such an excess of gamma-rays was never observed in coincidence with the neutrino flux by the early Solar Maximum Mission, therefore providing one of the strongest bounds on $|g_{a\gamma\gamma}|$ for $m_a \lesssim \mathcal{O}(\text{neV})$ [27, 171]. Based on this, a revisit and update have been done for the SN 1987A case in past years with the modified supernova and Galactic magnetic field models, leading to a limit: $|g_{a\gamma\gamma}| \lesssim 5.3 \times 10^{-12}\,\text{GeV}^{-1}$ for $m_a \lesssim 4.4 \times 10^{-10}\,\text{eV}$ (see Fig. 1.18, labeled with "SN1987A $-\ \gamma$") [37, 172].

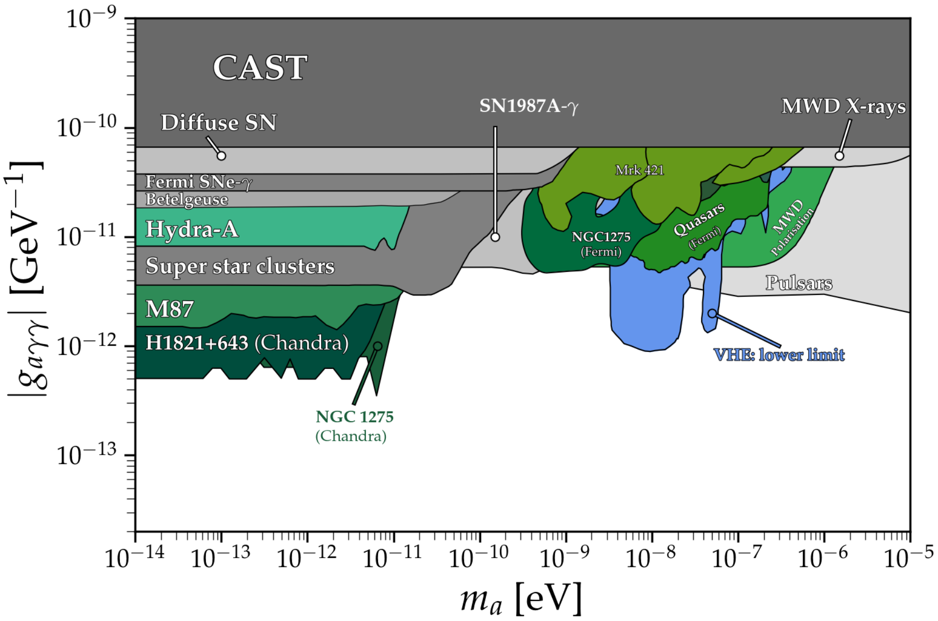

FIGURE 1.18: Exclusion region plot of photon-ALP coupling from astrophysical constraints. The constraints with the corresponding photon appearance scenario are marked in gray, whereas the regions associated with photon disappearance are colored in green. Photon reappearance is indicated in blue. This plot is produced using a data collection from: `https://cajohare.github.io/AxionLimits/docs/ap.html`

Another constraints from supernova is done with the *Fermi*-LAT for observation of extragalactic supernovae (SNe). The authors derived a an upper bound for the photon-ALP coupling under the assumption that at least one SN is contained within the field of view of LAT [42]. The resulted upper bound is about a factor of 5 weaker than that of SN 1987A (see "Fermi SNe $-\ \gamma$" in Fig. 1.18).

In addition to observation of individual SN, it has also been proposed that emission of ALPs from all past SNe can lead to a diffuse gamma-ray background due to conversion (or decay) of $a \to \gamma$ in the presence of Galactic magnetic field. A conservative bound, $|g_{a\gamma\gamma}| \lesssim 5.0 \times 10^{-11}\,\mathrm{GeV}^{-1}$ (for $m_a < 10^{-11}\,\mathrm{eV}$) was derived using *Fermi*-LAT measurement of diffuse emission by [173]. This upper limit is improved by some of the authors from [173] and is shown in [174], where the authors account for additional contribution from isotropic gamma-ray emission and update the upper limit to be $|g_{a\gamma\gamma}| \lesssim 3.76\times 10^{-11}$ for $m_a < 10^{-11}\,\mathrm{eV}$ at a CL of 95%.

Similar to the way of constraining ALP parameters in previous cases, searching for ALPs with X-ray observations of various objects also offers valid exclusion regions of photon-ALP coupling. For example, in the X-ray observation of the red supergiant star, Betelgeuse, located in constellation of Orion, a 95%-CL upper limit of $|g_{a\gamma\gamma}| \lesssim (0.5 - 1.8) \times 10^{-11}\,\mathrm{GeV}^{-1}$ for $m_a < (5.5 - 3.5) \times 10^{-11}\,\mathrm{eV}$ (uncertainties come from modelling of magnetic field) is set using NuSTAR satellite telescope data [175]. On the other hand, non-excessive observation of hard X-ray photon flux from Quintuplet and Westerlund 1 super star clusters places another limit on the photon-ALP coupling: $|g_{a\gamma\gamma}| \lesssim 3.6 \times 10^{-12}\,\mathrm{GeV}^{-1}$ for $m_a < 5 \times 10^{-11}\,\mathrm{eV}$ [176]. Non-observation of X-rays from magnetic white dwarf (MWD) RE J0317-853 by Chandra result in constraints on ALP parameters with $|g_{a\gamma\gamma}| \lesssim 4.4 \times 10^{-11}\,\mathrm{GeV}^{-1}$ for $m_a < 5 \times 10^{-6}\,\mathrm{eV}$ [177].

Additionally, ALPs produced in the neutron star magnetospheres can resonantly convert into photons as they escape from neutrons. This would lead to a broadband enhancement to the intrinsic radio flux of the neutron star. In [178], the authors use numerical simulations and analytic models to derive a strong constraints on photon-ALP coupling in the mass range of $10^{-8}\,\mathrm{eV} < m_a < 10^{-5}\,\mathrm{eV}$ by comparing the predicted radio flux of neutron star with flux measurements of 27 nearby pulsars. The resulted exclusion region is shown in Fig. 1.18.

Constraints from photon disappearance scenario

The photon-ALP oscillation effect has meaningful implications on the propagation of photon beam, leaving an energy-dependent dimming signature on the photon flux as photons become undetectable when they convert into ALPs. This process can also lead to a change on the polarization state of photons [25, 54]. Unpolarized thermal photons emitted from MWD stars would show a linear polarization dependence on $g_{a\gamma\gamma}$ when the emitted photons mix with ALPs in the magnetosphere. An updated polarization analysis from [179] on two MWDs derive a solid conservative limit on photon-ALP coupling over a large region of m_a: $|g_{a\gamma\gamma}| \lesssim 5.4 \times 10^{-11}\,\mathrm{GeV}^{-1}$ (see “MWD polarization” in Fig. 1.18).

When probing photon-ALP coupling over the mass band of $\mathcal{O}(10^{-8}\,\mathrm{eV})$ *Fermi*-LAT appears to be the best instrument for this task, as the threshold energy (see Eq. (2.30)) for photon-ALP mixing to take place nicely aligns with the energy range (between 10 GeV and 100 GeV) of LAT's best sensitivity assuming an order of $\mathcal{O}(\mu\text{G})$ external magnetic field. Three exclusion regions (labeled as 'Mrk 421", "NGC1275" and "Quasars") are shown in Fig. 1.18 covering the mass range of $10^{-9}\,\text{eV} < m_a < 10^{-7}\,\text{eV}$. These constraints are obtained by searching for modulations on spectra of AGNs, and naturally, the resulted limits have a dependence on models chosen for the magnetic fields and lightly on instrument systematic uncertainties. An additional limit is set by the *Fermi*-LAT collaboration with its observation on radio galaxy NGC 1275 [49]. Located in the center of the Perseus cluster, NGC 1275 has a rather rich intra-cluster magnetic field environment, making it an ideal target for probing spectral irregularities induced by photon-ALP mixing. A dedicated simulation is conducted by the LAT team to include as many realizations as possible for the turbulent field in the intra-cluster environment. As a result, they exclude couplings $|g_{a\gamma\gamma}| > 5 \times 10^{-12}\,\text{GeV}^{-1}$ for $0.5\,\text{neV} \lesssim m_a \lesssim 5\,\text{neV}$ at a CL of 95%. Similar analyses have also been done in [180] and [43], where the authors performed combined analyses for the spectra of Markarian 421 using LAT+MAGIC and LAT+ARGO-YBJ data, respectively (see Fig. 1.18 for region labeled with "Mrk 421"). However, as stated before, these limits are obtained under certain assumptions for the magnetic fields traversed by the photon-ALP beam, and thus give rise to relatively large uncertainties on the final results. In addition to the rich galaxy cluster environment, Ref. [181] focuses on the photon-ALP mixing in the jet magnetic field. A combined spectral analysis of three bright FSRQ-type AGNs are studied with *Fermi*-LAT data. Besides the photon-ALP mixing effect, the authors also consider extra contributions to spectral anomalies from photon-photon dispersion effect inside the jet. An upper bound of $|g_{a\gamma\gamma}| \lesssim 5 \times 10^{-12}\,\text{GeV}^{-1}$ over $5\,\text{neV} \lesssim m_a \lesssim 200\,\text{neV}$ is shown in Fig. 1.18.

If the probed mass range of ALP becomes even smaller ($m_a \lesssim 10^{-11}\,\text{eV}$), the corresponding energy band for searching of photon-ALP mixing would then fall into the X-ray band, where observations by X-ray photon detectors provide the most optimizing sensitivity. Luminous X-ray sources, such as galaxy cluster Hydra A, M87, radio-quiet quasar H1821+643 as well as radio galaxy NGC 1275, are shown as examples in Fig. 1.18. These target sources are all located within galaxy cluster environments with a relatively strong magnetic field that are more likely to host photon-ALP conversion for X-ray photons. For example, the absence of spectral anomalies in X-ray observations of Hydra-A by Chandra provides a conservative bound on the photon-ALP coupling with $|g_{a\gamma\gamma}| \lesssim 8.3 \times 10^{-12}\,\text{GeV}^{-1}$ for $m_a \lesssim 7 \times 10^{-12}\,\text{eV}$ [182]. Improvements on sensitivities have been achieved when also using Chandra observational data for analyses of quasar H1821+643 [183] and radio galaxy NGC 1275 [58], which, together, provide the most competitive upper bounds for $g_{a\gamma\gamma}$ over $m_a \lesssim 10^{-11}\,\text{eV}$ up to date.

Constraints from photon reappearance scenario

It has been shown that the Universe shows anomalous transparency towards VHE ($\mathcal{O}$(TeV)) γ-rays, where those γ-rays should have been absorbed by EBL photons via pair-production process [34]. This has attracted even more attention with the recent detection of up to 18 TeV energy photons from a gamma-ray burst by LHAASO [184]. Although the causes for such anomaly could arise from several reasons (e.g. violation of Lorentz invariance), ALPs are proposed as a promising solution to explain this observational result [29, 32, 34, 185]. Photons emitted from distant AGNs can evade absorption by other particles with a conversion into ALPs in the presence of astrophysical magnetic fields near source, and convert back to photons in the Galactic magnetic field of Milky Way. In [51], a statistical study on a large sample of VHE gamma-ray spectra detected by IACTs has set a lower limit on the photon-ALP coupling constant over a large range of ALP masses (shown as the light blue region in Fig. 1.18), where the conversions in different magnetic field configurations (intra-cluster, intergalactic and Galactic magnetic fields.) are taken into account.

The exclusion region associated with photon reappearance can be improved and probed by the next generations of ALP searching experiments, such as ALPS II [60] and IAXO [164, 165].

Chapter 2

Indications and interpretations for gamma-ray spectra modulations

The observed spectra of high energy (HE, $100\,\mathrm{MeV} \lesssim E \lesssim 100\,\mathrm{GeV}$) and very high energy (VHE, $E \gtrsim 100\,\mathrm{GeV}$) gamma-rays can be misleading, because photon beam can be affected by environmental effects during its propagation from the source to us, such that the observational data deviates from intrinsic emission of the source itself.

While the Universe is largely transparent to HE gamma-rays, hints for spectral modulation are indicated mostly in the spectra of VHE sources. For example, as it is commonly known VHE photons emitted from cosmological sources, such as BL Lac type blazars, would experience attenuation in pair-production process with ultraviolet (UV), optical, and infrared (IR) photons in the extragalactic background light (EBL) (see Appendix A for more details of EBL). Such attenuation would seriously cause a sharp drop to spectrum shape in the VHE range according to conventional physics, although enhanced flux at higher energies are indicated with respect to the expectation from conventional physics (see examples of Fig. 5 in [33] and Fig. 1 in [186]). On the other hand, these relativistic e^+e^- pairs produced by HE (VHE) photons interacting with UV- (optical-, infrared-) EBL photons can induce secondary emission of HE and VHE photons by up-scattering cosmic microwave background (CMB) photons via the inverse Compton (IC) process and therefore initiate a cascade process, which in return, would modulate the spectra of the observed VHE sources. Also, axion-like particles have been proposed as an alternative solution for addressing the enhancement or flatness of the observed VHE spectra [33, 186].

2.1 Indications for gamma-ray spectra modulation

As discussed above, studies have shown that for intrinsic (EBL-corrected) spectra of some blazars a flatness or an even upturn at the TeV energy range is indicated [187]. In Fig. 2.1 we show three cases of EBL-corrected spectra of blazars for such spectral irregularities. This abnormal transparency of Universe to VHE photons has been discussed explicitly in the Ph.D thesis by M. Meyer [35] as well as other references [34, 186]. We shall only give a short introduction of it. At first attempt, EBL parameters (such as EBL intensities) have been chosen to be lower to resolve the hardening of the spectra in the VHE range as done in Ref. [52]. However, detection of VHE photons from distant extragalactic sources by imaging atmospheric Cherenkov telescopes (IACTs) such as HESS [114], MAGIC [115] and VERITAS [116], suggests that the EBL intensity is already in good agreement with galaxy counts and various EBL models motivated by observations of extragalactic sources [52, 188, 189]. Thus, the hardening on VHE range of spectra of extragalactic sources is less likely related to the EBL intensities or the EBL models. Additional efforts have also been made to explain the hard VHE spectra based on modifications to the one-zone synchrotron self-Compton (SSC) model, such as relative shocks mechanism [194], production in extended jets [195] and other mechanisms. Despite the agreement between these modified models with observations, little is investigated about the origin of the hardening feature.

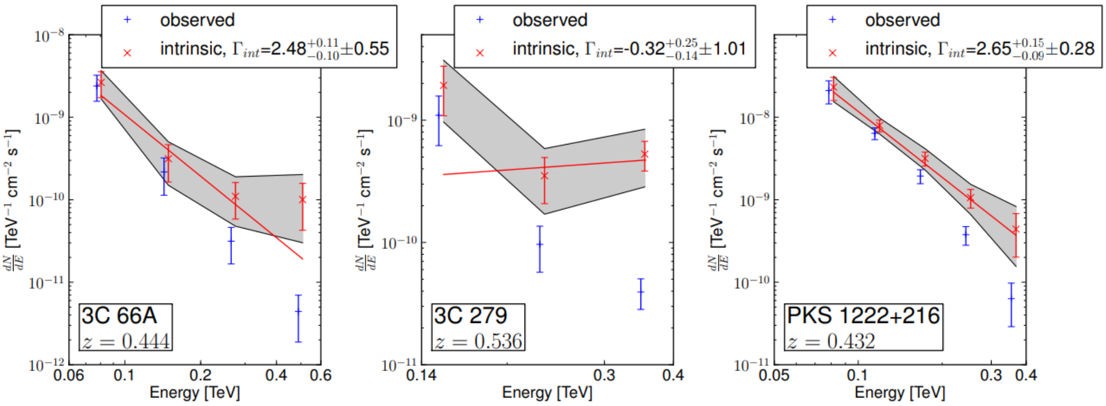

FIGURE 2.1: VHE spectra of blazars 3C 66A [190], 3C 279 [191] and PKS 1222+216 [192] measured by MAGIC. The blue data points are extracted directly from MAGIC observation, while the red data points are the EBL de-absorbed data points using Dominguez et al. EBL model [193]. Red lines are the best-fitting PowerLaw curves for each spectra. Uncertainties for the de-absorbed data points are plotted within the gray-shaded regions. Figure is taken from Fig. [187].

.

In Ref. [34] the authors investigated 50 energy spectra of TeV blazars, where the transition to optical depth $\tau > 2$ (see Appendix. A for optical depth) takes place at energies between 0.4 TeV and 21 TeV for all spectra. They found an upturn of the absorption-corrected spectrum is visible in the transition region for all of these sources with a combined significance of $4.2\,\sigma$. Despite the systematic uncertainties has been included, yet, it is found to be not sufficient to account for the hardening effects. The authors then attribute this to the pair-production anomaly (PPA) process, which can be caused by violation of Lorzentz invariance (LIV) or a postulated existence of axion-like particles (ALPs). The Lorentz invariance scheme predicts a fixed energy above which the optical depth is suppressed [34], whereas the observations imply that the anomaly is seen at widely different energies with respect to redshifts of the observed sources. The mixing of ALPs with photons (as introduced in Chapter 1), on the other hand, can also suppress the pair-production rate and therefore modify the intrinsic spectra. Depending on the coupling constant of photons to ALPs and the external magnetic field configurations, the mixing effect of photon-ALP can take place at a wide range of energies from MeV to TeV. This in turn can not only provide plausible solution to the abnormal transparency for VHE photons, but also provide a way for possible modulations in the HE range if there is any. This solution will be discussed explicitly in the later part of this Chapter.

On top of that, other hypotheses have also been proposed to provide alternative solutions to address the irregularities observed in HE and VHE spectra. Ref. [196] provides two assumptions on a study of a specific blazar Markarian 501 during flare states: the first assumption is similar to that of Ref. [34] where the TeV radiation not only comes from the source itself, but also the contribution from the development of electron-photon cascades in the intergalactic medium initiated by primary gamma-rays, which however relies on the strength of the intergalactic magnetic field (IGMF) to be at the level of $\leq 10^{-18}\,\mathrm{G}$ (similar studies has also been done in Ref. [197] where an example is taken and shown in Fig. 2.2); the other hypothesis follows that the upturn of spectra is resulted from the comptonization of ambient optical radiation by an ultra-relativistic conical cold outflow, but the Lorentz factor of bulk motion $\Gamma \sim 3.5 \times 10^7$ used for this outflow is of extreme situation and not so commonly discussed in other references.

Interestingly, in Ref. [197] the authors apply the electromagnetic cascade scheme to not only the VHE observational data analysis, but also to the HE observation, of blazar 1ES 0229+200 (shown in Fig. 2.2). We see that even after taking into account the cascade component of the gamma-rays the predicted flux is still not large enough to account for the observational data points above 2 TeV. Besides, it is noted that the predicted flux also starts to show a feature of flatness in the HE range covered by *Fermi*-LAT if the strength of the cascade process (related to the strength of the IGMF B-field) is relatively weak.

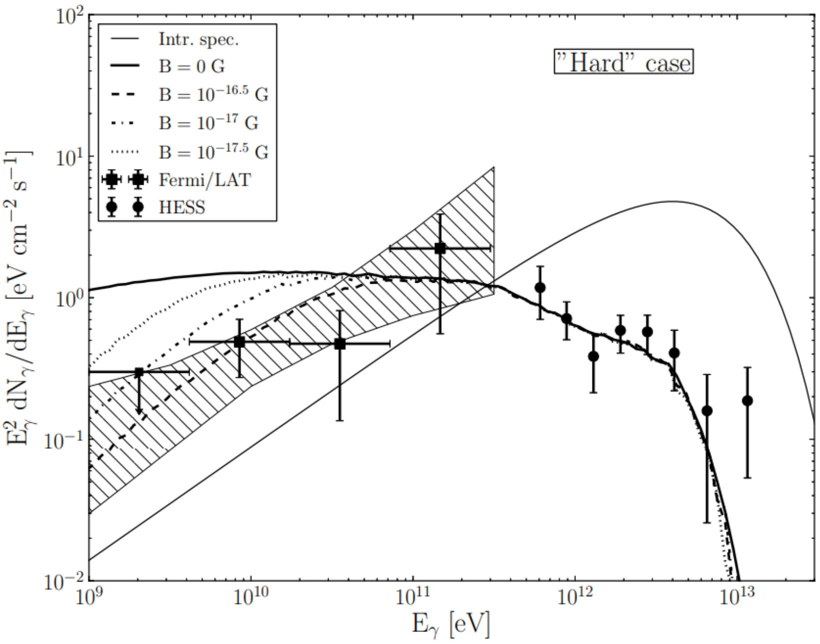

FIGURE 2.2: GeV-TeV spectral energy distribution (SED) of 1ES 0229+200 measured by *Fermi*-LAT and HESS. Lines labeled with different values of B-field strength of IGMF stand for the sum of contributions from both the intrinsic and cascade prediction. The shaded area stand for the 1 σ region of fitting *Fermi*-LAT data. Figure taken from Ref. [197].

2.2 Axion-like particles as an answer to spectral modulations

If we look further into the example shown in Fig. 2.2 we find that the hardening of flux cannot by fully accounted for by contribution of electromagnetic cascade, which indicates an alternative assumption to truly increase the predicted flux. This means additional contribution is needed for the model to fit better to the data. For this, the oscillation between photons and ALPs is proposed and can be used to compensate the absence of hardening found in e.g. cascade models [196, 197] or other models [194–196]. ALPs are very light pseudoscalar spin-zero bosons characterized by a two-photon coupling vertex $a\gamma\gamma$. Consequently, the $a\gamma\gamma$ coupling leads to photon-ALP mixing phenomenon, which takes place in the presence of an external magnetic field. Photon-ALP mixing gives rise to the oscillation effects between photons and ALPs [25, 132] which can be searched for as a signature on spectra of astrophysical objects, similar to the oscillation phenomenon observed between neutrinos with two different flavors [2]. In addition, the photon-ALP mixing can also be used to measure the initial polarization states of photons [54, 139].

Particularly, in VHE range of the spectrum, the hardening by photon-ALP oscillation can effectively take place via the process: $\gamma \to a \to \gamma$ or $a \leftrightarrow \gamma$, where HE and VHE γ-rays produced in AGNs can oscillate into ALPs in the presence of the external magnetic fields within or in vicinity of the source, traveling unimpeded in the intergalactic space and oscillate back into γ photons in Milky Way with Galactic magnetic field (GMF). Such process is shown in left panel of Fig. 2.3. In comparison to conventional physics, the $\gamma \to a \to \gamma$ process can reduce the loss of photon flux during its propagation to Earth, introduced as the photon reappearance channel in Chapter 1. On the other hand, the photon disappearance channel $\gamma \to a$ occurs (as shown in the right panel of Fig. 2.3, complemented by the photon appearance channel) when HE photons oscillate into ALPs in the presence of (e.g.) GMF, which would then lead to attenuation of photon flux at HE range. Together, the introduction of photon-ALP mixing effect provides a possible way to modulate the spectra of AGNs in a broad energy range. The specific energies where the modulation takes place and the strength of the modulation are governed by the ALP parameters: coupling constant of photons to ALPs $g_{a\gamma\gamma}$ and ALP mass m_a, as well as the external electromagnetic field characterized by its strength B and spatial extension s.

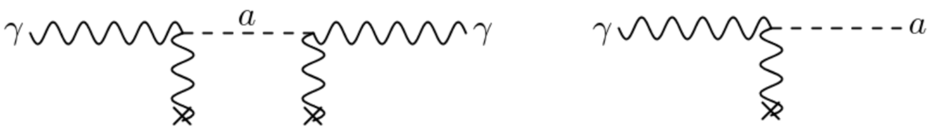

FIGURE 2.3: Left panel: Photon "appearance" channel $\gamma \to a \to \gamma$, Right panel: Photon "disappearance" $\gamma \to a$. The external magnetic fields are presented as "×".

2.2.1 Photon-ALP oscillation

As discussed above the photon-ALP mixing could occur in the presence of an external magnetic field. This is the basis for many experimental searches of ALPs. The mixing effect is described by the following Lagrangian [25]:

$$\mathcal{L} = -\frac{1}{4} g_{a\gamma\gamma} a F_{\mu\nu} \tilde{F}^{\mu\nu} = g_{a\gamma\gamma} a \mathbf{E} \cdot \mathbf{B}, \tag{2.1}$$

where $g_{a\gamma\gamma}$ is the photon-ALP coupling constant and a is the ALP field. **B** and **E** are the magnetic and electric fields respectively. $F_{\mu\nu}$ is the electromagnetic field tensor, $\tilde{F}^{\mu\nu}$ is its dual tensor.

In order to have a better understanding of phenomenon of photon-ALP conversion it is necessary to compute its conversion probability. Considering a polarized photon beam with energy E propagating in a magnetized, ionized plasma, where the electron density is denoted by n_e and an external homogeneous magnetic field $\mathbf{B}$ is present. The propagation direction of the photon beam is chosen to be the x_3-axis within an orthogonal reference frame while the x_1 and x_2 axes are chosen randomly. The propagation equation of the beam can be written as the following stationary wave equation, which is subject to the full ALP system Lagrangian [25, 59]:

$$\left(\frac{d^2}{dx_3^2} + E^2 + 2E\mathcal{M}\right)\Psi(x_3) = 0, \tag{2.2}$$

with

$$\Psi(x_3) = (A_1(x_3), A_2(x_3), a(x_3))^{\mathrm{T}}, \tag{2.3}$$

where $A_1(x_3)$ and $A_2(x_3)$ are the photon amplitudes with polarization along x_1 and x_2 axes respectively. $a(x_3)$ is the amplitude of ALP. For convenience of later discussion, we can introduce the basis of different states for Ψ: $|\gamma_1\rangle \equiv (1,0,0)^{\mathrm{T}}$, $|\gamma_2\rangle \equiv (0,1,0)^{\mathrm{T}}$, $|a\rangle \equiv (0,0,1)^{\mathrm{T}}$, where $|\gamma_1\rangle$ and $|\gamma_2\rangle$ are the two linear polarization states of photons along the x_1- and x_2-axis respectively, while $|a\rangle$ stands for the ALP state. $\Psi(x_3)$ can thus be rewritten as:

$$\Psi(x_3) = A_1(x_3)|\gamma_1\rangle + A_2(x_3)|\gamma_2\rangle + a(x_3)|a\rangle. \tag{2.4}$$

Furthermore, $\mathcal{M}$ in Eq. (2.2) denotes the photon-ALP mixing matrix, which can be expressed in the following form [59]:

$$\mathcal{M} = \begin{pmatrix} \Delta_{x_1x_1} & \Delta_{x_1x_2} & \Delta_{a\gamma}^{x_1} \\ \Delta_{x_2x_1} & \Delta_{x_2x_2} & \Delta_{a\gamma}^{x_2} \\ \Delta_{a\gamma}^{x_1} & \Delta_{a\gamma}^{x_2} & \Delta_a \end{pmatrix}, \tag{2.5}$$

where the terms [25, 33]

$$\Delta_{x_1x_1} \equiv \Delta_\perp \equiv \Delta_{\mathrm{pl}} + \Delta_\perp^{\mathrm{CM}} + \Delta_{\mathrm{CMB}}, \tag{2.6}$$

$$\Delta_{x_2x_2} \equiv \Delta_\parallel \equiv \Delta_{\mathrm{pl}} + \Delta_\parallel^{\mathrm{CM}} + \Delta_{\mathrm{CMB}}, \tag{2.7}$$

$$\Delta_{a\gamma}^{x_1} \equiv \frac{1}{2} g_{a\gamma\gamma} B_{x_1}, \tag{2.8}$$

$$\Delta_{a\gamma}^{x_2} \equiv \frac{1}{2} g_{a\gamma\gamma} B_{x_2}, \tag{2.9}$$

$$\Delta_a \equiv -\frac{m_a^2}{2E}. \tag{2.10}$$

Here we rewrite $\Delta_{x_1x_1}$ and $\Delta_{x_2x_2}$ as $\Delta_\parallel$ and $\Delta_\perp$[1] respectively according to the convention adopted in [25], which corresponds to two linear polarization states of photons, with **E** field either perpendicular ($\parallel$ mode) or parallel ($\perp$ mode) to the plane containing the external magnetic field $\mathbf{B}_e$ and direction of propagation x_3-axis. Diagonal terms $\Delta_\parallel$,

---

[1] Such notation is based on the findings originally defined in Ref. [198] where the author find the eigenstates of propagating beam are two linear polarized states of photons, with the **B** field parallel and perpendicular to the external magnetic field $\mathbf{B}_e$.

$\Delta_\perp$ and Δ_a are essentially the momentum differences of different states $(\parallel, \perp, a)$ in comparison to photons of the same energies in vacuum without the presence of any fields [25].

The vacuum has a refractive index of $n = E/k = 1$ (k is the photon momentum), given by the photon dispersion relation: $E^2 = k^2$. However this is not entirely true when we consider the propagation of photon beam taking place in the presence of an external $\mathbf{B}_e$ field, which would assign an effective mass of $\omega_{\rm pl}$ to photons due to the electric screening effects in plasma environment [25, 198]. Consequently, this brings out the first contribution to $\Delta_{\parallel,\perp}$ in addition to vacuum, field-free photons: $\Delta_{\rm pl} = -\frac{\omega_{\rm pl}^2}{2E}$. $\Delta_{\rm pl}$ emerges as a result of the effective photon mass produced in cold plasma (thermal motion of charged particles is ignored), where $\omega_{\rm pl}$ stands for the plasma frequency[2]. We make use of the numerical expression for $\Delta_{\rm pl}$ taken from [33] in our later calculation:

$$\Delta_{\rm pl} \equiv -\frac{\omega_{\rm pl}^2}{2E} \simeq -1.1 \times 10^{-10} \times \left(\frac{E}{\rm TeV}\right)^{-1} \times \left(\frac{n_e}{10^{-3}\,{\rm cm}^{-3}}\right) {\rm kpc}^{-1}, \tag{2.11}$$

where n_e is the electron number density in the medium with its typical value assumed to be $1.1 \times 10^{-2}{\rm cm}^{-3}$ [41].

The term $\Delta_{\parallel,\perp}^{\rm CM}$ stands for the Cotton-Mouton effect, which is associated with the birefringence effects of the vacuum (i.e., the QED vacuum polarization effects) expected from the Euler-Heisenberg Lagrangian [200, 201] in the presence of transverse magnetic field (see e.g. Fig. 1(a) in Ref. [25]). It arises from photon-photon interactions in a scenario where the photon frequency is relatively small, in comparison to electron mass and the transverse magnetic fields are very weak [25]. The other contribution to $\Delta_{\perp,\parallel}$ is the very small photon-photon dispersion effect [202], denoted as $\Delta_{\rm CMB}$, which is resulted from beam photons dispersion off the CMB photons (dispersion of photon beam off other radiation fields, such as fields within the source, is however beyond the scope of this work, but studied in [203]). The first off-diagonal term $\Delta_{x_1x_2}$ $(= \Delta_{x_2x_1})$ accounts for the mixing between two photon polarization states $|\gamma_1\rangle$ and $|\gamma_2\rangle$ and would lead to a Faraday rotation, and it will not contribute to the mixing between photons and ALPs in case of astrophysical gamma-ray propagation. Another off-diagonal term, $\Delta_{a\gamma}^{x_1,x_2}$, stems from the Lagrangian displayed in Eq. (2.1), indicating the contribution from photon-ALP mixing effect determined by the B-field components B_{x_1} and B_{x_2}. They are chosen to be along x_1- and x_2-axis respectively for the sake of simplicity.

---

[2] It is commonly referred as the frequency of the oscillation of electron charge density in plasma. The oscillation is resulted from the net of electric force pushing or pulling charged particles, i.e., as distances between them vary, the Coulomb force from all the neighboring charged particles reverses, acting as a restoring force. The frequency is basically assumed to vary as the square root of electron number density n_e: $\omega_{\rm pl} = \sqrt{4\pi n_e c^2/m_e}$, whereas insignificant positrons are typically assumed in plasma environment [25, 199].

The situation can be simplified starting with the propagation equation. Since the energies (GeV photons) we are interested in this work for photon-ALP mixing to take place are much larger than the ALP mass studied in astrophysical environments [43, 49, 50, 55, 57, 58], we can rewrite Eq. (2.2) as a Schrödinger-like equation with time variable replaced as x_3 following the same short oscillation wavelength approximation (of photon-ALP) employed in Ref. [25]:

$$\left(i\frac{d}{dx_3}+E+\mathcal{M}\right)\Psi(x_3)=0, \tag{2.12}$$

where the Hamiltonian of the system can be easily extracted as: $\mathcal{H}_0 \equiv -(E+\mathcal{M})$. Then solution of Eq. (2.12) can be easily obtained as:

$$\Psi(x_3)=e^{-i\mathcal{H}_0(x_3-x_3^0)}\Psi(x_3^0)=e^{iE(x_3-x_3^0)}e^{i\mathcal{M}(x_3-x_3^0)}\Psi(x_3^0), \tag{2.13}$$

where $e^{i\mathcal{H}_0(x_3,x_3^0)}$ is commonly defined as the transfer matrix $\mathcal{U}(x_3,x_3^0)$ in most of photon-ALP mixing studies.

The solution provided in Eq. (2.13) is in a neat, compact way, but in order to obtain the conversion probability of $\gamma \leftrightarrow a$ it is necessary to simplify the mixing matrix $\mathcal{M}$ in $\mathcal{H}_0$. Note first the contribution to two photon states involved in $\Delta_{x_1x_1}$ and $\Delta_{x_2x_2}$ can be reduced to only $\Delta_{\rm pl}$ since $\Delta_{\perp,\parallel}^{\rm CM}$ term associated with QED vacuum polarization effects can be omitted. This is because the external magnetic field considered here is much weaker compared to the critical B-field strength defined in [25]. The photon-photon dispersion effect in $\Delta_{\rm CMB}$ would lead to a strong contribution if the energy of the photons is sufficiently large (see e.g. Ref. [202]). It can thus be neglected for the range of *Fermi*-LAT energies analyzed in this work. Based on the conventions defined in equations above the direction of propagation for the photon beam is along the x_3-axis, $\Delta_{x_1x_1} \equiv \Delta_\perp$ is thus associated to the photon state with **E** vector perpendicular to the plane containing beam direction and external magnetic field $\mathbf{B}_e$. This indicates the B-field component B_{x_1} in $\Delta_{x_1x_1}$ is parallel to the direction of beam propagation. In contrast, the B-field component B_{x_2} associated with $\Delta_{x_2x_2}$ is perpendicular to beam propagation of direction. Following the argument made in [25], the longitudinal field gives an azimuthal symmetry, which can not be used for the transition from a photon to ALP. Therefore, $\Delta_{a\gamma}^{x_1}$ vanishes and only the transversal component $B_{x_2} = |\mathbf{B}_e|$ is effectively present for the photon-ALP mixing effect. We can then rewrite $\Delta_{a\gamma}^{x_2}$ as $\Delta_{a\gamma} = \frac{1}{2}g_{a\gamma\gamma}|\mathbf{B}_e|$ to get rid of extra subscription.

In this way, the mixing matrix is significantly simplified in the calculation of our work. It now has the following general form:

$$\mathcal{M} = \begin{pmatrix} \Delta_{\parallel} & 0 & 0 \\ 0 & \Delta_{\perp} & \Delta_{a\gamma} \\ 0 & \Delta_{a\gamma} & \Delta_{a} \end{pmatrix}. \tag{2.14}$$

$\mathcal{M}$ is still not completely diagonal despite simplification. Eigenvalues of $\mathcal{H}_0$ (more precisely, $\mathcal{M}$) needs to be solved in order to apply the Hamiltonian onto the initial state of the beam in Eq. (2.13). By diagonalizing $\mathcal{M}$ we find the eigenvalues to be [59]:

$$\lambda_1 = \Delta_{\mathrm{pl}}, \quad \lambda_2 = \frac{1}{2}(\Delta_{\mathrm{pl}} + \Delta_a - \Delta_{\mathrm{osc}}), \quad \lambda_3 = \frac{1}{2}(\Delta_{\mathrm{pl}} + \Delta_a + \Delta_{\mathrm{osc}}), \tag{2.15}$$

where Δ_{osc} has the form

$$\Delta_{\mathrm{osc}} \equiv \sqrt{(\Delta_a - \Delta_{\mathrm{pl}})^2 + 4\Delta_{a\gamma}^2}, \tag{2.16}$$

and the corresponding eigenvectors for $\lambda_{1,2,3}$ can be written as

$$v_1 = \begin{pmatrix} 1 \\ 0 \\ 0 \end{pmatrix}, \quad v_2 = \begin{pmatrix} 0 \\ \Delta_{a\gamma} \\ \lambda_2 - \Delta_{\mathrm{pl}} \end{pmatrix}, \quad v_3 = \begin{pmatrix} 0 \\ \Delta_{a\gamma} \\ \lambda_3 - \Delta_{\mathrm{pl}} \end{pmatrix}. \tag{2.17}$$

Then, Eq. (2.13) can be rewritten as the following with $\Psi(x_3^0)$ replaced as a linear combination of eigenvectors or eigenvalues:

$$\begin{aligned} \Psi(x_3) &= e^{iE(x_3 - x_3^0)} e^{i\mathcal{M}(x_3 - x_3^0)} (\mathcal{F}_1 v_1 + \mathcal{F}_2 v_2 + \mathcal{F}_3 v_3) \\ &= e^{i(E+\lambda_1)(x_3 - x_3^0)} \mathcal{F}_1 v_1 + e^{i(E+\lambda_2)(x_3 - x_3^0)} \mathcal{F}_2 v_2 + e^{i(E+\lambda_3)(x_3 - x_3^0)} \mathcal{F}_3 v_3 \end{aligned} \tag{2.18}$$

where $\mathcal{F}_{1,2,3}$ are the constant amplitudes of eigenvectors $v_{1,2,3}$. $\mathcal{F}_{1,2,3}$ can easily be solved and expressed in the forms of $A_1(x_3^0)$, $A_2(x_3^0)$ and $a(x_3^0)$:

$$\begin{aligned} \mathcal{F}_1 &= A_1(x_3^0), \\ \mathcal{F}_2 &= \frac{\Delta_{\mathrm{pl}} - \lambda_3}{\Delta_{a\gamma}(\lambda_2 - \lambda_3)} A_2(x_3^0) + \frac{1}{\lambda_2 - \lambda_3} a(x_3^0), \\ \mathcal{F}_3 &= -\frac{\Delta_{\mathrm{pl}} - \lambda_2}{\Delta_{a\gamma}(\lambda_2 - \lambda_3)} A_2(x_3^0) - \frac{1}{\lambda_2 - \lambda_3} a(x_3^0). \end{aligned} \tag{2.19}$$

By substituting Eq. (2.17) and (2.19) into Eq. (2.18) we can obtain the the transfer matrix $\mathcal{U}(x_3, x_3^0)$ as:

$$\Psi(x_3) = \mathcal{U}(x_3, x_3^0)\Psi(x_3^0) = \left[e^{i(E+\lambda_1)}\mathcal{T}_{0,1} + e^{i(E+\lambda_2)}\mathcal{T}_{0,2} + e^{i(E+\lambda_3)}\mathcal{T}_{0,3}\right]\Psi(x_3^0), \tag{2.20}$$

where we separate the transfer matrix into three matrices $\mathcal{T}_{0,(1,2,3)}$ associated with eigenvalues $\lambda_{1,2,3}$. They have the following explicit forms

$$\mathcal{T}(0,1) = \begin{pmatrix} 1 & 0 & 0 \\ 0 & 0 & 0 \\ 0 & 0 & 0 \end{pmatrix}, \tag{2.21}$$

$$\mathcal{T}(0,2) = \begin{pmatrix} 0 & 0 & 0 \\ 0 & \frac{\Delta_{\rm pl}-\lambda_3}{\lambda_2-\lambda_3} & \frac{\Delta_{a\gamma}}{\lambda_2-\lambda_3} \\ 0 & \frac{\Delta_{a\gamma}}{\lambda_2-\lambda_3} & -\frac{\Delta_{\rm pl}-\lambda_2}{\lambda_2-\lambda_3} \end{pmatrix} = \begin{pmatrix} 0 & 0 & 0 \\ 0 & \frac{\Delta_a-\Delta_{\rm pl}+\Delta_{\rm osc}}{2\Delta_{\rm osc}} & -\frac{\Delta_{a\gamma}}{\Delta_{\rm osc}} \\ 0 & -\frac{\Delta_{a\gamma}}{\Delta_{\rm osc}} & \frac{\Delta_a-\Delta_{\rm pl}-\Delta_{\rm osc}}{2\Delta_{\rm osc}} \end{pmatrix}, \tag{2.22}$$

$$\mathcal{T}(0,3) = \begin{pmatrix} 0 & 0 & 0 \\ 0 & -\frac{\Delta_{\rm pl}-\lambda_2}{\lambda_2-\lambda_3} & -\frac{\Delta_{a\gamma}}{\lambda_2-\lambda_3} \\ 0 & -\frac{\Delta_{a\gamma}}{\lambda_2-\lambda_3} & \frac{\Delta_{\rm pl}-\lambda_3}{\lambda_2-\lambda_3} \end{pmatrix} = \begin{pmatrix} 0 & 0 & 0 \\ 0 & \frac{\Delta_a-\Delta_{\rm pl}-\Delta_{\rm osc}}{2\Delta_{\rm osc}} & \frac{\Delta_{a\gamma}}{\Delta_{\rm osc}} \\ 0 & \frac{\Delta_{a\gamma}}{\Delta_{\rm osc}} & \frac{\Delta_a-\Delta_{\rm pl}+\Delta_{\rm osc}}{2\Delta_{\rm osc}} \end{pmatrix}. \tag{2.23}$$

$\mathcal{T}_{0,2}$ and $\mathcal{T}_{0,3}$ can be further simplified by introducing a so-called photon-ALP mixing angle α, defined as:

$$\alpha = \frac{1}{2}\mathrm{arctg}\Big(\frac{2\Delta_{a\gamma}}{\Delta_{\rm pl}-\Delta_a}\Big). \tag{2.24}$$

In this way, we have

$$\mathcal{T}(0,2) = \begin{pmatrix} 0 & 0 & 0 \\ 0 & \sin^2\alpha & -\sin\alpha\cos\alpha \\ 0 & -\sin\alpha\cos\alpha & \cos^2\alpha \end{pmatrix}, \tag{2.25}$$

and

$$\mathcal{T}(0,3) = \begin{pmatrix} 0 & 0 & 0 \\ 0 & \cos^2\alpha & \sin\alpha\cos\alpha \\ 0 & \sin\alpha\cos\alpha & \sin^2\alpha \end{pmatrix}. \tag{2.26}$$

In the most simplified case as considered above, the surviving probability of a photon polarized along the x_2-axis after traveling distance x_3 along x_3-axis in an external homogeneous $\mathbf{B}_e$ field is then given by:

$$p_{0,\gamma_2\to\gamma_2} = |\langle\Psi(x_3)|\Psi(0)\rangle|^2 = |\langle\gamma_2|\mathcal{U}(x_3,0)|\gamma_2\rangle|^2 = 1 - \sin^2(2\alpha)\sin^2\Big(\frac{\Delta_{\rm osc}x_3}{2}\Big), \tag{2.27}$$

which in turn gives the conversion probability of photon to ALP in the scenario considered in Eq. (2.27) (for $m_a \ll E$):

$$p_{0,\gamma_2 \to a} = 1 - p_{0,\gamma_2 \to \gamma_2} = \sin^2(2\alpha)\sin^2\left(\frac{\Delta_{\rm osc} x_3}{2}\right). \tag{2.28}$$

We see that in Eq. (2.28) the term $\Delta_{\rm osc}$ defined in Eq. (2.16) can be interpreted as the photon-ALP oscillation wave number. In this way, the corresponding oscillation length is then $L_{\rm osc} = \frac{2\pi}{\Delta_{\rm osc}}$. Also, it can be seen that the photon-ALP oscillation becomes maximal and energy-independent when the mixing angle $\alpha \approx \frac{\pi}{4}$, *i.e.*, $\Delta_{\rm osc} = g_{a\gamma\gamma}|\mathbf{B}_e|$ (since $\sin^2(2\alpha) = \frac{2\Delta_{a\gamma}}{\Delta_{\rm osc}}$). This maximal oscillation effect is defined as the *strong-mixing regime* [25, 33], and the condition to reach this regime is when energy of the beam is much greater than a certain critical energy E_c [33] defined within the following equation:

$$\frac{2\Delta_{a\gamma}}{\Delta_{\rm osc}} = \frac{1}{\sqrt{1 + \left(\frac{E_c}{E}\right)^2}}, \tag{2.29}$$

where E_c is

$$E_c \equiv \frac{E|\Delta_a - \Delta_{\rm pl}|}{2\Delta_{a\gamma}} \tag{2.30}$$

2.3 Photon-ALP mixing in case of AGNs

In our case of studying the propagation of photons emitted from a AGN, we consider in general three distinct magnetized regions that could induce possible conversions of $\gamma \leftrightarrow a$ along the propagation line of sight. This includes:

- Source region: jet magnetic field, host galaxy field, intra-cluster magnetic field.
- Intergalactic space: intergalactic magnetic field.
- Milky Way: galactic magnetic field.

The structure and strength of the magnetic field present in the Milky Way is well known via observations of Faraday rotation measures and synchrotron emission of the interstellar medium (see Chapter 3 for more details about various astrophysical magnetic fields). The magnetic field in the intergalactic space is relatively weak and constrained to be lower than $\mathcal{O}$(nG) [204] and not to be lower than 10^{-16}G [205]. In comparison to the magnetic fields in Milky Way and intergalactic space, the B-fields in source region are very poorly known and have different strengths or spatial structures depending on the line of sight.

Therefore, we model the magnetic field in source region under the assumption of it being a large-scale homogeneous B-field in a single domain. This way, the photon surviving probability derived in Eq. (2.27) can be used to describe the photon-ALP mixing in the presence of the magnetic fields in source region. The photon-ALP mixing effect in intergalactic space is neglected here due to the large uncertainty of IGMF parameters and the high possibility of its strength sitting at several orders lower than the upper limit. Sizeable modulation on spectra by photon-ALP mixing in intergalactic space can only be given when the strength of IGMF reaches its upper limit 1 nG with a coherence length of 1 Mpc [33, 36]. On the other hand, the attenuation effect in intergalactic space attributed to EBL photons is accounted for by adding an absorption matrix into Eq. (2.12), such that a modified Schrödinger-like equation can be rewritten as [25, 32, 202, 206]

$$\left(i\frac{d}{dx_3} + E + \mathcal{M} + iD\right)\Psi(x_3) = 0, \tag{2.31}$$

where D is the absorption matrix to account for photon attenuation by interacting with EBL photons, and it has the form of

$$D = \begin{pmatrix} \mathcal{C}(x_3) & 0 & 0 \\ 0 & \mathcal{C}(x_3) & 0 \\ 0 & 0 & 0 \end{pmatrix},$$

with $\mathcal{C}(x_3)$ associated to the optical depth $\tau(x_3)/2 = \int_0^{x_3} \mathcal{C}(x_3')dx_3'$. The solution provided in Eq. (2.13) now has the following form after including the absorption effect:

$$\begin{aligned}\Psi_1(x_3) &= \exp\left(i\int_{x_3^0}^{x_3}(E + \mathcal{M} + iD)dx_3'\right)\Psi(x_3^0) \\ &= \mathcal{U}_1(x_3, x_3^0)\Psi(x_3^0),\end{aligned} \tag{2.32}$$

where the explicit form of transfer matrix $\mathcal{U}_1(x_3, x_3^0)$, in analogy to $\mathcal{U}(x_3, x_3^0)$ shown in Eq. (2.20), can be calculated in a similar way.

Finally, as the photon-ALP beam continues to propagate from intergalactic space to Milky Way the magnetic field configuration changes. We take the regular component of the J&F GMF model [207] for describing the Galactic magnetic field, which includes a disk field, a toroidal halo field and a so-called out-of-plane field (see Sec. 3.4 for details). The mixing matrix in GMF is then modified as:

$$\mathcal{M}_2 = \begin{pmatrix} \Delta_{\parallel} & 0 & 0 \\ 0 & \Delta_{\perp} & \Delta_{a\gamma}^{\mathrm{GMF}} \\ 0 & \Delta_{a\gamma}^{\mathrm{GMF}} & \Delta_a \end{pmatrix}, \tag{2.33}$$

where $\mathcal{M}_2$ still follows Schrödinger-like equation as shown in Eq. (2.12), $\Delta_{a\gamma}^{\rm GMF} = \frac{1}{2}g_{a\gamma\gamma}B_T(x_3^1)$, and $B_T(x_3^1)$ is the transversal component of galactic magnetic field along the direction of propagation. The resulted wave function can then be easily solved as:

$$\Psi_2(x_3^1) = \mathcal{U}_2(x_3^1, x_3)\Psi_1(x_3, x_3^0) = \mathcal{U}_2(x_3^1, x_3)\mathcal{U}_1(x_3, x_3^0)\Psi(x_3^0), \tag{2.34}$$

where $\Psi_2(x_3^1)$ is the fully propagated wave function starting from source region, traveling through intergalactic space and ending in Milky Way. $\mathcal{U}_2(x_3^1)$ is the transfer matrix associated to mixing matrix $\mathcal{M}_2$ in Eq. (2.33).

Similar to the photon surviving probability shown in Eq. (2.27), the final photon surviving probability for an initially polarized photon beam can then be calculated as

$$p_{\gamma\to\gamma} = |\langle\Psi_2(x_3^1)|\Psi(x_3^0)\rangle|^2. \tag{2.35}$$

In this section, we consider three distinct regions for the propagation of photon/ALP beam and its possible oscillations. In source region we model the magnetic fields as a large-scale homogeneous field in a single domain, where the solution can be obtained using Eq. (2.20) neglecting absorption $\mathcal{C} = 0$. In the intergalactic space the photon-ALP mixing effect is neglected similar to other studies [33], such that $\mathcal{M} = 0$, i.e., only $\mathcal{C}$ contributes. Finally, in the Milky Way, we make use of regular component of J&F GMF model reported in [207], and the photon-ALP mixing is described with a different mixing matrix $\mathcal{M}_2$, where additional absorption caused by local radiation fields is omitted ($\mathcal{C} \approx 0$). A fully propagated wave function for an initially polarized state of photons is shown in Eq. (2.34), and a corresponding photon surviving probability is presented in Eq. (2.35).

Additionally, the formalism presented above can also be extended to the scenario where an initial un-polarized state is considered, which is done by introducing the density matrix and a Von-Neumann equation instead of Schrödinger-like equation [25, 206]. We refer the readers to references such as [33, 59] for details of un-polarized studies.

Chapter 3

Astrophysical environments as space magnets

According to commonly accepted idea, magnetic fields of different sizes in astronomical structures, from stars, galaxies, up to cluster of galaxies, are generated by amplification of a pre-existing weak magnetic field through different dynamo processes [208–211]. On the one hand, for small scales, turbulent and thermal motions of astrophysical plasmas are driven by dissipation of magnetic field energy, such that a continuous re-generation of the field is needed. This is the scenario, for example, of the magnetic fields of Earth, Sun, or other stars and planets, and it is also partially true for the Milky Way magnetic field. On the other hand, for large scales from hundreds of kpc to Mpc in galaxies and galaxy clusters, weak magnetic fields are assumed to exist and they conserve their strength on time scales comparable to the age of the Universe after amplified by dynamo and collision mechanisms due to lack of time for dissipating their energies into motions of gas and plasmas [205].

The γ-rays produced in distant blazars would need to traverse various magnetic fields, before their arrivals to Earth. These magnetic fields are with quite different structures and scales, including the jet magnetic field (JMF), intra-cluster magnetic field (ICMF), the inter-galactic magnetic field (IGMF) and finally the Galactic magnetic field (GMF).

In Fig. 3.1, we show an illustration for the full propagation of gamma-rays emitted from a distant blazar. JMF and ICMF, as the magnetic fields in the vicinity of source, contribute the first possible regions for conversion of photon to ALPs. In the second region, the intergalactic space, the photon beam is attenuated due to pair-production process with EBL photons. The present IGMF is, however, too weak to induce any prominent

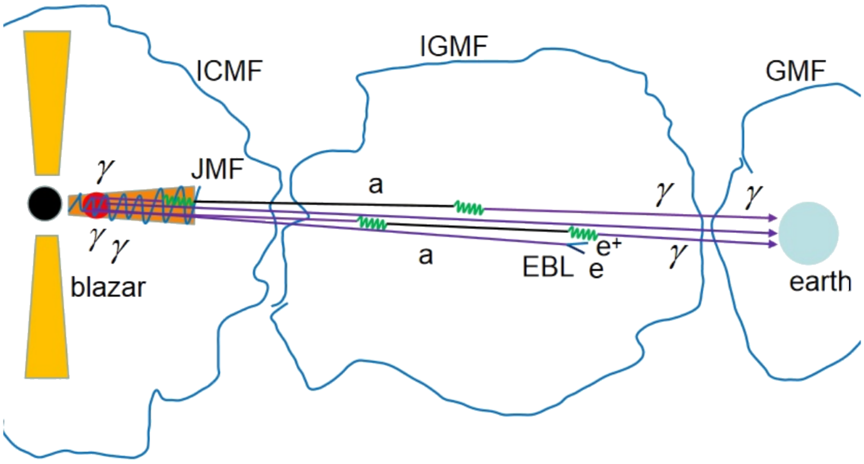

FIGURE 3.1: VHE gamma-rays emitted from a distant blazar when traveling through different magnetic environments along the ling of sight (image from Ref. [212]), where modulations from EBL absorption and photon-ALP mixing effect are presented for the intrinsic photon flux.

photon-ALP mixing effect. Finally, the Milky Way contributes the last possible conversion region for photon-ALP mixing. The three distinct magnetic environments are outlined individually with blue curves in Fig. 3.1.

3.1 Jet magnetic field

The jet environment has always been the subject of research interest for understanding origin of the particle accelerators, seen not only in AGNs, but also in other objects, such as protoplanetary nebulae, young stars and X-ray binaries. The jets in these objects are quite similar in terms of morphology, but their physical properties (size scales, transported energies and velocities) vary quite drastically from one to another. We discuss mainly the AGN jets in the following context.

In order to better understand the properties of the jet magnetic field (the scale of the field strength, the structure of the field) we here give a brief introduction for the formation of the jet in the framework of two mechanisms. In Blandford-Znadjek mechanism [213, 214] where the energy extracted from a Kerr black hole (BH) are used to power the jet with the help of a magnetic field. The basic idea follows that a rotating black hole is threaded by magnetic field lines generated from external currents flowing in an equatorial disk (accretion disk). These field lines are anchored into the disk with certain angles. Ionized particles are subject to Lorentz force and therefore follow around the field lines while rotating with the accretion disk. As a result, the charged particles are centrifugally accelerated along these field lines. Then the ionized gas tends to move outward along the field lines when the component of the centrifugal force is large enough to counter

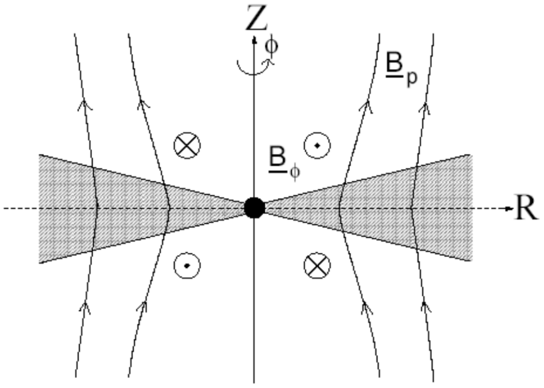

Figure 3.2: Schematic view of the general (BH-)-disk-driven model for the jet formation. Figure credit: Ref. [217].

gravity, and this outward acceleration would continue to be effective until a point where the inertia of the ionized gas causes it to lag behind the rotation of these external field lines. Thus, the existence of a strong toroidal magnetic field is a necessity to continue accelerating the ionized material (see Fig. 3.2 for a schematic view of the BH-disk-driven model). This leads to the formation of jet and its main accelerating engine in locations far from the black hole depending on rotation frequency of the accretion disk. Alternatively, if the magnetic field is coupled to the disk, the energy is extracted in a way following the disk-driven model (Blandford-Payne mechanism), where the angle between the poloidal component of the field line and disk surface is less than 60°, yet the basic idea of forming jet in this mechanism is similar to the previous BH-disk-driven model (see Ref. [215] for more details).

In Fig. 3.2 we show a schematic view of a general (BH-)disk-driven model, where such configuration can be found in a number of BH-disk simulations (see e.g. Ref. [216]). The cross-section of the accretion disk is shown in shade of gray and the BH is marked as a black solid point in the center. The toroidal component of the magnetic field starts to dominate the dynamics of the jet, collimating the outflow into a pair of jets perpendicular to the disk, as the field line goes asymptotically far from the central massive BH. The poloidal component is shown as a more realistic parabolic shape, where both the current net on accretion disk and BH are threaded by these field lines.

Motivated by the mechanism of jet formation shown above. Jet magnetic field close to the γ-ray emission region is, in most cases, modeled through a toroidal component at a scale of pc [218], and the B-field strength ranges from 0.1 G to 1 G [219, 220]. On the other hand, the B-field strength at kpc scale is observed in Fanaroff-Riley type II galaxies and has been estimated by rotation measures and synchrotron emission to be at a scale of $\mathcal{O}(\mu G)$ up to $100\,\mu G$ [219, 221, 222].

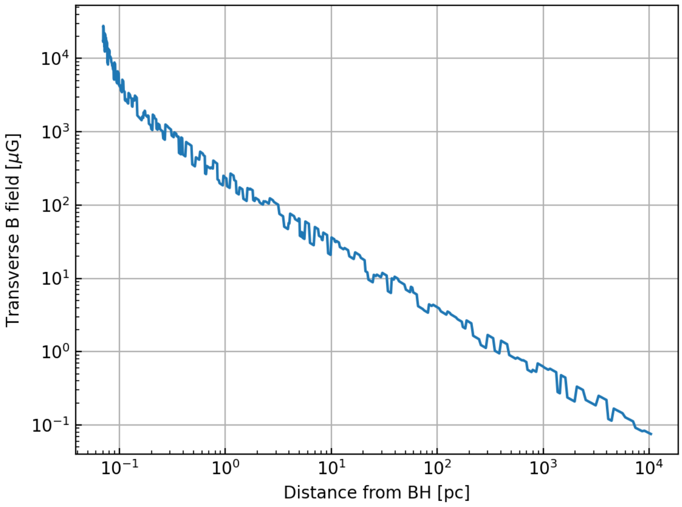

FIGURE 3.3: Blazar jet magnetic field in the case of Markarian 501 with toroidal dominated model.

In Fig. 3.3 we take a well-motivated example of Markarian 501[1] to give a relation of B-field strength and distance from black hole using the Helical-Tangled magnetic field model[2] [228]. It shows that the transverse component of B-field strength ranges from $\mathcal{O}(\mu\text{G})$ at kpc scale to $\mathcal{O}(100\,\mu\text{G})$ at pc scales within the model. This model is motivated by the synchrotron emission observations from several Fanaroff-Riley type I radio galaxies [229–231] and considered to be more realistic for describing the jet magnetic field [227] in both pc and kpc scales. It consists of a helical component and a tangled component, the former component is generated as the poloidal field lines are anchored into the rapidly rotating disk and twisted with it [216], while the latter is motivated for better characterizing the magnetic field at kpc scales[3] and is based on an ordered toroidal field together with a disordered poloidal field [227, 232, 233]. This configuration is also consistent with the analysis from Ref. [232], where the author showed that the produced profiles by helical field model are stronger than observed. Thus, such a combination of helical field in pc scales and tangled field (ordered toroidal + disordered poloidal) at kpc scales could describe well the complicated jet environment (for detailed analysis on some blazars, see e.g. [203, 233]) compared to other simplified purely toroidal models.

---

[1] The BL Lac Blazar Markarian 501 has been chosen as an ideal candidate for studying jet structures in many researches [223–227], as the very long baseline interferometry (VLBI) images of Markarian 501 show a number of different transverse structures that could be associated with different models[225].

[2] The plot is created using the implemented JMF model in gammaALPs package `https://github.com/me-manu/gammaALPs`. The relevant values of parameters for creating Figs. 3.3 and 3.4 can also be found on the package website.

[3] The polarization data from synchrotron emission implies that the large-scale ordered toroidal field leads to a consistence with the observation, but is not required. Particularly, for some cases at kpc scales, the strong toroidal field originated from large-scale poloidal field leads to disagreement with observational data.

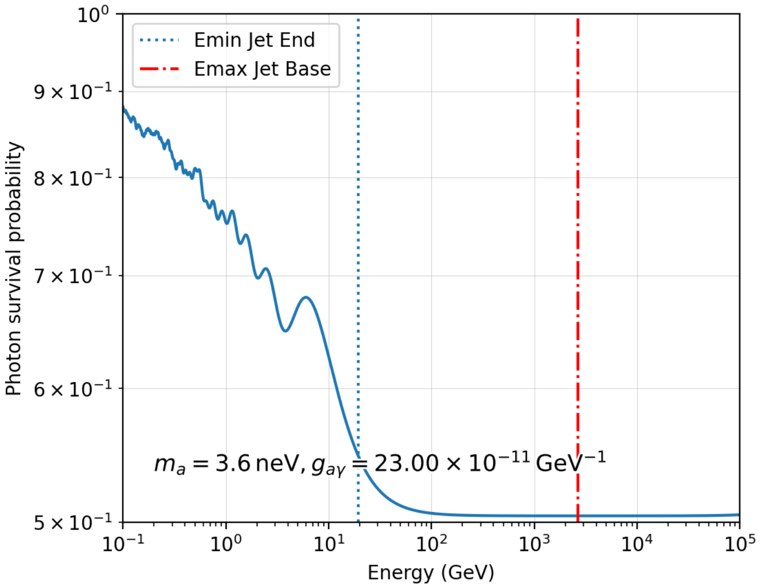

FIGURE 3.4: The corresponding photon survival probability when photon-ALP beam travel through the jet magnetic environment as shown in Fig. 3.3

The main structure of this magnetically dominated jet model is an accelerating jet base which arises from the disk-driven model, and when the flow is accelerated up to really high Lorentz factors the net radiation force (exerted via e.g. Compton scattering) starts to act oppositely upon the bulk movement, the jet therefore transits to a decelerating conical jet [234]. The transverse component field strength of the JMF with this particular model drops as $1/r^{\alpha}$ in the parabolic base, where α is the parabolic base index, and goes roughly as $1/r$ in the conical jet [203, 233].

As discussed above, the JMF has a very strong transverse B-field component to the propagation direction of the photon/ALP beam. The presence of such strong external magnetic field could contribute greatly to the photon-ALP mixing effect despite its comparatively smaller size than other magnetized environments. In Fig. 3.4 we present the photon surviving probability for propagation of photon beam in JMF environment with the helical-tangled jet magnetic field model described above. The set of B-field parameters used for calculation of photon-ALP conversion probability are provided within this particular model[4]. The ALP parameters are set at values from pulsar analysis [40]. The vertical blue dotted line and red dotted-dashed line stand for energy boundaries of gamma-ray emission in jet base and end respectively.

The JMF, as one of most prominent magnetic fields in the vicinity of AGNs, are of great importance in contributing the first possible region for conversion of photons to ALPs. However, the results shown here are based on a particular model of JMF and thus could lead to different outcome when alternative models are used.

---

[4] `https://gammaalps.readthedocs.io/en/latest/tutorials/mixing_HelicalTangled_jet.html`

3.2 Intra-cluster magnetic field

Intra-cluster magnetic field (ICMF): Magnetic fields associated with the intra-cluster medium in clusters of galaxies have been studied intensively in the past decades through various methods, observations, simulations, theoretical modelling, etc. It is investigated mostly in the radio band from studies of rotation measure (RM) of polarized radio galaxies and synchrotron emission of diffuse sources. Studies have shown that a B-field of $\mathcal{O}(\mu G)$ is commonly observed in intra-cluster regions (see Ref. [235] for a review), with values up to tens of μG at the core of the clusters [235–238]. High resolution RM images show a nearly Gaussian RM distribution in a lot of cases, which suggests the magnetic field component follows an isotropic distribution along the line of sight. Interestingly, on the other hand, some of many RM distributions also show clear signs for a non-Gaussianity feature when averaging over large-scale areas after subtracting galactic contribution. Therefore, the magnetic field must be tangled on very small scales in order to account for the small-scale structure shown in RM images, and at the same time, also fluctuate on orders of magnitude larger than the radio source size for the production of non-zero $\langle \mathrm{RM} \rangle$. Thus, a divergence-free homogeneous, isotropic and gaussian turbulent magnetic field model with zero mean would offer a better description for the B-field in ICM, and it would account for both large-scale and small-scale fluctuations seen in observations [36, 235, 239]. On top of that, turbulent field with simple cell-like structure, where B-field strength is constant in each cell (of coherence length at order of $\sim 10\,\mathrm{kpc}$) but varies randomly from one to another, is also commonly considered for modelling the ICMF [236, 240].

In the following subsections we take an example of NGC 1275 to show the B-field variation and the corresponding photon-ALP mixing with two different models: X-ray cavity regular field model and Gaussian turbulent model. Besides, we present here also a brief introduction on a more realistic but complicated model: magnetohydrodynamic (MHD) model.

3.2.1 X-ray cavity regular field model

Jet originating from AGN in the center of the cluster can inflate bubbles of hot, relativistic plasma into the surrounding thermal gas of the intra-cluster medium (ICM), which makes the bubbles become buoyantly unstable and then rise up away from the cluster core until they can reach large radii before colliding or dispersing. These bubbles, or cavities, in principle, could be observed in some high-resolution images of clusters as regions with suppressed X-ray emission. Therefore, such cavities are often referred as the X-ray cavity. In the example of Perseus cluster, a number of such cavities have been observed within hundred of kpc from the center of the cluster, NGC 1275 [241, 242, 242–244]. According to Chandra observations in Ref. [241], a ridge of around 93 kpc away from the center of the cluster has been identified and is interpreted as a relic of a collapsed bubble. Although, it is still under debate that whether or not this "cavity" falls along the line of sight from earth to the center of cluster, and also if it reaches an equilibrium when the bubble is turning into the thermal gas of ICM, such that the electron density is different from inside and outside the cavity [245, 246]. In Fig. 3.5 we use the regular model implemented in Ref. [246] where they take into consideration the X-ray cavity field with a regular magnetic field.

As an example of studying this regular magnetic field in intra-cluster environment, the case of NGC 1275 is used here, the most popular target for searches of spectral irregularities in ALP context, for both X-ray and gamma-ray bands. Suggested by Ref. [245], the following solution is provided for regular B-field at large scales:

$$B_r = 2\cos\theta f(r_1)/r_1^2, \tag{3.1}$$

$$B_\theta = -\sin\theta f'(r_1)/r_1, \tag{3.2}$$

$$B_\phi = \alpha \sin\theta f(r_1)/r_1. \tag{3.3}$$

where

$$f = \mathcal{C}(\alpha\cos(\alpha r_1) - \sin(\alpha r_1)/r_1) - F_0 r_1^2/\alpha^2, \tag{3.4}$$

$$F_0 = \mathcal{C}\alpha^2(\alpha\cos\alpha - \sin\alpha). \tag{3.5}$$

α is the lowest nonzero root of $\tan\alpha = 3\alpha/(3-\alpha^2)$, $r_1 \equiv r/R$ with R as the cavity radius. $\mathcal{C}$ is the normalization constant evaluated at $r = 0$. In the X-ray cavity around NGC 1275, the viewing angle $\theta = 45°$ is assumed as well as the cavity radius $R = 93\,\text{kpc}$ [241]. As for the normalization of the field it is chosen in such a way that the Faraday Rotation Measurement of $\sim 7300\,\text{rad/m}^2$ [247] for the central direction could output the electron density obtained from X-ray observation. This normalization would result a field strength of $8.3\,\mu\text{G}$ in the center.

In Fig. 3.5 we plot the corresponding B-field components for this regular model, where the B-field strength slowly decreases to very weak field as the location of measurement stays further away from the center of the cavity, and down to $0\,\mu\text{G}$ B-field when reaching the full radius of cavity.

The photon surviving probability is shown in Fig. 3.6 with an initial unpolarized photon beam (see Ref. [246] for details), where the values of ALP parameter $(g_{a\gamma\gamma}, m_a)$ from pulsar analysis [40] is used and shown in the plot. In comparison to the case where we only have ICM as an external magnetic field contributing to photon-ALP conversion, we

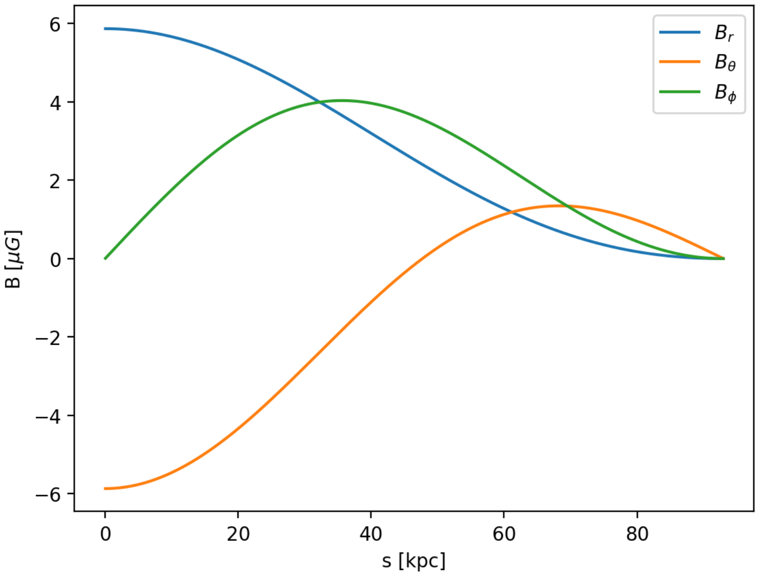

Figure 3.5: The regular component of the intra-cluster magnetic field for the ALP signal from [40]. Longitudinal, B_r, and two transverse components, B_θ, B_ϕ, are the magnetic fields for the X-ray cavity around NGC 1275.

also plot the scenario where the photon beam traverses multiple astrophysical magnetic environments. We can see at the lower energies the conversion ratio is mainly dominated by the photon-ALP mixing taking place in ICM, with small fluctuations at hundreds of MeV originating from the GMF environment (GMF model used here is from Jansson and Farrar [207]). Whereas relatively large conversion ratio of $\gamma \to a$ occurs at several GeV when photon-ALP mixing takes place over different components of GMF model. As it reaches even higher energies, the photon-ALP mixing becomes maximal in the ICM and GMF, and EBL absorption starts to dominate.

3.2.2 Gaussian Turbulent field model

Faraday rotation measurements and non-thermal emission (e.g. synchrotron emission) from radio observations suggest evidence for the existence of turbulent magnetic field with strength at $\mathcal{O}(\mu G)$ in galaxy clusters [235, 248]. The strength of the turbulent B-field follows the electron density of the ICM [36]:

$$B^{ICM}(r) = B_0^{ICM}(n^{ICM}(r)/n^{ICM}(r=0))^{\eta^{ICM}}, \tag{3.6}$$

where η^{ICM} is a scaling factor, a value of $\eta^{ICM} = 0.5$ is chosen here motivated from MAGIC observations of the Perseus cluster [249], n^{ICM} is the electron density of the ICM, which can be written with the model from Ref. [250]. B_0^{ICM} is the root mean square of the B-field of ICM, a value of $10\mu G$ is chosen here based on lower limit of B_0^{ICM} from

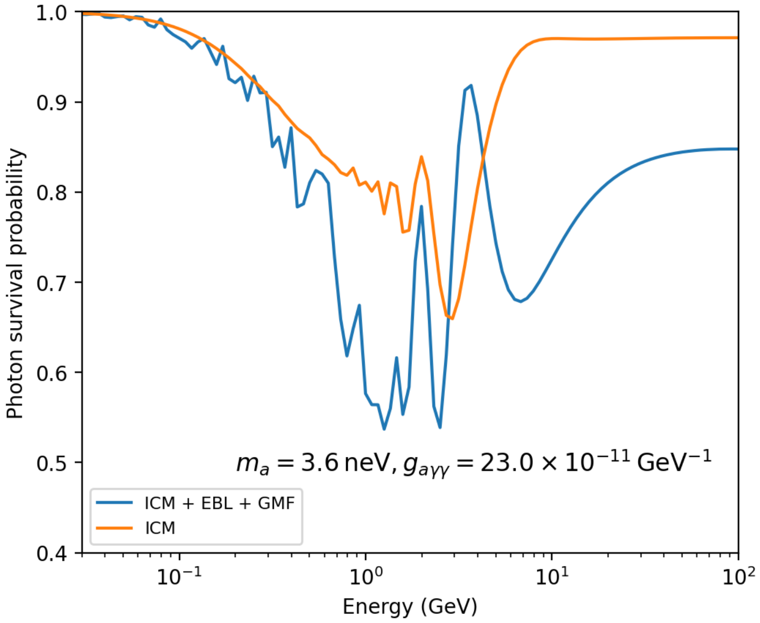

FIGURE 3.6: Photon surviving probability in the presence of the intra-cluster medium only (orange solid line), in comparison to various magnetic environments combined (blue solid line). The ICM environment is modelled with the regular model of cluster from [246].

MAGIC [249]. The maximum and minimum turbulence scales related to energy density ($M(k) \propto k^q$) are chosen to be $k_H = 2\pi/\Lambda_{min}$ and $k_L = 2\pi/\Lambda_{max}$ respectively. The values of these turbulence scales used here are the same as the ones from Ref. [49], as well as the other relative parameters. As for the turbulence spectrum index, q, is assumed to be $q = -2.8$ from RMs of the cool-core cluster A 2199 [251].

We show in Fig. 3.7 distributions of 10 random realization of turbulent B-field as a function of turbulence scale for NGC 1275 in the intra-cluster environment, where we can see that B-field distribution (plotted with blue and orange solid lines) in two panels are two components transversal to the propagation direction of the photon flux. In comparison to the regular B-field in Fig. 3.5 the turbulent B-field is in a state of extreme oscillation, and the strength of the B-field (as well as the oscillation) tends to decrease as the turbulence scale increases. The maximum radius assumed here for the size of the clusters is 500 kpc, at which very small B-field variation would be seen. On contrary, the B-field is in strong turbulence near the core of clusters (roughly $0 \sim 100\,\text{kpc}$ [36]). The maximum variation for the amplitude of the B-field depends on the $\mathcal{B}_{rms}$ (in this case, we assume the value of $10\,\mu$G).

In Fig. 3.8 we show the corresponding photon surviving probabilities for each realization of the turbulent magnetic field shown in Fig. 3.5. The oscillation mainly takes place in the lower energy end for the ALP parameters chosen here, which is due to the resulted small critical energies $E_c \propto \frac{m_a^2}{B_T g_{a\gamma\gamma}}$ here (see Ref. [33, 46] for details), and as the energies

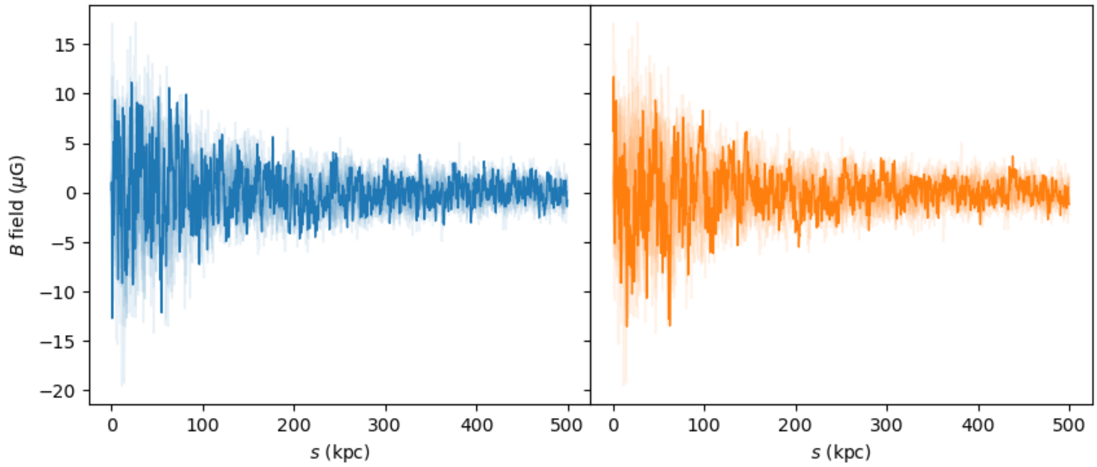

FIGURE 3.7: 10 random realizations of the ICM turbulent B-field in the case of NGC 1275. The two color lines in two panels correspond respectively to two components of the B-field transversal to the propagation of the photon beam. Random one of the ten realizations in each panel is indicated with dark colored lines while the rest are shown with light colored lines.

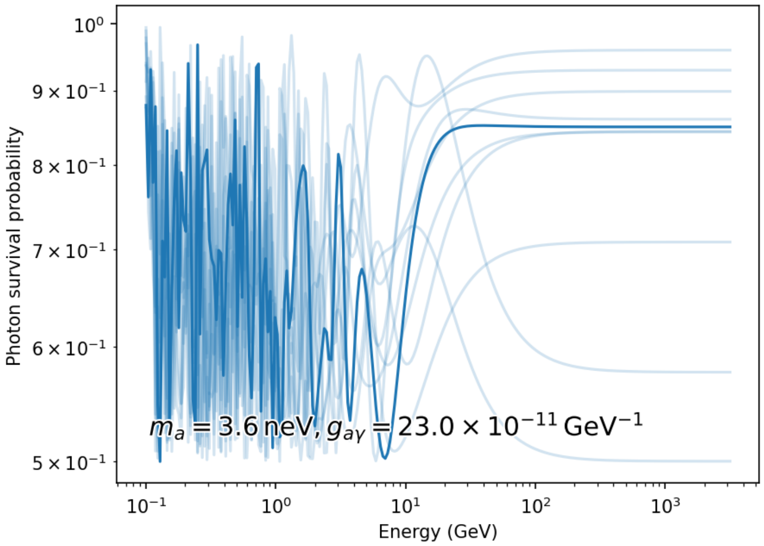

FIGURE 3.8: Photon survival probability for each realization of the B-field in Fig. 3.7.

reach about 100 GeV and above, the photon-ALP oscillation enters the strong mixing regime and becomes energy independent. On top of that, in the random magnetic fields we realize here the maximum conversion probability basically ranges from 0.5 to 1 within the analyzed energy range.

3.2.3 Magnetohydrodynamic model

In this subsection we present yet another magnetic field model for the intra-cluster medium, with more complicated and realistic structures in comparison to the first two models shown previously, namely the Magnetohydrodynamic model.

Clusters of galaxies are filled with a hot, diluted, magnetized plasma as well as the intra-cluster medium, which produces great amounts of X-rays for evident observations. The ICM is near local hydrostatic equilibrium and is characterized by significant MHD turbulence. The magnetic field is considered to originate from the motions of gas by dynamo process [252], which is powered by many different processes, both internally and externally. These processes include jet-driven activity resulting in ICM shocks and cavities [253], turbulent wakes of individual galaxies [237, 254], and cluster mergers [255, 256].

Refs. [257, 258] show that the formation of magnetized galaxy clusters from an initial density perturbation field could be derived using MHD cosmological simulations. The $\mathcal{O}(\mu G)$ level field presently observed in galaxy clusters can be reproduced by the evolution of the magnetic field through MHD dynamos (e.g. cluster collapse and cluster mergers), where the seed magnetic field is initially a weak field at orders of 10^{-9} G with large redshift.

Particularly, many MHD simulations and calculations show that the turbulence is the main source responsible for driving nonlinear amplification. In Refs. [257, 259] the authors investigate the origin, distribution, strength and evolution of the magnetic fields, and the results show that the dynamo process of MHD can significantly change the structure and strength of cluster-wide magnetic fields, and also give rise to the amplification of the B-field intensity.

In Fig. 3.9 we show an example of a dedicated simulation of MHD model field in the NGC 1275 cluster environment [252], where a cross-section of the magnetic field initialized with a weak seed field is shown in the left panel from MHD simulations. The seed magnetic field grows exponentially after enough number of turnover times of rms velocity. During the evolution of the seed field, the magnetic field is highly non-Gaussian but weak in field strength. The dynamo process achieves saturation when the magnetic energy density reaches a value at the same scale of the dynamo kinematic energy density. On the right panel, we show, as a comparison, the structure of the Gaussian turbulent field.

The information we can obtain from this example illustration is that the two models, MHD model and Gaussian turbulent model, are very different from each other in terms of structures and field strength. Many large coherent structures can be visually observed only in the MHD model. This implies the constraints or structures in general are conservative in the picture of Gaussian turbulent field model.

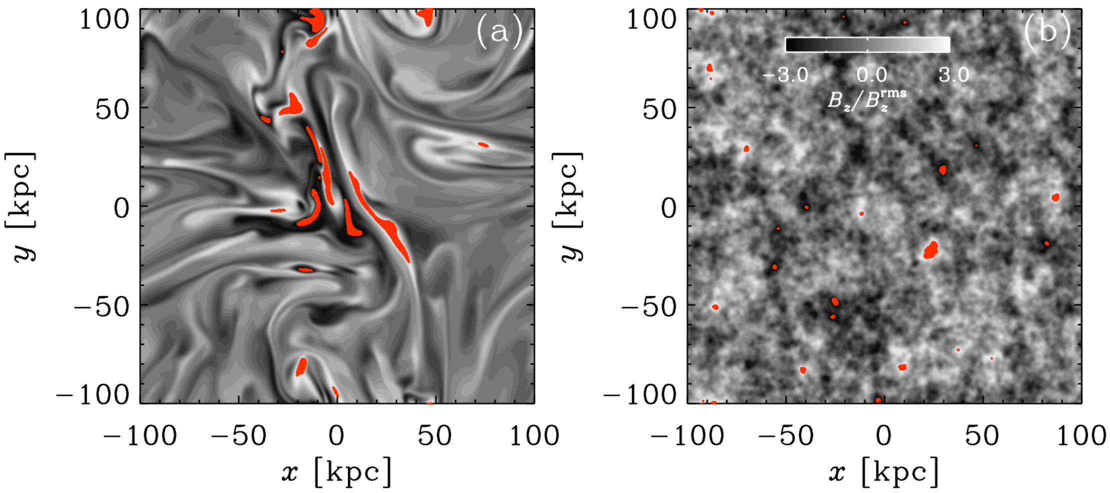

Figure 3.9: Left panel: cross-section of simulated magnetic field with MHD models when the dynamo process reaches saturation. Right panel: a Gaussian turbulent field model with the same power spectrum. The red regions indicate where $|B| > 3B_{rms}$ (figures are taken from Ref. [252]).

3.3 Intergalactic magnetic field

In comparisons to the jet magnetic field or intra-cluster magnetic field, the intergalactic magnetic field is rather weak. Faraday rotation measurements offer some upper bounds on the strength of IGMF from the polarization plane of linearly polarized radio emission from distant quasars (for details see Ref. [205]). The B-field is with an upper limit of $\mathcal{O}$(nG) over a large scale of coherent length (normally at orders of Mpc). Regarding the morphology of the IGMF, very little is known. The most simple assumption is a cell-like structure, where the B-field strength is constant in each cell and increases with cosmic expansion, and the B-field direction varies randomly from one cell to the next one. This is discussed in the following context with more details.

The intergalactic medium, more precisely, the voids of the large scale structure (LSS), is the place where the primordial seed field lives if weak magnetic field were in actual presence in the early universe before the start of structure formation. In comparison to the magnetic field present in galaxies or galaxy clusters, the magnetic field in voids did not go through many amplifications due to the absence of the dynamos and compression of IGM [205], and because of the lack of amplification, the magnetic field in voids is one of the weakest field ($\mathcal{O}$(nG)) in astrophysical environment. Alternatively, it has been suggested that the considered magnetic fields generated by quasar outflows in the low-redshift universe could also provide hints on the origin of large-scale magnetic fields [260].

In general, large scale magnetic fields are assumed to have a cell-like structure, particularly in the case of the IGMF [32]. To be more specific, the magnetic field in the cell-like structure is constant over a single domain of size L while changing randomly its direction from one domain to the other but keep approximately the same strength. Conveniently, this particular IGMF model proposed in Ref. [32] is implemented in the `gammaALPs` python package, here in Fig. 3.10 we make use of the package to give an example of how the magnetic field varies in the redshift space. Owing to the the high electrical conductivity of IGM, the flux conservation during the cosmic expansion implies the B-field would scale with the volume, to the power of 2/3 according to Ref. [32] (see Eq. 126 in the reference). Therefore, the strength of transversal B-field slightly increases from the first domain where it extends from $z = 0$ to Δz.

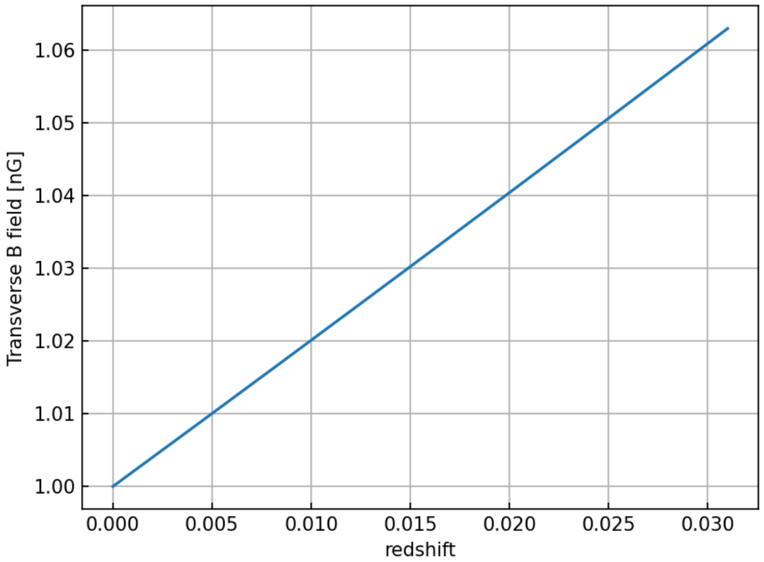

FIGURE 3.10: The absolute values of transversal B-field in multiple domains as a function of source redshift along the line of sight in the intergalactic space with cell-like model.

Followed by the B-field described in Ref. [32], we calculate the photon surviving probability with different ALP masses in the IGMF environment in Fig. 3.11, with one random B-field realization, where the upper limit $B_{rms}^{IGMF} = 10^{-9}\,\mathrm{G}$ for IGMF is taken, showing the maximal photon-ALP mixing when photon flux traverses the intergalactic space. The curves associated with different ALP masses indicate possible photon-ALP conversions at different energies. The EBL absorption is taken into account when calculating the photon-ALP conversion, and for comparison, we plot the scenario where only EBL absorption is considered. As we can see from Fig. 3.11, the modulation on flux by photon-ALP mixing is considerably small compared to the photon-ALP mixing in other astrophysical environments (such as JMF or ICMF) due to the very weak magnetic field strength, and the modulation induced on photon flux is basically dominated by the

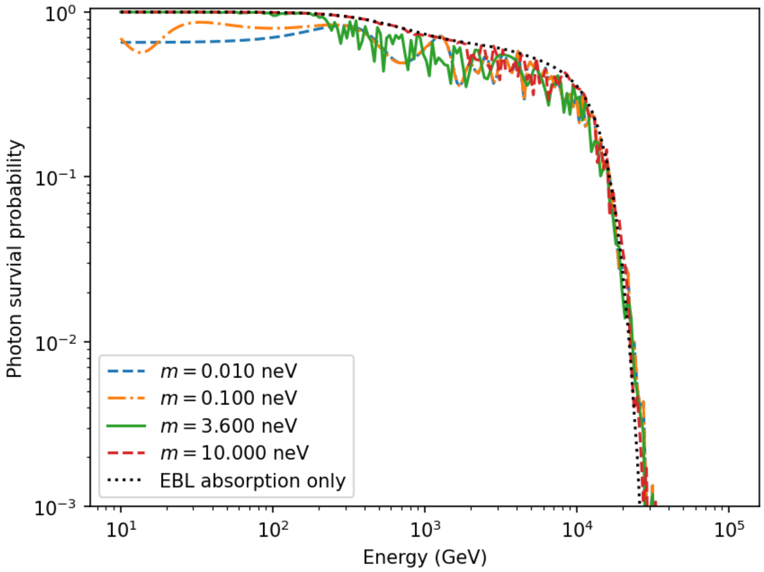

Figure 3.11: Photon surviving probability in the presence of the intergalactic magnetic field (of voids) calculated using a cell-like model described in [32]. For comparison reasons, scenarios with different masses of ALPs are plotted as well. The EBL absorption (with Dominguez at el. EBL model [261]) is also plotted as the black dotted line.

EBL absorption with the ALP mass ($m_a = 3.6\,\text{neV}$) employed in this work, despite the maximum field strength for IGMF is taken. Based on this, we therefore neglect the photon-ALP mixing effect in IGMF for our later calculation in Chapter 4. However, the photon-ALP mixing effect should be treated with caution in IGMF when smaller ALP mass is considered, as shown in Fig. 3.11.

On top of that, the filaments of IGMF, connecting galaxy clusters, are expected to have a stronger B-field strength compared to the magnetic fields in voids and could contribute additional photon-ALP conversion regions in the intergalactic space.

The detection of magnetic fields in filaments has drawn much attention in the past years, the upper limit of which is provided by a variety of approaches [262–268]. The intensity of the magnetic fields in filaments and its time evolution can offer us extra information about these structures in cosmic web and evolution of extragalactic sources that dominate the amplification of cosmic magnetic fields. Rotation measure with red shift z and polarization of extragalactic sources play an important role in studying the evolution of magnetic fields. Cosmological simulations have been used to study the conditions for generating magnetic fields in filaments ranging from a few nG to tens of nG depending on whether additional astrophysical source field seeding is involved. For example, in Ref. [268], the authors analyzed the behaviour of extragalactic source RMs with red shift and fractional polarization in a low-density environment using 144 MHz data from Low Frequency Array (LOFAR) radio telescopes. The same is measured at the frequency of 1.4 GHz. They found that the observed residual RM and fractional polarization are likely to have an origin to local source environment at 1.4 GHz, while a cosmic filament environment is favored at 144 MHz. The estimate for strength of filament field is done by attributing the total residual RM and fractional polarization to cosmic web filaments, such that an average magnetic field per filament is obtained to be around 32 nG.

3.4 Magnetic field of the Milky Way

In comparison to other astrophysical magnetic environments discussed in the previous sections the magnetic field of Milky Way is better studied and well measured. The structure of the Galactic magnetic field (GMF) can be divided into two main parts: a large-scale regular component and a turbulent component. The turbulent field can be described by a cellular structure with a strength of scale of μG over a coherence length of 10^{-2} pc [269], whereas the strength of the regular component of GMF is predicted to be in the order of $\mathcal{O}(\mu\mathrm{G})$ [270, 271] with a size of about 10 kpc [271] for the coherence length. RMs on galactic pulsars have indicated that this regular component is parallel to the Galactic plane. In the following we give the principles of observational tools used for measuring GMF and the modelling of relevant components of GMF for the purpose of searches for photon-ALP mixing effects.

Faraday rotation measures (RMs) and synchrotron radiation are among the best tools for probing and studying the large-scale Galactic magnetic field. Synchrotron radiation has been used mostly in the past for studying external galaxies, while Faraday rotation measures has been used as the main method of studying magnetic field in our Milky Way [270, 272]. In Fig. 3.12 we illustrates how different components of magnetic field are derived from measurements (RM and synchrotron emission).

Galactic synchrotron radiation is produced by charged particles (mostly cosmic-ray electrons) moving spiralling along the interstellar magnetic field lines [274]. Synchrotron emissivity is in general proportional to $B_\perp$, cosmic-ray electron density, the index of power-law-distributed energy spectrum of cosmic-ray electrons and the frequency of the emitted electrons at energy E (as shown in Fig. 3.12). In order to probe the Galactic magnetic field with synchrotron emission, a sky map of polarization is required at certain frequencies. On one hand, the frequencies are conveniently chosen at values where polarized radiation is dominated by synchrotron emission, and the Faraday rotation of synchrotron data is negligible (see e.g. Refs. [207, 275]), such that the stokes parameters of polarization sky map are independent of RM and then the intensity of polarized synchrotron emission can be calculated using the sum of the squares of stokes parameters.

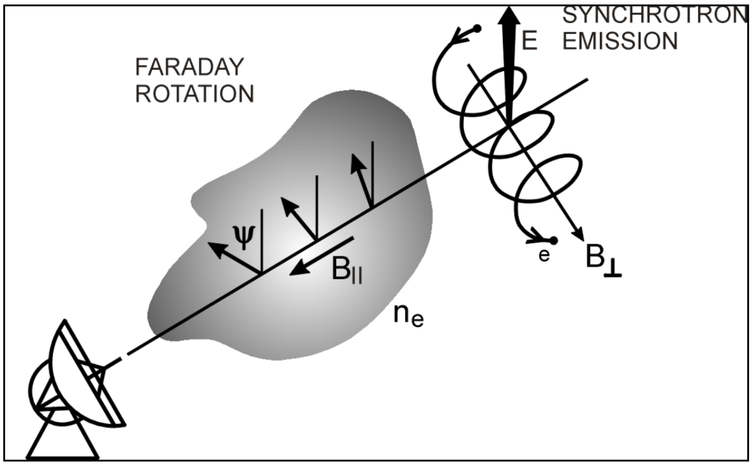

FIGURE 3.12: Illustration for connections of RMs and synchrotron emission to different components of magnetic field along the line of sight. n_e is the thermal electron density, $B_{\|}$ is the magnetic field component along the line of sight, Ψ is the Faraday rotation angle, and $B_{\perp}$ the magnetic field component perpendicular to the direction of electron propagation. Figure credit: Ref. [273]

Depolarization effects (such as Faraday depolarization) [273, 275], on the other hand, also have to be included when calculating the polarized synchrotron intensity.

Rotation measures provide additional constraints on magnetic field strength (parallel component of magnetic field to the propagation of electromagnetic wave), which is done by measuring the change of polarization angle when an electromagnetic wave travels through a magnetized medium (e.g., Galactic magnetic field) as shown in Fig. 3.12. The rotation angle is proportional to the product of squared wavelength and RM: $\Delta\theta = \mathrm{RM}\,\lambda^2$ where RM is defined as the following form in units of rad m^{-2} [207, 275]:

$$\mathrm{RM} \simeq 0.81 \int_0^L \left(\frac{n_e}{\mathrm{cm}^{-3}}\right)\left(\frac{B_{\|}}{\mu\mathrm{G}}\right)\left(\frac{\mathrm{d}z}{\mathrm{pc}}\right), \tag{3.7}$$

In principle, pulsars are among the most ideal sources for studying and constraining Galactic magnetic field for the reason that they are intrinsically highly polarized. Also, most of the pulsars are located closely to the Galactic plane, which makes them good candidates for studying the structure of (large-scale) Galactic magnetic field. However, the distances for large majority of pulsars are poorly measured, and because RM is determined as an integral quantity along the line of sight where the direction of magnetic field reverses many times, such that the predicted RMs are not accurate.

As done in Refs. [207, 275], polarized extragalactic radio sources can also be used as good candidates to measure Faraday rotation effects and provide constraints on GMF. Contributions to the observed RM towards extragalactic radio sources can be roughly divided into two parts: extragalactic RM and galactic RM. Extragalactic RM includes the

RM of polarized radio emission originated within sources, and foreground RMs from intergalactic magnetized medium. In comparison to the very small RM from extragalactic space, RM from Milky Way is much larger and generally dominates the contribution to the whole measured RM at Earth for most of the radio sources [276, 277]. Galactic contribution to the RM has been estimated from collections of observations of extragalactic radio sources in Refs. [207, 278].

It is then possible to model the GMF with a set of parameters which can be fitted using the observational data of RM and synchrotron emission. The turbulent component is however too small to induce any photon-ALPs mixing effect due to its very small coherence length. Thus, in this work, we adopt the large-scale regular component of GMF model from Ref. [207] (referred as J&F model in later context) in the context of ALP searches.

The J&F GMF modelling for the large-scale component is based on observational measurements of synchrotron emission and RM [279] (turbulent component modeling can be found in Ref. [280]). It consists of three components: a disk field, a toroidal halo field and a so-called out-of-plane X component field. We show the halo and X components of J&F GMF model in Fig. 3.13. The large-scale out-of-plane component arises from the observational indications of external galaxies [281, 282], with which the fit to the data is dramatically improved in comparison to the previous GMF model in [275]. The X component, as shown in the figure, is chosen to be axis-symmetric and poloidal since the azimuthal component is separately incorporated in the toroidal halo component, which we shall discuss briefly later. The field is set to be 0 for $r > 20\,\text{kpc}$ and 1kpc-radius sphere around the galactic center. The reason for that is because the estimated radius of Milky Way is about 15 kpc-20 kpc. As for the zero-strength field in galactic center, the reason for such simplification is that the B-field is dominated by different processes than those

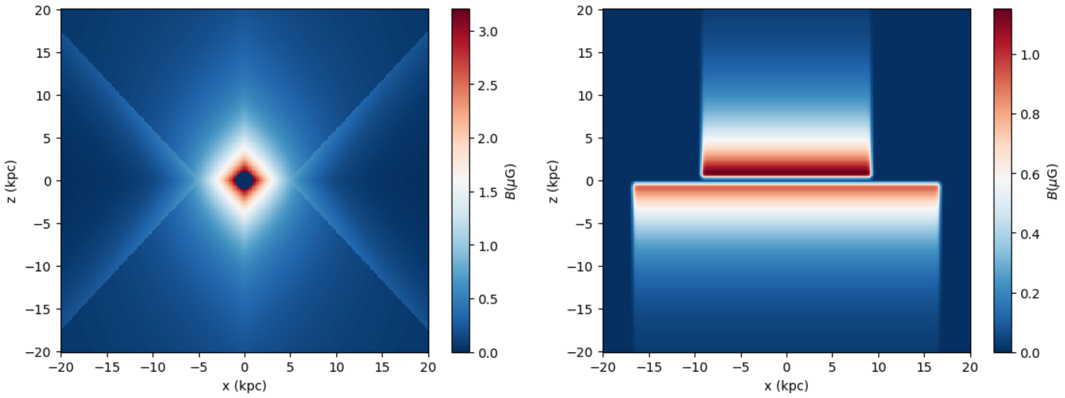

FIGURE 3.13: Left panel: x-z slice of GMF showing only the B-field in the so-called X (out-of-plane) component with J&F model. Right panel: x-z slice of GMF showing only the toroidal component with J&F model. Colorbars in both panels indicate the strength of the B-field. Both subplots are created using the python package `gammaALPs`.

of global GMF, which makes it very complicated and the center field only affects very few of the data points (less than 0.2%) used for the modelling. Similarly, the first feature we can see in the x-z slice of halo toroidal component is the gap within $z = \pm 1\,\mathrm{kpc}$. On top of that, we can see the halo toroidal component is anti-symmetric with respect to the disk component, both the strength and radial extensions. Besides, the strength of the B-field in both northern and southern sides are decreasing exponentially along the direction of z. The specific forms for the way of variation of B-field in either the X component or the halo toroidal component are chosen in the way such that it fits better to the data and therefore describe better the pattern from RMs and synchrotron polarization map [207]. The disk component of the GMF is, however, not strongly relevant to the study in this work as the arrival direction of the gamma-rays from most of the extragalactic AGNs does not align with the galactic plane (see Fig. 3.14 for the positions of the sample sources in galactic coordinates). In comparison to other GMF models (e.g. Pshirkov GMF model [283]), the out-of-plane field and halo strengths are predicted to be larger, which would result in a stronger photon-ALP mixing effect in certain regions in the sky. In Fig. 3.14 we show a sky map of photon-ALP conversion probability in a scenario where an unpolarized photon beam enters the Milky Way with the energy of the photons at 100 GeV and ALP parameters at $g_{a\gamma\gamma} = 23 \times 10^{-11}\,\mathrm{GeV}^{-1}$, $m_a = 3.6\,\mathrm{neV}$ [40]. The

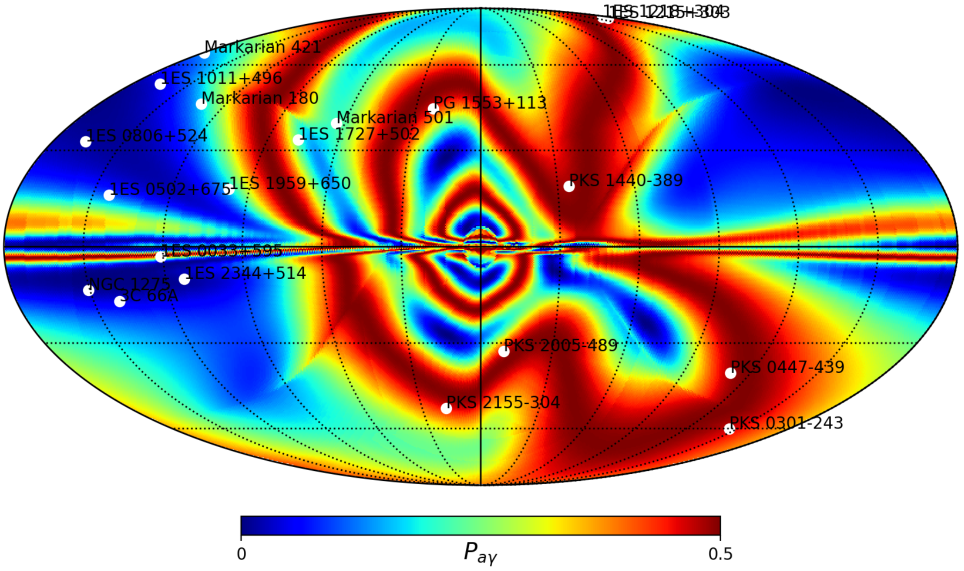

Figure 3.14: The skymap of probability distribution of photons converting into ALPs in the presence of the J&F GMF under the assumption of an unpolarized photon beam entering the Milky Way with the energy of 100 GeV. The values of the ALP parameters used in this particular plot are motivated from the pulsar analysis in Ref. [40]. Sample sources used in this work are marked as white points.

sampled sources (see Chapter 4 for selection of the sample sources) used in this work are marked as white points. The colorbar of the plot is set in a way for better visualization.

The pattern shown in the skymap is considered to be highly model-dependent. As we can see from the figure that the maximal probability of photons converting into ALPs is around 0.5, which is the case for some sources such as 1ES 1215+303, PKS 1440-389 and PKS 2005-304. However, depending on the line of sight for observations, the GMF environment makes very small contribution to the photon-ALP mixing effect for nearly half of the sample sources. Combining both Fig. 3.14 and Fig 3.15 we can see firstly that for sources, such as 1ES 0033+595 and 1ES 2344+514, the oscillation takes place at slightly smaller energies, this is because these sources are located near the galactic plane where the magnetic field is slightly stronger (see Fig. 3.13), which leads to smaller critical energies ($E_c \propto m_a^2/(g_{a\gamma\gamma}B)$) and larger conversion probabilities ($p_{\gamma\to a} \propto g_{a\gamma\gamma}^2 B^2 s^2$). However, the conversion probabilities becomes smaller when the energy of photons are slightly larger than the critical energies, which is due to oscillation effects from Eq. (2.28). Furthermore, as the photon energy is much larger than the critical energy ($E \gg E_c$), the mixing effect becomes maximal and energy-independent. On the other hand, large conversion probabilities obtained in sources such as 1ES 1215+303, PKS 1440-389 and PKS 2155-304, are mainly driven by the large strength of halo and X components in J&F GMF model.

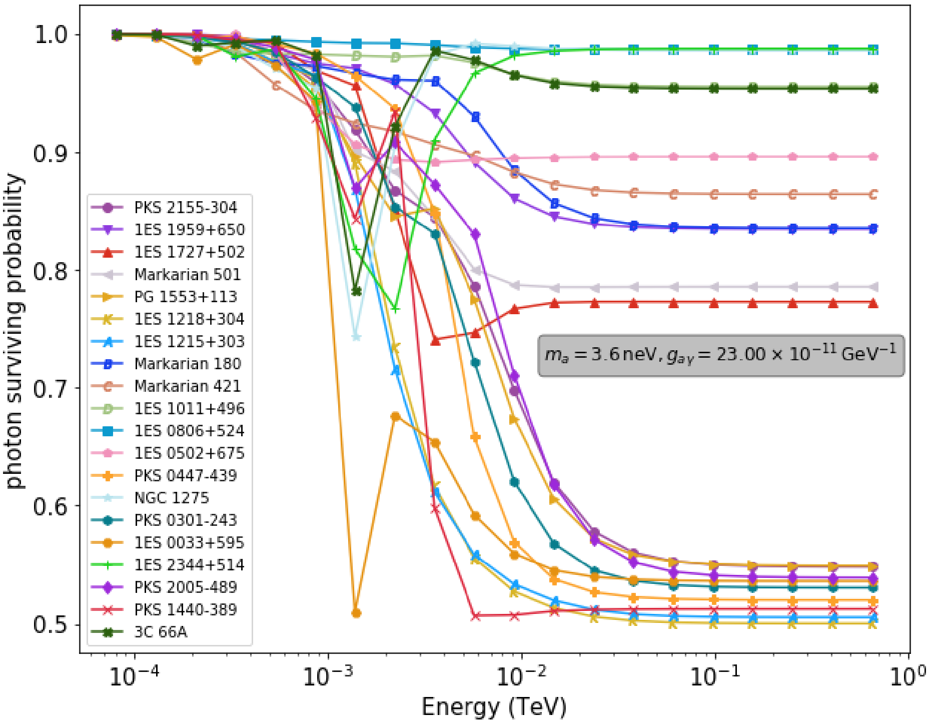

FIGURE 3.15: Photon surviving probability as a function of energy for sample sources collected in this study. The probability for photon-ALP mixing effect is calculated in the presence of only GMF regular component. An unpolarized beam is assumed here for the initial state of photons.

The photon/ALP beam crosses the GMF environment before being detected. Since the B-field strength in the GMF is relatively large, ALPs that produced or converted in the source region fields (JMF, ICMF) can oscillate back into photons when they travel through the GMF. As we show in Figs. 3.14 and 3.15 the GMF environment is very important in the searches of photon-ALP mixing signatures where the probability of converting into ALPs can reach nearly 0.5 for a purely unpolarized photon beam at higher energies.

Chapter 4

Searches of photon-ALP mixing effect in AGN spectra

In order to account for the modulations seen in the high-energy gamma-ray spectra, we introduce the photon-ALP mixing effect. However, the detection sensitivity of photon-ALP mixing in high energy gamma-ray spectra is closely related to the uncertainties on the measurements of differential flux. The appearance of such modulations would then require strong mixing effects of photon-ALP, i.e., large conversion probability $p_{\gamma\to a}$ (see Eq. (2.28)) to achieve higher signal-to-noise ratio. Therefore, large distances and considerably strong transverse magnetic field to the direction of the propagation are preferred conditions for the searches of these modulations. Extragalactic sources are ideal targets that can be used for spectra study, especially AGNs, for their intense emission of VHE gamma-rays, and the complexity of B-field configuration along the line of sight for propagation of gamma-rays.

AGN Blazars are powerful sources of emission across the electromagnetic spectrum and are observed to be sources of high-energy gamma-ray photons. The special jet orientation explains the general features possessed by blazars: very high luminosity, very rapid variation and high polarization compared to quasars. In principle, an ideal blazar high state should last long enough to offer us a relatively stable determination of the photon flux and index, and the source should remain steady in general while in high flux state, such that average GeV and TeV measurements could represent well the source during this high but not rapidly variable state. This could potentially allow us to explore the very high energy (VHE, $E \gtrsim 100\,\mathrm{GeV}$) range of γ rays if needed. The AGN samples in our selection not only serve well this point, but they can also be used to search for the photon-ALP conversions $\gamma \to a$ and $\gamma \to a \to \gamma$ simultaneously at different energy regions.

In this chapter, we will follow these approaches and show the results from our published work of [46], where we used a certain methodology to process the data and fit observational data to the model with photon-ALP mixing.

4.1 Source selection and data reduction

4.1.1 Source selection

In order to cover a large range of energy for associating various scales of magnetic fields with AGN spectra, we select AGNs which have a hard gamma-ray spectrum and are sufficiently bright to measure the flux accurately. Thus we impose the following criteria on our selection of samples from the fourth *Fermi*-LAT source catalogue, 4FGL [108]. These criteria are:

1. Source type (association): AGN of BL Lac blazar type.
2. Red shift: z known or constrained to be at $z < 0.5$.
3. TeV association: in order to potentially extend to very high energies (VHE: $E >$ 100 GeV), we require the sources to have an association to known VHE sources (*TeVCAT* flag[1]).
4. Hard spectrum: photon index is smaller than 2.
5. Signal-to-noise ratio: detection significance larger than 50 standard deviations.
6. Photon statistics: number of predicted photons (N_{pred}) should exceed 1600.

We show the collection of sources that pass the cuts in Table 4.1. 19 of these sources are BL Lac blazars. In addition, we include one more radio galaxy, NGC 1275, which is located at the center of the Perseus cluster that most likely supports an extended magnetic field [241] and as well as a turbulent one [247]. This highly magnetized environment is ideal for searching of photon-ALP mixing effects and it has motivated several studies on searching for such effects using *Fermi*-LAT data in energy spectrum of NGC 1275 [44, 49, 246].

---

[1] `http://tevcat.uchicago.edu/`

Table 4.1: AGN sources selected for this study (in order of right ascension). The information listed are Galactic longitude (l) and latitude (b), red shift (z). Also, detection significance, photon index, and predicted event counts from Fermi 4FGL catalog.

AGN name	Source type	$l[^\circ]$	$b[^\circ]$	z	Detection signif. (σ)	Photon index	$N_{\rm pred}$
1ES 0033+595	HBL	120.90	−3.02	0.467	68	1.765	2954
3C 66A	IBL	140.15	−16.76	0.34	182	1.971	15207
PKS 0301-243	HBL	214.63	−60.19	0.2657	108	1.914	5623
NGC 1275	Radio Galaxy	150.58	−13.26	0.017559	245	2.114	35561
PKS 0447-439	HBL	248.81	−39.91	0.343	167	1.865	12536
1ES 0502+675	HBL	143.79	15.89	0.34	64	1.601	1718
1ES 0806+524	HBL	166.25	32.94	0.138	100	1.881	5147
1ES 1011+496	HBL	165.53	52.71	0.212	169	1.838	9806
Markarian 421	HBL	179.88	65.01	0.031	344	1.781	30562
Markarian 180	HBL	131.91	45.64	0.045	50	1.798	1623
1ES 1215+303	HBL	189.01	82.05	0.131	146	1.933	10779
1ES 1218+304	HBL	182.21	82.74	0.182	83	1.722	3285
PKS 1440-389	HBL	325.65	18.71	0.1385	78	1.845	3788
PG 1553+113	HBL	21.92	43.96	$\lesssim 0.5$	120	1.681	10046
Markarian 501	HBL	63.60	38.86	0.034	173	1.790	11127
1ES 1727+502	HBL	77.07	33.54	0.055	60	1.790	2251
1ES 1959+650	HBL	98.00	17.67	0.048	169	1.817	11700
PKS 2005-489	HBL	350.37	−32.61	0.071	70	1.838	3115
PKS 2155-304	HBL	17.74	−52.25	0.116	239	1.850	17766
1ES 2344+514	HBL	112.89	−9.90	0.044	71	1.811	3201

4.1.2 *Fermi*-LAT data reduction

In this study we collect 10 years of *Fermi*-LAT data taken from Aug. 4, 2008 to Aug. 4, 2018 in the energy range of 100 MeV-500 GeV. Events within a region of interest (ROI) defined as a cone centered on each source with a half-opening angle of 10° are selected. After applying such filtration on the events, LAT data processed in `Pass 8` is then downloaded together with the spacecraft file from the *Fermi* data server. Flux determination and spectral modelling of the sources in Table 4.1 are achieved by using the maximum likelihood optimization method. We give a step-by-step brief introduction of how we proceed the binned likelihood analysis (see Fermi Science Data Center for detailed documentation[2]).

- `gtselect (evclass=128, evtype=3)`
  Depends on the specific purpose of the analysis, photon events that have been presorted into different classes should be selected correspondingly using command `gtselect`. For example, “Ultracleanveto” class (`evcalss=1024`) is recommended for checking cosmic-ray induced systematics as well as diffuse emission studies. However, the AGN samples listed in Table 4.1 are categorized as point sources (`evcalss=128`), which, following the instructions of LAT instruments, should be processes with `P8R3_SOURCE_V2` IRFs file. Furthermore, since the energy resolution in low energy band of our analysis is poor, a hidden parameter `evtype=3` can be used to include all converting events within all point spread functions (PSF) and all energy subclass in the front and back of the tracker on LAT telescope. Then, only gamma-ray events with reconstructed zenith angles smaller than 90° are selected for the purpose of reducing contamination by gamma-rays from Earth’s limb.

- `gtmktime ((DATA_QUAL>0)&&(LAT_CONFIG==1))`
  The photon events can be further processed again to remove the “bad” events using `gtmktime`. This command is used to create a list of Good Time Intervals (GTIs) based on the specified cuts provided in the `gtselect` step. A GTI is a period of time when the data is considered vaild, i.e., the data is collected over the selected time range and this also excludes the time when the observed source is close to Earth’s limb. All “bad” events outside the GTIs would then be removed from the event file. In this work, we use the default parameter setting for the removal of bad quality data, `((DATA_QUAL>0)&&(LAT_CONFIG==1))`.

- `gtbin`
  `gtbin` is then used to perform the event-binning tasks, including time binning for

---

[2] https://fermi.gsfc.nasa.gov/ssc/data/analysis/scitools/binned_likelihood_tutorial.html

creating lightcurves, spatial(&energy) binning for producing counts cube and energy binning for spectral analysis. The counts cube is a three-dimensional counts map with an energy axis and it is used as an input for binned likelihood analysis. Accuracy of likelihood analysis is determined by two important parameters: spatial bin size and energy bin size. We set the spatial bin size to be 0.1°, and we distribute 13 energy bins per decade (within the selected energy range) in order to accommodate rapid variations in the effective area within low energy ranges. Under such binning configuration the energy dispersion is corrected by introducing 3 additional energy bins beyond the selected energy range following recommendations from LAT instrument team.

- `gtltcube` and `gtexpcube2`

  The spectra presented later in this work use differential flux for related analysis, and in order to convert the counts map into a differential flux map we need to compute the livetime cube and exposure cube. `gtltcube` tool is used to calculate the integrated livetime as a function of sky position and off-axis (or inclination) angle (between the direction to a source and the z-axis of the LAT instrument) using the downloaded spacecraft file and event file (with updated GTIs) as an input. Livetime cube, as the name suggests, is essentially the accumulated time during which the LAT is detecting and taking event data, and thus it depends on how long the LAT spends on the target source in an observation and what the associated inclination angles are during different time of the observation. The livetime cube is therefore a function of sky coordinates and binned inclination angles.

  Then, an exposure map can be calculated using the `gtexpcube2` tool with livetime cube as an input. An usual notion of binned exposure map with an energy axis in unit of "$\mathrm{cm}^2\,\mathrm{s}$" is the integral of effective area multiplied by time for a given position in the sky. The main inputs for calculating the exposure cube are: the livetime cube which contains the information of exposure time, coordinate projection and geometry for exposure map to match; the IRFs (including PSF, effective area, energy dispersion matrix) which are functions of energy and inclination angles as well as photon classifications, responsible for mapping from livetime cube to exposure cube. It should be noted that the geometry and energy bin configuration for count cube produced from `gtbin`, livetime cube from `gtltcube`, exposure cube from `gtexpcube2`, all should be the same in order to proceed to further analysis. However, the exposure used in likelihood analysis is more complicated since it is an integral of the total IRF over the entire ROI space. For likelihood analysis the exposure in each cube is calculated as:

$$\epsilon(E,\phi) = \int_{\text{ROI}} dE' d\phi' dt R(E',\phi';E,\phi,t), \tag{4.1}$$

where E' and ϕ' stand for the measured energies and measured directions respectively.

- Target source model and Background models

  The first background contribution comes from all of the sources around our target source within the ROI. Models should be created for all the sources within the ROI with good predictions of source locations and spectral forms (e.g., PowerLaw form, Logparabola form). Fortunately, we can make use of the source models already defined by the LAT team in the 4FGL catalogue, which consist of a spectral and spatial model components, in unit of $\text{cm}^{-2}\text{s}^{-1}\text{MeV}^{-1}$, for all point sources within the ROI. Moreover, it should be noted that sources well outside the ROI may also contribute to the photon counts to sources within ROI due to the large PSF of LAT at low energies. Thus, the ROI has to be extended to few more degrees in order to give a better estimate on photon count. In this work, the extended ROI width is set to be 15° for this purpose. The source model for each source (including the target source) within the extended-ROI can then be further multiplied with the corresponding exposure cubes in their locations, and convolved with exposure cube over energy bins to give a source model count map using the following form:

  $$N_{\text{pred}} = \int dE d\phi \, (dN/dE)_{\text{model}} \, \epsilon(E,\phi). \tag{4.2}$$

  However, this source count map has to be further modified with the second background contribution: diffuse backgrounds. They are modeled with pre-processed templates of the Galactic diffuse emission, `gll_iem_v07.fits`, and the extragalactic isotropic radiation, `iso_P8R3_SOURCE_V2_v1.txt`. The energy dispersion for the background templates is already taken into account[3].

  This step can be done by using the `gtsrcmap` tool.

- `gtlike`

  The `gtlike` tool performs the maximum likelihood method to fit the source models described in the previous step to the LAT data in order to obtain an estimate on the set of the parameters used for the source models within the extended ROI width. The optimizer used in our work when running `gtlike` is the MINUIT. The spectral parameters of the target source are left free before the optimizing and fitting process. Other parameters that enter the fitting process include the

---

[3] https://fermi.gsfc.nasa.gov/ssc/data/analysis/documentation/

spectral normalization parameters for all sources within 3 degrees of the ROI center, as well as all parameters of isotropic and Galactic diffuse components.

Therefore, the likelihood value is the product of probabilities of observing the detected counts in each bin. It is calculated with both the observed count and modeled count data, defined as

$$L = \exp(-N_{\text{pred}}) \prod_i \frac{m_i^{n_i}}{n_i!}, \tag{4.3}$$

where $N_{\text{pred}} = \sum_i m_i$ is the total number of counts predicted by the source model within the entire ROI, as described in Eq. (4.2). m_i and n_i are respectively the modeled count number and observed count number in the i-th bin. Additionally, it should be noted that if the bin sizes are small enough, i.e. the observed count in each bin is $\leqslant 1$, then $n_i! \simeq 1$, which would simplify the calculation of the likelihood.

The details for the likelihood fitting method will be given later in this chapter.

In Fig. 4.1 we show an example of the processed data product of Markarian 421, where on the left panel we present the observed photon count map generated by `gtbin`, while the modeled count map is shown on the right panel after running `gtlike` for fitting to source models and the diffuse backgrounds. The differences between the two figures in Fig. 4.1 could be due to that the size of the binning in model source map is too small. Also, the extended ROI width is not large enough to include enough additional sources to account for the its large PSF effects on the sources within the ROI. Moreover, it is also possible that the ROI sources are not well described by the intrinsic spectral model.

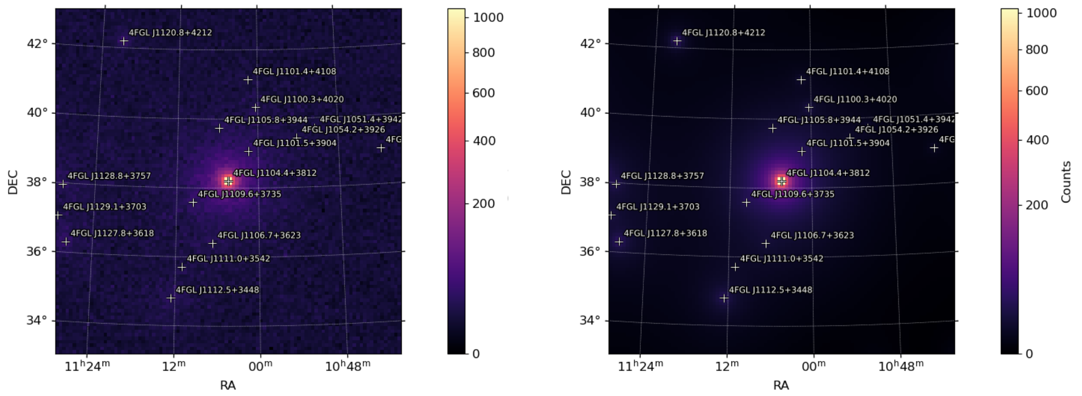

FIGURE 4.1: Left panel: 10-years LAT observation of photon counts map within 10° of the ROI where Mkn 421 is placed in the center. Right panel: the model count map in comparison to the one on the left panel, the models for sources within (as well as few degrees outside) the ROI are from the *Fermi* 4FGL catalogue, the diffuse backgrounds are modeled with templates of the Galactic diffuse emission `gll_iem_v07.fits`, and the extra-galactic isotropic radiation `iso_P8R3_SOURCE_V2_v1.txt`.

In the case of our study, we perform a standard binned likelihood analysis, as described above, with the following specific parameters used in `gtselect`, `gtmktime`, `gtbin`, `gtltcube` and `gtexpcube2`. These parameters are listed in Table 4.2 as a standard configuration file for the *Fermi*-LAT data reduction in our later analysis.

Table 4.2: Configuration parameters for processing LAT data.

Access	**Parameters**	
Selection	E_{min}	100 MeV
	E_{max}	500 GeV
	zenith cut	90 deg
	event class	128
	event type	3
	observation time start	Aug. 4th, 2008
	observation time stop	Aug. 4th, 2018
	target source	Markarian 421
Binning	ROI width	10.0 deg
	bin size	0.1 deg
	Energy bins perdec	13
Model	extended ROI width	15 deg
	Galactic diffuse	`gll_iem_v07.fits`
	Isotropic emission	`iso_P8R3_SOURCE_V2_v1.txt`
	catalogue	4FGL

As for the differential flux points in each bin to be fit or to plot, we can obtain them from the observed count cube generated by `gtselect` and `gtbin` where we bin the data in both spatial (bin size is 0.1°) and energy dimensions (13 energy bins per decade) with the width of 10° for the ROI size. The resulted count array we obtain from the count cube is in the dimension of $(48 \times 100 \times 100)$. We then sum the count cube and exposure cube along the energy axis, and apply the summed exposure cube to the summed count cube in each energy bin to get the final energy-distributed differential flux in units of "photon/$(\mathrm{MeV\,cm^2\,s})$". The resulted energy spectra for likelihood analysis and other related analysis (e.g. χ^2) are in general displayed as the spectral energy distributions (SEDs). The SEDs are then derived by multiplying the individual differential flux values in each bin with the squared geometrical mean energy of each bin. An example of the SED for Markarian 421 is displayed in Fig. 4.2.

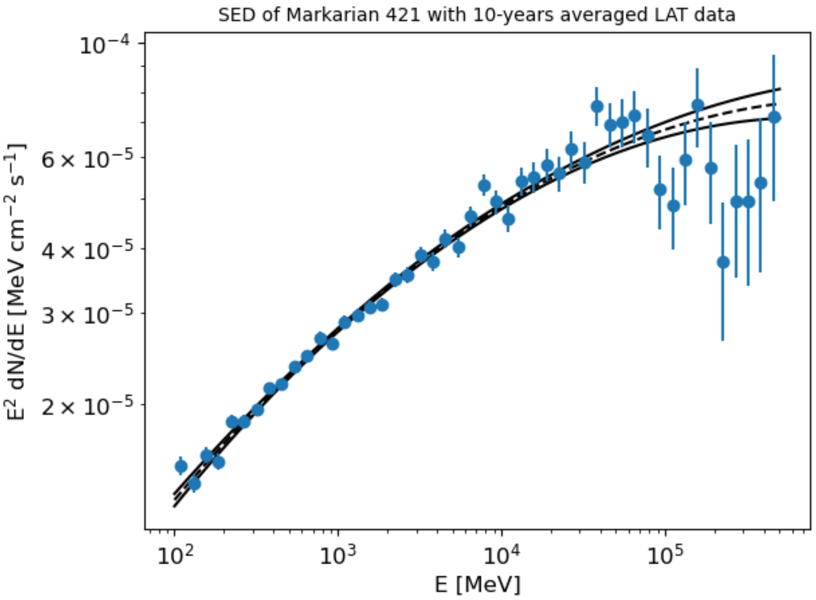

FIGURE 4.2: The spectral energy distribution of Mkn 421 using averaged 10-years LAT data. The blue points stands for the spectral points chosen with configured parameters listed in Table 4.2. The dashed line is the nominal fit with likelihood fitting using source model of Mkn 421 from 4FGL catalogue, and the two black solid lines around it correspond to the 1-sigma contours.

4.2 Analysis and results

4.2.1 Spectral models

The energy spectra of the sources listed in Table 4.1 are compared with two models under the assumptions of two hypotheses respectively: the null hypothesis $H_0(\overline{ALPS})$ assumes no photon-ALP mixing effects taking place, whereas the alternative hypothesis $H_1(ALPS)$ includes photon-ALP mixing.

The intrinsic model of sources in our study is either described by the Logparabola model or in a some cases by a PowerLaw. The specific forms for these two spectral models are given in Eq. (4.4)

$$\left(\frac{dN}{dE}\right)_{intr.} = N_0 \left(\frac{E}{E_b}\right)^{-(\alpha+\beta\ln(E/E_b))}, \tag{4.4}$$

and Eq. (4.5)

$$\left(\frac{dN}{dE}\right)_{intr.} = N_0 \left(\frac{E}{E_b}\right)^{-\alpha}, \tag{4.5}$$

respectively, where N_0 is the normalization parameter measured at scale energy E_b (normally fixed at a constant value), α is the power-law index and β the curvature parameter. The choice of which intrinsic spectral form to use for a specific sample source is based upon the LAT 4FGL source catalogue.

Before we introduce the photon-ALP mixing effect to modulate the energy flux in SEDs of these sample sources, we can first model the known attenuation effect to the observed photon flux at higher energies, i.e., the extragalactic background light (EBL) absorption effect, where the high-energy gamma-ray photons are absorbed by the soft EBL photons in the extragalactic space via pair production $\gamma_{\mathrm{VHE}} + \gamma_{\mathrm{EBL}} \rightarrow e^+e^-$ when they travel through the extragalactic space (see Appendix A for a general introduction of EBL).

The strength of attenuation on the γ rays by EBL is characterized with the optical depth $\tau_{\gamma\gamma}(E_\gamma, z_0)$. Available EBL models can be used to provide values of optical depth for a given source. Since the optical depth in the energy and red shift range considered here is relatively small ($\tau_{\gamma\gamma} \ll 2$ for almost all the sources, see Fig. 4.3), the choice of a specific EBL model is not important, but needs to be included. We make use of Domínguez et al. EBL model [193] as it provides consistent results of EBL density in comparison to all other models in the wavelength band (from ultraviolet to near-infrared) of our analysis, and it is conveniently integrated in the *PhotonALPsConv* package[4].

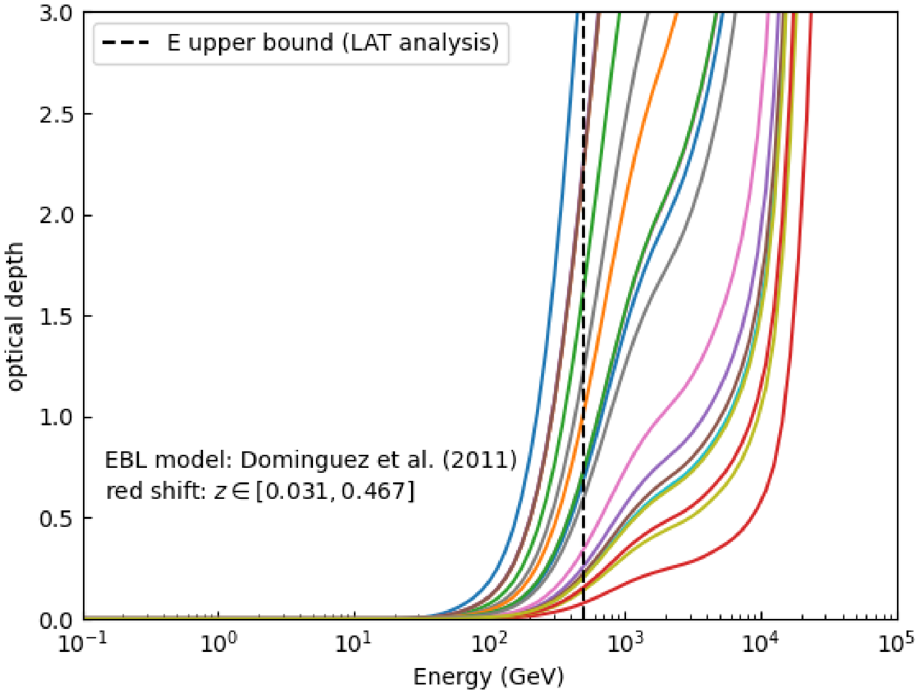

FIGURE 4.3: Optical depth calculated as a function of energy for sources listed in Table 4.1 (PG 1553+113 is not included due to poorly constrained red shift) using Domínguez et al. EBL model [193]. The black dashed vertical line indicates the upper energy bound for out LAT analysis.

---

[4] https://github.com/me-manu/PhotALPsConv

Thus, the intrinsic spectral model under H_0 hypothesis is consequently modified to account for the absorption induced by EBL. The spectral model under H_0 now becomes:

$$H_0 : \quad \left(\frac{dN}{dE}\right)_{w/o\,ALP} = e^{-\tau_{\gamma\gamma}} \left(\frac{dN}{dE}\right)_{intr.}, \tag{4.6}$$

where $(dN/dE)_{intr.}$ is the source model referring to Eq. (4.4) or Eq. (4.5).

As for the alternative hypothesis H_1 with the photon-ALP mixing, the spectrum is further multiplied by the photon surviving probability $p_{\gamma\gamma}$. It is a function of photon energy E, photon-ALP coupling $g_{a\gamma\gamma}$, ALP mass m_a, transversal (constant) B-field strength B and its effective spatial extension s. The spectrum model under alternative hypothesis H_1 can then be written in the form of

$$H_1 : \quad \left(\frac{dN}{dE}\right)_{w/\,ALP} = \left(\frac{dN}{dE}\right)_{intr.} p_{\gamma\gamma}(E, m_a, g_{a\gamma\gamma}, B, s), \tag{4.7}$$

where photon survival probability $p_{\gamma\gamma}$ is calculated with Eq. (2.35).

Note that there are four more parameters in H_1 hypothesis comparing to H_0. In order to make the general problem of estimating free parameters numerically tractable, we fix the values of ALP parameters at $m_a = 3.6\,\text{neV}$, $g_{a\gamma\gamma} = 2.3 \times 10^{-10}\,\text{GeV}^{-1}$, which have been found to be a possible signal region of ALPs and favorable to explain spectral modulations presented in the SED analysis of Galactic pulsars [40].

4.2.2 Parameter estimates: null hypothesis

The two spectral models under two hypotheses in Eqs. (4.6) and (4.7) are then fit to the observational data obtained in the form of SED points after LAT data reduction. For the likelihood fitting of the SED we use the forward-folding method as implemented in fermitools described in Subsec. 4.1.2. The modified spectral models under both H_0 and H_1 cannot use directly the `gtlike` tool for likelihood fitting since the spectral models from 4FGL catalogue are intrinsic source models. Instead, the effect of EBL absorption $e^{-\tau_{\gamma\gamma}}$ and $p_{\gamma\gamma}$ are implemented by calling the `gtlike` tool together with a so-called `filefunction` model from Fermipy package[5]. This way, we can determine best-fitting likelihood values for both hypotheses H_0 and H_1. Specifically, we use a grid search to locate the best-fitting parameters of (B, s) under hypothesis H_1 given the number of fitted parameters is exceeding three. For each chosen pair value of (B, s) we optimize the parameters of $(dN/dE)_{\text{intr.}}$ using the likelihood fitting method.

---

[5] https://fermipy.readthedocs.io/en/latest/

Additionally, in order to check the consistency of the likelihood results and potentially extend the analyzed LAT energy range to VHE region, we also employ a χ^2-minimization fitting method with the following definition for the *Fermi*-LAT data

$$\chi^2 = \sum_{i=1}^{N} \frac{(D_{ij}\Psi_j - \phi_i)^2}{\sigma_i^2}, \tag{4.8}$$

where N is the number of energy bins used in the SED ($N = 18$ for all sources analyzed with χ^2 method), $D_{ij}\Psi_j$ and ϕ_i are respectively the expected and observed γ-ray flux in the i-th bin with its corresponding statistical uncertainty σ_i. The model flux Ψ_j is corrected using the energy dispersion matrix D_{ij}, which describes how the true energies are redistributed in measured energies. This is because the LAT instrument only has finite energy resolution, the energy dispersion matrix helps reduce systematic uncertainties at all energies, especially at energies below 1 GeV (see Chapter 1 for detailed information of LAT's energy resolution). We extract the energy dispersion matrix using `gtdrm` tool for each source in the collection of our analysis. An example of energy resolution for our selection of data (evtype=3) is shown in Fig. 4.4, where we extract D_{ij} with the parameters listed in Table 4.2: 48 logarithmic-spaced energy bins between 100 MeV and 500 GeV for the measured energies and 54 for the reconstructed true energies (since we applied `edisp_bins=-3`, indicating three extra bins are added both below and above the analyzed energy range to account for energy dispersion).

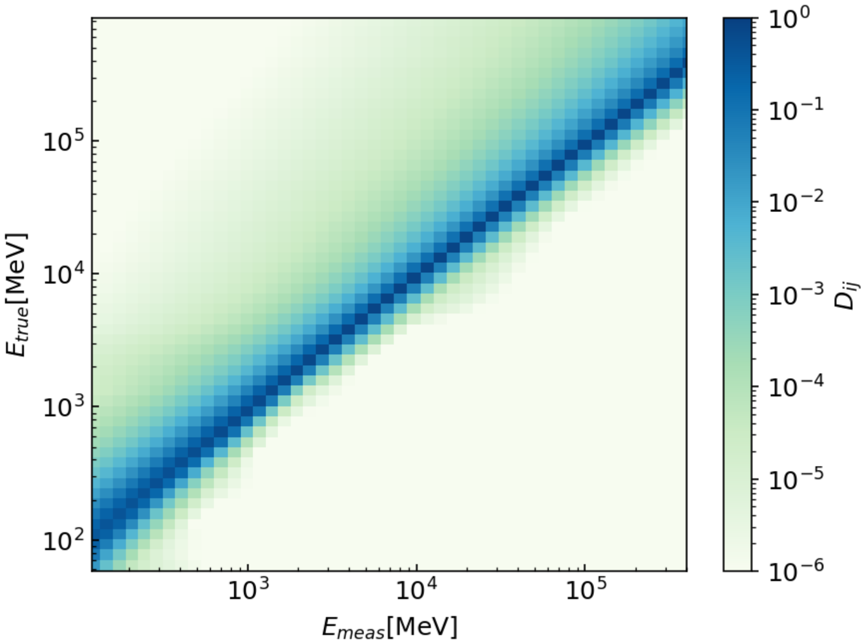

FIGURE 4.4: Energy dispersion matrix used in the likelihood analysis of Mkn 421.

In Table 4.3 we show the best-fitting parameters estimated under the null hypothesis H_0 with the likelihood fitting method (see Table B.1 in Appendix B for χ^2 estimates). We find for each source a maximum likelihood value L^0_{max} (or a minimized $\chi^2_{w/oALP}$ in χ^2 analysis) with the best-fitting normalization parameter N_0, PowerLaw index α, curvature parameter β and the scaled energy parameter E_b. The corresponding uncertainties for each parameter are calculated at a confidence level of 68%.

Table 4.3: Best-fitting parameters for null hypothesis with likelihood method using the modeled spectra from Eq. (4.6), where sources with no curvature parameter are modeled with *PowerLaw*, and the rest is with *Logparabola*. The normalization is given in units of $10^{-12}\mathrm{MeV}^{-1}\mathrm{cm}^{-2}\mathrm{s}^{-1}$. The estimated uncertainties (1σ) are listed as well (except for the scaling energy E_b which is kept fixed at the value from the catalogue).

AGN name	N_0	α	β $\times 10^{-3}$	E_b [MeV]
1ES 0033+595	0.363(0.015)	1.68(0.03)	−4(12)	3177
3C 66A	10.9(0.1)	1.88(0.01)	39(4)	1211
PKS 0301-243	5.66(0.12)	1.83(0.02)	31(8)	954.4
NGC 1275	56.1(0.4)	2.04(0.004)	60(3)	883.6
PKS 0447-439	4.62(0.07)	1.74(0.01)	52(5)	1605
1ES 0502+675	0.0593(0.0026)	1.48(0.03)	–	6322
1ES 0806+524	2.31(0.06)	1.80(0.02)	26(8)	1297
1ES 1011+496	7.6(0.1)	1.75(0.01)	33(5)	1066
Markarian 421	18.0(0.1)	1.73(0.005)	19(2)	1286
Markarian 180	0.164(0.008)	1.77(0.03)	–	2679
1ES 1215+303	9.04(0.14)	1.84(0.01)	44(5)	1066
1ES 1218+304	0.215(0.007)	1.69(0.02)	–	4442
PKS 1440-389	1.01(0.03)	1.70(0.03)	56(11)	2014
PG 1553+113	3.93(0.06)	1.56(0.01)	38(5)	1847
Markarian 501	4.57(0.07)	1.70(0.01)	17(4)	1478
1ES 1727+502	0.202(0.008)	1.75(0.03)	–	3005
1ES 1959+650	3.22(0.05)	1.76(0.01)	23(5)	1733
PKS 2005-489	0.526(0.016)	1.80(0.02)	–	2398
PKS 2155-304	15.4(0.2)	1.77(0.01)	35(3)	1136
1ES 2344+514	0.807(0.03)	1.73(0.03)	50(12)	1938

4.2.3 Parameter estimates: ALP hypothesis

The alternative hypothesis has two additional parameters that are used to characterize the B-field for photon-ALP mixing: field strength B and its effective spatial extension

s. The B-field that enters the fitting refers to the large-scale constant magnetic fields within the source and its vicinity (including JMF, ICMF and other possible magnetic fields), whereas the IGMF is neglected for its very weak field strength, and Milky Way environment is included with the regular component of the J&F GMF model (see Chapter 3 for detailed description of various astrophysical magnetic fields and its contribution to photon-ALP mixing).

For each pair of (B, s) we maximize the likelihood value L^1_{max} by fitting the intrinsic spectral parameters N_0, α and β for a discrete set of pairs of B and s located on a logarithmic grid with (150×150) steps where B is in the range of $(10^{-3}\,\mu\mathrm{G},\ 1\,\mu\mathrm{G} - 10^3\,\mu\mathrm{G})$ and s in the range of $(10^{-2}\,\mathrm{kpc} - 1\,\mathrm{kpc},\ 10^3\,\mathrm{kpc} - 10^4\,\mathrm{kpc})$. The ranges are chosen in such a way that the critical energy (see Eq. (2.30)) could fall into the analyzed LAT energy range. In case there are multiple local maxima found on the logarithmic grid of (B, s), we choose the maximum which minimizes the total energy present in the magnetic field given by $\propto s^3 B^2$. The same criterion is also used for the grid search with χ^2 values.

Significance of alternative hypothesis H_1 against null hypothesis H_0 is estimated via test statistics. We introduce the test statistic (TS) defined within likelihood ratio test:

$$TS(B, s) = -2 \times (\ln(L^0_{max}) - \ln(L^1_{max}(B, s))). \tag{4.9}$$

As an example, we use consistently source Mkn 421 to show the results of searches of best-fitting parameters in Fig. 4.5 with likelihood method (for figures of other sources see figures B.1 to B.18 in Appendix B). As we can see from Fig. 4.5 that the value of TS varies in a characteristic way for different combinations of B and s. For small values of (B, s) pair the resulting photon-ALP conversion probability is too small to have an impact for the modulation on the spectrum, and therefore, the likelihood values under two respective hypotheses are close to each other. This is shown as $TS \approx 0$ in the left corner of Fig. 4.5. However, when values B and s become higher, a large part of the parameter space is excluded. Particularly, a repetitive pattern of local maxima occurs and are aligned along increasing values of B and s. The local maxima is associated to the condition when $s \cdot \Delta_{\mathrm{osc}} > 2\pi$ and therefore multiple oscillations take place.

The global maximum, indicated with a white triangle error bar in Fig. 4.5, is found to be $TS(\hat{B}, \hat{s}) = 18.5$ for $\hat{B} = 21.0\,\mathrm{nG}$ and $\hat{s} = 216.4\,\mathrm{kpc}$ (see Table B.4 in Appendix B for global maxima of other sources). In this case, the local maximum, which corresponds to the parameters with the smallest required value of $B^2 \cdot s^3$ to build up the magnetic field, is located at the same values of $(\hat{B}, \hat{s})$ as the ones for global maximum. We mark down

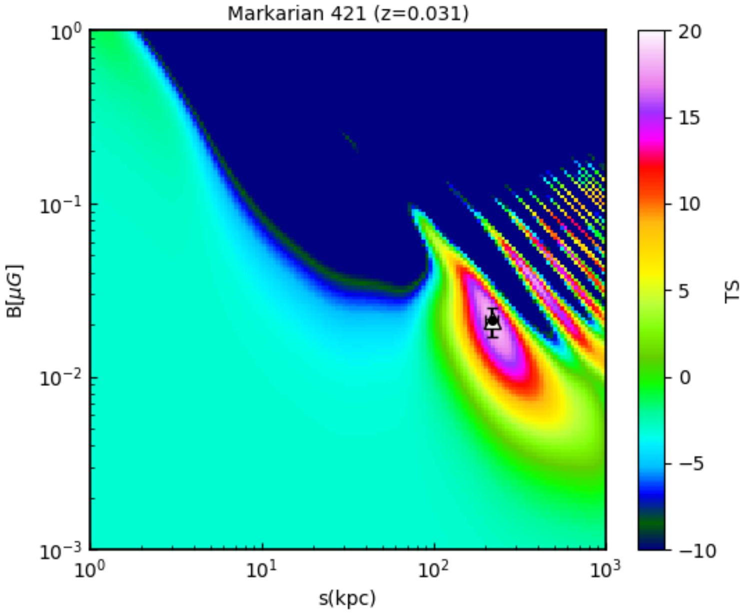

FIGURE 4.5: (B, s) grid map where the color bar indicates the test statistics TS which is twice the difference of log-likelihood values between null and ALP hypotheses. The black and white markers correspond to the local and global best-fitting parameters respectively.

this local maximum $TS(\hat{B}_0 = 21.0\,\mathrm{nG}, \hat{s}_0 = 216.4\,\mathrm{kpc}) = 18.5$ as a black point error bar in Fig. 4.5.

In a similar and consistent way, we can obtain the best-fitting parameters for $(\hat{B}_0, \hat{s}_0)$ of the chosen local maxima with the smallest magnetic field energy for the rest of sources under ALP hypothesis. The resulted best-fitting parameters are listed in Table 4.4.

We see from Table 4.4 that the best-fitting distance $\hat{s}_0$ ranges from $\approx 0.1\,\mathrm{kpc}$ (for the case of 1ES 1218+304) up to $\approx 262\,\mathrm{kpc}$ (for the case of Markarian 180). The bulk of the source spectra favors a conversion region within a distance range of 1 kpc to 200 kpc with a magnetic field strength between 10 nG and 10 μG.

Similar to the approach used for the TS values defined by likelihood ratio, we define here another TS value to use within the $\Delta\chi^2$ test in order to check the consistency and robustness of the results obtained with likelihood method:

$$\Delta\chi^2 = \chi^2_{\mathrm{w/o\,ALP}} - \chi^2_{\mathrm{w/\,ALP}}, \tag{4.10}$$

where $\Delta\chi^2$ is calculated on the same logarithmic grid of (B, s) and the best-fitting parameters which maximize the $\Delta\chi^2$ are obtained[6]. In comparison to Fig. 4.5 we show

---

[6] It should be noted that the definition of $\Delta\chi^2$ and the sign is chosen in a such a way that we can compare the values of $\Delta\chi^2$ and TS.

TABLE 4.4: Best-fitting parameters of local maxima for ALP hypothesis with likelihood method using the modeled spectra from Eq. (4.7). B and s are additional free parameters relating to the strength and length scale for the external magnetic field that is responsible for photo-ALP mixing effects. The normalisation is given in units of $10^{-12}\mathrm{MeV}^{-1}\mathrm{cm}^{-2}\mathrm{s}^{-1}$. Parameters uncertainties (1σ) are included.

AGN name	N_0	α	β $\times 10^{-3}$	E_b [MeV]	$\hat{B}_0$ [nG]	$\hat{s}_0$ [kpc]
1ES 0033+595	0.593(0.023)	1.54(0.03)	36(12)	3177	54.9 (27.9)	81.8 (28.4)
3C 66A	12.5(0.2)	1.80(0.01)	43(6)	1211	322.7 (46.1)	7.2 (0.9)
PKS 0301-243	10.4(2.8)	1.78(0.05)	41(10)	954.4	24396.3(7912.3)	0.2 (0.1)
NGC 1275	103(5)	1.99(0.01)	82(3)	883.6	26268.2(1142.6)	0.2 (0.01)
PKS 0447-439	7.20(0.14)	1.55(0.01)	87(6)	1605	1675.6(157.3)	2.0 (0.1)
1ES 0502+675	0.0731(0.0047)	1.49(0.03)	–	6322	820.5 (74.1)	12.2 (0.7)
1ES 0806+524	2.32(0.06)	1.78(0.02)	11(10)	1297	143.8 (21.2)	43.5 (3.8)
1ES 1011+496	7.67(0.12)	1.75(0.01)	25(6)	1066	27.1 (5.7)	206.2(24.1)
Markarian 421	19.1(0.2)	1.69(0.005)	13(2)	1286	21.0 (4.1)	216.4(18.4)
Markarian 180	0.177(0.008)	1.72(0.03)	–	2679	16.7 (11.9)	262.8(84.4)
1ES 1215+303	17.1(3.0)	1.77(0.06)	61(5)	1066	18574.9(4545.8)	0.3(0.1)
1ES 1218+304	0.426(0.015)	1.69(0.02)	–	4442	32031.9(7981.4)	0.1(0.04)
PKS 1440-389	1.76(0.09)	1.50(0.03)	105(12)	2014	2013.3(629.7)	2.2 (0.4)
PG 1553+113	4.96(0.10)	1.44(0.01)	43(6)	1847	846.0 (36.5)	11.1(0.3)
Markarian 501	7.88(1.40)	1.67(0.02)	24(4)	1478	29047.0(7747.1)	0.2(0.03)
1ES 1727+502	0.260(0.012)	1.72(0.02)	–	3005	1987.1(65.4)	9.3 (0.2)
1ES 1959+650	3.41(0.06)	1.71(0.01)	15(6)	1733	63.8 (29.5)	29.6 (8.1)
PKS 2005-489	0.707(0.048)	1.73(0.02)	–	2398	6400.6(374.4)	1.6 (0.1)
PKS 2155-304	30.8(0.3)	1.76(0.01)	42(3)	1136	30009.3(6113.0)	0.1(0.01)
1ES 2344+514	0.870(0.037)	1.62(0.04)	33(16)	1938	244.2 (71.1)	15.0 (2.9)

the corresponding grid of $\Delta\chi^2$ values for the case of Mkn 421. Similar patterns of repetitive oscillations are observed when comparing the $\Delta\chi^2$ values to the TS values on the same grid. Also, similar best-fitting values of $(\hat{B}, \hat{s})$ are found for the global maximum, as well as values of $(\hat{B}_0, \hat{s}_0)$ for the local maximum. However, there are some differences for results between likelihood and χ^2 analysis, which is due to the fact that χ^2 method is based upon a coarser binning of the energy spectra and therefore the oscillation features remain in some cases under-sampled.

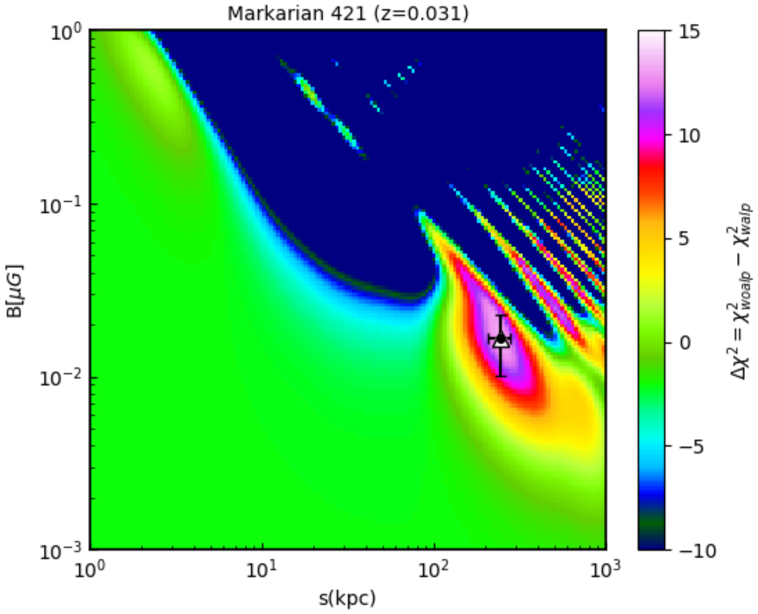

Figure 4.6: (B, s) grid map where the color bar indicates the difference of χ^2 values fitted in null and ALP hypotheses. The black and white markers correspond to the local and global best-fitting parameters respectively.

For χ^2 analysis of other sources, we obtain the best-fitting parameters of $(\hat{B}, \hat{s})$ and $(\hat{B}_0, \hat{s}_0)$ in the same way as done for the case of Mkn 421. The results for local and global best-fitting parameters are listed in Tables B.2 and B.3 in Appendix B, respectively.

The best-fitting parameters obtained in both likelihood (Tables 4.3 and 4.4) and χ^2 (Tables B.1 and B.2) fitting can then be put into the spectral models of H_0 and H_1 to illustrate the spectral modulations induced by photon-ALP mixing. We show in Figs. 4.7 and 4.8 the observed SED data points together with the model curves from Eqs. (4.6) and (4.7). The SED data points are obtained with likelihood binning using 48 energy bins in between 100 MeV and 500 GeV for Fig. 4.7, while in Fig. 4.6 the SED points are obtained through a coarser binning of 18 total bins in the same analyzed energy range. In both the likelihood and χ^2 fitted SEDs, the best-fitting curve for the null hypothesis is shown as a green dashed line, whereas for alternative (H_1) hypothesis is a blue solid

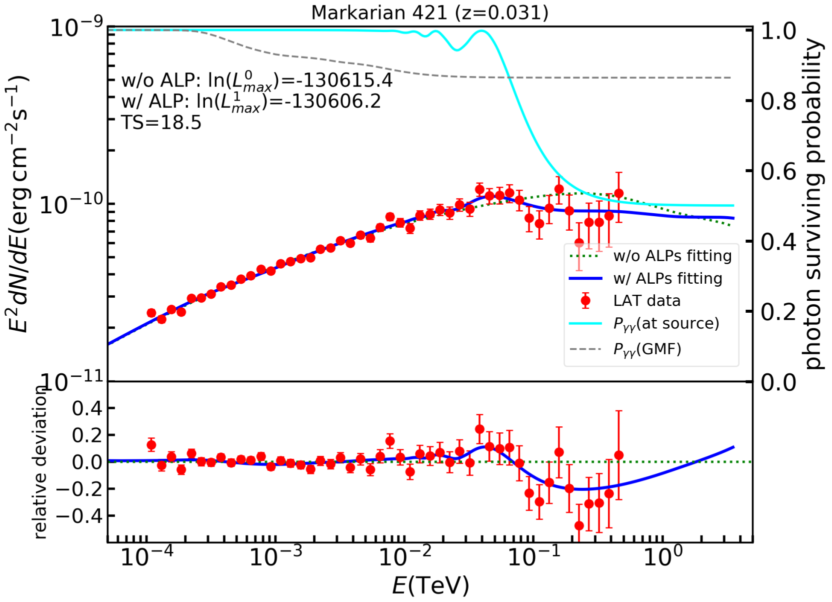

FIGURE 4.7: the spectral energy distribution for source Mkn 421 with likelihood fitting method. The red data points are collected from a 10-yrs LAT observation. The blue straight line is the best-fitting model with photon-ALP mixing effects included, and the green dashed line is the best-fitting model without the assumption of photon-ALP mixing. The cyan solid line is the photon surviving probability at source and the gray dashed line is the photon surviving probability at Milky Way. In the lower panel, we show the relative deviations of the flux points and “w/ ALP” scenario from the baseline (“w/o ALP”).

line. Additionally, we show the photon surviving probabilities calculated in both figures for two conversion regions considered here: the photon surviving probability at source region is indicated as a cyan solid line, while the photon surviving probability marked as a gray dashed line implies photon-ALP mixing in the Milky Way environment only. In Fig. 4.7 we see the modulations induced by photon-ALP mixing occur mainly between 50 GeV and 500 GeV, determined by the best-fitting parameter values of (B, s) obtained in the fitting process. Similar modulations are observed in Fig. 4.8 due to the fact that the resulted fitting values from χ^2 are close to the ones obtained in likelihood fitting. The deviations in the lower panel of both figures provide indications of the strength of relative amplitude of modulations brought by photon-ALP mixing effect, which, in the case of Mkn 421, is about 15%.

4.2.4 Hypotheses testing

After we obtain TS values for each source during the likelihood and χ^2 fitting, we need to convert the TS values into a level of significance to either accept or reject the null hypothesis H_0. This can be done by deriving the TS distribution under the

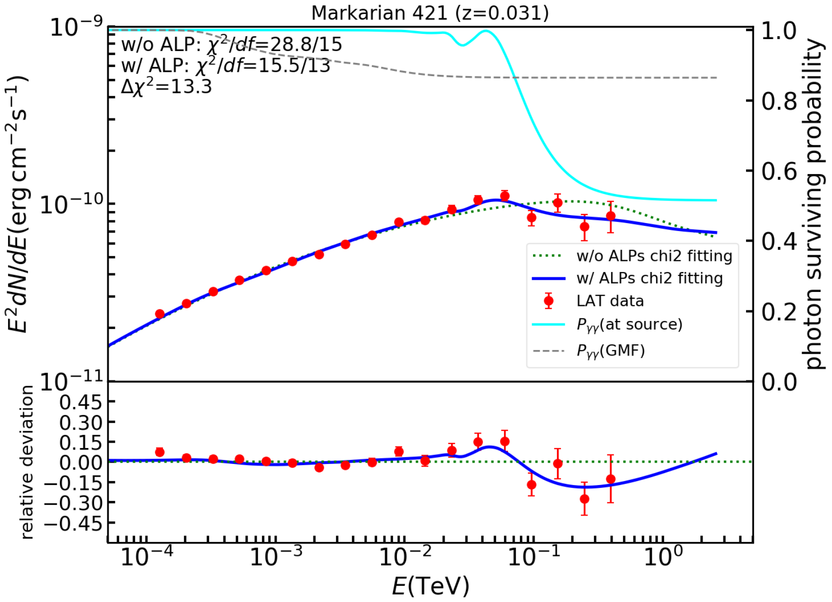

FIGURE 4.8: SED for source Mkn 421 with χ^2 fitting. Descriptions for legends are the same as in Fig. 4.7.

null hypothesis from Monte-Carlo simulation following a similar procedure as described in Ref. [49]. For this, we generate 400 sets of simulated gamma-ray spectra for each source under the null hypothesis in the so-called pseudoexperiments (PE). In order to obtain the simulated gamma-ray spectra for an individual target source, we generate a simulation of the ROI using the current best-fitting model for all the sources within the ROI, where the simulation is then done by adding Poisson fluctuations on data counts cube, and then replace the observed photon counts with the simulated event numbers in counts cube. The newly created counts cube are then processed by an analysis thread which follows closely the steps for obtaining the observed SED data points described in Subsec. 4.1.2. The specific tool used in this step is the `gta.simulate_roi` from `fermipy` package 0.19.0 [284].

The resulting simulated data sets are then subject to the same data fitting procedure as outlined above in Subsec. 4.2.2 and 4.2.3. For simulated data in one PE we calculate the test statistic values, TS and $\Delta\chi^2$. In this way, this results in two distributions with 400 values of TS associated to Eq. (4.9) and $\Delta\chi^2$ in Eq. (4.10), respectively, for each source.

Following Wilks' theorem, the null distribution of test statistics can be best approximated by a non-central χ^2 distribution (NCD) when the number of simulation is sufficiently high [285].

Again, we use Mkn 421 as an example to present in Fig. 4.9 the distribution of TS values (colored in green) with likelihood ratio test, where the black dashed line represents a fit to the simulated TS distribution, parameterized as a non-central χ^2 function with a degree of freedom (df) of $\sim$ 0 and non-centrality (nc) of 19.11. The cumulative distribution function (CDF) is marked as a red solid line, which is based on the NCD fitting curve. The blue dot-dash vertical line at position of $TS = 18.5$ indicates the local maximum of TS value from likelihood fitting, whereas the gray dotted line stands for the TS value of global maximum (the two lines overlap in this case). With the accumulated NCD shown in Fig. 4.9, we are able to derive the probability of obtaining a TS value larger than the one found in the data ($TS = 18.5$) to be $p(TS > 18.5; df = 0.00, nc = 19.11) = 2.79 \times 10^{-4}$, which corresponds to a significance level of $3.6\,\sigma$. In Fig. 4.10, the $\Delta\chi^2$ distribution from $\Delta\chi^2$ test shows a similar shape of distribution, which can be approximated by a NCD function with $df = 4.38$ and $nc = 9.82$. This leads to a slightly less significant result with $p(\Delta\chi^2 > 13.3; df = 4.38, nc = 9.82) = 7.39 \times 10^{-3}$, corresponding to a significance of $2.7\,\sigma$. Upon closer inspection, the binning for the χ^2-fit is under-sampling the modulation predicted for the spectrum under ALP hypothesis H_1. We conclude from both the likelihood ratio and $\Delta\chi^2$ tests, in the case of Mkn 421, the H_1 hypothesis with photon-ALP mixing is preferred over the null hypothesis.

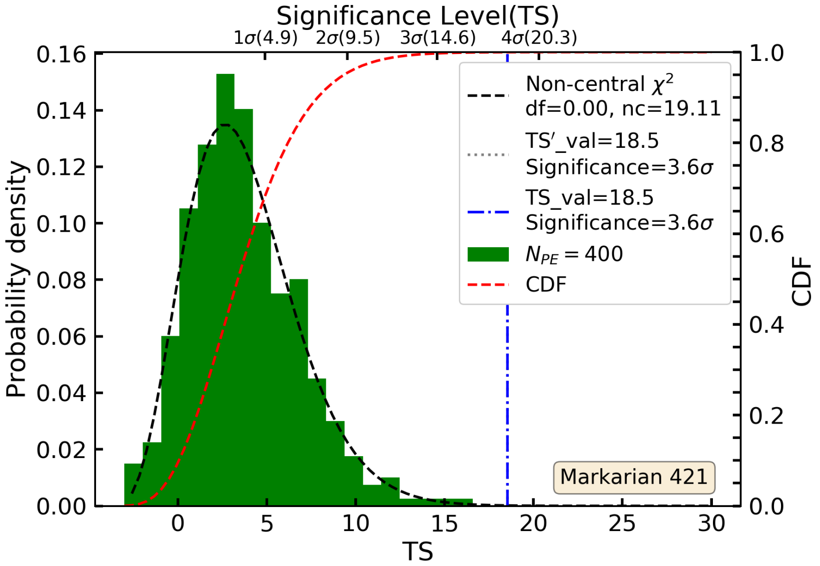

FIGURE 4.9: Simulated null distribution for Mrk 421 from likelihood ratio test. The black dashed line indicates a fit to the distribution with a non-central χ^2 function. The red solid line represents the resulting cumulative distribution function (CDF). The TS value derived from the local maximum of original data is marked as a blue (dot-dash) vertical line, while the TS value obtained from the global maximum is marked as a gray dotted line (in this case, the blue line coincides with the gray line).

Following the same approach, we present the TS values for all sources in Table 4.5, as well as their corresponding significance levels derived from null distribution of each

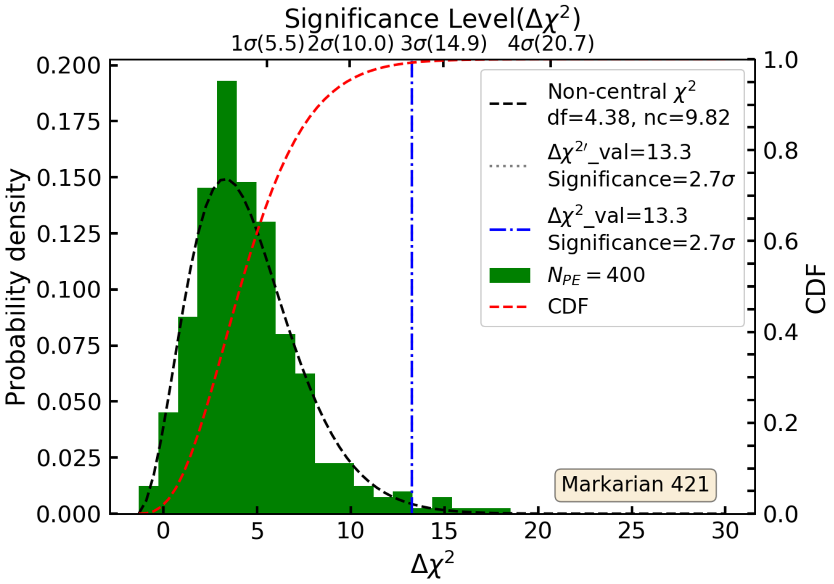

FIGURE 4.10: Simulated null distribution from $\Delta\chi^2$ test for the same source. The legends of the lines are the same as described in Fig. 4.9.

source. 18 out of 20 TS values obtained from likelihood analysis are positive, indicating an overall preference for the alternative hypothesis with photon-ALP mixing. On top of that, positive $\Delta\chi^2$ values are also obtained for 15 sources in the χ^2 analysis, and goodness of fit for the hypothesis H_1 is acceptable for 12 out of 20 spectra. In particular, the resulting values of $\chi^2(df) = 38.2(14)$ and $\chi^2(df) = 32.7(14)$ are too large to be acceptable for the cases of 1ES 0502+675 and 1ES 1727+502, respectively. Such poor fit is also indicated in their corresponding probabilities of obtaining a larger χ^2 value: $p(\chi^2 > 38.2, df = 14) = 4.8 \times 10^{-4}$ for 1ES 0502+675 and $p(\chi^2 > 25.9, df = 14) = 3.2 \times 10^{-3}$ for 1ES 1727+502. This can also be seen from a closer inspection upon their SEDs, shown in Fig. 4.11. As we can see from the SED fitting and residuals in Fig. 4.11 that

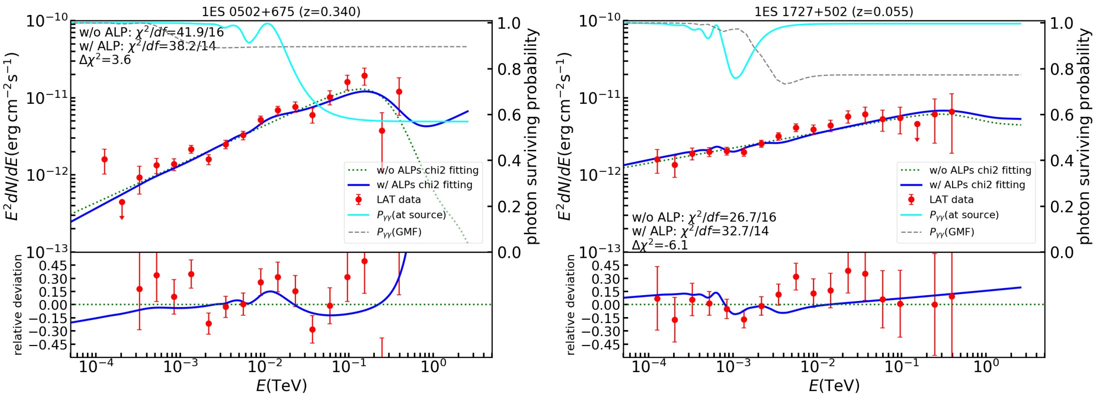

FIGURE 4.11: Left panel: SED for source 1ES 0502+675 with χ^2 fitting. Right panel: SED for source 1ES 1727+502 with χ^2 fitting. Description of legends used here is the same as in Fig. 4.7.

TABLE 4.5: Best-fitting log-likelihood and χ^2 values of the local maxima for null (H_0) and ALP hypotheses (H_1). TS values are calculated with Eqs. (4.9) and (4.10) for likelihood ratio test and $\Delta\chi^2$ test respectively. Corresponding significance levels for both tests are listed as well.

AGN name	H_0 $\ln(L^0_{max})$	H_1 $\ln(L^1_{max})$	TS	z-score (H_1/H_0)	H_0 $\chi^2_{\text{w/o ALP}}/df$	H_1 $\chi^2_{\text{w/ ALP}}/df$	$\Delta\chi^2$	z-score (H_1/H_0)
1ES 0033+595	712253.0	712257.2	8.4	2.1	22.2/15	14.2/13	8.1	1.9
3C 66A	−122858.4	−122856.5	3.8	2.0	20.6/15	16.3/13	4.3	2.3
PKS 0301-243	−154508.6	−154508.2	0.7	0.5	16.3/15	16.4/13	−0.2	0.5
NGC 1275	26767.7	26777.6	19.8	3.6	25.6/15	22.6/13	3.1	1.8
PKS 0447-439	−146200.2	−146199.2	2.0	1.9	26.2/15	25.8/13	0.4	1.5
1ES 0502+675	−44659.7	−44656.4	6.7	1.3	41.9/16	38.2/14	3.6	0.4
1ES 0806+524	−159751.7	−159750.4	2.6	0.2	20.5/15	16.6/13	3.9	0.5
1ES 1011+496	−153504.9	−153502.4	5.0	0.8	12.7/15	9.2/13	3.5	0.4
Markarian 421								
10yrs LAT	−130615.4	−130606.2	18.5	3.6	28.8/15	15.5/13	13.3	2.7
simul. LAT+MAGIC	–	–	–	–	33.4/15	20.7/13	12.6	1.8
Markarian 180	−132628.5	−132627.9	1.0	0.01	23.8/16	20.5/14	3.3	0.4
1ES 1215+303	−143988.2	−143984.9	6.6	2.0	15.5/15	13.4/13	2.1	1.2
1ES 1218+304	−145577.4	−145577.9	−1.0	0.9	19.0/16	20.2/14	−1.2	1.1
PKS 1440-389	60781.3	60783.1	3.7	1.3	18.9/15	17.0/13	3.5	0.6
PG 1553+113	−152448.4	−152450.6	−4.2	0.02	17.8/15	27.7/13	−9.9	0.0
Markarian 501	−95747.1	−95746.2	1.7	0.4	18.5/15	17.2/13	1.4	0.3
1ES 1727+502	−154208.5	−154207.4	2.4	0.4	26.7/16	32.7/14	−6.1	0.0
1ES 1959+650	−49456.2	−49453.9	4.6	0.7	21.6/15	16.3/13	5.3	0.9
PKS 2005-489	−166314.9	−166309.0	11.4	2.1	33.9/16	20.9/14	12.9	2.1
PKS 2155-304								
10yrs LAT	−144503.6	−144503.1	0.9	1.5	15.8/15	19.5/13	-3.6	0.5
simul. LAT+H.E.S.S.	–	–	–	–	33.3/18	29.2/16	4.1	1.6
1ES 2344+514	−61475.6	−61472.2	6.7	1.2	15.2/15	14.0/13	1.2	0.5

there are some additional features presented in the spectra which are not well described by the photon-ALP mixing model. For example, some features shown in the low-energy range can be attributed to modulations induced by photon-photon dispersion. Although the tiny effect of photon-photon dispersion off of the CMB can modify the photon-ALP oscillation in the high-energy band, the hard spectra of radiation in Galaxy or source regions would prevent them from having significant impact on dispersion for high-energy band. Whereas in smaller energies between 100 MeV and 100 GeV, the photon-photon dispersion would contribute considerably to the observed photon flux [286]. The modelling of such radiation fields in Galaxy or source regions would require energy densities of, for example, the host galaxy, the AGN field and the synchrotron field within the jet, which is rather complicated and beyond the scope of this work (see Ref. [203] for impacts of other dispersion impacts on photon-ALP mixing).

In addition, in order to obtain an overall significance estimate from the all *Fermi* spectra combined, we perform a bootstrapping method to achieve that. First, we sum the TS values of the individual sources in Table 4.5 to obtain a total TS value:

$$TS_{\text{tot}} = \sum_i TS_i, \tag{4.11}$$

where TS_i is the TS (or $\Delta\chi^2$) for the i-th individual source. Then, we combine the resulted TS values obtained from simulations in PEs through a bootstrapping approach. In order to constrain the uncertainty induced by the approach as much as possible, we take 10^7 sequences of 20 uniform random deviates denoted by $n_1, \dots, n_{20}$ to combine the sources in a random way:

$$PE = \{(TS_{n_1}, \dots, TS_{n_{20}}) | n_1, \dots, n_{20} \in \{1, \dots, 400\}\}. \tag{4.12}$$

The bootstrapping method employed here as suggested in Eq. (4.12) uses random sampling with replacement. In this way, this gives us a distribution of 10^7 values of TS^{PE}, where

$$TS^{PE} = \sum_i TS_{n_i}. \tag{4.13}$$

We therefore can benefit from the combinatorial factor of $400^{20} \approx 10^{52}$ different possibilities to combine the simulated data sets with the bootstrapping method. In a similar way, we perform the bootstrapping method to combine the $\Delta\chi^2$ values in the χ^2 analysis, where we sum up the individual $\Delta\chi^2$ values displayed in Table 4.5 to obtain a $\Delta\chi^2_{\text{tot}}$, and generate 10^7 values of $(\Delta\chi^2)^{PE}$ as done in the case of likelihood analysis.

We show in Fig. 4.12 the resulting distribution of TS^{PE}, where the probability density function can be parameterized by a NCD, similar to the case of individual sources.

The TS^{PE} distribution is well fit by the NCD curve, from which the probability to find a value of $TS^{PE} > TS_{tot}$ can be estimated to be $p(TS^{PE} > TS_{tot} = 98.9; df = 140.20, nc = 162.49) = 1.22 \times 10^{-7}$, corresponding to a z-score of 5.3. A similar value can also be obtained by counting the number of entries in the simulated distribution with $TS^{PE} > TS_{tot}$.

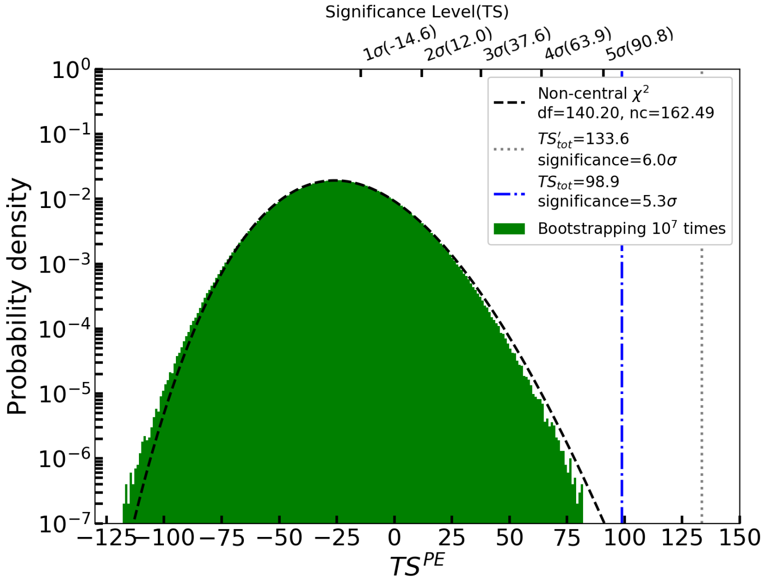

FIGURE 4.12: Combined full null TS distribution from likelihood ratio test using bootstrapping method. Black dashed line denotes the fitting to the histogram of TS^{PE} values with non-central χ^2 (NCD) function. Blue dotted-dashed line indicates the position of TS_{tot}. Gray dotted line stands for the position of TS'_{tot} summed over all global maximal values on (B, s) grid maps from likelihood analysis.

As for the $\Delta\chi^2$ based hypothesis test, we find a rather poor description of the underlying simulated distribution for small values of $\Delta\chi^2$, shown in Fig. 4.13. Notably, the distribution of $(\Delta\chi^2)^{PE}$ is rather narrow and shifted significantly to the bigger values of combined test statistics in comparison to the TS^{PE} distribution shown in Fig. 4.12. The higher values of $(\Delta\chi^2)^{PE}$ are relatively consistent with the ones in TS^{PE} distribution, whereas the lower end of $(\Delta\chi^2)^{PE}$ values is much bigger compared to the smallest value of TS^{PE}. Such differences are consistent with the findings from individual sources, and therefore, it is assumed that they arise from the difference in two null distributions of individual sources with likelihood ratio and $\Delta\chi^2$ tests respectively. Indeed, as we can see from the null distributions displayed in Appendix B, the TS distributions extend more to the smaller values of simulated test statistics or simply have more entries in the lower end of the distribution, particularly in the cases of NGC 1275, 1ES 1215+303, Mkn 501, PKS 1440-389, PKS 2155-304 and Mkn 421, due to different binning and fitting in two methods. The significance level for the combined $\Delta\chi^2$ test is estimated to

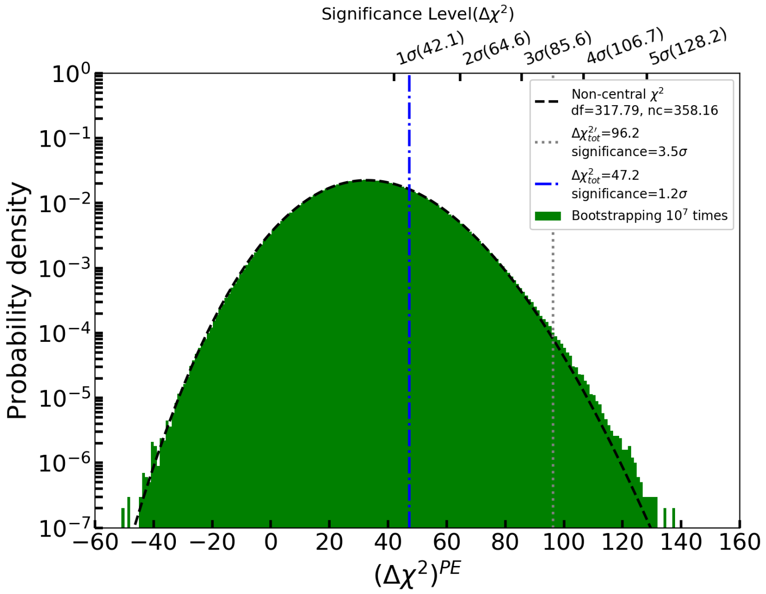

FIGURE 4.13: Combined full null $\Delta\chi^2$ distribution from $\Delta\chi^2$ test using bootstrapping method. Black dashed line denotes the fitting to the histogram of $(\Delta\chi^2)^{PE}$ values with non-central χ^2 (NCD) function. Blue dotted-dashed line indicates the position of $\Delta\chi^2_{tot}$. Gray dotted line stands for the position of $\Delta\chi^{2\prime}_{tot}$ summed over all global maximal values on (B, s) grid maps from χ^2 analysis.

be much smaller than the value found for the TS-based distribution, at a significance level of $1.4\,\sigma$.

4.3 Combined spectra of HE and VHE observations

The large collection area of ground-based instruments extends the high energy range accessible by *Fermi*-LAT towards very high energies, where photon statistics limit the sensitivity for space based instruments. The downside of the ground-based techniques is a limited field of view. Therefore, the VHE spectrum is in most cases recorded during flaring states whereas the HE spectrum is recorded quasi-continuously with the all-sky instrument of *Fermi*-LAT. Thus, the flare-selected observation of AGN with ground based instruments introduces a bias in the observed energy spectrum towards a high flux-state which is not necessarily representative of a truly time-averaged spectrum.

Instead, we combine HE and VHE data which are recorded contemporaneously with *Fermi*-LAT and ground-based instruments. We consider examples for the combination of HE and VHE data for PKS 2155-304 and Mkn 421.

4.3.1 Combined spectrum of PKS 2155-304

PKS 2155-304 is a high-peak frequency BL Lac object at redshift $z = 0.116$. It is the first extragalactic VHE gamma-ray source discovered in the southern sky [287], and it has been closely monitored during both the flares and the period of quiescence [288]. Particularly, this source has been extensively observed by HESS and the available statistics make possible an accurate determination of its spectrum [289, 290].

In Fig. 4.14 we show a lightcurve of PKS 2155-304 in the analyzed time range (August 2008 to August 2018) using LAT observation. The events are selected using the cuts listed in Table 4.2. The photon counts of PKS 2155-304 are integrated into 120 bins of one month. The resulting lightcurve has an average energy flux of $2.75 \times 10^{-10}\,\mathrm{erg cm^{-2} s^{-1}}$ with a flux variability of 0.45. This result shows that the relatively low flux states within LAT energy range are found to be between 60 months (2013) and 70 months (2014). At the same time, in VHE range from HESS-II mono observations of PKS 2155-304 [291], the spectrum level is also found to be in low states, consistent with the level reported for the quiescent state observed by HESS from observations during 2005-2007 [288].

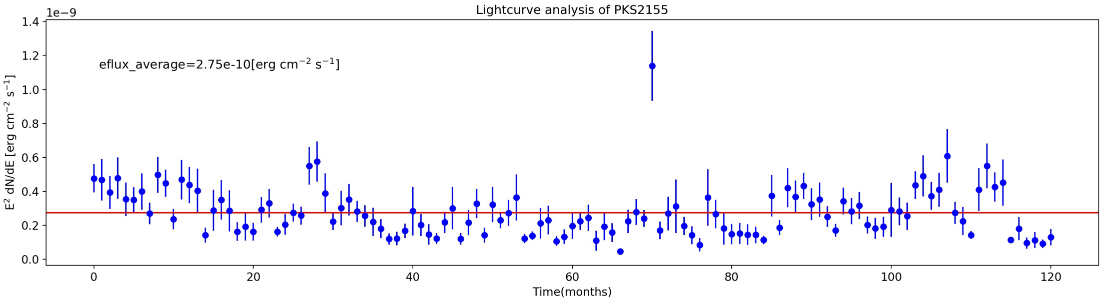

FIGURE 4.14: The lightcurve of PKS 2155-304 with *Fermi*-LAT within the analyzed time range listed in Table 4.2. The size of the time bins is chosen to be 1 month. The red solid line indicates the averaged energy flux.

Additionally, a galaxy cluster of size of 372 kpc is observed around this source [292], which indicates that a rather significant magnetic field is expected in the vicinity of the source or within the source, and this will be an advantageous environment to search for photon-ALP mixing effects.

Based on the results shown in Fig. 4.14 and Ref. [291], we consider a quasi-simultaneous observation to avoid the combination of data sets averaged over different flux states. Non-simultaneous spectral data could lead to an apparent break or irregularities close to the transition energy of the two instruments. Moreover, the constraint on available contemporaneous observation time can lead to larger statistical uncertainties on the detected photon counts which in return reduce the sensitivity of the spectral features.

Such quasi-simultaneous observation can be found, for example, in Ref. [291], where a spectral break is reported in the transition energy region during contemporaneous observations from HE of *Fermi*-LAT and VHE of HESS-II observations in 2013. The lower threshold of HESS-II observations provides more constraint in the overlapping energy region covered with space and ground based instruments in comparison to the smaller HESS Phase I instrument [288]. We re-analyse the contemporaneous *Fermi*-LAT data set used in Ref. [291] with identical binning to combine the two measurements to test whether the introduction of photon-ALP mixing model could better describe the break feature of the spectrum or in general the shape of the combined HE and VHE spectrum.

We follow a similar process as to the χ^2 fitting for individual source. In Fig. 4.15 we show a scan of $\Delta\chi^2(B, s)$ from the combined SED data points (HESS-II observation and contemporaneous re-analyzed LAT observation of PKS 2155-304 in 2013) under the ALP hypothesis H_1. The local best-fitting parameters are found to locate at $\hat{B}_0 = 5.5\,\mu$G with $\hat{s}_0 = 0.2\,$kpc, where the resulted $\Delta\chi^2 = 4.1$ is obtained. The global maximum $(\hat{B}, \hat{s})$, marked with a white triangle, coincides with the local maximum which is indicated with a black point. As we can see from the plot, the signal of photon-ALP mixing is

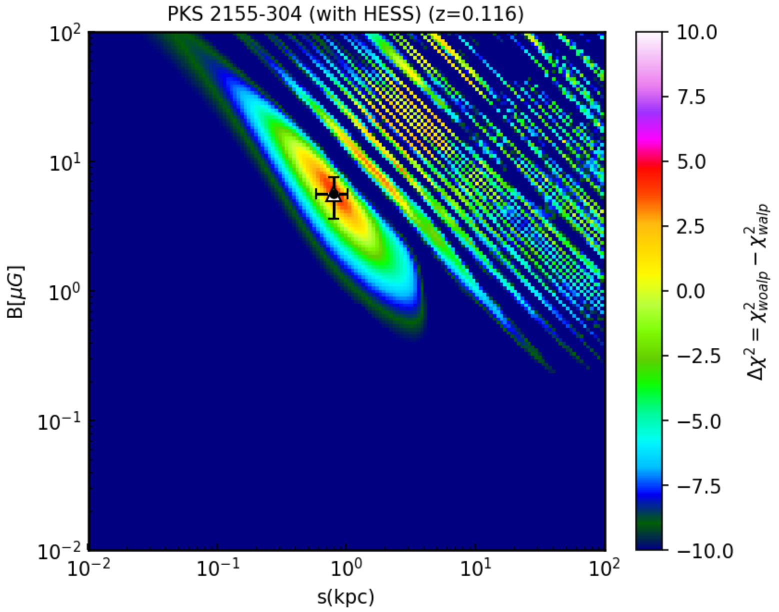

FIGURE 4.15: $\Delta\chi^2$ for a grid of values of B-field strength B and distance s. The color bar indicates the $\Delta\chi^2$ values when fitting the combined contemporaneous LAT and H.E.S.S. data in 2013. The black point marker indicates the local maximum of $\Delta\chi^2$ derived from the fit of the SED to the combined spectrum, while the white triangle marker represents the global best-fitting parameters.

constrained rather strictly to the higher values of B and s for the fitting of the combined

HE and VHE spectrum of PKS 2155-304. The fitting to the magnetic fields favors a small size of magnetic field but with rather strong field strength, which is closely related to the configuration of the AGN lobe environment (see Subsec. 3.1 for details).

The resulting spectral energy distribution is shown in Fig. 4.16 using the best-fitting parameters shown in Fig. 4.15. The black data points are extracted from the HESS-II observation [291] in 2013 (from Apr. 21 to Nov. 5), while the red date points are obtained from re-analyzing LAT observation during the same period of time using the parameters listed in Table 4.6. The LAT data points used in Ref. [291] are also plotted here as the empty gray circles for simple comparison[7]. The blue solid and green dashed lines are the modelled curves under H_0 and H_1 respectively. Photon surviving probabilities at source and GMF environments are denoted as the cyan solid line and gray dashed line respectively. We can see the flux measurements are consistent between two instruments in the overlapping energy region between 80 GeV and 300 GeV. However, no prominent spectral break is observed in the transition energy band of two instruments. Also, the spectral curve (denoted as blue solid line) modified with photon-ALP mixing effect shows no preference for modulation in the overlapping region. Instead, the modulations are observed in the low-energy range due to the large value of best-fitting parameters $\hat{B}_0$.

TABLE 4.6: Configuration parameters for re-extracting LAT data in 2013 using cuts based on Ref. [291].

Access	**Parameters**	
Selection	$\mathrm{E_{min}}$	100 MeV
	$\mathrm{E_{max}}$	500 GeV
	zenith cut	90 deg
	event class	128
	event type	3
	observation time start	Apr. 21st, 2013
	observation time stop	Nov. 5th, 2013
	target source	PKS 2155-304
Binning	ROI width	10.0 deg
	bin size	0.1 deg
	Energy bins perdec	2
Model	extended ROI width	15 deg
	Galactic diffuse	`gll_iem_v07.fits`
	Isotropic emission	`iso_P8R3_SOURCE_V2_v1.txt`
	catalogue	4FGL

---

[7] The main difference between the LAT data reported in Ref. [291] and the LAT data re-analyzed here arises from the instrument response functions, where in Ref. [291] a `P8R2_SOURCE_V6` is used whereas an updated `P8R3_SOURCE_V2` is used for our analysis. `P8R3` implements additional set of simple cuts to reduce the residual background by rejecting these background events, thus resulting a slightly lower flux count on the source spectrum [293].

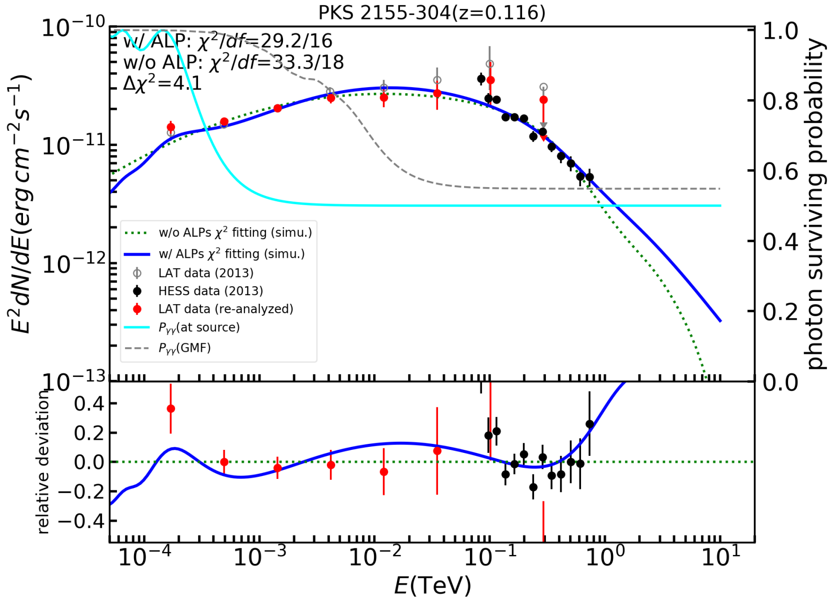

FIGURE 4.16: The spectral energy distribution for PKS 2155-304 during contemporaneous observations with HESS-II and *Fermi*-LAT in 2013. The red data points represent the 2013 LAT observations, and the black data points are from HESS during the same year. The blue solid and green dashed lines are the best-fitting models under H_0 and H_1 hypotheses respectively. The cyan solid and gray dashed lines stand for the photon surviving probabilities in different regions along the line of sight.

We see from Fig. 4.15 and 4.16 that the improvement is not so significant with the introduction of photon-ALP mixing effect. Only a $\Delta\chi^2$ of 4.1 is obtained. In Fig. 4.17 we convert this $\Delta\chi^2$ value into a level of significance by simulating the LAT and HESS-II measurements under the null hypothesis. The LAT data simulation is done in a similar way as discussed before in Subsec. 4.2.4, where we simulate the entire ROI by adding fluctuations to the count cube and then proceed the normal analysis to extract the flux points. The simulation of HESS-II data are done individually for each bin, where we simulate each flux bin in a Gaussian distribution with the flux measurement as the mean of distribution and its error bar as the standard deviation. Each simulated HESS-II data set then comprises the randomly-selected flux value from Gaussian distribution in each bin. $\Delta\chi^2$ values are calculated in each simulated LAT+HESS data sets and the resulted $\Delta\chi^2$ distribution is shown in Fig. 4.17. A significance of $1.6\,\sigma$ is derived with respect to $\Delta\chi^2 = 4.1$.

4.3.2 Combined spectrum of Markarian 421

The northern, nearby AGN Mkn 421 ($z = 0.031$) is another highly variable BL Lac type object that has been closely monitored since the discovery of its VHE emission [294].

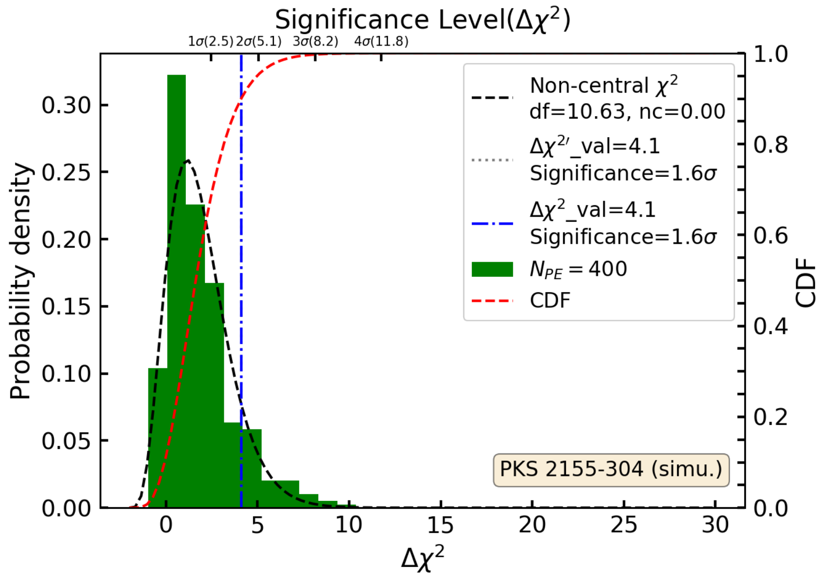

Figure 4.17: Simulated null distribution from $\Delta\chi^2$ test for 2013 HESS and LAT observations. The black dashed line indicates a fit to the distribution with a non-central χ^2 function. The red solid line represents the resulting cumulative distribution function (CDF). The $\Delta\chi^2$ value derived from the original data is marked as a blue (dot-dash) vertical line.

While a number of simultaneous multi-wavelength observations have been carried out for this source, we select the result reported by Ref. [295] during a simultaneous observation campaign from January to June of 2009 with LAT and MAGIC telescopes. The combined energy spectrum of Mkn 421 covers a very broad energy range with substantial overlap between the two instruments, where a similar spectral break is indicated with respect to Ref. [291].

The scan of the parameters B and s for the combined spectrum shows several maxima as presented in Fig. 4.18, which would favor either a large magnetic field of several μG on kpc scales or a very weak magnetic field of several nG over Mpc distance. We select the local maximum to be the one with $\hat{B}_0 = 4.3\,\mu\text{G}$ and $s = 1.0\,\text{kpc}$, which corresponds to a minimized field energy with respect to $\propto B^2 s^3$. This local maximum is marked as a black cross, and in this case, the global maximum (marked with a white triangle) coincides with the chosen local maximum.

The critical energy calculated with the best-fitting parameters of $(\hat{B}_0, \hat{s}_0)$ of local maximum is found to be around 100 MeV. This is indicated in the SED of the combined spectrum of Mkn 421 (see left panel of Fig. 4.19). The gray empty circle points and black solid points are respectively the LAT data and MAGIC data used in the combined analysis of contemporaneous observations conducted in Ref. [295]. We re-analyze the LAT observation with the updated version of IRFs and background templates of *Fermi*-LAT Science Tools, and extract the LAT SED data points (marked as red data

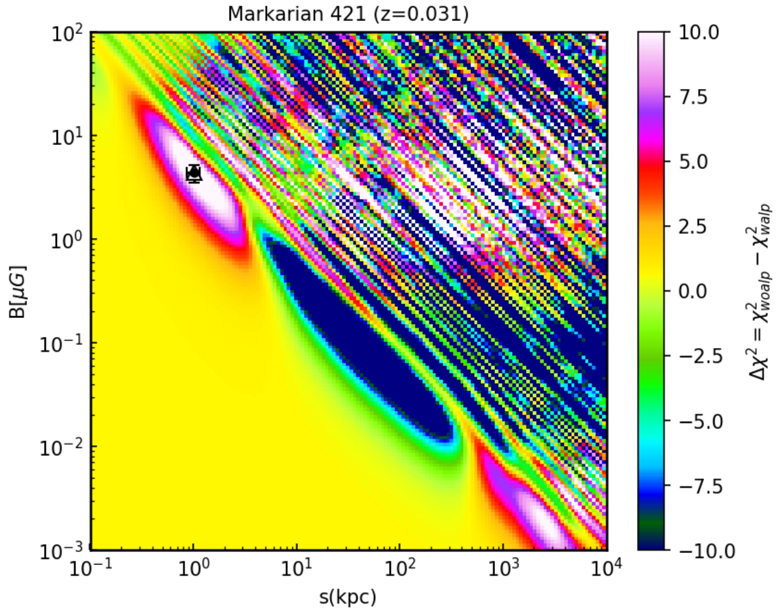

FIGURE 4.18: $\Delta\chi^2$ distribution as functions of B-field strength B and distance s. The color bar indicates the $\Delta\chi^2$ values when fitting the combined time-averaged LAT and MAGIC data [295]. The black point marker indicates the local maximum of $\Delta\chi^2$ derived from the fit of the SED to the time averaged spectrum, while the white triangle marker stands for the global maximum of $\Delta\chi^2$.

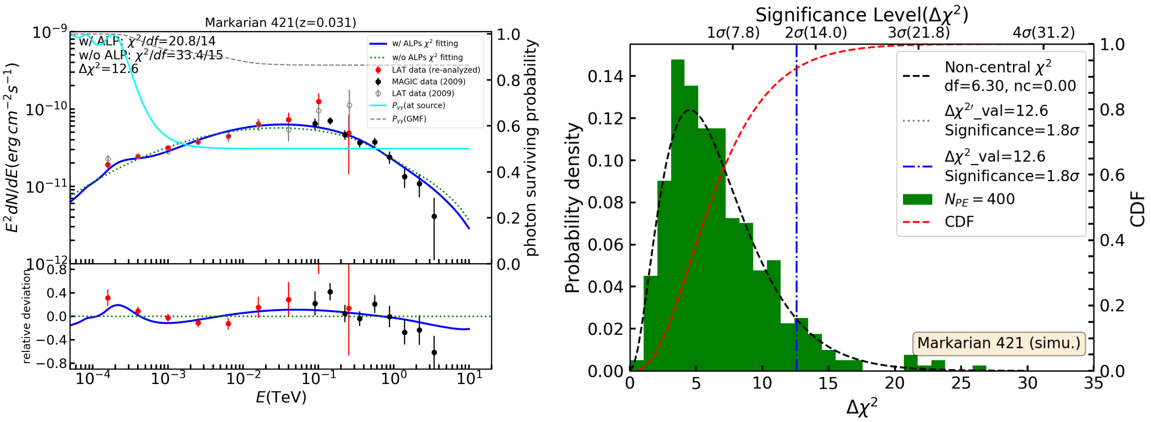

FIGURE 4.19: Left panel: the spectral energy distribution for Markarian 421 during contemporaneous observations with MAGIC and *Fermi*-LAT in 2009. The red data points represent the 2009 re-analyzed LAT observations, and the black data points are from extracted from MAGIC [295] during the same year. The gray empty circle points are extracted from the LAT analysis performed in [295]. The blue solid and green dashed lines are the best-fitting models under H_0 and H_1 hypotheses respectively. The cyan solid and gray dashed lines stand for the photon surviving probabilities in different regions along the line of sight. Right panel: simulated null distribution from $\Delta\chi^2$ test for 2009 MAGIC and LAT observations. The black dashed line indicates a fit to the distribution with a non-central χ^2 function. The red solid line represents the resulting cumulative distribution function (CDF). The $\Delta\chi^2$ value derived from the original data is marked as a blue (dot-dash) vertical line.

points) using the same cuts employed in Ref. [295]. Additionally, it should be noted that the MAGIC data extracted from Ref. [295] are originally de-absorbed data using Franceschini et al. EBL model [296]. We make use the Dominguze et al. EBL model [193] to have it corrected with absorption to obtain the observational data, which then are further scaled with respect to their energies[8] before entering the combined χ^2 fitting process.

The combined spectrum for Mkn 421 shows a softening just below TeV energies, deviating noticeably from the log-parabola shape (indicated with green dashed line in Fig. 4.19). A $\Delta\chi^2 = 12.6$ is achieved for the improvement of the goodness of fit under H_1 hypothesis. However, the resulting $\chi^2_{H_1}(df) = 20.7(13)$ is slightly larger than expected due to the two flux points between 100 GeV and 200 GeV which deviate by more than two standard deviations from the fit. Furthermore, in the right panel of Fig. 4.19 we show the $\Delta\chi^2$ distribution under the null hypothesis, with which a significance level of $1.8\,\sigma$ is derived for the corresponding $\Delta\chi^2 = 12.6$.

The results obtained in this Chapter are obtained following closely the pulsar analysis results performed in [40]. Fixed values of $g_{a\gamma\gamma} = 2.3 \times 10^{-10}\,\mathrm{GeV}^{-1}$ and $m_a = 3.6\,\mathrm{neV}$ from pulsar signal region are used in this study for estimating magnetic field in the source-intrinsic region. It is noted that this combination of ALP parameter is not consistent with the parameter bound reported by CAST [39]. Such tension is explicitly discussed and reconciled in another work of ours [44]. The CAST experiment searches for ALPs produced in the Sun, where very dense stellar environment is present. The upper limit provided by CAST [39] can be, however, relaxed when taking into account the environmental effects of dense plasma for ALP production inside the Sun.

In [44], the $g_{\gamma\gamma}$ is proposed to be a environmental dependent quantity and no longer a constant [298].

$$g_{a\gamma\gamma} \to g_{a\gamma\gamma}(\eta), \tag{4.14}$$

where η is a parameter used to characterize the surrounding environment, such as its temperature, plasma frequency, etc.. As it is shown in Fig. 7 of [44] that all environmental parameters become smaller with increasing radial distance from the center of the Sun. In order to produce compatible results in lower densities as found by pulsar analysis in Galactic medium, $g_{a\gamma\gamma}(\eta)$ is assumed to be suppressed with larger values of η at the core of the star. Subsequently, the resulted ALP flux produced in the inner region of the Sun is strongly suppressed, allowing to relax the bound previously set in [39], and leading to a compatible finding with the pulsar claim. Moreover, the pulsar signal obtained in [40] is updated and profiled over uncertainties induced by the use of

---

[8] It is found that the VHE observational data from ground-based instrument can be calibrated with a scaling factor to better character data during a fitting process, see Ref. [297] for more details.

J&F GMF model (see Fig. 3 in [44]). Combining with the relaxing bound of CAST, the tension between two ALP parameter results can be resolved.

In the case of this study, the modulation features shown in the SEDs can also be fit with ALP parameters allowed by the constraints of CAST ($g_{a\gamma\gamma} < 6.6 \times 10^{-11}\,\mathrm{GeV}^{-1}$). This way, the required product of best-fitting parameters of $\hat{B}_0$ and $\hat{s}_0$ would need to increase to higher values by a factor of ≈ 4, which would still be within the range of reasonable values for astrophysical magnetic environments (see Fig. 5.1 in Chapter 5 for a projection of best-fitting parameters of (B, s) over various magnetic environments). In case of other analyses which provide upper bound on photon-ALP coupling smaller than the pulsar signal, the expected product of required B-field strength and scale would be pushed to higher end of the astrophysically motivated values (see labeled dashed lines shown in Fig. 5.1).

In this chapter, we show a systematic and statistic analysis for searching of the photon-ALP mixing effect on AGN spectra. After inspecting the above results, we see that the ALP hypothesis is preferred by the statistical analysis of the AGN gamma-ray spectra. The best-fitting parameters of B-field strength and its spatial extension are falling into the ranges of various astrophysical environments along the line of sight quite well. We can see from the SEDs that moderate modulations are observed in most of the cases for both likelihood and χ^2 analysis results. A detailed summary of the results obtained here is given in Chapter 5.

Chapter 5

Summary and outlook

In this thesis, gamma-ray spectra of distant AGNs have been studied explicitly within the framework of photon-ALP mixing. Photon-ALP mixing can induce energy-dependent modulations on AGN spectra. The resulted modulation features are associated with three mixing channels, the *photon disappearance*, photon appearance and photon reappearance. In this work, we focus on the AGN spectral modulations associated with photon disappearance channel in the energy range of 100 MeV to 500 GeV probed by *Fermi*-LAT. The photon-ALP mixing effect is characterized by a set of parameters, including coupling constant of photons to ALPs $g_{a\gamma\gamma}$, ALP mass m_a, and also equally important, the external magnetic fields that provide such conversion regions. In particular, the energy where the mixing occurs on the SED is determined by the critical energy $E_c \propto m_a^2/(g_{a\gamma\gamma}B)$ (see also Eq. (2.30)), while the strength of the mixing depends on photon-ALP conversion probability $p_{\gamma\to a} \propto g_{a\gamma\gamma}^2 B^2 s^2$ (see e.g. Eq. (2.28)). Motivated by the Galactic pulsar analysis conducted in [40] where a possible region of ALP signal was spotted at $g_{a\gamma\gamma} \simeq 2.3 \times 10^{-10}\,\mathrm{GeV}^{-1}$ with $m_a \simeq 3.6\,\mathrm{neV}$, we choose to fix the ALP parameter at this particular signal region in order to, for the first time, estimate the strength (B) and spatial extension (s) of magnetic fields within the source-intrinsic region. We want to stress that the estimated results would still remain valid for different combinations of $g_{a\gamma\gamma}$ and m_a because of the degeneracy shown in critical energy E_c and photon-ALP conversion probability $p_{\gamma\to a}$. Using 20 AGN spectra recorded during 10 years of *Fermi*-LAT observations we obtain a significance level of $5.3\,\sigma$ with the introduction of photon-ALP mixing effect in a robust likelihood analysis. The B-field strength of source-intrinsic field for 20 sources are found in ranges of values over several orders of magnitudes from 10 nG to tens μG, with their corresponding spatial extension from hundreds of kpc to hundreds of pc. An improvement up to $6\,\sigma$ is also achieved when choosing the global best-fitting parameters of B and s. The local maximum is chosen to minimize the energy requirement to sustain a magnetic field with energy density $\propto B^2$ over a volume $\propto s^3$.

The magnetic fields in the vicinity of a target AGN source includes the jet magnetic field, host galaxy field and intra-cluster magnetic fields. These various field environments are modeled as one single large-scale homogeneous field in our work (see Chapters 2 and 3 for detailed justification). In addition to possible conversion region near sources for photon-ALP mixing, we also take into account other conversion regions, such as the Galactic magnetic field of Milky Way, which is modeled using the J&F GMF model from [207]. Photon-ALP mixing effect in intergalactic magnetic field is, however, neglected here due to its very weak B-field strength and limited available knowledge of its structure. The photon-ALP beam are propagated through these three distinct regions (source region, intergalactic space, Milky Way) with a simplified transfer matrix. Free parameters of (B, s) used for describing source region field are largely optimized in both the likelihood and χ^2-minimization approaches. The resulting (locally) best-fitting parameters of (B, s) are one of the major output of this thesis (see Fig. 5.1) and they are in very good agreement with the strength and scales of the realistic astrophysical environments that are possibly present in the vicinity of the considered sources. In smaller sizes of magnetized environments, they include the magnetic field in the outer region of AGN jet (lobes) [219, 221, 222] as well as the host galaxy magnetic field. In a wider radius to the considered sources, galaxy groups or galaxy clusters, which are known to provide an intra-cluster magnetic field with a turbulent and large scale components [49, 235–238, 241, 246, 247, 301], are expected to host some of these objects. On the other hand, the recent low-frequency radio observations have reported important evidence for the presence of a large scale magnetic field in the circumgalactic medium (CGM) [302]. The largest size of magnetic field that is likely to present on the outskirts source region environment would be the filament of intergalactic magnetic field [262–268], which could contribute additional photon-ALP conversion region. The intergalactic magnetic field in voids, however, is too weak to participate in the photon-ALP mixing [205].

It is also interesting to note that there is a noticeable six-source cluster located in the range of $150\,\mathrm{pc} < s < 300\,\mathrm{pc}$ with $20\,\mu\mathrm{G} < B < 30\,\mu\mathrm{G}$ in Fig. 5.1. Similar scales of magnetic field with roughly the same order of B-field strength are observed and present in the central 200 pc of the Milky Way (the Galactic center field, GCF) [303]. Additionally, the best-fitting parameters of source region field are compared to the prediction of formation of magnetic fields from magnetohydrodynamical simulation [299, 300], and found to be in well consistence with the predicated tracing line of B-field[1].

---

[1] The converted B-field values shown here are from Illustris TNG-300 simulation setup in Ref. [299]

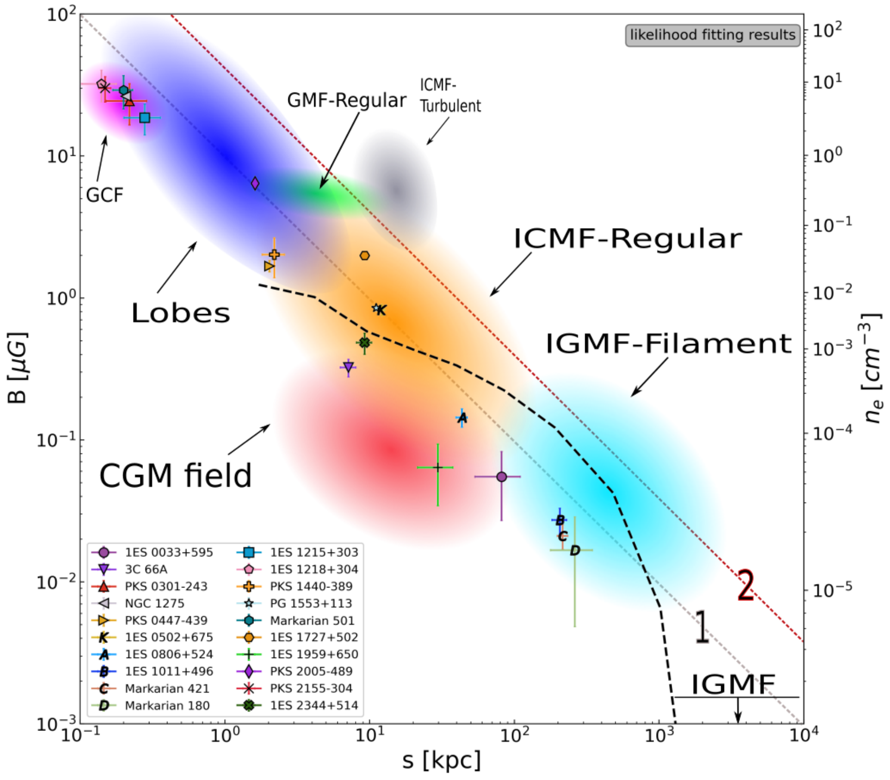

FIGURE 5.1: Likelihood best-fitting results of $(\hat{B}_0, \hat{s}_0)$ associated with Table 4.4. The black dashed line stands for the cosmological magnetohydrodynamic simulation for radio haloes and magnetic fields in galaxy clusters, in relation to the average electron density n_e [299, 300]. Two dashed lines labeled with “1” and “2” indicate the product of B and s with constant values of $10\,\mu\mathrm{G}\cdot\mathrm{kpc}$ and $40\,\mu\mathrm{G}\cdot\mathrm{kpc}$ respectively.

The best-fitting parameters of $(\hat{B}_0, \hat{s}_0)$ shown here are obtained as a result of ALP parameters fixed at the pulsar signal [40]. It is, however, important to note that these meaningful projections of field strength and scale from individual sources would still remain valid for a different combination of $g_{a\gamma\gamma}$ and m_a due to the degeneracy of parameters contained in E_c and $p_{\gamma\to a}$ (see e.g. red dashed line in Fig. 5.1 for smaller $g_{a\gamma\gamma}$).

Strongest improvement of H_1/H_0 can be found in individual cases such as Mkn 421 and NGC 1275, where the largest signal-to-noise ratio is observed. A resulting TS value of 18.5 is obtained for Mkn 421 (see Fig. 4.7) and a $TS = 19.8$ for NGC 1275 (see Fig. B.22), corresponding to a significance level of 3.6σ for both sources. However, in the case of, e.g., PG 1553+113, additional modulation features on the SED are seen but not captured with model. This subsequently leads to a negative TS value of 4.2, for which the H_0 model is preferred instead, indicating a more complicated magnetic field model is needed for the source-intrinsic model of these sources.

Consistent results of best-fitting parameters as well as test statistic values are found using both the likelihood method and χ^2-minimization approach. The main difference between the two fitting methods is the binning configuration. The relatively large bin size used in χ^2 analysis gives rise to an under-sampling of the spectral features, which are instead well captured in the SEDs obtained with likelihood fitting. Therefore, a less significant result is given by the χ^2-based analysis.

The overall estimated improvement of H_1 hypothesis against H_0 hypothesis is made by combining the likelihood analysis results of all 20 sources in a bootstrapping way. When combining the likelihood results for the local maxima in the plane of (B, s) we obtain a total value of $TS_{\rm tot} = 98.9$ (see Fig. 4.12). This value increases to $TS'_{\rm tot} = 133.6$ when selecting global maxima of all sources. Mock data-sets that have been simulated for individual sources under the null hypothesis are combined using bootstrapping method in order to estimate the overall significance of H_1/H_0. A p-value of 1.2×10^{-7} is obtained for $TS_{\rm tot} = 98.9$ of local maxima, corresponding to a $5.3\,\sigma$.

Possible improvements or outlook of the work presented in this thesis can go into directions of the following aspects. The best-fitting parameters of B and s obtained using likelihood (or χ^2) fitting method in this work can be improved with great potential using other approaches in terms of computing efficiency. Instead of scanning the whole grid map of (B, s) where relatively large part of the area are shown with negative TS values (see e.g. Fig. 4.5), one could choose another approach in determining the local maximum for best-fitting parameters. For example, a method based on the Bayes' Theorem is presented in in Appendix C for estimating best-fitting parameters. Alternatively, one could also use Machine Learning technique for spotting spectral anomalies, and estimate the oscillation amplitude, location of photon-ALP mixing based on this.

Another follow-up work on this would be using some of the realistic magnetic field models for testing or instead estimating ALP parameters. The output of B-field parameters in this work can be used as an input for root-mean-square values of e.g. a turbulent magnetic field in intra-cluster magnetic field or galactic center field of host galaxies. A feedback for the validity of the new input parameters can be tested by performing a refit to the same spectral data. Furthermore, the resulting test statistics can be used to search again for photon-ALP signatures or otherwise put constraints on photon-ALP coupling $g_{a\gamma\gamma}$.

In addition, the energy range analyzed here can be extended to VHE range by combining with the ground-based observational data, as a more complete probe on spectral features induced by both the photon disappearance and reappearance channels. We have demonstrated in Chapter 4 two examples of such a HE+VHE spectral analysis. Despite the resulting improvements are not as significant as expected in cases of Mkn 421 and PKS 2155-304, possibly more spectral features may be captured in other cases with an extended coverage for analyzed energies, especially in the overlapping area between two different instruments.

Appendix A

Extragalactic background light

The extragalactic background radiation associated with various electromagnetic frequencies, from radio to gamma–rays, plays a key role in the history of cosmic evolution and formation of the cosmological structures. They are also fundamental sources of opacity for the propagation of high-energy cosmic particles and photons [304, 305]. One of these radiation components is the very intense Cosmic Microwave Background (CMB). The CMB photons behave as a wall to the propagation of the ultra-high-energy (UHE) cosmic particles and photons in the regime of PeV energy [306] through pair production process $\gamma_{\mathrm{CMB}} + \gamma_{\mathrm{UHE}} \to e^+e^-$.

The other important component of this background radiation is the extragalactic background light (EBL), which covers a wide range of wavelength, from ultraviolet (0.1μm) to far infrared (1000μm). This wavelength range is mainly responsible for the attenuation of high and very-high-energy γ rays emitted from astrophysical sources (e.g. AGNs) in the energy range of tens of GeV to 100 TeV through a similar pair production process $\gamma_{\mathrm{EBL}} + \gamma_{\mathrm{VHE}} \to e^+e^-$. The estimated value for EBL photon energy, which is sensitive to the LAT analysis conducted in this work, is given by the relation: $E_{\mathrm{EBL}} = (2m_ec^2)^2/(2E_\gamma(1-\mu))$, where E_{EBL} and E_γ stand for the energies of EBL photons and extragalactic γ rays respectively in the comoving frame of interaction, m_ec^2 is the rest electron energy and $\theta = \arccos(\mu)$ the interaction angle. The cross section of this pair production can then be calculated and found to be strongly peaked around $E^*_{\mathrm{EBL}} \approx 0.8(E_\gamma/\mathrm{TeV})^{-1}$ eV [307]. Therefore, the EBL at ultraviolet through optical is the main source of opacity for propagation of γ rays emitted from AGNs or GRBs within LAT energy band. The choice of EBL models for our analysis is therefore based on this.

EBL is essentially accumulated starlight in the history of Universe. They originate from various processes and sources during cosmic evolution, including star formation processes, gas and AGNs. The intensity of EBL from ultraviolet to near-infrared wave band is considered to be dominated by direct starlight emission, whereas at larger values of wavelength (namely, mid-infrared through far-infrared), the intensity is subject to thermal radiation from interstellar dust which is heated by starlight. Direct measurement of the EBL is very challenging due to the bright foreground sources such as galactic pulsars and zodiacal light [308]. The first lower limit on EBL density is derived from galaxy number counts as possible contribution from unknown sources remains unresolved [309]. Its upper limit can be estimated using *Fermi*-LAT spectral index in high energy range as a regarded index in the VHE range [53, 307]. Discussion of other different limits for constraining EBL is beyond the scope of this work.

However, the resulted opacity effects by pair production can consequently lead to cutoffs on energy spectra which can be measured in most VHE spectral observations of Blazar objects with different IACTs (see e.g. HESS [310], MAGIC [311]) and *Fermi*-LAT [307]. Such energy- and redshift-dependent softening features in observed spectra of extragalactic sources can be used to constrain the absorption strength, named as optical depth $\tau_{\gamma\gamma}(E_\gamma, z_0)$. It is defined as a threefold integral over distance l, the interaction angle $\theta = arccos(\mu)$ and energy of EBL photons:

$$\tau_{\gamma\gamma}(E_\gamma, z_0) = \frac{1}{2}\int_0^{z_0} \frac{dl}{dz}dz \int_{-1}^{1}(1-\mu)d\mu \int_{E^*_{\rm EBL}}^{\infty} n_{\rm EBL}(E'_{\rm EBL}, z)\sigma_{\gamma\gamma}(E'_{\rm EBL}, E'_\gamma, \mu)dE'_{\rm EBL}, \tag{A.1}$$

where $n_{\rm EBL}(E'_{\rm EBL})$ is the comoving EBL photon number density with energy $E'_{\rm EBL} = (1+z)E_{\rm EBL}$ at redshift z, $\sigma_{\gamma\gamma}$ is the interaction cross section and the primed variables denote redshifted energies [53].

The calculation of opacity of EBL to propagation of γ rays, as shown in Eq. (A.1), requires a specific modelling on evolution of the comoving EBL photon number density as a function of redshift. $n_{\rm EBL}$ can be associated to the EBL intensity, which can be derived from γ-ray observations of AGNs. Another important element in Eq. (A.1) for optical depth is the γ-γ cross section, $\sigma_{\gamma\gamma}$, which smooths out the strong variations in EBL spectrum due to its large width over a wide range of energies.

A number of different approaches have been developed to model the intensity and spectral distribution of EBL at $z = 0$ in the past two decades (see Refs. [308, 312] for a detailed review of various EBL models). One one hand, backward evolution models, as the name suggest, use a backward extrapolation of local galaxy population to obtain SEDs of galaxies and stars, which can then be fit to the observed number counts. These type of models include Franceschini et al. [296] and Domínguez et al. [193]. On the other hand, the forward evolution models start from the cosmological initial conditions and evolve the SEDs of galaxies with time to fit present observations. For example, Kneiske et al. [313] and Finke et al. [314] EBL models are obtained with the forward evolution method. On top of that, semi-analytical model (see Gilmore et al. EBL model [315] for an example) is also used for modelling EBL. They are based upon a Lambda cold dark matter hierarchical structural formation scenario, where cosmological parameters are derived from Wilkinson Microwave Anisotropy Probe 5-year observation.

Appendix B

Additional fitted spectra and best-fitting parameters

This appendix shows the additional best-fitting parameters for sources discussed in Chapter 4 and their corresponding fitted spectra (SEDs) under the null hypothesis H_0 and ALP hypothesis H_1 with both likelihood and χ^2-minimization methods. On top of that, we also show the grid maps of (B, s) that are used to estimate the best-fitting parameters for each source, as well as simulations conducted under null hypothesis for determining the significance of H_1/H_0. After inspecting individual source case by case, we find that there are some interesting features shown in some of the SEDs, which are not well described by our model and indicating the preference of a more complicated B-field model.

In Table B.1 we show the best-fitting parameters estimated using χ^2 approach under H_0, the same fitting done with likelihood is shown correspondingly in Table 4.3 of Chapter 4. The best-fitting parameters obtained for local maximums (of $-\Delta\chi^2$ values) under H_1 hypothesis using χ^2 method are shown in Table B.2 (see Table 4.4 for the corresponding likelihood results).

Then in Tables B.3 and B.4 we list the best-fitting parameters obtained under ALP hypothesis for global maximums using χ^2 and likelihood methods respectively. In Table B.5 we present the final results of the hypotheses tests with both likelihood and χ^2 methods when selecting the global maximums for best-fitting parameters of all sources (see Table 4.5 in Chapter 4 for the hypotheses tests of local maximums).

In figures B.1 to B.18 we show the grid maps of (B, s) with likelihood and χ^2 methods that are used to obtain the best-fitting parameters listed in Tables 4.4, B.2, B.3 and B.4. The corresponding resulted spectral energy distributions are presented in figures B.19

Table B.1: Best-fitting parameters for the null hypothesis with the χ^2 method using the modeled spectra from Eq. (4.6). The estimated uncertainties (1σ) for each fitting parameters are listed as well. The value of $E_b = 10^5$ MeV is fixed, the normalisation is given in units of $10^{-15}\mathrm{MeV}^{-1}\mathrm{cm}^{-2}\mathrm{s}^{-1}$.

AGN name	N_0	α	β $\times 10^{-3}$
1ES 0033+595	1.083(0.115)	1.71(0.08)	1(13)
3C 66A	1.10(0.09)	2.28(0.04)	45(5)
PKS 0301-243	0.509(0.064)	2.17(0.06)	36(8)
NGC 1275	0.802(0.046)	2.70(0.02)	70(3)
PKS 0447-439	1.29(0.10)	2.20(0.04)	55(5)
1ES 0502+675	0.86(0.07)	2.50(0.03)	–
1ES 0806+524	0.46(0.05)	2.11(0.06)	33(8)
1ES 1011+496	1.15(0.09)	2.06(0.04)	32(5)
Markarian 421			
10yrs LAT	6.34(0.20)	1.92(0.02)	22(2)
simul. LAT+MAGIC	3.28(0.18)	2.12(0.02)	50(5)
Markarian 180	0.226(0.026)	2.19(0.03)	–
1ES 1215+303	0.772(0.069)	2.28(0.04)	48(5)
1ES 1218+304	1.02(0.07)	2.29(0.02)	–
PKS 1440-389	0.484(0.06)	2.20(0.07)	63(11)
PG 1553+113	3.96(0.21)	1.87(0.03)	37(5)
Markarian 501	2.41(0.13)	1.86(0.03)	17(4)
1ES 1727+502	0.344(0.033)	2.20(0.02)	–
1ES 1959+650	1.60(0.11)	1.98(0.04)	26(5)
PKS 2005-489	0.572(0.043)	2.18(0.02)	–
PKS 2155-304			
10yrs LAT	2.44(0.13)	2.13(0.03)	40(3)
simul. LAT+H.E.S.S.	1.32(0.04)	2.22(0.03)	53(7)
1ES 2344+514	0.321(0.06)	2.23(0.11)	61(16)

to B.36, where results on the left and right panels are obtained with likelihood and χ^2 fitting methods respectively.

In figures B.37 to B.42 we show the simulated null distributions from likelihood ratio and $\Delta\chi^2$ tests. They are used to make estimates on the significance of H_1/H_0 for individual source, which is shown in previous Tables 4.5 and B.5.

TABLE B.2: Best-fitting parameters of local maxima for ALP hypothesis with χ^2 method. Parameters uncertainties (1σ) are included. The value of $E_b = 10^5$ MeV is fixed, the normalisation is given in units of $10^{-15}\text{MeV}^{-1}\text{cm}^{-2}\text{s}^{-1}$.

AGN name	N_0	α	β $\times 10^{-3}$	$\hat{B}_0$ [nG]	$\hat{s}_0$ [kpc]
1ES 0033+595	1.74(0.20)	1.78(0.08)	188(12)	7547.5(3281.5)	1.5(0.6)
3C 66A	1.89(0.26)	2.20(0.05)	46(5)	374.7(62.6)	6.9(0.8)
PKS 0301-243	0.950(0.145)	2.18(0.12)	46(13)	21672.5(2918.8)	0.3(0.01)
NGC 1275	1.47(0.02)	2.74(0.01)	76(1)	39621.7(317.6)	0.1(1.6)
PKS 0447-439	2.46(0.22)	2.30(0.07)	909	1731.8(283.0)	2.0(0.2)
1ES 0502+675	1.35(0.21)	2.59(0.05)	–	104.4(54.0)	53.5(17.4)
1ES 0806+524	0.581(0.075)	2.00(0.07)	21(9)	25.5(10.2)	202.6(36.2)
1ES 1011+496	1.42(0.14)	1.98(0.05)	24(6)	35.7(7.3)	170.5(17.0)
Markarian 421					
10yrs LAT	8.71(0.43)	1.84(0.02)	16(3)	16.5(6.4)	242.0(35.1)
simul. LAT+MAGIC	7.25(0.37)	2.15(0.02)	71(5)	4344.2(845.6)	1.0(0.1)
Markarian 180	0.308(0.040)	2.25(0.03)	–	20.2(11.0)	226.2(72.9)
1ES 1215+303	1.44(0.16)	2.36(0.07)	69(12)	7385.9(5817.8)	0.4(0.3)
1ES 1218+304	1.98(0.14)	2.29(0.02)	–	295842.8(65007.2)	0.0(0.01)
PKS 1440-389	0.859(0.121)	2.38(0.08)	110(12)	2326.0(1404.3)	1.9(0.5)
PG 1553+113	7.40(0.40)	1.78(0.04)	40(5)	840.1(88.9)	10.9(1.0)
Markarian 501	4.07(0.38)	1.87(0.02)	24(3)	29607.5(3114.0)	0.2(0.02)
1ES 1727+502	0.479(0.044)	2.23(0.02)	–	1355.6(341.8)	6.8(1.3)
1ES 1959+650	2.33(0.31)	1.89(0.05)	22(5)	137.7(67.8)	11.1(3.4)
PKS 2005-489	1.01(0.09)	2.24(0.02)	–	8025.7(2126.2)	1.3(0.3)
PKS 2155-304					
10yrs LAT	4.69(0.24)	2.16(0.03)	43(3)	60241.1(10007.3)	0.1(0.01)
simul. LAT+H.E.S.S.	2.69(0.09)	2.34(0.02)	86(7)	5589.7(1975.4)	0.8(0.2)
1ES 2344+514	0.731(0.132)	2.15(0.12)	75(17)	619.9(204.6)	7.5(1.5)

TABLE B.3: Best-fitting parameters for ALP hypothesis with χ^2 method using the modeled spectra from Eq. (4.7). Parameters uncertainties (1σ) are included. The value of $E_b = 10^5$ MeV is fixed, the normalisation is given in units of $10^{-15}\mathrm{MeV}^{-1}\mathrm{cm}^{-2}\mathrm{s}^{-1}$.

AGN name	N_0	α	β $\times 10^{-3}$	$\hat{B}$ [nG]	$\hat{s}$ [kpc]
1ES 0033+595	1.77(0.20)	1.75(0.08)	13(13)	17047.7(2689.8)	3.8(0.6)
3C 66A	1.89(0.26)	2.20(0.05)	46(5)	374.8(62.6)	6.9(0.8)
PKS 0301-243	0.955(0.078)	2.17(0.05)	46(5)	88403.9(532.1)	1.8(0.01)
NGC 1275	1.43(0.13)	2.75(0.03)	78(4)	33752.1(9973.8)	0.1(0.03)
PKS 0447-439	2.50(0.19)	2.23(0.04)	74(6)	8922.0(54.8)	57.7(0.4)
1ES 0502+675	1.42(0.17)	2.57(0.03)	–	910.7(6.9)	272.8(1.8)
1ES 0806+524	0.617(0.085)	1.98(0.07)	19(10)	51.8(7.6)	278.5(28.4)
1ES 1011+496	1.79(0.16)	1.89(0.04)	16(6)	120.9(1.6)	855.7(8.9)
Markarian 421					
10yrs LAT	8.71(0.44)	1.84(0.02)	16(3)	16.5(6.6)	242.2(37.4)
simul. LAT+MAGIC	7.25(0.37)	2.15(0.02)	71(5)	4344.2(845.6)	1.0(0.1)
1ES 1215+303	1.44(0.16)	2.36(0.07)	69(12)	7392.7(5743.8)	0.4(0.3)
1ES 1218+304	2.00(0.14)	2.30(0.02)	–	308906.8(516.5)	7.3(0.01)
PKS 1440-389	0.931(0.119)	2.28(0.08)	91(12)	30894.1(26.7)	200.5(0.2)
PG 1553+113	7.29(0.16)	1.88(0.01)	53(1)	2647.4(0.0)	226832.3(0.4)
Markarian 501	4.40(0.25)	1.85(0.03)	15(5)	59644.3(1303.1)	2.5(0.1)
1ES 1727+502	0.446(0.042)	2.18(0.02)	–	61936.7(16.3)	395.7(0.1)
1ES 1959+650	2.75(0.29)	1.81(0.05)	13(7)	180.6(1.8)	627.7(3.5)
PKS 2005-489	0.895(0.076)	2.22(0.02)	–	11432.8(151.3)	20.4(0.3)
PKS 2155-304					
10yrs LAT	4.51(0.24)	2.11(0.03)	49(4)	4912.4(1.4)	925.6(0.2)
simul. LAT+H.E.S.S.	2.69(0.09)	2.34(0.02)	86(7)	5589.7(1975.4)	0.8(0.2)
1ES 2344+514	0.690(0.152)	2.21(0.12)	83(17)	1159.7(390.0)	11.9(3.3)

Table B.4: Best-fitting parameters for ALP hypothesis with likelihood method using the modeled spectra from Eq. (4.7). The normalisation is given in units of $10^{-12}\mathrm{MeV}^{-1}\mathrm{cm}^{-2}\mathrm{s}^{-1}$. Parameters uncertainties (1σ) are included.

AGN name	N_0	α	β $\times 10^{-3}$	E_b [MeV]	$\hat{B}$ [nG]	$\hat{s}$ [kpc]
1ES 0033+595	0.629(0.025)	1.54(0.03)	42(12)	3177	911.9(1.5)	911.4(1.3)
3C 66A	12.5(0.2)	1.80(0.01)	43(6)	1211	311.0(44.4)	7.3(1.0)
PKS 0301-243	11.1(0.4)	1.81(0.02)	38(10)	954.4	50660.9(314.0)	1.3(0.01)
NGC 1275	102(2)	1.98(0.01)	85(3)	883.6	14007.6(694.6)	0.2(0.01)
PKS 0447-439	7.09(0.13)	1.56(0.01)	83(6)	1605	2151.5(41.6)	5.5(0.1)
1ES 0502+675	0.083(0.004)	1.38(0.03)	–	6322	830.6(0.7)	1000.0(0.7)
1ES 0806+524	2.31(0.06)	1.79(0.02)	12(10)	1297	74.6(2.4)	435.4(12.4)
1ES 1011+496	7.68(0.10)	1.73(0.01)	17(5)	1066	118.6(0.9)	723.0(5.0)
Markarian 421	19.1(0.2)	1.69(0.005)	13(2)	1286	21.1(4.2)	216.3(18.4)
Markarian 180	0.182(0.008)	1.70(0.03)	–	2679	98.5(1.5)	870.1(11.9)
1ES 1215+303	17.9(0.4)	1.81(0.01)	53(7)	1066	47661.7(202.6)	1.4(0.01)
1ES 1218+304	0.418(0.015)	1.68(0.02)	–	4442	241288.9(42.7)	9.4(0.002)
PKS 1440-389	1.75(0.06)	1.51(0.03)	100(13)	2014	3331.2(38.9)	11.7(0.1)
PG 1553+113	5.66(0.09)	1.45(0.01)	49(5)	1847	3496.4(0.0)	98466.5(0.1)
Markarian 501	8.35(0.34)	1.70(0.01)	17(5)	1478	85669.0(71.4)	3.2(0.003)
1ES 1727+502	0.297(0.017)	1.75(0.03)	–	3005	226832.0(0.6)	690.1(0.002)
1ES 1959+650	3.39(0.06)	1.70(0.01)	9(5)	1733	89.5(0.9)	831.8(10.0)
PKS 2005-489	0.747(0.050)	1.76(0.02)	–	2398	21312.2(78.1)	5.6(0.02)
PKS 2155-304	30.9(0.4)	1.76(0.01)	40(5)	1136	344288.2(57.1)	5.4(0.001)
1ES 2344+514	1.07(0.05)	1.56(0.03)	61(14)	1938	482.4(82.1)	9.2(1.1)

Table B.5: Best-fitting log-likelihood and χ^2 values for null (H_0) and ALP hypotheses (H_1). TS values are calculated with Eqs. (4.9) and (4.10) for likelihood ratio test and $\Delta\chi^2$ test respectively. Corresponding significance levels for both tests are listed as well.

AGN name	H_0 $\ln(L^0_{max})$	H_1 $\ln(L^1_{max})$	TS	z-score (H_1/H_0)	H_0 $\chi^2_{\mathrm{w/o\,ALP}}/df$	H_1 $\chi^2_{\mathrm{w/\,ALP}}/df$	$\Delta\chi^2$	z-score (H_1/H_0)
1ES 0033+595	712253.0	712257.8	9.6	2.3	22.2/15	13.5/13	8.7	2.0
3C 66A	−122858.4	−122856.5	3.8	2.0	20.6/15	16.3/13	4.3	2.3
PKS 0301-243	−154508.6	−154507.9	1.4	0.6	16.3/15	16.3/13	−0.1	0.5
NGC 1275	26767.7	26777.6	19.8	3.6	25.6/15	22.4/13	3.2	1.8
PKS 0447-439	−146200.2	−146199.1	2.3	2.0	26.2/15	22.6/13	3.6	2.1
1ES 0502+675	−44659.7	−44656.2	7.0	1.3	41.9/16	37.0/14	4.9	0.8
1ES 0806+524	−159751.7	−159750.3	2.9	0.2	20.5/15	16.4/13	4.1	0.5
1ES 1011+496	−153505.0	−153500.7	8.6	1.6	12.7/15	8.0/13	4.7	0.7
Markarian 421								
10yrs LAT	−130615.4	−130606.2	18.5	3.6	28.8/15	15.5/13	13.3	2.7
simul. LAT+MAGIC	–	–	–	–	33.4/15	15.2/13	18.2	1.8
Markarian 180	−132628.4	−132627.7	1.4	0.01	23.8/16	19.8/14	4.0	0.5
1ES 1215+303	−143988.2	−143984.0	8.4	2.2	15.5/15	13.4/13	2.1	1.2
1ES 1218+304	−145577.3	−145576.5	1.6	1.3	19.0/16	19.9/14	−0.9	1.1
PKS 1440-389	60781.3	60783.8	5.0	1.5	18.9/15	16.1/13	2.7	0.8
PG 1553+113	−152448.5	−152447.6	1.7	0.4	17.8/15	14.7/13	3.1	0.5
Markarian 501	−95747.1	−95742.8	8.7	1.7	18.5/15	12.8/13	5.7	1.0
1ES 1727+502	−154208.5	−154205.2	6.8	1.4	26.7/16	22.7/14	3.9	0.3
1ES 1959+650	−49456.2	−49453.1	6.3	1.1	21.6/15	13.5/13	8.1	1.5
PKS 2005-489	−166314.9	−166307.9	13.6	2.5	33.9/16	17.7/14	16.2	2.6
PKS 2155-304								
10yrs LAT	−144503.6	−144502.7	1.7	1.5	15.8/15	14.3/13	1.5	1.1
simul. LAT+H.E.S.S.	–	–	–	–	33.3/18	29.2/16	4.1	1.6
1ES 2344+514	−61482.2	−61480.1	4.3	1.2	15.2/15	13.8/13	1.4	0.5

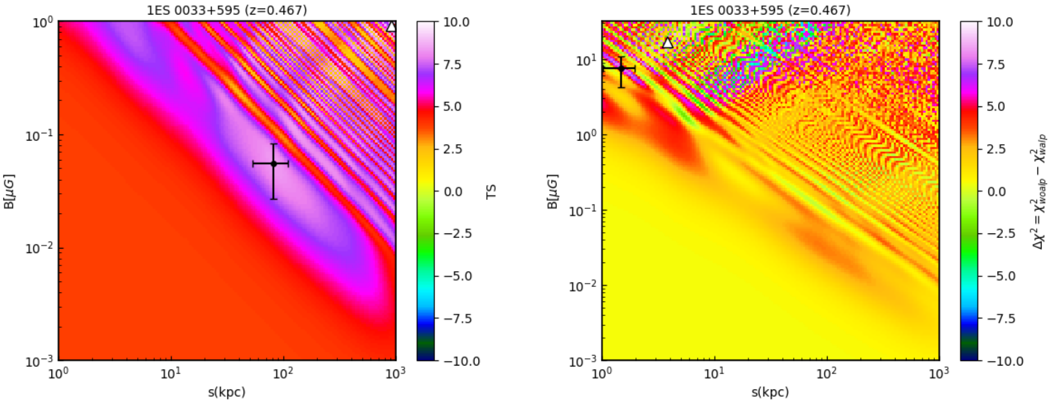

FIGURE B.1: Left panel: (B, s) grid map where the color bar indicates the test statistics TS which is twice the difference of log-likelihood values between null and ALP hypotheses. The black and white marker correspond to the local and global best-fitting parameters respectively. Right panel: same as the left panel, but with χ^2 minimization fitting methods.

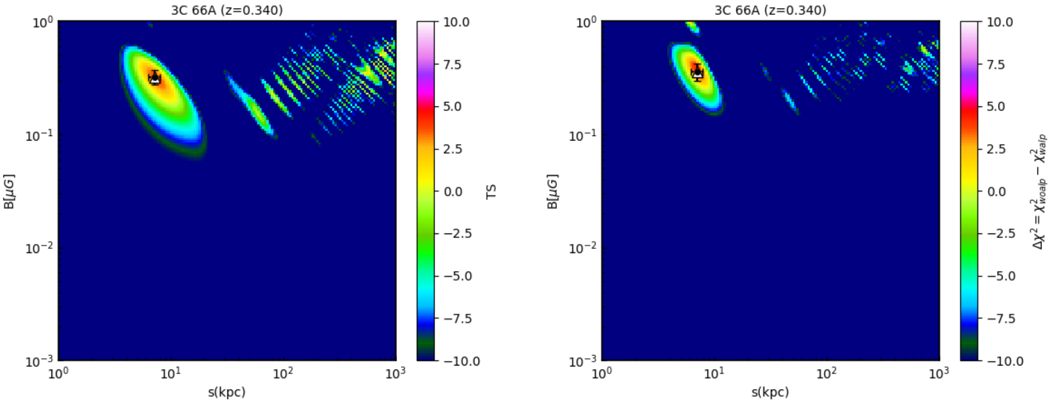

FIGURE B.2: 3C 66A, same as Fig. B.1.

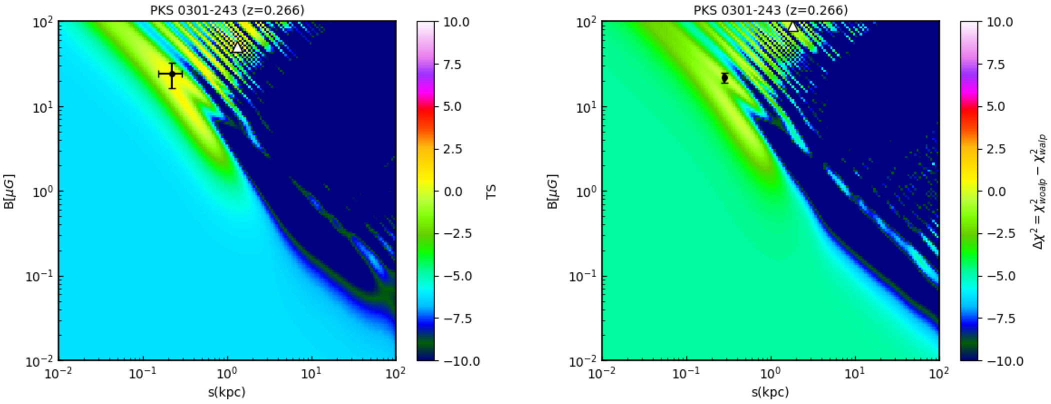

FIGURE B.3: PKS 0301-243, same as Fig. B.1.

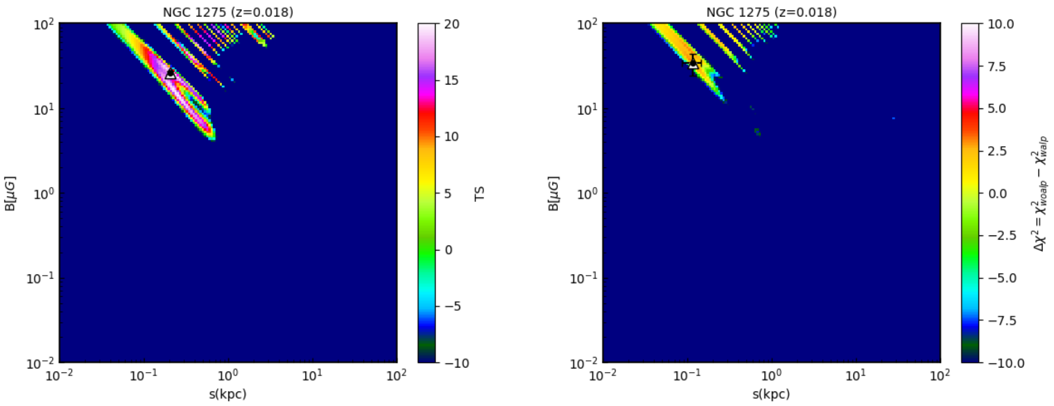

FIGURE B.4: NGC 1275, same as Fig. B.1.

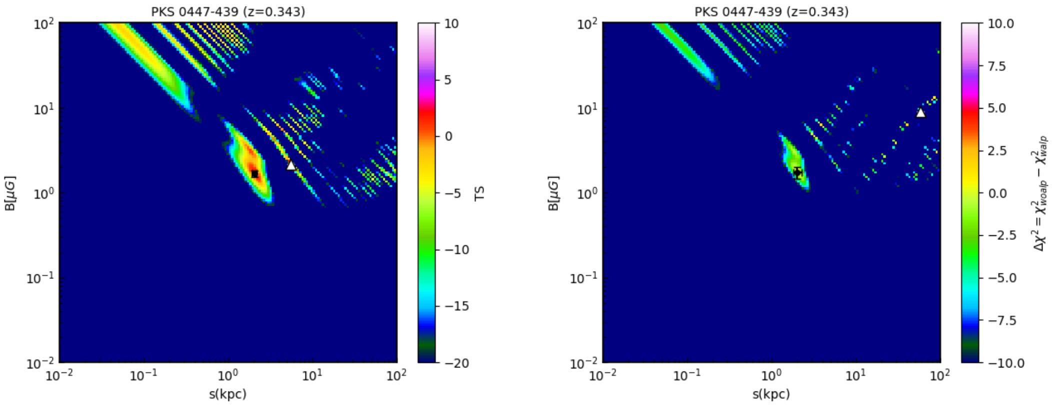

FIGURE B.5: PKS 0447-439, same as Fig. B.1.

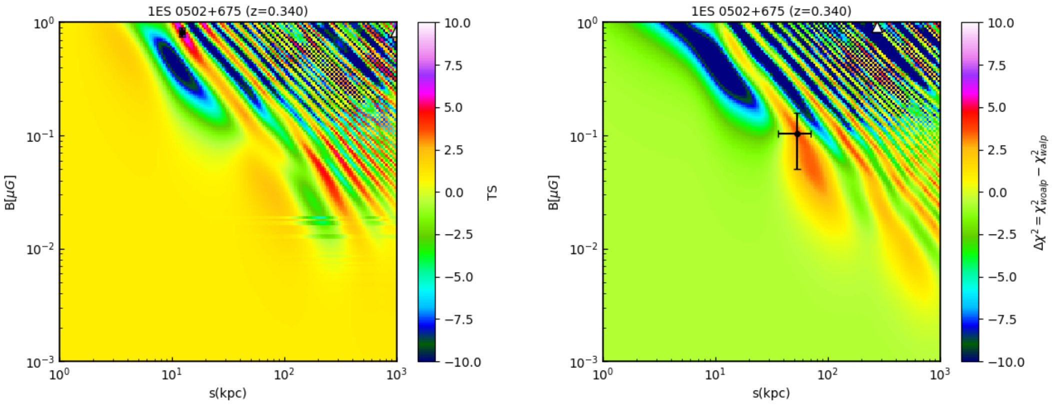

FIGURE B.6: 1E 0502+675, same as Fig. B.1.

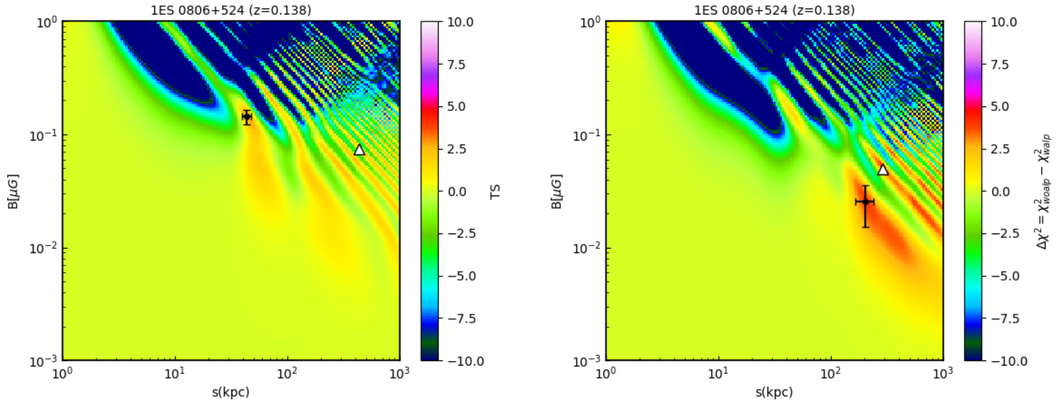

Figure B.7: 1ES 0806+524, same as Fig. B.1.

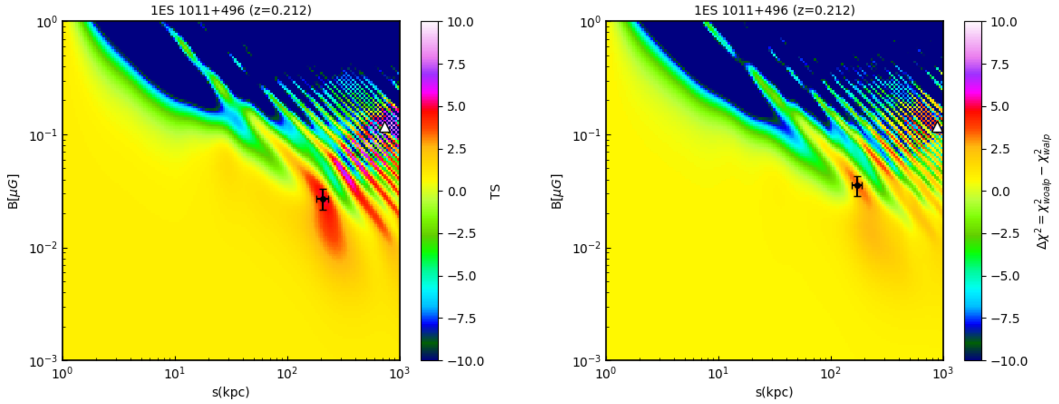

Figure B.8: 1ES 1011+496, same as Fig. B.1.

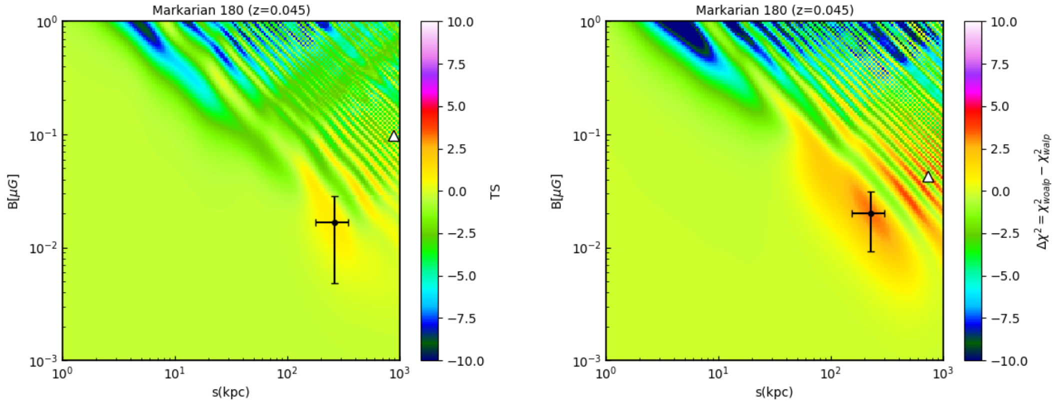

Figure B.9: Markarian 180, same as Fig. B.1.

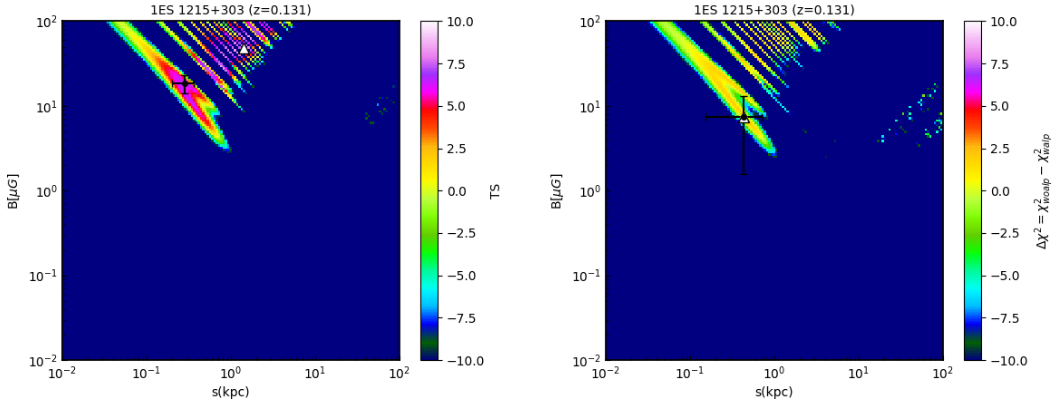

FIGURE B.10: 1ES 1215+303, same as Fig. B.1.

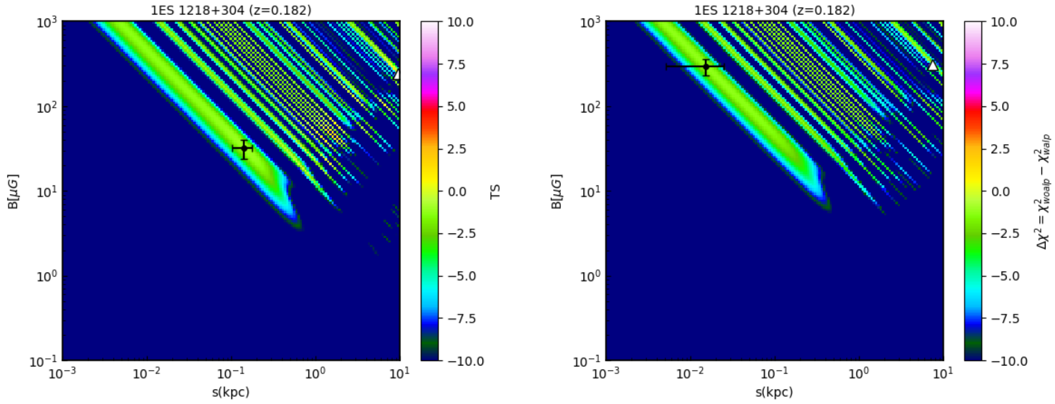

FIGURE B.11: 1ES 1218+304, same as Fig. B.1.

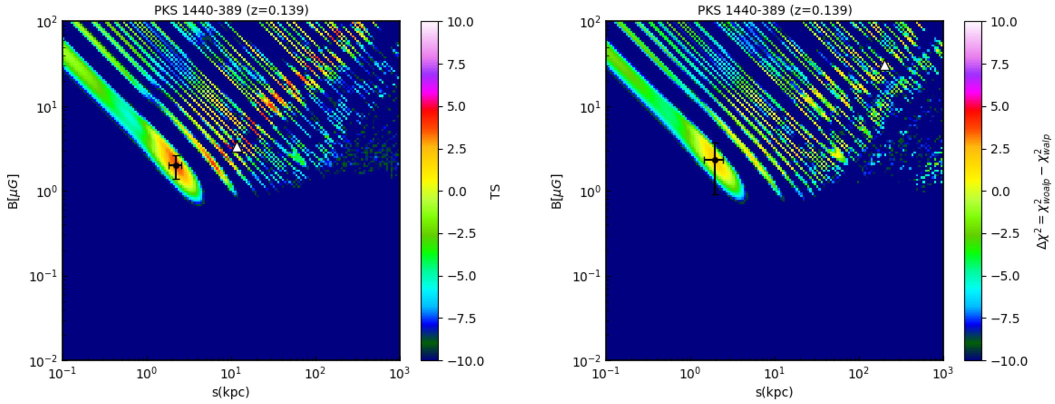

FIGURE B.12: PKS 1440-389, same as Fig. B.1.

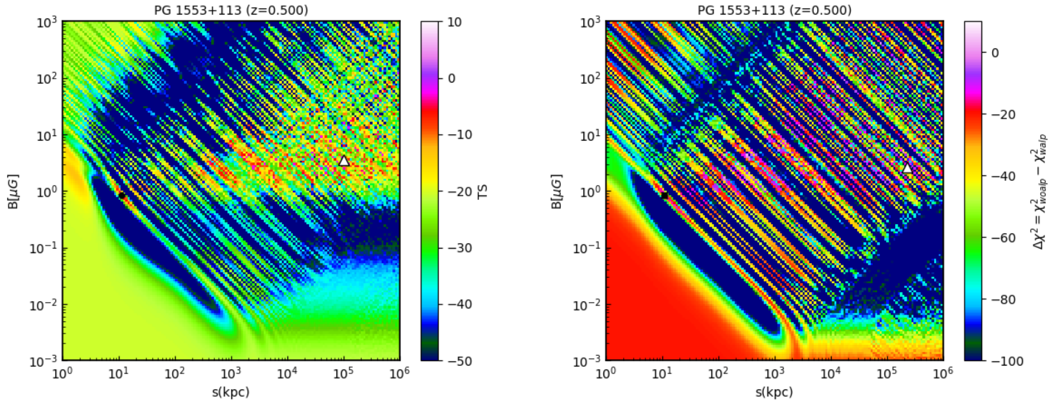

FIGURE B.13: PG 1553+113, same as Fig. B.1.

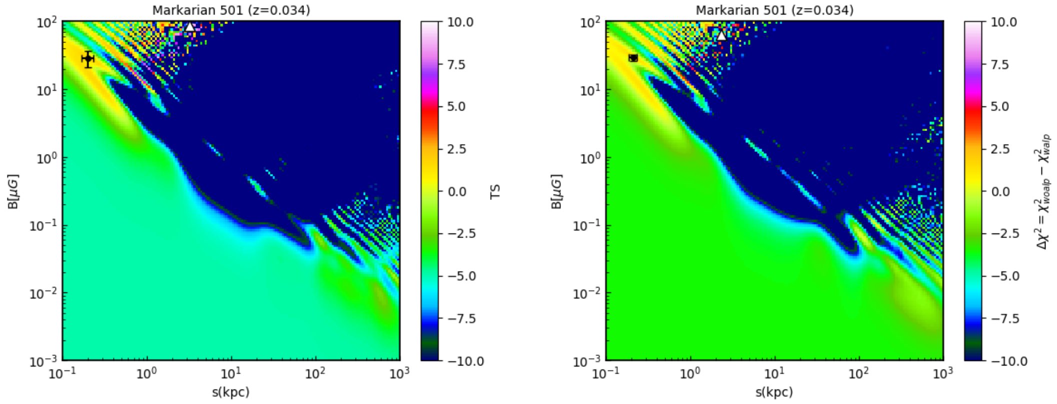

FIGURE B.14: Markarian 501, same as Fig. B.1.

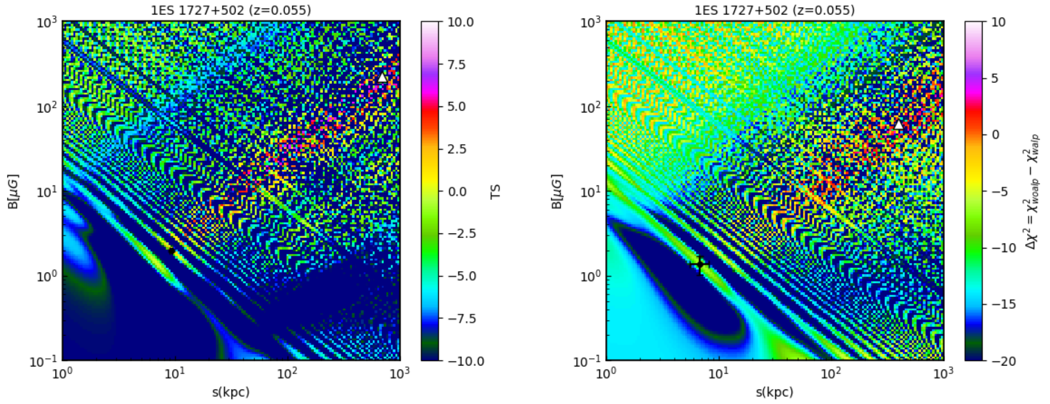

FIGURE B.15: 1ES 1727+502, same as Fig. B.1.

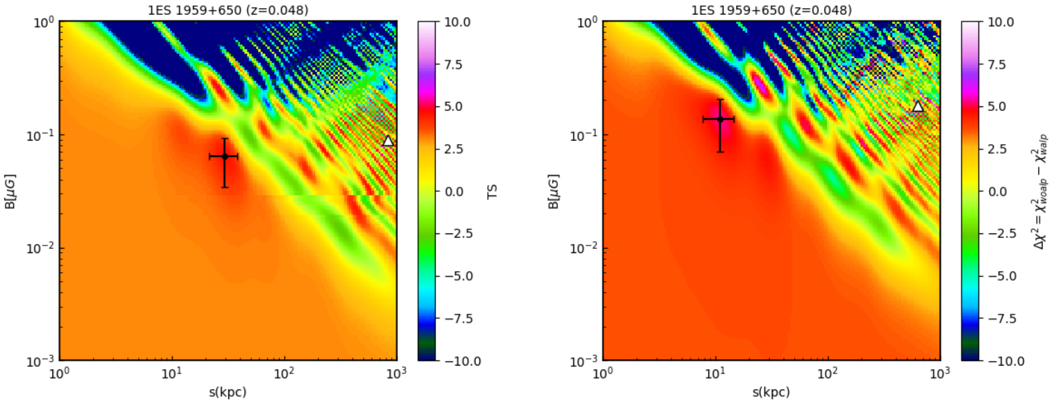

Figure B.16: 1ES 1959+650, same as Fig. B.1.

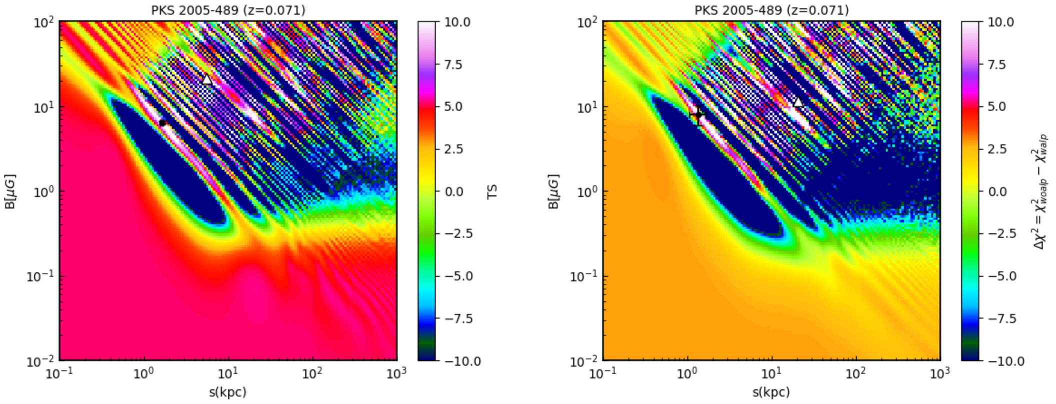

Figure B.17: PKS 2005-304, same as Fig. B.1.

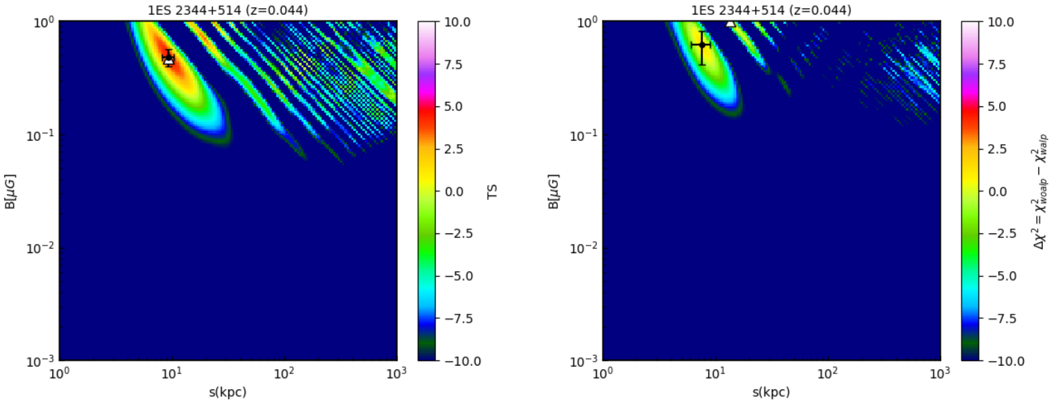

Figure B.18: 1ES 2344+514, same as Fig. B.1.

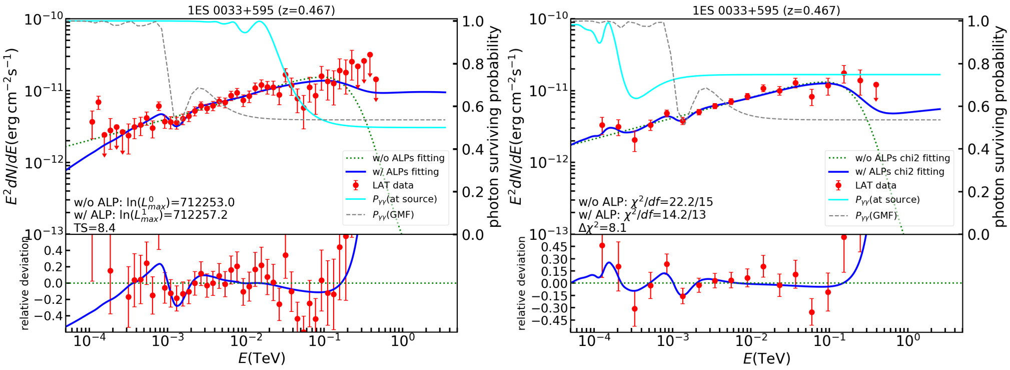

FIGURE B.19: Left panel: the spectral energy distribution for source 1ES 0033+595 with likelihood fitting method. The red data points are collected from a 10-yrs LAT observation. The blue straight line is the best-fitting model with photon-ALP mixing effects included, and the green dashed line is the best-fitting model without the assumption of photon-ALP mixing. The cyan solid line is the photon surviving probability at source and the gray dashed line is the photon surviving probability at Milky Way. In the lower panel, we show the relative deviations of the flux points and "w/ ALP" scenario from the baseline ("w/o ALP"). Right panel: same as left panel, but with χ^2 fitting method.

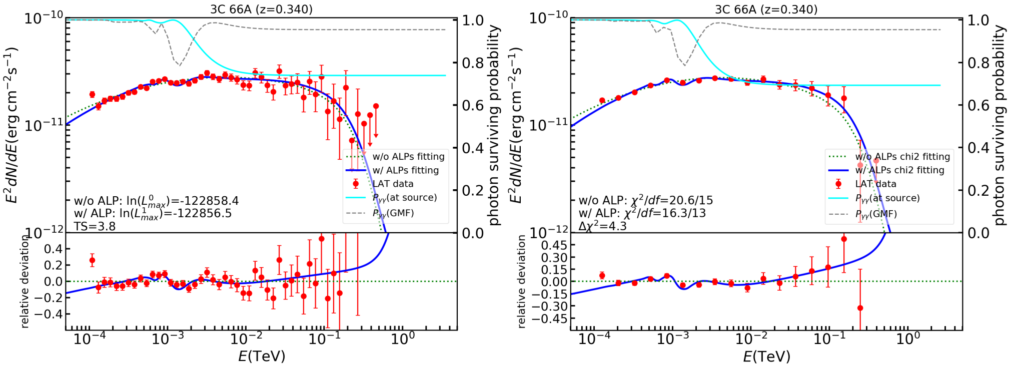

FIGURE B.20: 3C 66A, same as Fig. B.19.

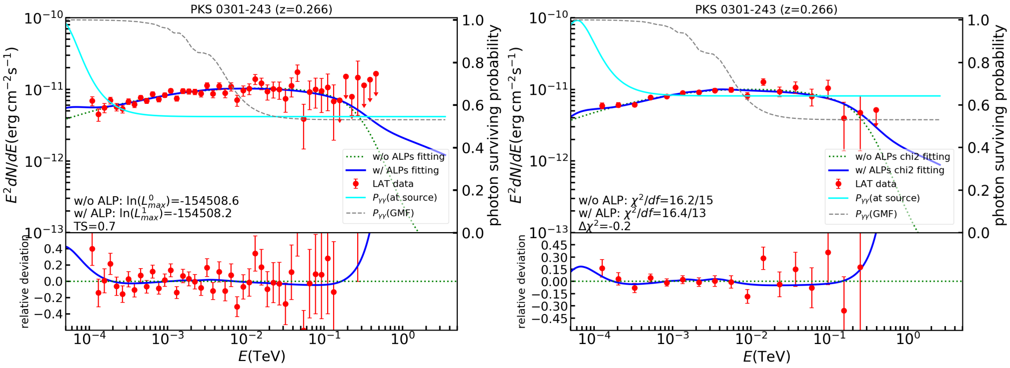

FIGURE B.21: PKS 0301-243, same as Fig. B.19.

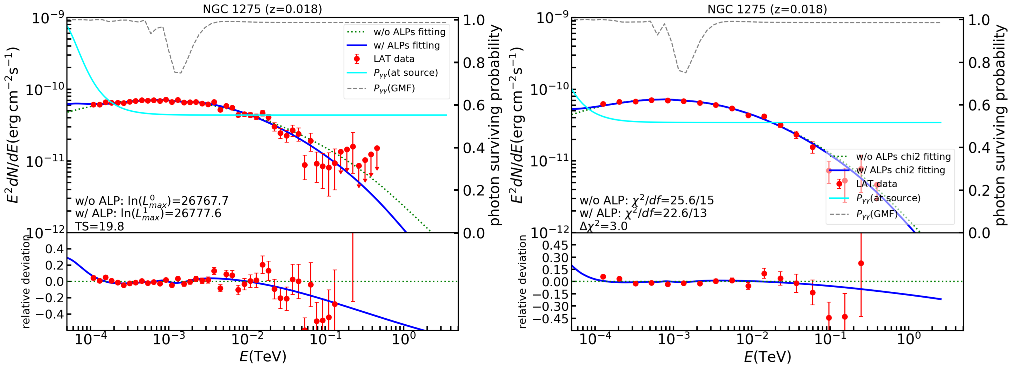

Figure B.22: NGC 1275, same as Fig. B.19.

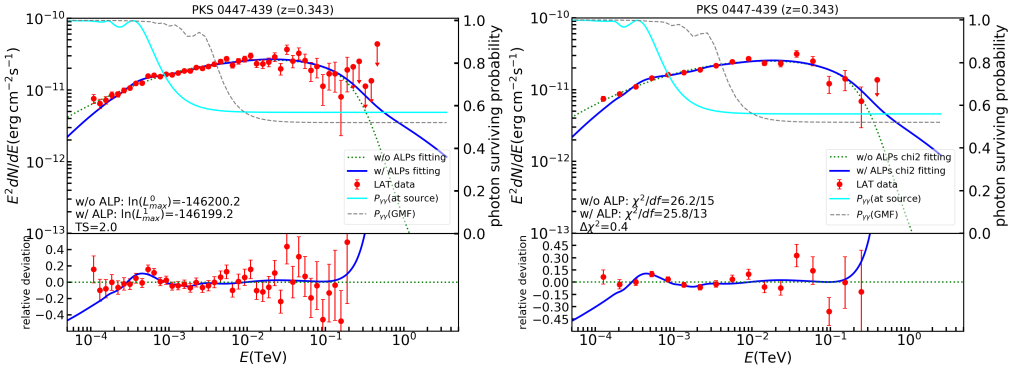

Figure B.23: PKS 0447-439, same as Fig. B.19.

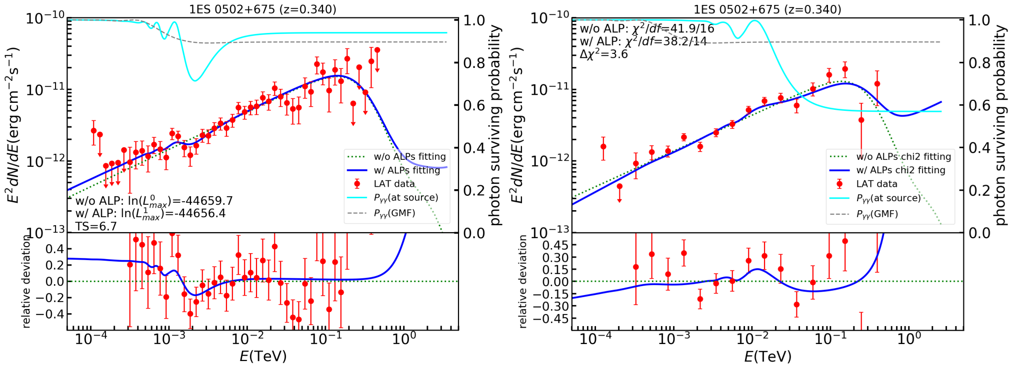

Figure B.24: 1ES 0502+675, same as Fig. B.19.

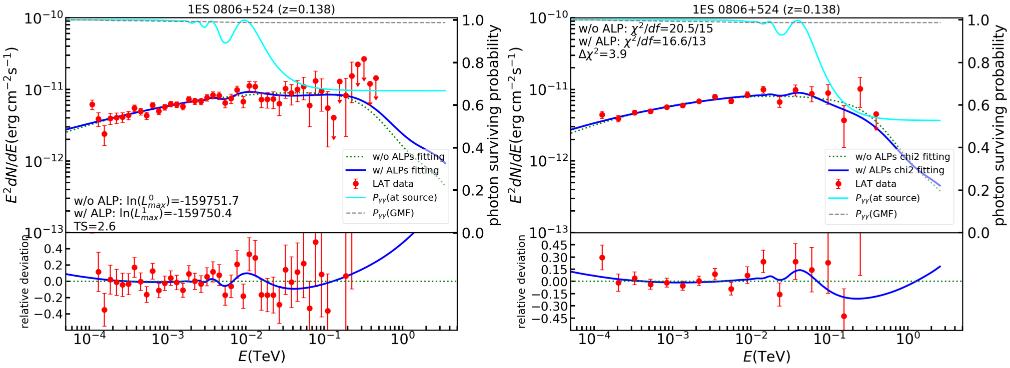

FIGURE B.25: 1ES 0806+524, same as Fig. B.19.

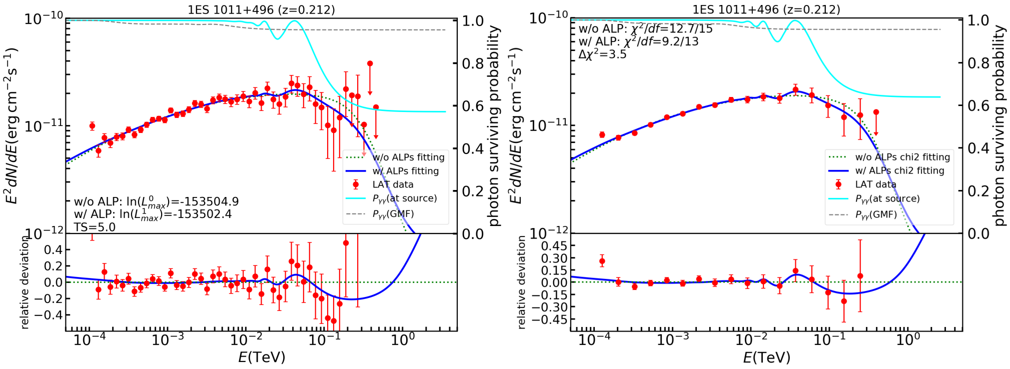

FIGURE B.26: 1ES 1011+496, same as Fig. B.19.

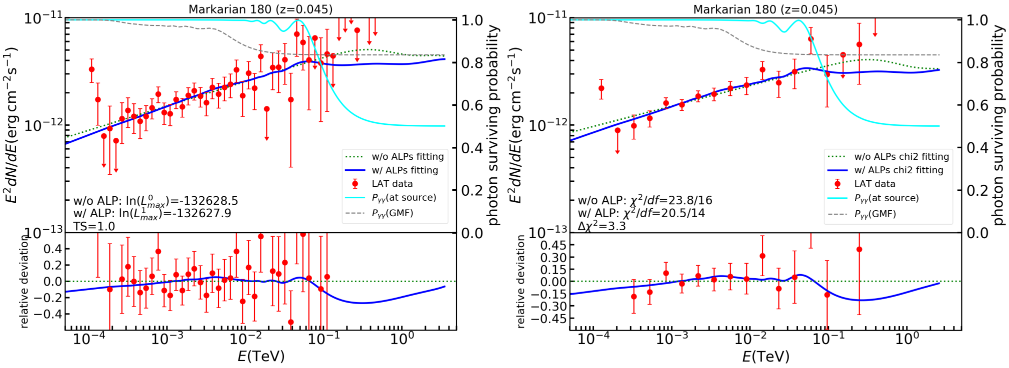

FIGURE B.27: Markarian 180, same as Fig. B.19.

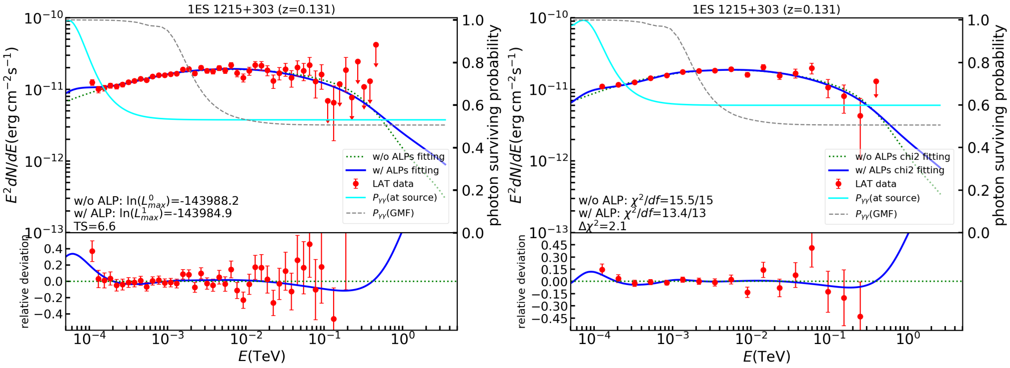

FIGURE B.28: 1ES 1215+303, same as Fig. B.19.

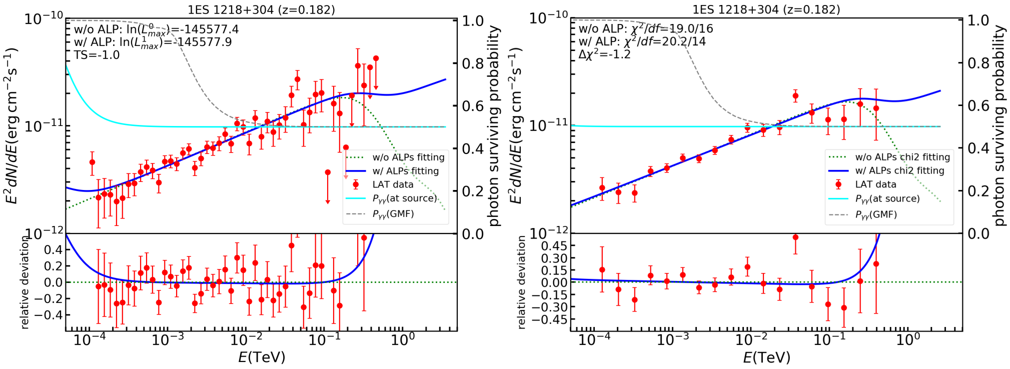

FIGURE B.29: 1ES 1218+304, same as Fig. B.19.

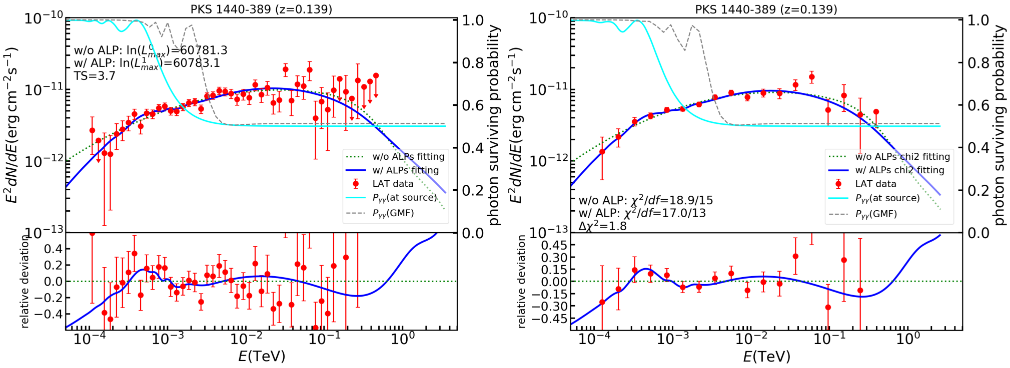

FIGURE B.30: PKS 1440-389, same as Fig. B.19.

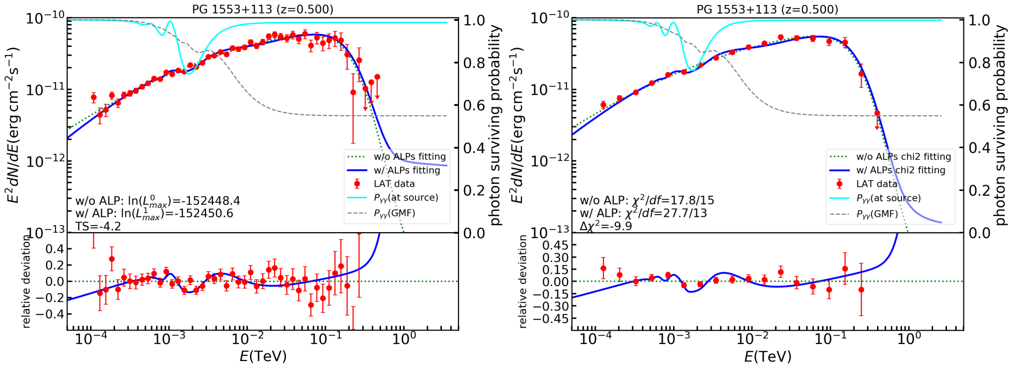

FIGURE B.31: PG 1553+113, same as Fig. B.19.

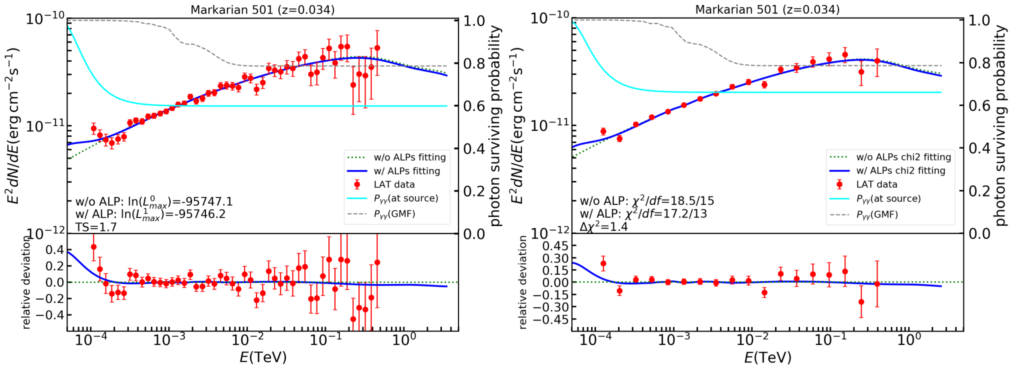

FIGURE B.32: Markarian 501, same as Fig. B.19.

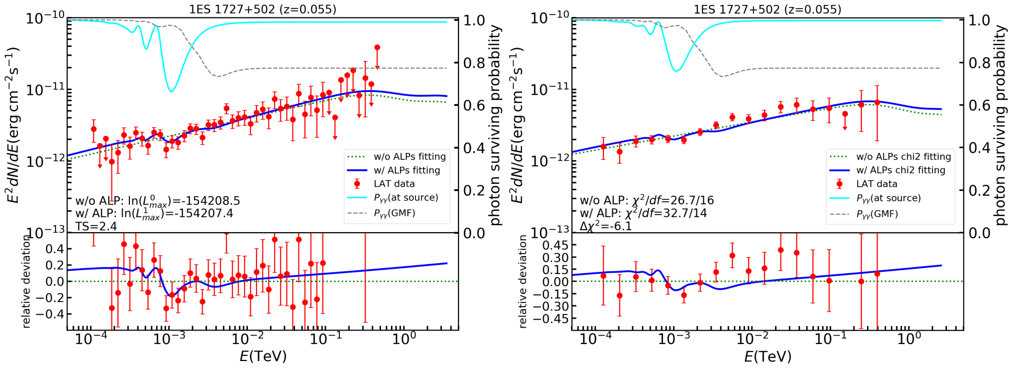

FIGURE B.33: 1ES 1727+502, same as Fig. B.19.

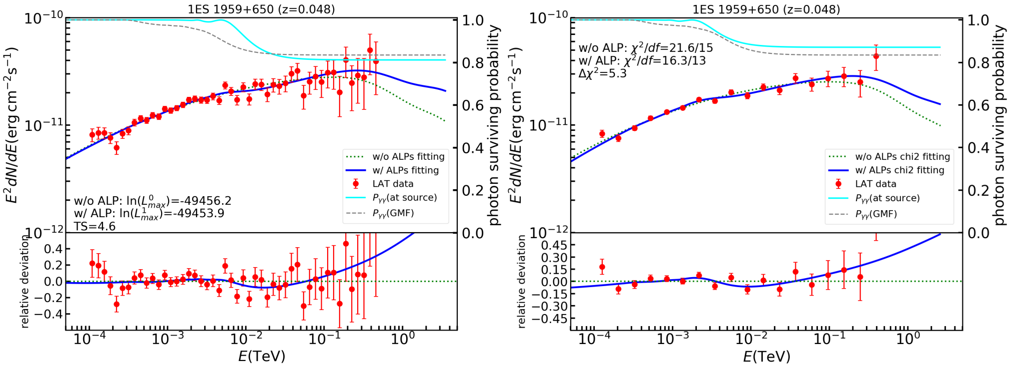

FIGURE B.34: 1ES 1959+650, same as Fig. B.19.

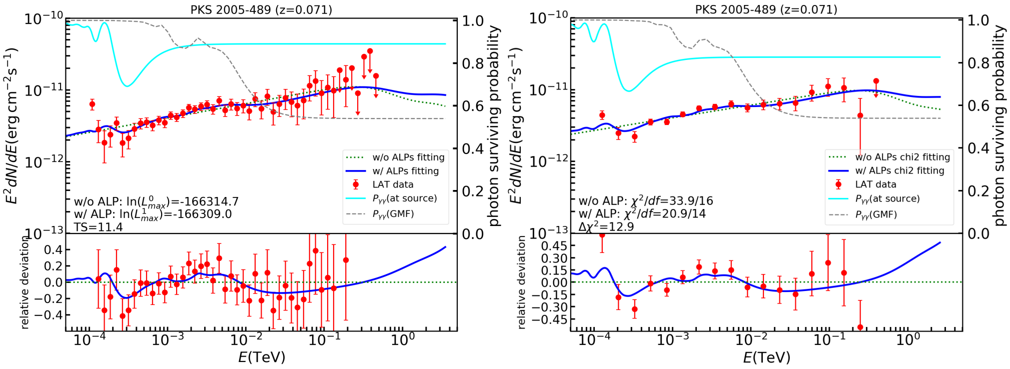

FIGURE B.35: PKS 2005-489, same as Fig. B.19.

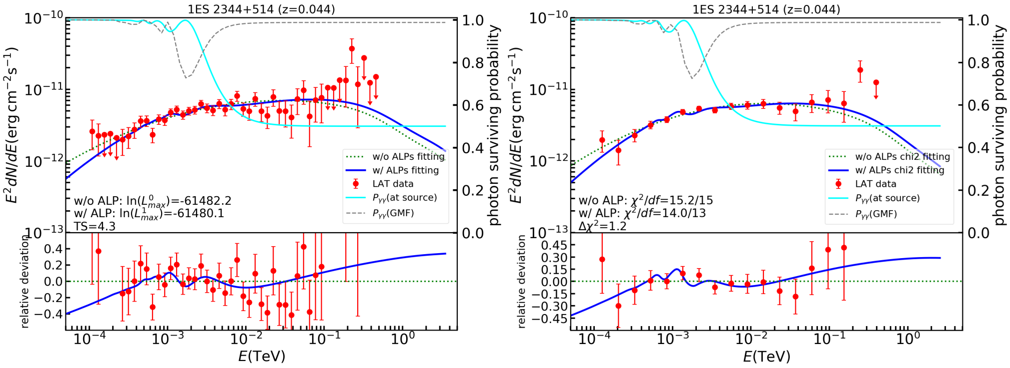

FIGURE B.36: 1ES 2344+514, same as Fig. B.19.

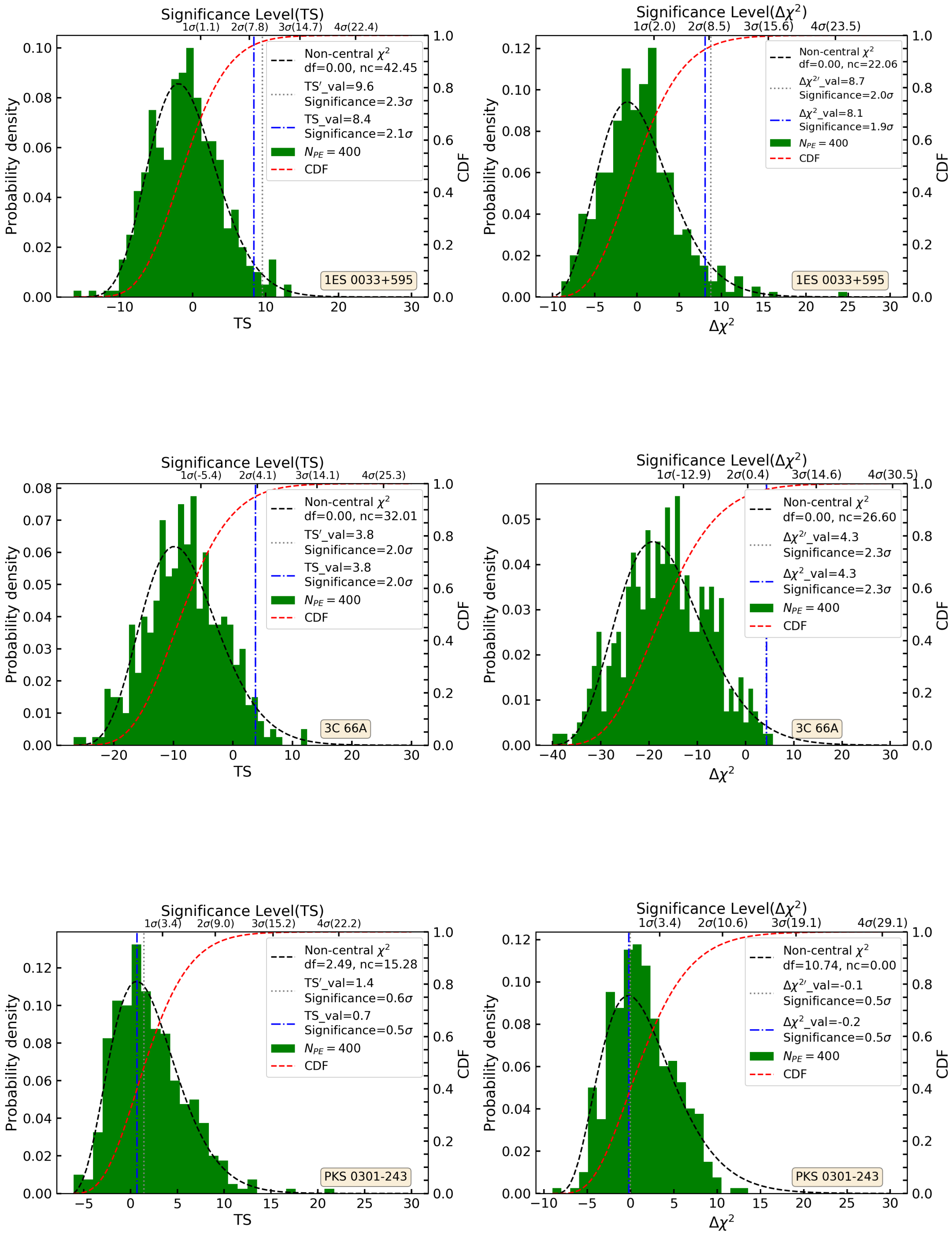

FIGURE B.37: From top to bottom: simulated null distributions for 1ES 0033+595, 3C 66A and PKS 0301-243. Left panels: Simulated null distribution from likelihood ratio test. Right panels: Simulated null distribution from $\Delta\chi^2$ test for the same sources. The black dashed line indicates a fit to the distribution with a non-central χ^2 function. The red solid line represents the resulting cumulative distribution function (CDF). The TS($\Delta\chi^2$) value derived from the local maxima of original data is marked as a blue (dot-dash) vertical line, while the TS($\Delta\chi^2$) value obtained from the global maxima is marked as a gray dotted line (in this case, the blue line coincides with the gray line).

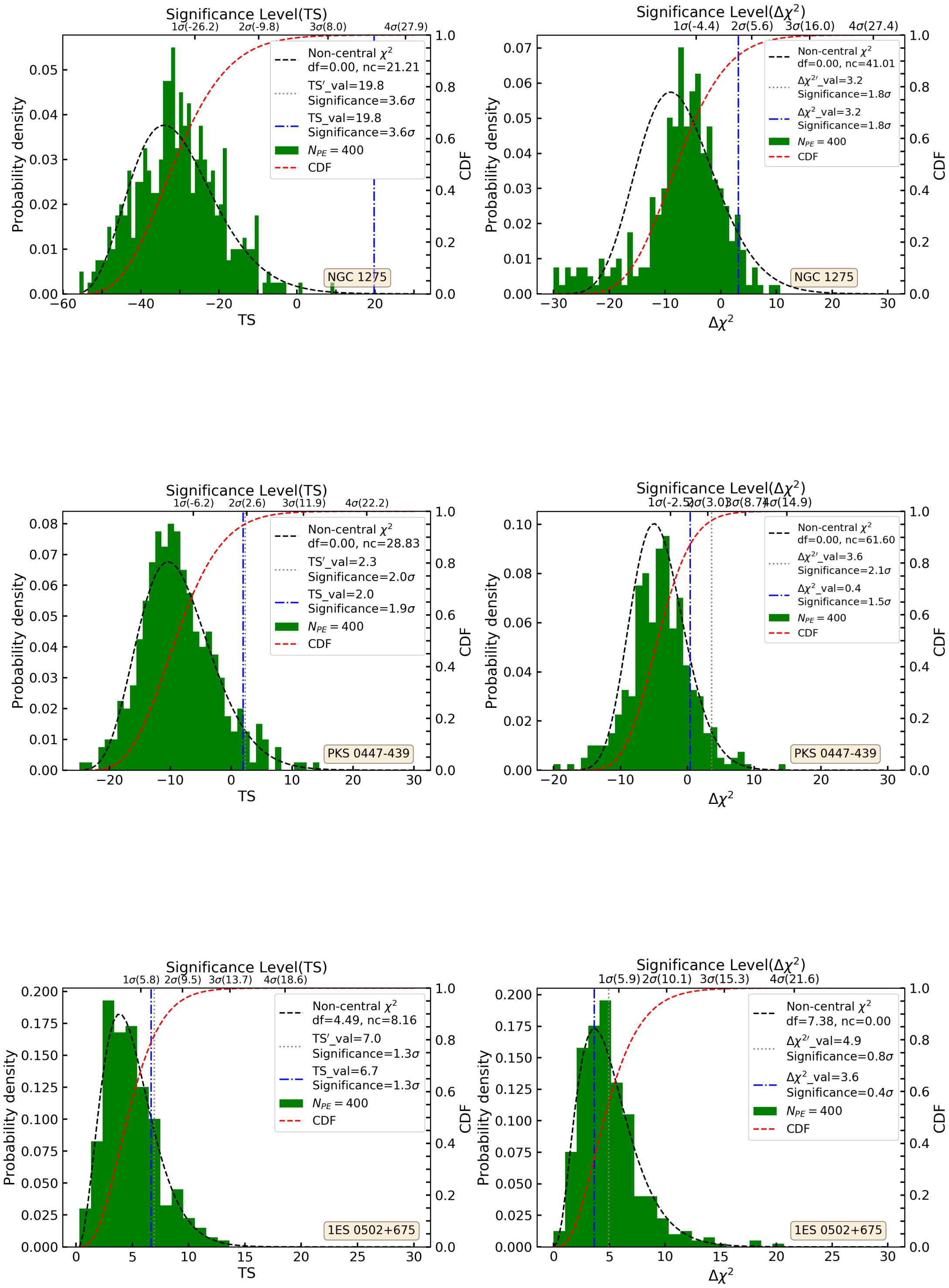

FIGURE B.38: From top to bottom: NGC 1275, PKS 0447-439 and 1ES 0502+675, same as Fig. B.37.

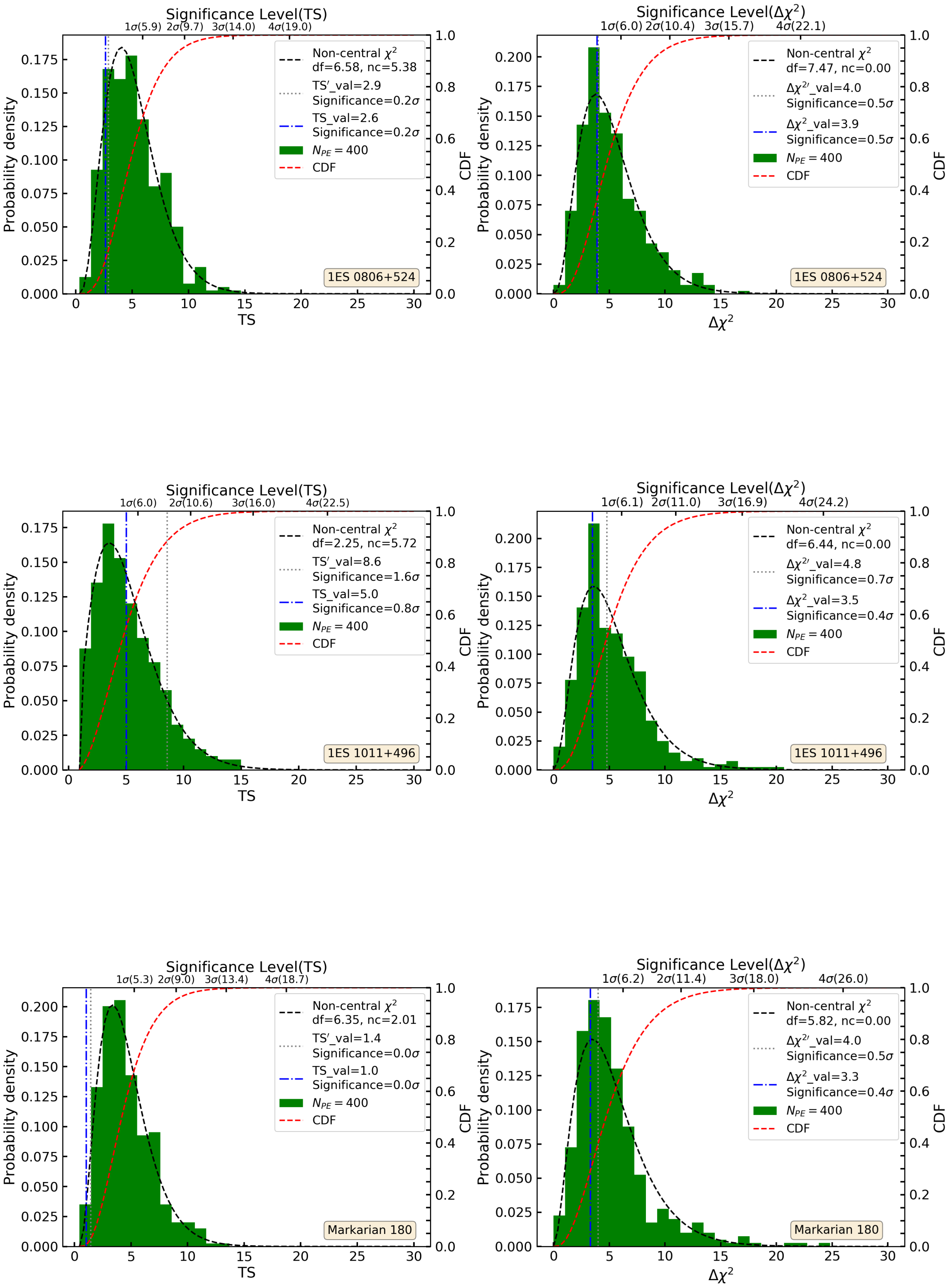

FIGURE B.39: From top to bottom: 1ES 0806+524, 1ES 1011+496 and Markarian 180, same as Fig. B.37.

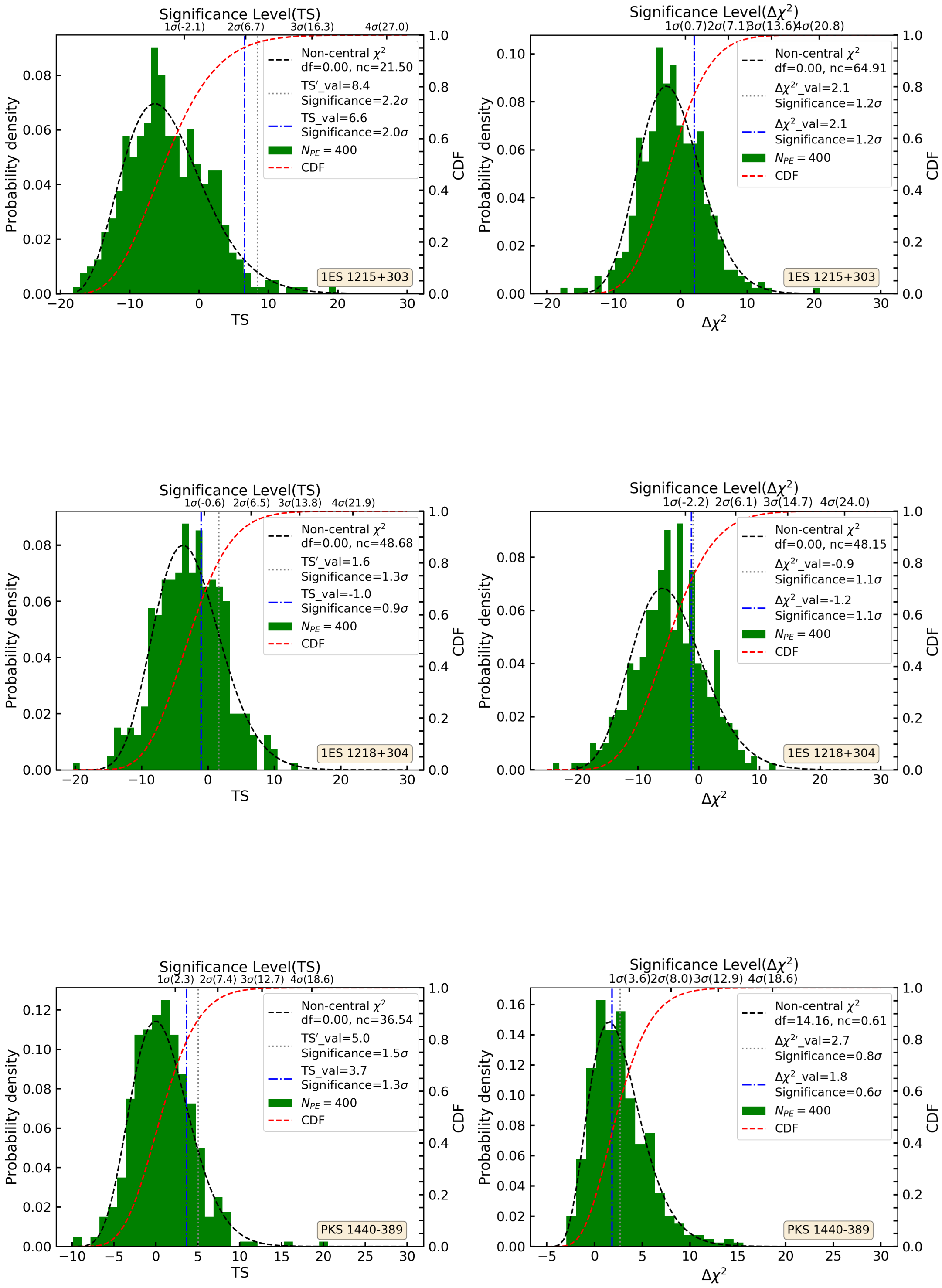

Figure B.40: From top to bottom: 1ES 1215+303, 1ES 1218+304 and PKS 1440-389, same as Fig. B.37.

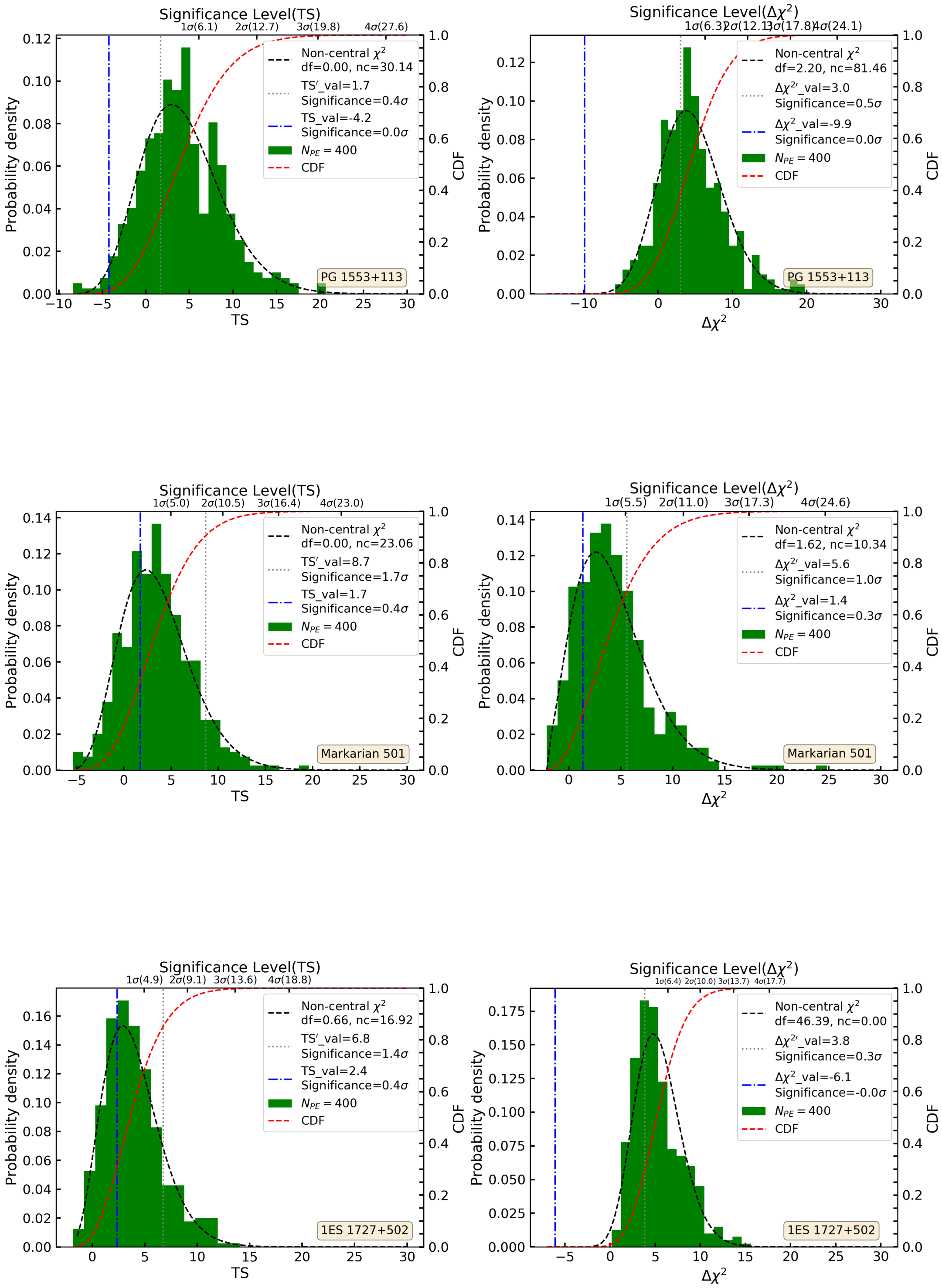

Figure B.41: From top to bottom: PG 1553+113, Markarian 501 and 1ES 1727+502, same as Fig. B.37.

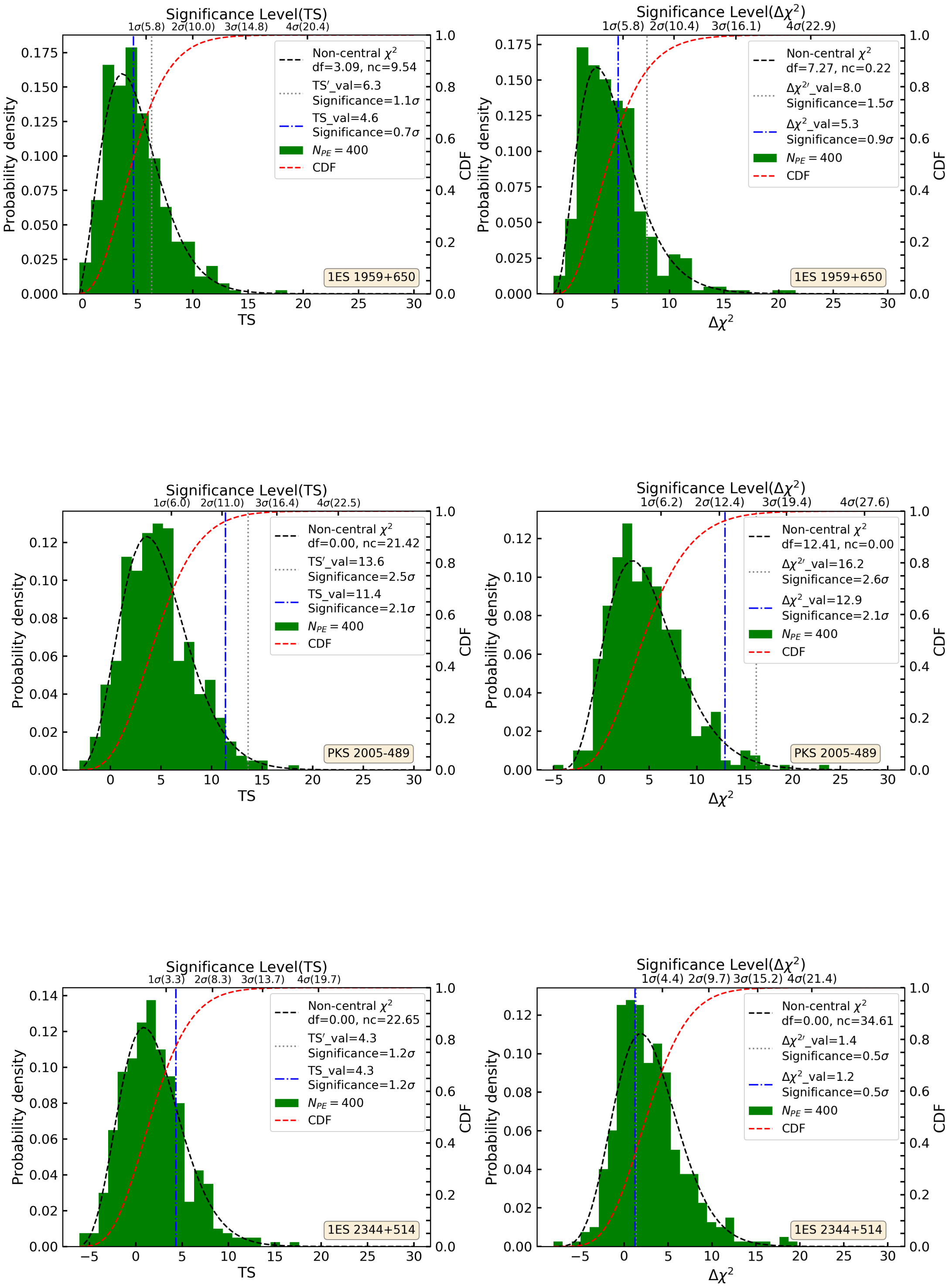

FIGURE B.42: From top to bottom: 1ES 1959+650, PKS 2005-304 and 1ES 2344+514, same as Fig. B.37.

Appendix C

Parameter estimates with Markov Chain Monte Carlo method

The parameter estimates demonstrated in Chapter 4 can be potentially achieved with alternative methods, which, in principle, could improve computing efficiency of the way of locating the best-fitting parameters of (B, s). We present here a method based on the Bayes' Theorem. Our main goal is to probe the source-dependent magnetic environment, we start with the idea of Bayes' Theorem:

$$P(\mathbf{\Theta}_M|\mathbf{D}, M) = \frac{P(\mathbf{D}|\mathbf{\Theta}_M, M)P(\mathbf{\Theta}_M|M)}{P(\mathbf{D}|M)}, \tag{C.1}$$

where M represents the photon-ALP mixing model characterized by a homogeneous field in the source region, and $\mathbf{\Theta}_M = (B, s)$ is the corresponding parameters entailed in model M. $\mathbf{D}$ are the SED points observed by *Fermi*-LAT for an individual source. $P(\mathbf{D}|\mathbf{\Theta}_M, M)$ describes the probability of successfully reconstructing spectral data $\mathbf{D}$ using a specifically chosen set of parameters (B, s) within model M. $P(\mathbf{\Theta}_M|M)$ stands for the probability of having a particular set of (B, s) for the photon-ALP mixing model M before conditioning on observed SED data points $\mathbf{D}$, commonly referred as the prior. $P(\mathbf{\Theta}_M|\mathbf{D}, M)$ is the probability that the underlying parameter is actually $\mathbf{\Theta}_M$ given the observed data D and model M. Thus $P(\mathbf{\Theta}_M|\mathbf{D}, M)$ is normally referred as the posterior. Finally, $P(\mathbf{D}|M)$ is a normalization constant which broadly quantifies how well can the model M describes the observed data D after averaging over all realizations of $\mathbf{\Theta}_M$ values.

The core of this method is the assumption that we have no knowledge about the true magnetic field configuration in source region or its field strength and spatial extension that characterize the SED data points observed by LAT instrument. In this way, the magnetic field model we provide should always be a simplification of what a true field represents. Thus we model the source region field as a large-scale homogeneous field mentioned before. If we assume our model is correct, we can use the posterior probability to make an estimate on parameters (B, s) that we think is an educated predication for the true value of (B, s).

The Markov Chain Monte Carlo (MCMC) method can be used for sampling and thereafter approximating the posterior $P(\mathbf{\Theta}_M|\mathbf{D}, M)$ distribution. We will start by creating a chain of parameter values $\mathbf{\Theta}_M = \{\mathbf{\Theta}_1 \to \mathbf{\Theta}_2 \to \cdots \to \mathbf{\Theta}_n\}$, where $\mathbf{\Theta}_i$ stands for an unique combination values of (B, s), over n iterations such that the number of iterations m_i centered on $\mathbf{\Theta}_i$ is proportional to posterior $P(\mathbf{\Theta}_i|\mathbf{D}, M)$. Therefore, the density of sampling (m_i/n) generated from MCMC at each particular $\mathbf{\Theta}_i$ is approximately the corresponding posterior at $\mathbf{\Theta}_i$.

We will make use of the Metropolis-Hastings (MH) Algorithm for sampling, following closely these steps:

1. We will first choose arbitrary values for our model parameters $\mathbf{\Theta}_i = (B_0, s_0)$. This can be generated from two normal distributions $N(B_0, \sigma^2_{B_0})$ and $N(s_0, \sigma^2_{s_0})$, where σ_{B_0} and σ_{s_0} will be used as the ranges for searching of true $\mathbf{\Theta}_M$. This step can be done using the `scipy` python package.
2. Then, we will decide whether the initially chosen $\mathbf{\Theta}_i$ is the true $\mathbf{\Theta}_M$ by evaluating if a nearby $\mathbf{\Theta}'_{i+1}$ describes the data better.
3. For this, we need to calculate the transition probability defined as

$$p_{\mathbf{\Theta}_i \to \mathbf{\Theta}'_{i+1}} = \frac{P(\mathbf{\Theta}_i|\mathbf{D}, M)}{P(\mathbf{\Theta}'_{i+1}|\mathbf{D}, M)} = \frac{P(\mathbf{D}|\mathbf{\Theta}_i, M)P(\mathbf{\Theta}_i|M)}{P(\mathbf{D}|\mathbf{\Theta}'_{i+1}, M)P(\mathbf{\Theta}'_{i+1}|M)}, \tag{C.2}$$

   where $P(\mathbf{D}|\mathbf{\Theta}_i, M)$ is the likelihood value for a given $\mathbf{\Theta}_i$, which can be calculated directly from performing the likelihood fitting of H_1 to observed data (as done in Ref. [46]). As for the prior, we will assume a normal distribution for simplicity: $N(\mathbf{\Theta}_{\text{prior}}, \sigma_{\mathbf{\Theta}_{\text{prior}}})$. $\mathbf{\Theta}_{\text{prior}}$ and σ_{prior} are our anticipated values for the true $\mathbf{\Theta}$ and its uncertainty. Therefore, $P(\mathbf{\Theta}_i|M) = N(\mathbf{\Theta}_{\text{prior}}, \sigma_{\mathbf{\Theta}_{\text{prior}}}; \mathbf{\Theta}_i)$. $P(\mathbf{D}|\mathbf{\Theta}'_{i+1}, M)$ and $P(\mathbf{\Theta}'_{i+1}|M)$ can be computed in a similar way.
4. We then will compare the value of $p_{\mathbf{\Theta}_i \to \mathbf{\Theta}'_{i+1}}$ to 1. If $p_{\mathbf{\Theta}_i \to \mathbf{\Theta}'_{i+1}} < 1$ and we will accept the jump and set $\mathbf{\Theta}_{i+1} = \mathbf{\Theta}'_{i+1}$. In contrast, if $p_{\mathbf{\Theta}_i \to \mathbf{\Theta}'_{i+1}} > 1$ we will reject the jump of $\mathbf{\Theta}_i \to \mathbf{\Theta}'_{i+1}$ and set $\mathbf{\Theta}_{i+1} = \mathbf{\Theta}_i$.
5. Set $i = i + 1$ and repeat the above steps.

The combination of generating such Markov Chain and the Monte Carlo nature of simulating new positions makes it possible for us to estimate the best approximating parameters of (B, s) for each individual source with the emergence of anomalies. It is very doable and can be achieved with the help of a number of Python-based packages[1].

---

[1] `https://github.com/Gabriel-p/pythonMCMC`

Appendix D

Initial investigation on the ultrahigh energy cosmic-rays from the local Supercluster

The term "local Supercluster" typically refers to the supercluster of galaxies that contains our own Milky Way along with many other galaxies. It is a part of larger-scale cosmic structure of the Universe. The local Supercluster is centered on the Virgo Clusters of galaxies, and therefore, the local supercluster is also named as the Virgo Supercluster, in the outskirts of which we (in the Milky Way, in the Local Group) are situated ($\sim 20\,\mathrm{Mpc}$ away). However, not much is known about the inter-cluster medium.

The AUGER experiment reported a statistically significant correlation between the arrival direction of the highest cosmic-ray ($> 10^{19}\,\mathrm{eV}$) events and nearby AGNs in 2008 [316], and these cosmic-ray events and AGNs are also coarsely aligned with the Super-galactic plane as shown in Fig. D.1. The first puzzle related to this observational result is the propagation of these ultrahigh energy cosmic rays, as they would interact strongly with other particles and background radiation fields, thus suffering significant energy loss and can only travel short distances. Consequently, the flux of the cosmic-rays is expected to be greatly suppressed by the so-called Greisen-Zatsepin-Kuzmin effect [317, 318].

Also, it is interesting to notice that a large fraction of these cosmic-ray events are closely aligned with some of the AGNs, and along with the Super-galactic plane. This provides us with some hints on the possible origin of these cosmic-rays and their acceleration within the local Supercluster. Given the over-density of galaxies in the Supercluster it is possible that the cosmic-rays are accelerated while confined within the local Supercluster environment: energetic cosmic-ray particles would interact with cosmic diffuse

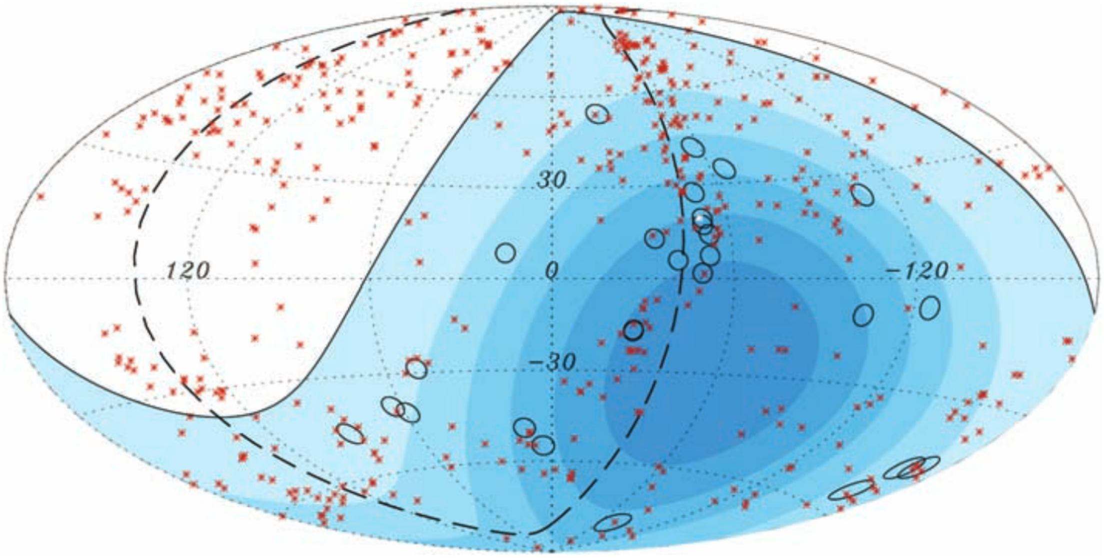

Figure D.1: Skymap of cosmic-rays detected by the AUGER experiment with Hammer-Aitoff projection of the celestial sphere in galactic coordinates. 27 cosmic-ray events with the highest energies are marked with empty circles. 472 AGNs are shown as red asterisks. The solid line gives the border of the field of view of the AUGER observatory, and the colored contours stand for integrated exposure, with darker color indicating higher exposure. Super-galactic plane is marked as the dashed line, and Cen A, as one of the closest AGNs, illustrated as a white dot (figure taken from [316]).

photon fields (such as the CMB, the local large scale cosmic radiation field), leading to secondary particles of pions, electrons, neutrinos and high-energy photons, and furthermore, the electromagnetic cascades via processes, e.g., IC scattering, pair-production. This then results in a high-energy gamma-ray flux from the Super-galactic plane, and more generally, the entire Supercluster region.

If such acceleration mechanism is indeed the cause to give rise of the ultrahigh energy cosmic-rays, we should in principle get hints from observing the high-energy gamma-ray emission from the local Supercluster region. In the first phase of investigation, we make use of the *Fermi*-LAT to survey the whole sky over 14 years within the energy range of 1 GeV to 10 GeV. The lower bound of the analyzed energy is chosen based on the size of the LAT PSF, which has values larger than 1° for energies below 1 GeV (see Fig. 1.10), whereas the upper bound of the analyzed energy is set to be 10 GeV to reduce effects of possible energy dependence of individual source count distribution with its flux (see e.g. [319]). We select photon events within event class of `P8R3_ULTRACLEANVETO`, this is the cleanest Pass 8 data event with a very low level of cosmic-ray contamination (this event class is also recommended by the LAT team for checking cosmic-ray induced systematics). We show the sky map survey with the stated cuts in Fig. D.2, where we outline the most prominent AGN in the Virgo cluster, M 87, with a red solid point, as

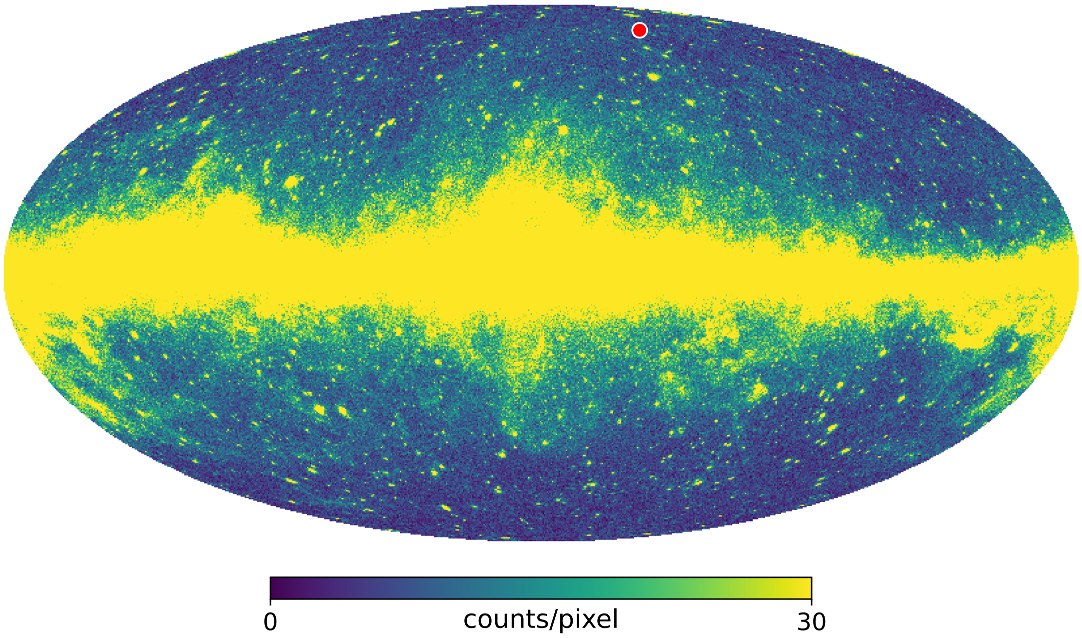

FIGURE D.2: Skymap of gamma-ray photon events observed by *Fermi*-LAT in a Mollweide projection with galactic coordinates. We select events within event class `evclass=1024` (see Chapter 1 and 4 for details of event class), standing for the cleanest event class with the a very low background contamination, and the energy cut applied to select gamma-ray photon events is 1 GeV $<$ E $<$ 10 GeV. The near center of the local Supercluster, M 87, is outlined with a red solid point.

it is close to the center of the Virgo Cluster and therefore, the near center of the local Supercluster.

As we can see from Fig. D.2[1] that it has already provided very rich information about the gamma-ray emission from all over the sky, particularly around the Galactic plane indicated with the brightest color. These gamma-ray emissions are known as the continuum diffuse gamma-ray emission, which is produced within our Galaxy by interactions of high-energy cosmic-rays with interstellar matter and low-energy radiation fields near the Galactic plane.

In order to see more clearly the high-energy photon emission from the local Supercluster, we need to model the foreground Galactic diffuse emission as it extends to about 10° galactic latitude, and therefore, contaminates the emission region of the local Supercluster. Fortunately, such template already exists and is provided by the LAT as a fits file: the `gll_iem_v02_P6_V11_DIFFUSE.fit`[2], as shown in Fig. D.3. This model accounts for the majority of the sources for diffuse emissions, for example, cosmic-ray protons hit

---

[1] The skymap is at a resolution of $N_{side} = 256$, and this applies for all sky maps shown in later context.

[2] The version used here (`https://fermi.gsfc.nasa.gov/ssc/data/p6v11/access/lat/BackgroundModels.html`) is an old version of diffuse model offered by LAT team (issued together with Pass 6 data) as the most recent one `gll_iem_V07.fits` are not suitable for the investigation of medium or large scale diffuse structures within the LAT data.

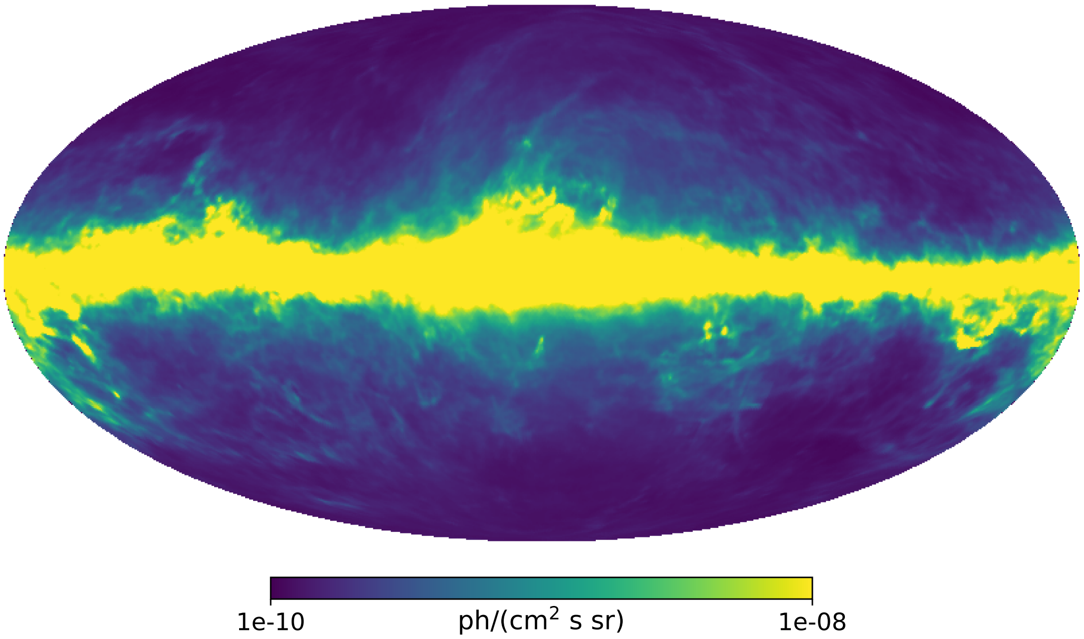

FIGURE D.3: The Mollweide projection of all-sky map of the Galactic diffuse emission with flux integrated in the energy range of 1 GeV to 10 GeV, using the diffuse template `gll_iem_v02_P6_V11_DIFFUSE.fit` provided by LAT team. The color scale indicates the flux of γ-rays per unit of solid angle, in units of photon/(cm^2 s sr).

interstellar gas, giving rise to pions which decay later to gamma-rays ($pp \rightarrow \pi^0 \rightarrow \gamma\gamma$); cosmic-ray electrons IC upscattering starlight or CMB photons, producing high-energy gamma-rays; electrons bremsstrahlung off of ambient gas. The template model is derived from studying the distribution of interstellar gas in Galactocentric rings with the (21 cm) radio spectral line surveys of hydrogen and CO. Diffuse emission of gamma-rays is constructed by fitting the gamma-ray emissivities of the Galactocentric rings in different energy bands to the observational data of LAT.

On the other hand, a weaker diffuse component with extragalactic in origin, observed with almost isotropic distribution all over the sky, is commonly named as the isotropic emission background and has to be subtracted as well. The isotropic emission is also already modeled by the LAT team: `iso_P8R3_ULTRACLEANVETO_V3_v1.txt`[3] as the newest version available and is used here. Isotropic emission is a result of extragalactic diffuse gamma-rays, unresolved extragalactic sources and residual cosmic-ray emission. The template used here is derived from a fit (shown in Fig. D.4) to the all-sky emission excluding $|b| < 10^\circ$ and regions around celestial pole in energy range of 3 MeV $-$ 1 TeV, such that the contamination from Galactic diffuse emission and emission from Earth's limb can be reduced.

---

[3] https://fermi.gsfc.nasa.gov/ssc/data/access/lat/BackgroundModels.html

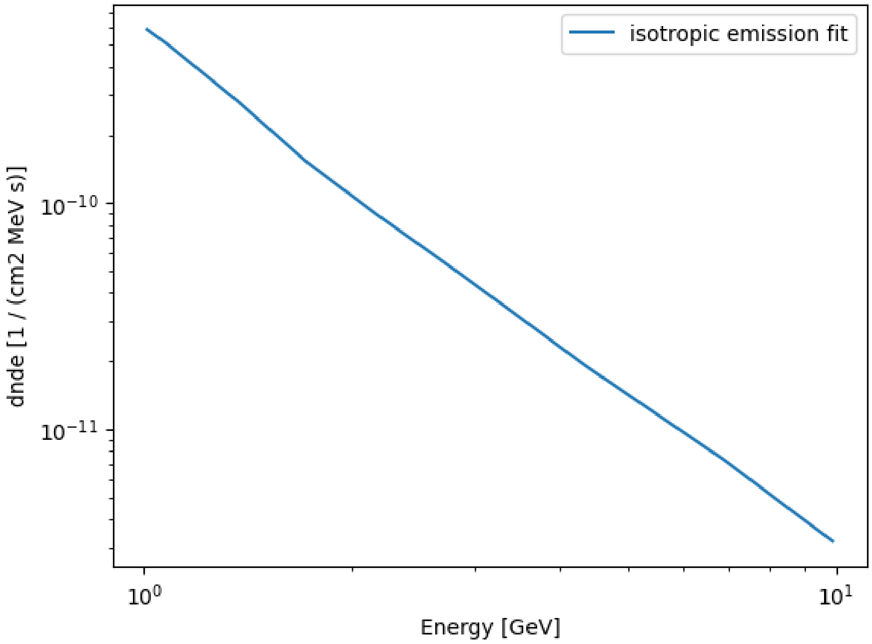

FIGURE D.4: The isotropic emission in energy range of 1 GeV to 10 GeV. Data are taken from the template `iso_P8R3_ULTRACLEANVETO_V3_v1.txt` by LAT.

In order to obtain a residual map of the gamma-ray sky, we need to convert the units of Galactic diffuse and isotropic emission (as shown in Figs. D.3 and D.4) into single photon counts, for which an all-sky exposure map is required. We present in Fig. D.5 the corresponding exposure map measured by LAT in the sky survey conducted for Fig. D.2. Then, we obtain the all-sky count map of isotropic and Galactic diffuse emissions by integrating over spectral bins for each pixel, and simply multiply the corresponding exposure values in each pixel.

Moreover, as seen in Fig. D.2 the gamma-ray sky includes significant contributions from some extremely bright point sources as well, it is then also necessary to model these point sources for later subtraction. We use the *Fermi* 4FGL-DR3 point source catalogue for this purpose, where the specific file can be downloaded together from the *Fermi* science website[4]. In the source catalogue extragalactic point sources are provided with their spectral information, where a specific spectral model for individual source is tested and employed by the LAT team. We take these spectral models for point sources from the catalogue and integrate over spectral energy bins used in diffuse and isotropic emission templates, then mapping to a total photon count per point source with the measured exposure map presented in Fig. D.5. However, the integrated photon flux from these point sources are distributed over certain areas (around sources) of the sky due to PSF of the LAT instrument, i.e., photon count contribution from an individual source is spread over surrounding pixels. A larger PSF smoothing is implied (and will be used)

---

[4] `https://fermi.gsfc.nasa.gov/ssc/data/access/lat/12yr_catalog/`

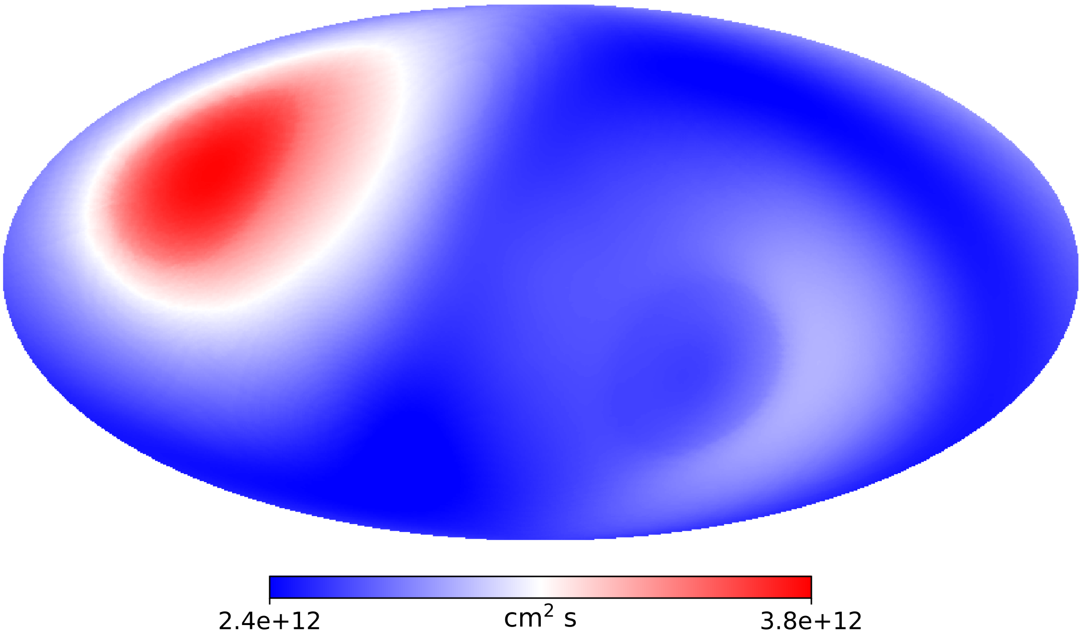

FIGURE D.5: The corresponding exposure map measured by LAT for a 14-year all-sky survey conducted in Fig. D.2, in units of cm^2 s.

in our analysis since a relatively high resolution of $N_{side} = 256$ is employed here for all skymaps. Based on previous works of accounting for this effect [319, 320] and the LAT performance of PSF (see Fig. 1.10), the integrated photon flux is then convolved with an effective averaged PSF width of 1.5° (approximating to an 95% containment radius) over the analyzed energy range for each point source. A "PSF-corrected" count map from point source contribution is shown in Fig. D.6.

Finally, we obtain the residual gamma-ray sky count map by subtracting the Galactic diffuse emission, isotropic emission as well as point source contributions from the survey map (shown in Fig. D.2). Furthermore, we highlight some of the structures and emission regions by smoothing the residual gamma-ray skymap with a Gaussian kernel of 1° for each pixel, at the expense of introducing extra small uncertainties for residual photon counts. The resulted residual sky map after smoothing is presented in Fig. D.7.

The residual sky map shown in Fig. D.7 provides valuable information about unknown diffuse emissions all over the sky, for example, intensive emission from the so-called *Fermi* bubble structures located on both sides of the Galactic plane [321], and more interestingly from the local Supercluster. In order to obtain a better view of the emission region from the local Supercluster, we project the residual skymap in the supergalactic coordinate system, then project again onto a M87-centered offset frame, as shown in Fig. D.8. This way, we have the supergalactic plane displayed as the dotted orange line right at zero latitude of the new offset frame, and M 87 is placed on the supergalactic plane and center of the new projection.

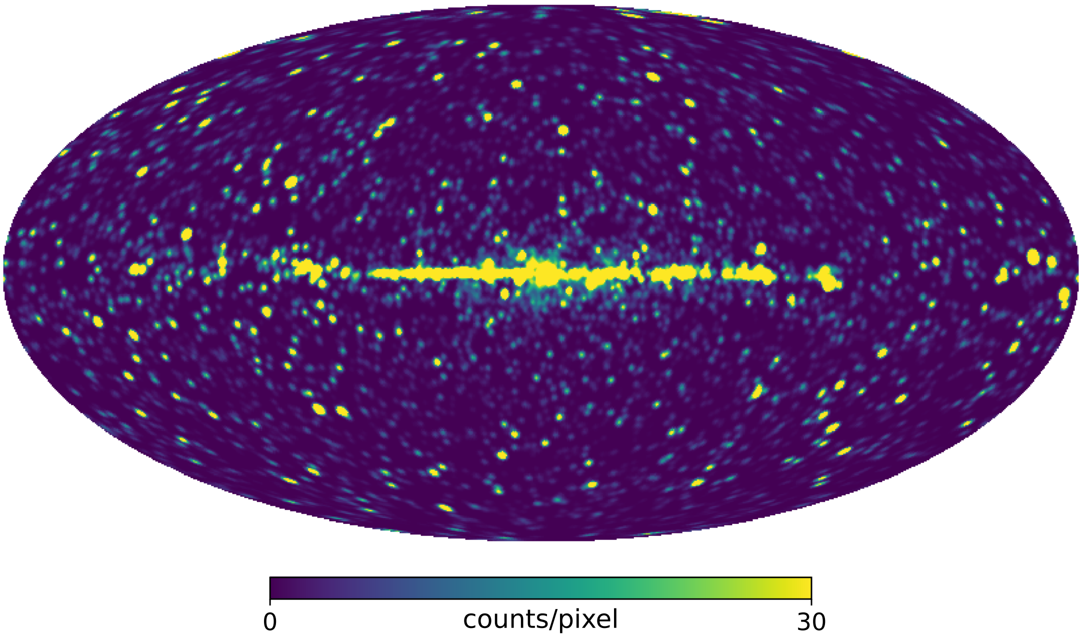

FIGURE D.6: The 4FGL-DR3 point source count map integrated over the energy range 1 GeV − 10 GeV and convolved with exposure and PSF.

As we can see from Fig. D.8 that the high-energy gamma-ray diffuse emission around the Virgo cluster spreads over a very large area, starting on the left from Centaurus A (indicated with the pink circle), centered on the Virgo cluster (the red solid point), and all the way extending to more than 60 degrees of longitude to the right of central emission. This high-energy gamma-ray diffuse emission produced by secondary particles of ultrahigh energy cosmic-rays indeed confirms our suspicion of the origin of the highest energy cosmic-rays from the local Supercluster, but not confidently, as some of the observed cosmic-ray events (as shown in Fig. D.1) are more than 30 Mpc away from the center of the local Supercluster. However, by combining the results shown in Fig. D.8 and Fig. D.1 some strong implications can be obtained: 1) the anisotropic feature of the arrival directions of the ultrahigh-energy cosmic-rays and their extragalactic origin [322]; 2) large fraction of these highest energy cosmic-rays are very likely to originate from the local Supercluster, then accelerated to ultrahigh energies by the over-density of galaxies in the Supercluster.

The over-density of galaxies in the local Supercluster offer the basic requirement to accelerate charged particles: the ability to magnetically confine particles of required energies with relatively small losses of energies. For cosmic-ray particles with energies $E > 10^{19}\,\mathrm{eV}$ and charge Z, observation by AUGER implies an approximating relation for the magnetic environment B and size of the system R via the Hillas condition $(R/\mathrm{pc})(B/\mathrm{G}) \gtrsim (E/10^{20}\,\mathrm{eV})/Z$ [323]. The dense local Supercluster environment is ideal

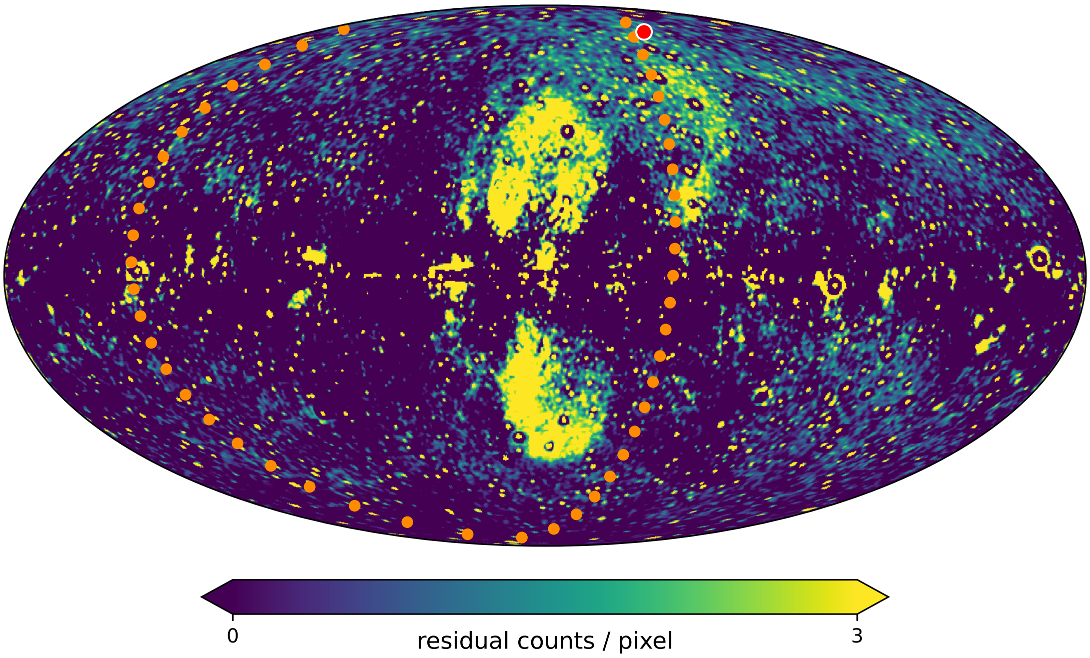

Figure D.7: The residual (smoothed) skymap for a 14-year gamma-ray sky survey with *Fermi*-LAT, where the red solid point outlined the position of M 87, the near center of the local Supercluster. The supergalactic plane is marked with a thick orange dotted line.

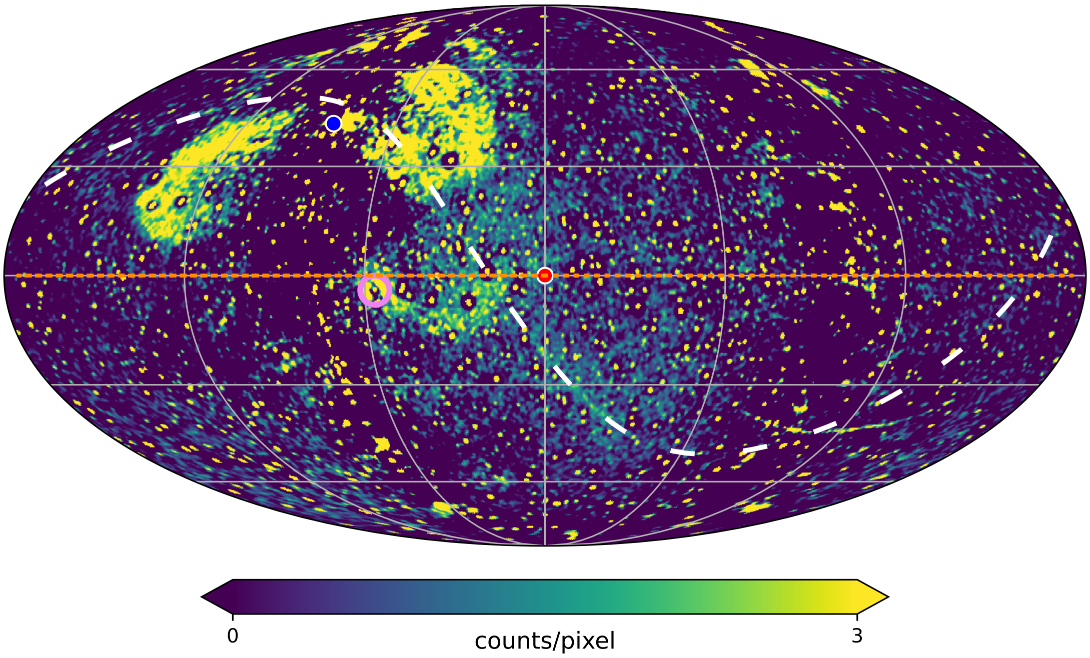

Figure D.8: The residual (smoothed) skymap for a 14-year gamma-ray sky survey with *Fermi*-LAT, projected in an offset frame centered on M 87. The red and blue solid points in the plot stand for the positions of M 87 and Galactic center respectively, while the pink colored circle indicates the position of Centaurus A. The thick white dashed line shows the trail by movement of the Sun, whereas the thin orange dotted line indicates the supergalactic plane.

to meet this requirement (see e.g. [324–326]), as the size of the local Supercluster is estimated to be more than tens of Mpc with a locally enhanced extragalactic magnetic field assumed to be $\gtrsim 10^{-8}\,\mathrm{G}$ [322].

This first-phase investigation on the mystery ultrahigh energy cosmic-ray from the perspective of secondary gamma-ray emissions from the local Supercluster opens a new window for many interesting questions, such as the gamma-ray distribution from propagation of cosmic-rays in the local Supercluster, the energy loss of cosmic-rays and secondary gamma-rays, acceleration mechanisms of cosmic-rays and production of gamma-rays, as well as the composition of observed cosmic-rays for the resulted flux of gamma-rays.

Appendix E

Acronyms

SM	Standard model
HE	High-energy
VHE	Very high energy
AGN	Active galactic nucleus
DM	Dark matter
ALPs	Axion-like particles
SMBH	Supermassive black hole
BLR	broad line region
BL Lac	BL Lacertae
FSRQ	Flat spectrum radio quasar
LAT	Large area telescope
IACT	Imaging air Cherenkov telescope
CAST	CERN Axion Solar Telescope
ALPS	Any Light Particle Search
HESS	High Energy Stereoscopic System
MAGIC	Major Atmospheric Gamma-ray Imaging Cherenkov Telescopes
VERITAS	Very Energetic Radiation Imaging Telescope Array System
EBL	Extragalactic background light
SED	Spectral energy distribution
GMF	Galactic magnetic field
IGMF	Intergalactic magnetic field
ICMF	Intra-cluster magnetic field
JMF	Jet magnetic field
TS	Test statistics
SSC	Synchrotron-self Compton
IC	Inverse Compton
LSW	Light-Shining-through-Walls
MHD	magnetohydrodynamical

List of Figures

List of Tables

Bibliography

[1] Y. Fukuda *et al.*, “Evidence for oscillation of atmospheric neutrinos,” *Phys. Rev. Lett.*, vol. 81, pp. 1562–1567, 1998.

[2] Q. R. Ahmad *et al.*, “Direct evidence for neutrino flavor transformation from neutral current interactions in the Sudbury Neutrino Observatory,” *Phys. Rev. Lett.*, vol. 89, p. 011301, 2002.

[3] T. Mannel, “Theory and phenomenology of cp violation,” *Nuclear Physics B - Proceedings Supplements*, vol. 167, pp. 170–174, 2007. Proceedings of the 7th International Conference on Hyperons, Charm and Beauty Hadrons.

[4] C. Coriano and N. Irges, “Windows over a New Low Energy Axion,” *Phys. Lett. B*, vol. 651, pp. 298–305, 2007.

[5] H. Baer, M. Haider, S. Kraml, S. Sekmen, and H. Summy, “Cosmological consequences of Yukawa-unified SUSY with mixed axion/axino cold and warm dark matter,” *JCAP*, vol. 02, p. 002, 2009.

[6] A. M. Zeitlin, “Conformal Field Theory and Algebraic Structure of Gauge Theory,” *JHEP*, vol. 03, p. 056, 2010.

[7] S. Chang, S. Tazawa, and M. Yamaguchi, “Axion model in extra dimensions with TeV scale gravity,” *Phys. Rev. D*, vol. 61, p. 084005, 2000.

[8] K. R. Dienes, E. Dudas, and T. Gherghetta, “Invisible axions and large radius compactifications,” *Phys. Rev. D*, vol. 62, p. 105023, 2000.

[9] J. Jaeckel and A. Ringwald, “The Low-Energy Frontier of Particle Physics,” *Ann. Rev. Nucl. Part. Sci.*, vol. 60, pp. 405–437, 2010.

[10] R. D. Peccei and H. R. Quinn, “CP Conservation in the Presence of Instantons,” *Phys. Rev. Lett.*, vol. 38, pp. 1440–1443, 1977.

[11] A. Tan *et al.*, “Dark Matter Results from First 98.7 Days of Data from the PandaX-II Experiment,” *Phys. Rev. Lett.*, vol. 117, no. 12, p. 121303, 2016.

[12] E. Aprile *et al.*, “Dark Matter Search Results from a One Ton-Year Exposure of XENON1T,” *Phys. Rev. Lett.*, vol. 121, no. 11, p. 111302, 2018.

[13] G. Aad *et al.*, “Summary of the ATLAS experiment’s sensitivity to supersymmetry after LHC Run 1 — interpreted in the phenomenological MSSM,” *JHEP*, vol. 10, p. 134, 2015.

[14] G. Arcadi, M. Dutra, P. Ghosh, M. Lindner, Y. Mambrini, M. Pierre, S. Profumo, and F. S. Queiroz, “The waning of the WIMP? A review of models, searches, and constraints,” *Eur. Phys. J. C*, vol. 78, no. 3, p. 203, 2018.

[15] M. Goodsell and A. Ringwald, “Light Hidden-Sector U(1)s in String Compactifications,” *Fortsch. Phys.*, vol. 58, pp. 716–720, 2010.

[16] S. Weinberg, “A New Light Boson?,” *Phys. Rev. Lett.*, vol. 40, pp. 223–226, 1978.

[17] A. Ringwald, “Exploring the Role of Axions and Other WISPs in the Dark Universe,” *Phys. Dark Univ.*, vol. 1, pp. 116–135, 2012.

[18] F. Wilczek, “Problem of Strong P and T Invariance in the Presence of Instantons,” *Phys. Rev. Lett.*, vol. 40, pp. 279–282, 1978.

[19] I. Batković, A. De Angelis, M. Doro, and M. Manganaro, “Axion-Like Particle Searches with IACTs,” *Universe*, vol. 7, no. 6, p. 185, 2021. [Erratum: Universe 8, 74 (2022)].

[20] T. W. Donnelly, S. J. Freedman, R. S. Lytel, R. D. Peccei, and M. Schwartz, “Do Axions Exist?,” *Phys. Rev. D*, vol. 18, p. 1607, 1978.

[21] M. Dine, W. Fischler, and M. Srednicki, “A Simple Solution to the Strong CP Problem with a Harmless Axion,” *Phys. Lett. B*, vol. 104, pp. 199–202, 1981.

[22] A. R. Zhitnitsky, “On Possible Suppression of the Axion Hadron Interactions. (In Russian),” *Sov. J. Nucl. Phys.*, vol. 31, p. 260, 1980.

[23] J. E. Kim, “Weak Interaction Singlet and Strong CP Invariance,” *Phys. Rev. Lett.*, vol. 43, p. 103, 1979.

[24] M. A. Shifman, A. I. Vainshtein, and V. I. Zakharov, “Can Confinement Ensure Natural CP Invariance of Strong Interactions?,” *Nucl. Phys. B*, vol. 166, pp. 493–506, 1980.

[25] G. Raffelt and L. Stodolsky, “Mixing of the Photon with Low Mass Particles,” *Phys. Rev. D*, vol. 37, p. 1237, 1988.

[26] A. A. Anselm, “Experimental Test for Arion <—> Photon Oscillations in a Homogeneous Constant Magnetic Field,” *Phys. Rev. D*, vol. 37, p. 2001, 1988.

[27] J. A. Grifols, E. Masso, and R. Toldra, “Gamma-rays from SN1987A due to pseudoscalar conversion,” *Phys. Rev. Lett.*, vol. 77, pp. 2372–2375, 1996.

[28] C. Csaki, N. Kaloper, and J. Terning, “Effects of the intergalactic plasma on supernova dimming via photon axion oscillations,” *Phys. Lett. B*, vol. 535, pp. 33–36, 2002.

[29] M. Simet, D. Hooper, and P. D. Serpico, “The Milky Way as a Kiloparsec-Scale Axionscope,” *Phys. Rev. D*, vol. 77, p. 063001, 2008.

[30] A. Mirizzi and D. Montanino, “Stochastic conversions of TeV photons into axion-like particles in extragalactic magnetic fields,” *JCAP*, vol. 0912, p. 004, 2009.

[31] N. Bassan, A. Mirizzi, and M. Roncadelli, “Axion-like particle effects on the polarization of cosmic high-energy gamma sources,” *JCAP*, vol. 05, p. 010, 2010.

[32] A. De Angelis, G. Galanti, and M. Roncadelli, “Relevance of axion-like particles for very-high-energy astrophysics,” *Phys. Rev. D*, vol. 84, p. 105030, 2011. [Erratum: Phys.Rev.D 87, 109903 (2013)].

[33] D. Horns, L. Maccione, M. Meyer, A. Mirizzi, D. Montanino, and M. Roncadelli, “Hardening of TeV gamma spectrum of AGNs in galaxy clusters by conversions of photons into axion-like particles,” *Phys. Rev. D*, vol. 86, p. 075024, 2012.

[34] D. Horns and M. Meyer, “Indications for a pair-production anomaly from the propagation of VHE gamma-rays,” *JCAP*, vol. 02, p. 033, 2012.

[35] M. Meyer, *The Opacity of the Universe for High and Very High Energy γ-Rays.* PhD thesis, Hamburg U., 2013.

[36] M. Meyer, D. Montanino, and J. Conrad, “On detecting oscillations of gamma rays into axion-like particles in turbulent and coherent magnetic fields,” *JCAP*, vol. 09, p. 003, 2014.

[37] A. Payez, C. Evoli, T. Fischer, M. Giannotti, A. Mirizzi, and A. Ringwald, “Revisiting the SN1987A gamma-ray limit on ultralight axion-like particles,” *JCAP*, vol. 02, p. 006, 2015.

[38] G. Sigl, “Astrophysical Haloscopes,” *Phys. Rev. D*, vol. 96, no. 10, p. 103014, 2017.

[39] V. Anastassopoulos *et al.*, “New CAST Limit on the Axion-Photon Interaction,” *Nature Phys.*, vol. 13, pp. 584–590, 2017.

[40] J. Majumdar, F. Calore, and D. Horns, "Search for gamma-ray spectral modulations in Galactic pulsars," *JCAP*, vol. 04, p. 048, 2018.

[41] G. Galanti, F. Tavecchio, M. Roncadelli, and C. Evoli, "Blazar VHE spectral alterations induced by photon–ALP oscillations," *Mon. Not. Roy. Astron. Soc.*, vol. 487, no. 1, pp. 123–132, 2019.

[42] M. Meyer and T. Petrushevska, "Search for Axionlike-Particle-Induced Prompt γ-Ray Emission from Extragalactic Core-Collapse Supernovae with the *Fermi* Large Area Telescope," *Phys. Rev. Lett.*, vol. 124, no. 23, p. 231101, 2020. [Erratum: Phys.Rev.Lett. 125, 119901 (2020)].

[43] H.-J. Li, J.-G. Guo, X.-J. Bi, S.-J. Lin, and P.-F. Yin, "Limits on axion-like particles from Mrk 421 with 4.5-year period observations by ARGO-YBJ and Fermi-LAT," *Phys. Rev. D*, vol. 103, no. 8, p. 083003, 2021.

[44] G. A. Pallathadka *et al.*, "Reconciling hints on axion-like-particles from high-energy gamma rays with stellar bounds," *JCAP*, vol. 11, p. 036, 2021.

[45] J. H. Matthews, C. S. Reynolds, M. C. D. Marsh, J. Sisk-Reynés, and P. E. Rodman, "How Do Magnetic Field Models Affect Astrophysical Limits on Light Axion-like Particles? An X-Ray Case Study with NGC 1275," *Astrophys. J.*, vol. 930, no. 1, p. 90, 2022.

[46] Q. Yu and D. Horns, "Searching for photon-ALPs mixing effects in AGN gamma-ray energy spectra," *JCAP*, vol. 05, p. 029, 2023.

[47] A. De Angelis, O. Mansutti, and M. Roncadelli, "Axion-Like Particles, Cosmic Magnetic Fields and Gamma-Ray Astrophysics," *Phys. Lett. B*, vol. 659, pp. 847–855, 2008.

[48] W. B. Atwood *et al.*, "The Large Area Telescope on the Fermi Gamma-ray Space Telescope Mission," *Astrophys. J.*, vol. 697, pp. 1071–1102, 2009.

[49] M. Ajello *et al.*, "Search for Spectral Irregularities due to Photon–Axionlike-Particle Oscillations with the Fermi Large Area Telescope," *Phys. Rev. Lett.*, vol. 116, no. 16, p. 161101, 2016.

[50] A. Abramowski *et al.*, "Constraints on axionlike particles with H.E.S.S. from the irregularity of the PKS 2155-304 energy spectrum," *Phys. Rev. D*, vol. 88, no. 10, p. 102003, 2013.

[51] M. Meyer, D. Horns, and M. Raue, "First lower limits on the photon-axion-like particle coupling from very high energy gamma-ray observations," *Phys. Rev. D*, vol. 87, no. 3, p. 035027, 2013.

[52] F. Aharonian *et al.*, "A Low level of extragalactic background light as revealed by gamma-rays from blazars," *Nature*, vol. 440, pp. 1018–1021, 2006.

[53] M. Meyer, M. Raue, D. Mazin, and D. Horns, "Limits on the extragalactic background light in the Fermi era," *Astronomy and Astrophysics*, vol. 542, p. A59, June 2012.

[54] L. Maiani, R. Petronzio, and E. Zavattini, "Effects of Nearly Massless, Spin Zero Particles on Light Propagation in a Magnetic Field," *Phys. Lett. B*, vol. 175, pp. 359–363, 1986.

[55] M. C. D. Marsh, H. R. Russell, A. C. Fabian, B. P. McNamara, P. Nulsen, and C. S. Reynolds, "A New Bound on Axion-Like Particles," *JCAP*, vol. 12, p. 036, 2017.

[56] K. Kohri and H. Kodama, "Axion-Like Particles and Recent Observations of the Cosmic Infrared Background Radiation," *Phys. Rev. D*, vol. 96, no. 5, p. 051701, 2017.

[57] C. Zhang, Y.-F. Liang, S. Li, N.-H. Liao, L. Feng, Q. Yuan, Y.-Z. Fan, and Z.-Z. Ren, "New bounds on axionlike particles from the Fermi Large Area Telescope observation of PKS 2155-304," *Phys. Rev. D*, vol. 97, no. 6, p. 063009, 2018.

[58] C. S. Reynolds, M. C. D. Marsh, H. R. Russell, A. C. Fabian, R. Smith, F. Tombesi, and S. Veilleux, "Astrophysical limits on very light axion-like particles from Chandra grating spectroscopy of NGC 1275," *Astrophys. J.*, vol. 890, p. 59, 2020.

[59] G. Galanti and M. Roncadelli, "Axion-like Particles Implications for High-Energy Astrophysics," *Universe*, vol. 8, no. 5, p. 253, 2022.

[60] R. Bähre *et al.*, "Any light particle search II —Technical Design Report," *JINST*, vol. 8, p. T09001, 2013.

[61] A. Ayala, I. Domínguez, M. Giannotti, A. Mirizzi, and O. Straniero, "Revisiting the bound on axion-photon coupling from Globular Clusters," *Phys. Rev. Lett.*, vol. 113, no. 19, p. 191302, 2014.

[62] A. De Angelis and M. Mallamaci, "Gamma-Ray Astrophysics," *Eur. Phys. J. Plus*, vol. 133, p. 324, 2018.

[63] S. R. Coleman and S. L. Glashow, "High-energy tests of Lorentz invariance," *Phys. Rev. D*, vol. 59, p. 116008, 1999.

[64] U. Jacob and T. Piran, "Inspecting absorption in the spectra of extra-galactic gamma-ray sources for insight on Lorentz invariance violation," *Phys. Rev. D*, vol. 78, p. 124010, 2008.

[65] J. Kormendy and L. C. Ho, “Coevolution (Or Not) of Supermassive Black Holes and Host Galaxies,” *Ann. Rev. Astron. Astrophys.*, vol. 51, pp. 511–653, 2013.

[66] G. G. Madejski and M. Sikora, “Gamma-Ray Observations of Active Galactic Nuclei,” *Ann. Rev. Astron. Astrophys.*, vol. 54, pp. 725–760, 2016.

[67] M. J. Rees, “Black Hole Models for Active Galactic Nuclei,” *Ann. Rev. Astron. Astrophys.*, vol. 22, pp. 471–506, 1984.

[68] P. Padovani *et al.*, “Active galactic nuclei: what’s in a name?,” *Astron. Astrophys. Rev.*, vol. 25, no. 1, p. 2, 2017.

[69] R. M. Wagner, *Measurement of Very High Energy Gamma-Ray Emission from Four Blazars Using the MAGIC Telescope and a Comparative Blazar Study.* PhD thesis, Munich, Tech. U., 2006.

[70] C. M. Urry and P. Padovani, “Unified schemes for radio-loud active galactic nuclei,” *Publ. Astron. Soc. Pac.*, vol. 107, p. 803, 1995.

[71] P. Padovani, “Gamma-ray emitting AGN and unified schemes,” in *32nd Rencontres de Moriond: High-Energy Phenomena in Astrophysics*, pp. 7–16, 1997.

[72] H. Landt, P. Padovani, E. S. Perlman, and P. Giommi, “A Physical classification scheme for blazars,” *Mon. Not. Roy. Astron. Soc.*, vol. 351, p. 83, 2004.

[73] T. Kudoh, S. Aoki, S. Koide, and K. Shibata, “Are blazar jets magnetically driven outflows ?,” *Astronomische Nachrichten*, vol. 320, p. 311, Jan. 1999.

[74] D. L. Meier, S. Koide, and Y. Uchida, “Magnetohydrodynamic Production of Relativistic Jets,” *Science*, vol. 291, pp. 84–92, Jan. 2001.

[75] R. B. Duran, A. Tchekhovskoy, and D. Giannios, “Simulations of AGN jets: magnetic kink instability versus conical shocks,” *Mon. Not. Roy. Astron. Soc.*, vol. 469, no. 4, pp. 4957–4978, 2017.

[76] J.-M. Martí, “Numerical Simulations of Jets from Active Galactic Nuclei,” *Galaxies*, vol. 7, p. 24, Jan. 2019.

[77] F. Huško and C. G. Lacey, “Active galactic nuclei jets simulated with smoothed particle hydrodynamics,” 5 2022.

[78] E. Fermi, “On the Origin of the Cosmic Radiation,” *Phys. Rev.*, vol. 75, pp. 1169–1174, 1949.

[79] E. M. de Gouveia Dal Pino, “Astrophysical jets and outflows,” *Adv. Space Res.*, vol. 35, p. 908, 2005.

[80] E. M. d. Gouveia Dal Pino, P. P. Piovezan, and L. H. S. Kadowaki, "The role of magnetic reconnection on jet/accretion disk systems," *Astron. Astrophys.*, vol. 518, p. A5, 2010.

[81] E. M. de Gouveia Dal Pino, "Probing magnetohydrodynamical scenarios for jet production," *Astronomische Nachrichten*, vol. 327, p. 454, June 2006.

[82] B. Kapanadze, S. Vercellone, and P. Romano, "Stochastic acceleration in the relativistic jets of BL Lacertae objects," *New Astronomy*, vol. 79, p. 101393, Aug. 2020.

[83] B. Kapanadze, "The First- and Second-Order Fermi Acceleration Processes in BL Lacertae Objects," *Galaxies*, vol. 6, no. 4, p. 125, 2018.

[84] J. P. v. d. Berg, M. Boettcher, A. Dominguez, and M. Lopez-Moya, "Systematic Physical Characterization of the Gamma-Ray Spectra of 2FHL Blazars," *Astrophys. J.*, vol. 874, p. 47, 2019.

[85] M. Bottcher, D. E. Harris, and H. Krawczynski, eds., *Relativistic jets from active galactic nuclei.* 2012.

[86] L. Ballo *et al.*, "Spectral energy distributions of 3c 279 revisited: bepposax observations and variability models," *Astrophys. J.*, vol. 567, p. 50, 2002.

[87] G. Fossati, L. Maraschi, A. Celotti, A. Comastri, and G. Ghisellini, "A Unifying view of the spectral energy distributions of blazars," *Mon. Not. Roy. Astron. Soc.*, vol. 299, pp. 433–448, 1998.

[88] K. Mannheim, P. L. Biermann, and W. M. Kruells, "A novel mechanism for non-thermal X-ray emission," *Astron. Astrophys.*, vol. 251, pp. 723–731, Nov. 1991.

[89] F. A. Aharonian, "Proton synchrotron radiation of large-scale jets in active galactic nuclei," *Mon. Not. Roy. Astron. Soc.*, vol. 332, p. 215, 2002.

[90] A. Mucke and R. J. Protheroe, "A Proton synchrotron blazar model for flaring in Markarian 501," *Astropart. Phys.*, vol. 15, pp. 121–136, 2001.

[91] A. Muecke, R. J. Protheroe, R. Engel, J. P. Rachen, and T. Stanev, "BL Lac Objects in the synchrotron proton blazar model," *Astropart. Phys.*, vol. 18, pp. 593–613, 2003.

[92] M. Pohl and R. Schlickeiser, "On the conversion of blast wave energy into radiation in AGNs and GRBs," *Astron. Astrophys.*, vol. 354, p. 395, 2000.

[93] K. Mannheim, “Possible production of high-energy gamma-rays from proton acceleration in the extragalactic radio source Markarian 501,” *Science*, vol. 279, p. 684, 1998.

[94] M. Cerruti, A. Zech, C. Boisson, and S. Inoue, “A hadronic origin for ultra-high-frequency-peaked BL Lac objects,” *Mon. Not. Roy. Astron. Soc.*, vol. 448, no. 1, pp. 910–927, 2015.

[95] M. Ackermann *et al.*, “Detection of the Characteristic Pion-Decay Signature in Supernova Remnants,” *Science*, vol. 339, p. 807, 2013.

[96] G. E. Romero, D. F. Torres, M. M. K. Bernado, and I. F. Mirabel, “Hadronic gamma-ray emission from windy microquasars,” *Astron. Astrophys.*, vol. 410, pp. L1–L4, 2003.

[97] M. Boettcher, A. Reimer, K. Sweeney, and A. Prakash, “Leptonic and Hadronic Modeling of Fermi-Detected Blazars,” *Astrophys. J.*, vol. 768, p. 54, 2013.

[98] F. Massaro, D. J. Thompson, and E. C. Ferrara, “The extragalactic gamma-ray sky in the Fermi era,” *Astron. Astrophys. Rev.*, vol. 24, no. 1, p. 2, 2016.

[99] D. J. Thompson *et al.*, “Calibration of the Energetic Gamma-Ray Experiment Telescope (EGRET) for the Compton Gamma-Ray Observatory,” *Astrophys. J. Suppl.*, vol. 86, pp. 629–656, 1993.

[100] R. C. Hartman *et al.*, “The Third EGRET catalog of high-energy gamma-ray sources,” *Astrophys. J. Suppl.*, vol. 123, p. 79, 1999.

[101] A. A. Abdo *et al.*, “Fermi Large Area Telescope First Source Catalog,” *Astrophys. J. Suppl.*, vol. 188, pp. 405–436, 2010.

[102] P. F. Michelson, W. B. Atwood, and S. Ritz, “Fermi gamma-ray space telescope: High-energy results from the first year,” *Rept. Prog. Phys.*, vol. 73, p. 074901, 2010.

[103] A. A. Abdo *et al.*, “The Spectrum of the Isotropic Diffuse Gamma-Ray Emission Derived From First-Year Fermi Large Area Telescope Data,” *Phys. Rev. Lett.*, vol. 104, p. 101101, 2010.

[104] M. Ajello *et al.*, “Fermi Large Area Telescope Performance after 10 Years of Operation,” *Astrophys. J. Supp.*, vol. 256, no. 1, p. 12, 2021.

[105] A. A. Abdo *et al.*, “Fermi Large Area Telescope Bright Gamma-ray Source List,” *Astrophys. J. Suppl.*, vol. 183, pp. 46–66, 2009.

[106] "Fermi Large Area Telescope Second Source Catalog," *Astrophys. J. Suppl.*, vol. 199, p. 31, 2012.

[107] F. Acero *et al.*, "Fermi Large Area Telescope Third Source Catalog," *Astrophys. J. Suppl.*, vol. 218, no. 2, p. 23, 2015.

[108] S. Abdollahi *et al.*, "*Fermi* Large Area Telescope Fourth Source Catalog," *Astrophys. J. Suppl.*, vol. 247, no. 1, p. 33, 2020.

[109] J. Ballet, T. H. Burnett, S. W. Digel, and B. Lott, "Fermi Large Area Telescope Fourth Source Catalog Data Release 2," 5 2020.

[110] S. Abdollahi *et al.*, "Incremental Fermi Large Area Telescope Fourth Source Catalog," *Astrophys. J. Supp.*, vol. 260, no. 2, p. 53, 2022.

[111] M. Ajello *et al.*, "The Fourth Catalog of Active Galactic Nuclei Detected by the Fermi Large Area Telescope," *Astrophys. J.*, vol. 892, p. 105, 2020.

[112] A. M. Hillas, "Evolution of ground-based gamma-ray astronomy from the early days to the Cherenkov Telescope Arrays," *Astropart. Phys.*, vol. 43, pp. 19–43, 2013.

[113] T. C. Weekes *et al.*, "Observation of TeV gamma rays from the Crab nebula using the atmospheric Cerenkov imaging technique," *Astrophys. J.*, vol. 342, pp. 379–395, 1989.

[114] J. A. Hinton, "The Status of the H.E.S.S. project," *New Astron. Rev.*, vol. 48, pp. 331–337, 2004.

[115] E. Lorenz and MAGIC Collaboration, "Status of the 17 m diameter Magic telescope," in *International Cosmic Ray Conference*, vol. 7 of *International Cosmic Ray Conference*, p. 2789, Aug. 2001.

[116] T. C. Weekes, H. Badran, S. D. Biller, I. Bond, S. Bradbury, J. Buckley, D. Carter-Lewis, M. Catanese, S. Criswell, W. Cui, P. Dowkontt, C. Duke, D. J. Fegan, J. Finley, L. Fortson, J. Gaidos, G. H. Gillanders, J. Grindlay, T. A. Hall, K. Harris, A. M. Hillas, P. Kaaret, M. Kertzman, D. Kieda, F. Krennrich, M. J. Lang, S. LeBohec, R. Lessard, J. Lloyd-Evans, J. Knapp, B. McKernan, J. McEnery, P. Moriarty, D. Muller, P. Ogden, R. Ong, D. Petry, J. Quinn, N. W. Reay, P. T. Reynolds, J. Rose, M. Salamon, G. Sembroski, R. Sidwell, P. Slane, N. Stanton, S. P. Swordy, V. V. Vassiliev, and S. P. Wakely, "VERITAS: the Very Energetic Radiation Imaging Telescope Array System," *Astroparticle Physics*, vol. 17, pp. 221–243, May 2002.

[117] D. Bose, V. R. Chitnis, P. Majumdar, and B. S. Acharya, "Ground-based gamma-ray astronomy: history and development of techniques," *Eur. Phys. J. ST*, vol. 231, no. 1, pp. 3–26, 2022.

[118] H. Anderhub *et al.*, "Design and Operation of FACT – The First G-APD Cherenkov Telescope," *JINST*, vol. 8, p. P06008, 2013.

[119] B. S. Acharya *et al.*, *Science with the Cherenkov Telescope Array.* WSP, 11 2018.

[120] M. Tavani *et al.*, "Science with e-ASTROGAM: A space mission for MeV–GeV gamma-ray astrophysics," *JHEAp*, vol. 19, pp. 1–106, 2018.

[121] R. J. Gould and G. P. Schreder, "Opacity of the Universe to High-Energy Photons," *Phys. Rev.*, vol. 155, pp. 1408–1411, 1967.

[122] A. A. Zdziarski and R. Svensson, "Propagation of gamma-rays at cosmological redshifts," *Nucl. Phys. B Proc. Suppl.*, vol. 10, pp. 81–88, 1989.

[123] J. Biteau and M. Meyer, "Gamma-Ray Cosmology and Tests of Fundamental Physics," *Galaxies*, vol. 10, no. 2, p. 39, 2022.

[124] J. R. Primack, A. Dominguez, R. C. Gilmore, and R. S. Somerville, "Extragalactic Background Light and Gamma-Ray Attenuation," *AIP Conf. Proc.*, vol. 1381, no. 1, pp. 72–83, 2011.

[125] J. V. Jelley, "Absorption of High-energy Gamma-rays within Quasars and other Radio Sources," *Nature*, vol. 211, pp. 472–475, July 1966.

[126] F. Aharonian, D. Khangulyan, and L. Costamante, "Formation of hard VHE gamma-ray spectra of blazars due to internal photon-photon absorption," *Mon. Not. Roy. Astron. Soc.*, vol. 387, pp. 1206–1214, 2008.

[127] C. Abel *et al.*, "Measurement of the Permanent Electric Dipole Moment of the Neutron," *Phys. Rev. Lett.*, vol. 124, no. 8, p. 081803, 2020.

[128] H.-Y. Cheng, "The Strong CP Problem Revisited," *Phys. Rept.*, vol. 158, p. 1, 1988.

[129] R. L. Workman *et al.*, "Review of Particle Physics," *PTEP*, vol. 2022, p. 083C01, 2022.

[130] S. L. Cheng, C. Q. Geng, and W. T. Ni, "Axion - photon couplings in invisible axion models," *Phys. Rev. D*, vol. 52, pp. 3132–3135, 1995.

[131] D. Espriu, F. Mescia, and A. Renau, "Axion-Higgs interplay in the two Higgs-doublet model," *Phys. Rev. D*, vol. 92, no. 9, p. 095013, 2015.

[132] P. Sikivie, "Experimental Tests of the Invisible Axion," *Phys. Rev. Lett.*, vol. 51, pp. 1415–1417, 1983. [Erratum: Phys.Rev.Lett. 52, 695 (1984)].

[133] A. V. Sokolov and A. Ringwald, "Electromagnetic Couplings of Axions," 5 2022.

[134] Y. K. Semertzidis and S. Youn, "Axion dark matter: How to see it?," *Sci. Adv.*, vol. 8, no. 8, p. abm9928, 2022.

[135] N. Turok, "Almost Goldstone bosons from extra dimensional gauge theories," *Phys. Rev. Lett.*, vol. 76, pp. 1015–1018, 1996.

[136] P. Svrcek and E. Witten, "Axions In String Theory," *JHEP*, vol. 06, p. 051, 2006.

[137] A. Ringwald, "From Axions to Other WISPs," in *4th Patras Workshop on Axions, WIMPs and WISPs*, pp. 17–20, 10 2008.

[138] A. Arvanitaki, S. Dimopoulos, S. Dubovsky, N. Kaloper, and J. March-Russell, "String Axiverse," *Phys. Rev. D*, vol. 81, p. 123530, 2010.

[139] G. Galanti, "Photon-ALP interaction as a measure of initial photon polarization," *Phys. Rev. D*, vol. 105, no. 8, p. 083022, 2022.

[140] N. Du *et al.*, "A Search for Invisible Axion Dark Matter with the Axion Dark Matter Experiment," *Phys. Rev. Lett.*, vol. 120, no. 15, p. 151301, 2018.

[141] K. M. Backes *et al.*, "A quantum-enhanced search for dark matter axions," *Nature*, vol. 590, no. 7845, pp. 238–242, 2021.

[142] B. M. Brubaker *et al.*, "First results from a microwave cavity axion search at 24 μeV," *Phys. Rev. Lett.*, vol. 118, no. 6, p. 061302, 2017.

[143] B. T. McAllister, G. Flower, J. Kruger, E. N. Ivanov, M. Goryachev, J. Bourhill, and M. E. Tobar, "The ORGAN Experiment: An axion haloscope above 15 GHz," *Phys. Dark Univ.*, vol. 18, pp. 67–72, 2017.

[144] R. Barbieri, C. Braggio, G. Carugno, C. S. Gallo, A. Lombardi, A. Ortolan, R. Pengo, G. Ruoso, and C. C. Speake, "Searching for galactic axions through magnetized media: the QUAX proposal," *Phys. Dark Univ.*, vol. 15, pp. 135–141, 2017.

[145] P. Brun *et al.*, "A new experimental approach to probe QCD axion dark matter in the mass range above 40 μeV," *Eur. Phys. J. C*, vol. 79, no. 3, p. 186, 2019.

[146] Y. K. Semertzidis *et al.*, "Axion Dark Matter Research with IBS/CAPP," 10 2019.

[147] O. Kwon *et al.*, "First Results from an Axion Haloscope at CAPP around 10.7 μeV," *Phys. Rev. Lett.*, vol. 126, no. 19, p. 191802, 2021.

[148] S. De Panfilis, A. C. Melissinos, B. E. Moskowitz, J. T. Rogers, Y. K. Semertzidis, W. Wuensch, H. J. Halama, A. G. Prodell, W. B. Fowler, and F. A. Nezrick, “Limits on the Abundance and Coupling of Cosmic Axions at 4.5-Microev $<$ m(a) $<$ 5.0-Microev,” *Phys. Rev. Lett.*, vol. 59, p. 839, 1987.

[149] W. Wuensch, S. De Panfilis-Wuensch, Y. K. Semertzidis, J. T. Rogers, A. C. Melissinos, H. J. Halama, B. E. Moskowitz, A. G. Prodell, W. B. Fowler, and F. A. Nezrick, “Results of a Laboratory Search for Cosmic Axions and Other Weakly Coupled Light Particles,” *Phys. Rev. D*, vol. 40, p. 3153, 1989.

[150] C. Hagmann, P. Sikivie, N. S. Sullivan, and D. B. Tanner, “Results from a search for cosmic axions,” *Phys. Rev. D*, vol. 42, pp. 1297–1300, Aug 1990.

[151] C. Bartram *et al.*, “Search for Invisible Axion Dark Matter in the 3.3–4.2 μeV Mass Range,” *Phys. Rev. Lett.*, vol. 127, no. 26, p. 261803, 2021.

[152] S. J. Asztalos *et al.*, “An Improved RF cavity search for halo axions,” *Phys. Rev. D*, vol. 69, p. 011101, 2004.

[153] T. Braine *et al.*, “Extended Search for the Invisible Axion with the Axion Dark Matter Experiment,” *Phys. Rev. Lett.*, vol. 124, no. 10, p. 101303, 2020.

[154] C. Bartram *et al.*, “Axion dark matter experiment: Run 1B analysis details,” *Phys. Rev. D*, vol. 103, no. 3, p. 032002, 2021.

[155] C. Boutan *et al.*, “Piezoelectrically Tuned Multimode Cavity Search for Axion Dark Matter,” *Phys. Rev. Lett.*, vol. 121, no. 26, p. 261302, 2018.

[156] L. Zhong *et al.*, “Results from phase 1 of the HAYSTAC microwave cavity axion experiment,” *Phys. Rev. D*, vol. 97, no. 9, p. 092001, 2018.

[157] D. Alesini *et al.*, “Galactic axions search with a superconducting resonant cavity,” *Phys. Rev. D*, vol. 99, no. 10, p. 101101, 2019.

[158] D. Alesini *et al.*, “Search for invisible axion dark matter of mass $\mathrm{m}_a = 43$ μeV with the QUAX–$a\gamma$ experiment,” *Phys. Rev. D*, vol. 103, no. 10, p. 102004, 2021.

[159] B. Yang, H. Yoon, M. Ahn, Y. Lee, and J. Yoo, “Extended Axion Dark Matter Search Using the CAPP18T Haloscope,” *Phys. Rev. Lett.*, vol. 131, no. 8, p. 081801, 2023.

[160] A. K. Yi *et al.*, “Axion Dark Matter Search around 4.55 μeV with Dine-Fischler-Srednicki-Zhitnitskii Sensitivity,” *Phys. Rev. Lett.*, vol. 130, no. 7, p. 071002, 2023.

[161] J. Jeong, S. Youn, S. Bae, J. Kim, T. Seong, J. E. Kim, and Y. K. Semertzidis, "Search for Invisible Axion Dark Matter with a Multiple-Cell Haloscope," *Phys. Rev. Lett.*, vol. 125, no. 22, p. 221302, 2020.

[162] D. Horns, J. Jaeckel, A. Lindner, A. Lobanov, J. Redondo, and A. Ringwald, "Searching for WISPy Cold Dark Matter with a Dish Antenna," *JCAP*, vol. 04, p. 016, 2013.

[163] F. Bajjali *et al.*, "First results from BRASS-p broadband searches for hidden photon dark matter," *JCAP*, vol. 08, p. 077, 2023.

[164] E. Armengaud *et al.*, "Conceptual Design of the International Axion Observatory (IAXO)," *JINST*, vol. 9, p. T05002, 2014.

[165] E. Armengaud *et al.*, "Physics potential of the International Axion Observatory (IAXO)," *JCAP*, vol. 06, p. 047, 2019.

[166] A. Abeln *et al.*, "Conceptual design of BabyIAXO, the intermediate stage towards the International Axion Observatory," *JHEP*, vol. 05, p. 137, 2021.

[167] A. A. Anselm, "Arion $\leftrightarrow$ Photon Oscillations in a Steady Magnetic Field. (In Russian)," *Yad. Fiz.*, vol. 42, pp. 1480–1483, 1985.

[168] K. Van Bibber, N. R. Dagdeviren, S. E. Koonin, A. Kerman, and H. N. Nelson, "Proposed experiment to produce and detect light pseudoscalars," *Phys. Rev. Lett.*, vol. 59, pp. 759–762, 1987.

[169] K. Ehret *et al.*, "New ALPS Results on Hidden-Sector Lightweights," *Phys. Lett. B*, vol. 689, pp. 149–155, 2010.

[170] R. Ballou *et al.*, "New exclusion limits on scalar and pseudoscalar axionlike particles from light shining through a wall," *Phys. Rev. D*, vol. 92, no. 9, p. 092002, 2015.

[171] J. W. Brockway, E. D. Carlson, and G. G. Raffelt, "SN1987A gamma-ray limits on the conversion of pseudoscalars," *Phys. Lett. B*, vol. 383, pp. 439–443, 1996.

[172] S. Hoof and L. Schulz, "Updated constraints on axion-like particles from temporal information in supernova SN1987A gamma-ray data," *JCAP*, vol. 03, p. 054, 2023.

[173] F. Calore, P. Carenza, M. Giannotti, J. Jaeckel, and A. Mirizzi, "Bounds on axionlike particles from the diffuse supernova flux," *Phys. Rev. D*, vol. 102, no. 12, p. 123005, 2020.

[174] F. Calore, P. Carenza, C. Eckner, T. Fischer, M. Giannotti, J. Jaeckel, K. Kotake, T. Kuroda, A. Mirizzi, and F. Sivo, "3D template-based Fermi-LAT constraints on the diffuse supernova axion-like particle background," *Phys. Rev. D*, vol. 105, no. 6, p. 063028, 2022.

[175] M. Xiao, K. M. Perez, M. Giannotti, O. Straniero, A. Mirizzi, B. W. Grefenstette, B. M. Roach, and M. Nynka, "Constraints on Axionlike Particles from a Hard X-Ray Observation of Betelgeuse," *Phys. Rev. Lett.*, vol. 126, no. 3, p. 031101, 2021.

[176] C. Dessert, J. W. Foster, and B. R. Safdi, "X-ray Searches for Axions from Super Star Clusters," *Phys. Rev. Lett.*, vol. 125, no. 26, p. 261102, 2020.

[177] C. Dessert, A. J. Long, and B. R. Safdi, "No Evidence for Axions from Chandra Observation of the Magnetic White Dwarf RE J0317-853," *Phys. Rev. Lett.*, vol. 128, no. 7, p. 071102, 2022.

[178] D. Noordhuis, A. Prabhu, S. J. Witte, A. Y. Chen, F. Cruz, and C. Weniger, "Novel Constraints on Axions Produced in Pulsar Polar-Cap Cascades," 9 2022.

[179] C. Dessert, D. Dunsky, and B. R. Safdi, "Upper limit on the axion-photon coupling from magnetic white dwarf polarization," *Phys. Rev. D*, vol. 105, no. 10, p. 103034, 2022.

[180] H.-J. Li, X.-J. Bi, and P.-F. Yin, "Searching for axion-like particles with the blazar observations of MAGIC and Fermi-LAT *," *Chin. Phys. C*, vol. 46, no. 8, p. 085105, 2022.

[181] J. Davies, M. Meyer, and G. Cotter, "Constraints on axionlike particles from a combined analysis of three flaring Fermi flat-spectrum radio quasars," *Phys. Rev. D*, vol. 107, no. 8, p. 083027, 2023.

[182] D. Wouters and P. Brun, "Constraints on Axion-like Particles from X-Ray Observations of the Hydra Galaxy Cluster," *Astrophys. J.*, vol. 772, p. 44, 2013.

[183] J. S. Reynés, J. H. Matthews, C. S. Reynolds, H. R. Russell, R. N. Smith, and M. C. D. Marsh, "New constraints on light axion-like particles using Chandra transmission grating spectroscopy of the powerful cluster-hosted quasar H1821+643," *Mon. Not. Roy. Astron. Soc.*, vol. 510, no. 1, pp. 1264–1277, 2021.

[184] Y. Huang, S. Hu, S. Chen, M. Zha, C. Liu, Z. Yao, Z. Cao, and T. L. Experiment, "LHAASO observed GRB 221009A with more than 5000 VHE photons up to around 18 TeV," *GRB Coordinates Network*, vol. 32677, p. 1, Oct. 2022.

[185] M. A. Sanchez-Conde, D. Paneque, E. Bloom, F. Prada, and A. Dominguez, "Hints of the existence of Axion-Like-Particles from the gamma-ray spectra of cosmological sources," *Phys. Rev. D*, vol. 79, p. 123511, 2009.

[186] A. Dominguez, M. A. Sanchez-Conde, and F. Prada, "Axion-like particle imprint in cosmological very-high-energy sources," *JCAP*, vol. 11, p. 020, 2011.

[187] A. Dominguez *et al.*, "Extragalactic background light inferred from AEGIS galaxy SED-type fractions," *PoS*, vol. TEXAS2010, p. 228, 2010.

[188] D. Mazin and M. Raue, "New limits on the density of the extragalactic background light in the optical to the far-infrared from the spectra of all known TeV blazars," *Astron. Astrophys.*, vol. 471, pp. 439–452, 2007.

[189] E. Aliu *et al.*, "Very-High-Energy Gamma Rays from a Distant Quasar: How Transparent Is the Universe?," *Science*, vol. 320, no. 5884, p. 1752, 2008.

[190] J. Aleksic *et al.*, "Observations of the Blazar 3C 66A with the MAGIC Telescopes in Stereoscopic Mode," *Astrophys. J.*, vol. 726, p. 58, 2011.

[191] J. Aleksic *et al.*, "MAGIC observations and multiwavelength properties of the quasar 3C279 in 2007 and 2009," *Astron. Astrophys.*, vol. 530, p. A4, 2011.

[192] J. Aleksic *et al.*, "MAGIC discovery of VHE Emission from the FSRQ PKS 1222+21," *Astrophys. J. Lett.*, vol. 730, p. L8, 2011.

[193] A. Dominguez *et al.*, "Extragalactic Background Light Inferred from AEGIS Galaxy SED-type Fractions," *Mon. Not. Roy. Astron. Soc.*, vol. 410, p. 2556, 2011.

[194] F. W. Stecker, M. G. Baring, and E. J. Summerlin, "Blazar Gamma-Rays, Shock Acceleration, and the Extragalactic Background Light," *Astrophys. J. Lett.*, vol. 667, pp. L29–L32, 2007.

[195] M. Böttcher, C. D. Dermer, and J. D. Finke, "The Hard VHE Gamma-ray Emission in High-Redshift TeV Blazars: Comptonization of Cosmic Microwave Background Radiation in an Extended Jet?," *Astrophys. J. Lett.*, vol. 679, p. L9, 2008.

[196] F. A. Aharonian, A. N. Timokhin, and A. V. Plyasheshnikov, "On the origin of highest energy gamma-rays from Mkn 501," *Astron. Astrophys.*, vol. 384, p. 834, 2002.

[197] I. Vovk, A. M. Taylor, D. Semikoz, and A. Neronov, "Fermi/LAT observations of 1ES 0229+200: implications for extragalactic magnetic fields and background light," *Astrophys. J. Lett.*, vol. 747, p. L14, 2012.

[198] S. L. Adler, “Photon splitting and photon dispersion in a strong magnetic field,” *Annals Phys.*, vol. 67, pp. 599–647, 1971.

[199] L. Tonks and I. Langmuir, “Oscillations in ionized gases,” *Phys. Rev.*, vol. 33, pp. 195–210, Feb 1929.

[200] W. Heisenberg and H. Euler, “Consequences of Dirac’s theory of positrons,” *Z. Phys.*, vol. 98, no. 11-12, pp. 714–732, 1936.

[201] V. Weisskopf, “The electrodynamics of the vacuum based on the quantum theory of the electron,” *Kong. Dan. Vid. Sel. Mat. Fys. Med.*, vol. 14N6, no. 6, pp. 1–39, 1936.

[202] A. Dobrynina, A. Kartavtsev, and G. Raffelt, “Photon-photon dispersion of TeV gamma rays and its role for photon-ALP conversion,” *Phys. Rev. D*, vol. 91, p. 083003, 2015. [Erratum: Phys.Rev.D 95, 109905 (2017)].

[203] J. Davies, M. Meyer, and G. Cotter, “Relevance of photon-photon dispersion within the jet for blazar axionlike particle searches,” *Phys. Rev. D*, vol. 105, no. 2, p. 023017, 2022.

[204] M. S. Pshirkov, P. G. Tinyakov, and F. R. Urban, “New limits on extragalactic magnetic fields from rotation measures,” *Phys. Rev. Lett.*, vol. 116, no. 19, p. 191302, 2016.

[205] R. Durrer and A. Neronov, “Cosmological Magnetic Fields: Their Generation, Evolution and Observation,” *Astron. Astrophys. Rev.*, vol. 21, p. 62, 2013.

[206] C. Csaki, N. Kaloper, M. Peloso, and J. Terning, “Super GZK photons from photon axion mixing,” *JCAP*, vol. 05, p. 005, 2003.

[207] R. Jansson and G. R. Farrar, “A New Model of the Galactic Magnetic Field,” *Astrophys. J.*, vol. 757, p. 14, 2012.

[208] E. N. Parker, “Hydromagnetic Dynamo Models,” *Astrophys. J.*, vol. 122, p. 293, 1955.

[209] R. M. Kulsrud, “A critical review of galactic dynamos,” *Ann. Rev. Astron. Astrophys.*, vol. 37, pp. 37–64, 1999.

[210] A. Brandenburg and K. Subramanian, “Astrophysical magnetic fields and nonlinear dynamo theory,” *Phys. Rept.*, vol. 417, pp. 1–209, 2005.

[211] R. M. Kulsrud and E. G. Zweibel, “The Origin of Astrophysical Magnetic Fields,” *Rept. Prog. Phys.*, vol. 71, p. 0046091, 2008.

[212] G. B. Long, W. P. Lin, P. H. T. Tam, and W. S. Zhu, “Testing the CIBER cosmic infrared background measurements and axionlike particles with observations of TeV blazars,” *Phys. Rev. D*, vol. 101, no. 6, p. 063004, 2020.

[213] R. D. Blandford and R. L. Znajek, “Electromagnetic extraction of energy from Kerr black holes.,” *"Mon. Not. Roy. Astron. Soc."*, vol. 179, pp. 433–456, May 1977.

[214] T. P. Ray, T. W. B. Muxlow, D. J. Axon, A. Brown, D. Corcoran, J. Dyson, and R. Mundt, “Large-scale magnetic fields in the outflow from the young stellar object T Tauri S,” *Nature*, vol. 385, pp. 415–417, Jan. 1997.

[215] R. D. Blandford and D. G. Payne, “Hydromagnetic flows from accretion disks and the production of radio jets.,” *"Mon. Not. Roy. Astron. Soc."*, vol. 199, pp. 883–903, June 1982.

[216] J. C. McKinney and R. D. Blandford, “Stability of relativistic jets from rotating, accreting black holes via fully three-dimensional magnetohydrodynamic simulations,” *"Mon. Not. Roy. Astron. Soc."*, vol. 394, pp. L126–L130, Mar. 2009.

[217] E. M. de Gouveia Dal Pino, “The Role of magnetic fields on astrophysical jets,” *AIP Conf. Proc.*, vol. 784, no. 1, pp. 183–194, 2005.

[218] M. C. Begelman, R. D. Blandford, and M. J. Rees, “Theory of extragalactic radio sources,” *Rev. Mod. Phys.*, vol. 56, pp. 255–351, 1984.

[219] F. Tavecchio, M. Roncadelli, and G. Galanti, “Photons to axion-like particles conversion in Active Galactic Nuclei,” *Phys. Lett. B*, vol. 744, pp. 375–379, 2015.

[220] T. Hovatta and E. Lindfors, “Relativistic Jets of Blazars,” *New Astron. Rev.*, vol. 87, p. 101541, 2019.

[221] M. Meyer and J. Conrad, “Sensitivity of the Cherenkov Telescope Array to the detection of axion-like particles at high gamma-ray opacities,” *JCAP*, vol. 12, p. 016, 2014.

[222] I. Feain, R. Ekers, T. Murphy, B. Gaensler, J.-P. Macquart, R. Norris, T. Cornwell, M. Johnston-Hollitt, J. Ott, and E. Middelberg, “Faraday Rotation Structure on Kiloparsec Scales in the Giant Radio Lobes of Centaurus A,” *Astrophys. J.*, vol. 707, pp. 114–125, 2009.

[223] M. Giroletti, G. Giovannini, L. Feretti, W. D. Cotton, P. G. Edwards, L. Lara, A. P. Marscher, J. R. Mattox, B. G. Piner, and T. Venturi, “Parsec scale properties of Markarian 501,” *Astrophys. J.*, vol. 600, pp. 127–140, 2004.

[224] M. Giroletti, G. Giovannini, W. D. Cotton, G. B. Taylor, M. A. Pérez-Torres, M. Chiaberge, and P. G. Edwards, “The jet of Markarian 501 from millions of Schwarzschild radii down to a few hundreds,” *”Astron. Astrophys.”*, vol. 488, pp. 905–914, Sept. 2008.

[225] B. G. Piner, N. Pant, P. G. Edwards, and K. Wiik, “Significant Limb-Brightening in the Inner Parsec of Markarian 501,” *”Astrophys. J. Lett.”*, vol. 690, pp. L31–L34, Jan. 2009.

[226] G. Giovannini, M. Giroletti, and G. B. Taylor, “The Jet of Markarian 501 from the Sub-Parsec to the kpc Scale,” in *Extragalactic Jets: Theory and Observation from Radio to Gamma Ray* (T. A. Rector and D. S. De Young, eds.), vol. 386 of *Astronomical Society of the Pacific Conference Series*, p. 256, June 2008.

[227] E. Murphy, T. V. Cawthorne, and D. C. Gabuzda, “Analysing the Transverse Structure of the Relativistic Jets of AGN,” *Mon. Not. Roy. Astron. Soc.*, vol. 430, p. 1504, 2013.

[228] W. J. Potter and G. Cotter, “New constraints on the structure and dynamics of black hole jets,” *Mon. Not. Roy. Astron. Soc.*, vol. 453, no. 4, pp. 4070–4088, 2015.

[229] R. A. Laing, J. R. Canvin, A. H. Bridle, and M. J. Hardcastle, “A relativistic model of the radio jets in 3C 296,” *Mon. Not. Roy. Astron. Soc.*, vol. 372, pp. 510–536, 2006.

[230] R. A. Laing, J. R. Canvin, and A. H. Bridle, “Magnetic fields in jets: ordered or disordered?,” *Astron. Nachr.*, vol. 327, p. 523, 2006.

[231] R. A. Laing, A. H. Bridle, P. Parma, L. Feretti, G. Giovannini, M. Murgia, and R. A. Perley, “Multifrequency VLA observations of the FR I radio galaxy 3C 31: morphology, spectrum and magnetic field,” *Mon. Not. Roy. Astron. Soc.*, vol. 386, p. 657, 2008.

[232] A. Papageorgiou, “Transverse polarization structure of parsec-scale radio jets.” PhD thesis, May 2005.

[233] J. Davies, M. Meyer, and G. Cotter, “Relevance of jet magnetic field structure for blazar axionlike particle searches,” *Phys. Rev. D*, vol. 103, no. 2, p. 023008, 2021.

[234] M. Sikora, H. Sol, M. C. Begelman, and G. M. Madejski, “Radiation drag in relativistic active galactic nucleus jets,” *”Mon. Not. Roy. Astron. Soc.”*, vol. 280, pp. 781–796, June 1996.

[235] F. Govoni and L. Feretti, “Magnetic field in clusters of galaxies,” *Int. J. Mod. Phys. D*, vol. 13, pp. 1549–1594, 2004.

[236] C. L. Carilli and G. B. Taylor, “Cluster magnetic fields,” *Ann. Rev. Astron. Astrophys.*, vol. 40, pp. 319–348, 2002.

[237] K. Subramanian, A. Shukurov, and N. E. L. Haugen, “Evolving turbulence and magnetic fields in galaxy clusters,” *Mon. Not. Roy. Astron. Soc.*, vol. 366, pp. 1437–1454, 2006.

[238] T. Akahori and D. Ryu, “Faraday Rotation Measure due to the Intergalactic Magnetic Field,” *Astrophys. J.*, vol. 723, pp. 476–481, 2010.

[239] M. Murgia, F. Govoni, L. Feretti, G. Giovannini, D. Dallacasa, R. Fanti, G. B. Taylor, and K. Dolag, “Magnetic fields and Faraday rotation in clusters of galaxies,” *Astron. Astrophys.*, vol. 424, pp. 429–446, 2004.

[240] K. T. Kim, P. P. Kronberg, P. E. Dewdney, and T. L. Landecker, “The Halo and Magnetic Field of the Coma Cluster of Galaxies,” *”Astrophys. J.”*, vol. 355, p. 29, May 1990.

[241] J. S. Sanders, A. C. Fabian, and R. J. H. Dunn, “Non-thermal x-rays, a high abundance ridge and fossil bubbles in the core of the Perseus cluster of galaxies,” *Mon. Not. Roy. Astron. Soc.*, vol. 360, pp. 133–140, 2005.

[242] A. C. Fabian, E. M. Hu, L. L. Cowie, and J. Grindlay, “The distribution and morphology of X-ray emitting gas in the core of the Perseus cluster.,” *”Astrophys. J.”*, vol. 248, pp. 47–54, Aug. 1981.

[243] H. Boehringer, W. Voges, A. C. Fabian, A. C. Edge, and D. M. Neumann, “A ROSAT HRI study of the interaction of the X-ray-emitting gas and radio lobes of NGC 1275,” *Mon. Not. Roy. Astron. Soc.*, vol. 264, pp. L25–L28, 1993.

[244] A. C. Fabian, J. S. Sanders, S. Ettori, G. B. Taylor, S. W. Allen, C. S. Crawford, K. Iwasawa, R. M. Johnstone, and P. M. Ogle, “Chandra imaging of the complex x-ray core of the Perseus cluster,” *Mon. Not. Roy. Astron. Soc.*, vol. 318, p. L65, 2000.

[245] K. N. Gourgouliatos, J. Braithwaite, and M. Lyutikov, “Structure of magnetic fields in intracluster cavities,” *Mon. Not. Roy. Astron. Soc.*, vol. 409, p. 1660, 2010.

[246] M. Libanov and S. Troitsky, “On the impact of magnetic-field models in galaxy clusters on constraints on axion-like particles from the lack of irregularities in high-energy spectra of astrophysical sources,” *Phys. Lett. B*, vol. 802, p. 135252, 2020.

[247] G. B. Taylor, N. E. Gugliucci, A. C. Fabian, J. S. Sanders, G. Gentile, and S. W. Allen, “Magnetic fields in the center of the perseus cluster,” *Mon. Not. Roy. Astron. Soc.*, vol. 368, pp. 1500–1506, 2006.

[248] L. Feretti, G. Giovannini, F. Govoni, and M. Murgia, “Clusters of galaxies: observational properties of the diffuse radio emission,” *Astron. Astrophys. Rev.*, vol. 20, p. 54, 2012.

[249] J. Aleksic *et al.*, “Constraining Cosmic Rays and Magnetic Fields in the Perseus Galaxy Cluster with TeV observations by the MAGIC telescopes,” *Astron. Astrophys.*, vol. 541, p. A99, 2012.

[250] E. Churazov, W. Forman, C. Jones, and H. Bohringer, “Xmm-newton observations of the perseus cluster I: the temperature and surface brightness structure,” *Astrophys. J.*, vol. 590, pp. 225–237, 2003.

[251] V. Vacca, M. Murgia, F. Govoni, L. Feretti, G. Giovannini, R. A. Perley, and G. B. Taylor, “The intracluster magnetic field power spectrum in A2199,” *Astron. Astrophys.*, vol. 540, p. A38, 2012.

[252] P. Carenza, R. Sharma, M. C. D. Marsh, A. Brandenburg, and E. Müller, “Magnetohydrodynamics predicts heavy-tailed distributions of axion-photon conversion,” 8 2022.

[253] G. Branduardi-Raymont, D. Fabricant, E. Feigelson, P. Gorenstein, J. Grindlay, A. Soltan, and G. Zamorani, “Soft X-ray images of the central region of the Perseus cluster.,” *"Astrophys. J."*, vol. 248, pp. 55–60, Aug. 1981.

[254] M. Ruszkowski and S. P. Oh, “Shaken and stirred: conduction and turbulence in clusters of galaxies,” *Astrophys. J.*, vol. 713, pp. 1332–1342, 2010.

[255] H. Xu, H. Li, D. C. Collins, S. Li, and M. L. Norman, “Turbulence and Dynamo in Galaxy Cluster Medium: Implications on the Origin of Cluster Magnetic Fields,” *Astrophys. J. Lett.*, vol. 698, pp. L14–L17, 2009.

[256] F. Vazza, E. Roediger, and M. Brueggen, “Turbulence in the ICM from mergers, cool-core sloshing and jets: results from a new multi-scale filtering approach,” *Astron. Astrophys.*, vol. 544, p. A103, 2012.

[257] K. Dolag, M. Bartelmann, and H. Lesch, “SPH simulations of magnetic fields in galaxy clusters,” 6 1999.

[258] K. Dolag, M. Bartelmann, and H. Lesch, “Evolution and structure of magnetic fields in simulated galaxy clusters,” *"Astron. Astrophys."*, vol. 387, pp. 383–395, May 2002.

[259] K. Roettiger, J. M. Stone, and J. O. Burns, "Magnetic field evolution in merging clusters of galaxies," *Astrophys. J.*, vol. 518, p. 594, 1999.

[260] S. Furlanetto and A. Loeb, "Intergalactic magnetic fields from quasar outflows," *Astrophys. J.*, vol. 556, p. 619, 2001.

[261] A. Dominguez *et al.*, "Extragalactic Background Light Inferred from AEGIS Galaxy SED-type Fractions," *Mon. Not. Roy. Astron. Soc.*, vol. 410, p. 2556, 2011.

[262] T. Vernstrom, B. M. Gaensler, S. Brown, E. Lenc, and R. P. Norris, "Low Frequency Radio Constraints on the Synchrotron Cosmic Web," *Mon. Not. Roy. Astron. Soc.*, vol. 467, no. 4, pp. 4914–4936, 2017.

[263] S. Brown, T. Vernstrom, E. Carretti, K. Dolag, B. M. Gaensler, L. Staveley-Smith, G. Bernardi, M. Haverkorn, M. Kesteven, and S. Poppi, "Limiting Magnetic Fields in the Cosmic Web with Diffuse Radio Emission," *Mon. Not. Roy. Astron. Soc.*, vol. 468, no. 4, pp. 4246–4253, 2017.

[264] V. Vacca *et al.*, "Observations of a nearby filament of galaxy clusters with the Sardinia Radio Telescope," *Mon. Not. Roy. Astron. Soc.*, vol. 479, no. 1, pp. 776–806, 2018.

[265] S. P. O'Sullivan *et al.*, "The intergalactic magnetic field probed by a giant radio galaxy," *Astron. Astrophys.*, vol. 622, p. A16, 2019.

[266] N. Locatelli, F. Vazza, A. Bonafede, S. Banfi, G. Bernardi, C. Gheller, A. Botteon, and T. Shimwell, "New constraints on the magnetic field in cosmic web filaments," *Astron. Astrophys.*, vol. 652, p. A80, 2021.

[267] T. Vernstrom, G. Heald, F. Vazza, T. J. Galvin, J. West, N. Locatelli, N. Fornengo, and E. Pinetti, "Discovery of magnetic fields along stacked cosmic filaments as revealed by radio and X-ray emission," *Mon. Not. Roy. Astron. Soc.*, vol. 505, no. 3, pp. 4178–4196, 2021.

[268] E. Carretti *et al.*, "Magnetic field strength in cosmic web filaments," *Mon. Not. Roy. Astron. Soc.*, vol. 512, no. 1, pp. 945–959, 2022.

[269] J.-L. Han, K. Ferriere, and R. N. Manchester, "The Spatial energy spectrum of magnetic fields in our galaxy," *Astrophys. J.*, vol. 610, pp. 820–826, 2004.

[270] J. L. Han, R. N. Manchester, A. G. Lyne, G. J. Qiao, and W. van Straten, "Pulsar rotation measures and the large-scale structure of Galactic magnetic field," *Astrophys. J.*, vol. 642, pp. 868–881, 2006.

[271] R. Beck, "Galactic and Extragalactic Magnetic Fields," *AIP Conf. Proc.*, vol. 1085, no. 1, pp. 83–96, 2009.

[272] J. C. Brown, M. Haverkorn, B. M. Gaensler, A. R. Taylor, N. S. Bizunok, N. M. McClure-Griffiths, J. M. Dickey, and A. J. Green, "Rotation Measures of Extragalactic Sources Behind the Southern Galactic Plane: New Insights into the Large-Scale Magnetic Field of the Inner Milky Way," *Astrophys. J.*, vol. 663, pp. 258–266, 2007.

[273] R. Beck and R. Wielebinski, *Magnetic Fields in the Milky Way and in Galaxies.* 2 2013.

[274] G. B. Rybicki and A. P. Lightman, *Radiative Processes in Astrophysics.* 1986.

[275] R. Jansson, G. R. Farrar, A. H. Waelkens, and T. A. Ensslin, "Constraining models of the large scale Galactic magnetic field with WMAP5 polarization data and extragalactic Rotation Measure sources," *JCAP*, vol. 07, p. 021, 2009.

[276] J. P. Leahy, "Small-scale variations in the Galactic Faraday rotation.," *Monthly Notices of the Royal Astronomical Society*, vol. 226, pp. 433–446, May 1987.

[277] D. H. F. M. Schnitzeler, "The latitude dependence of the rotation measures of NVSS sources," *Monthly Notices of the Royal Astronomical Society*, vol. 409, pp. L99–L103, Nov. 2010.

[278] N. Oppermann *et al.*, "An improved map of the Galactic Faraday sky," *Astron. Astrophys.*, vol. 542, p. A93, 2012.

[279] N. Jarosik *et al.*, "Seven-Year Wilkinson Microwave Anisotropy Probe (WMAP) Observations: Sky Maps, Systematic Errors, and Basic Results," *Astrophys. J. Suppl.*, vol. 192, p. 14, 2011.

[280] R. Jansson and G. R. Farrar, "The Galactic Magnetic Field," *Astrophys. J. Lett.*, vol. 761, p. L11, 2012.

[281] R. Beck, "Magnetism in galaxies - Observational overview and next generation radio telescopes," in *Advances in Plasma Astrophysics* (A. Bonanno, E. de Gouveia Dal Pino, and A. G. Kosovichev, eds.), vol. 274, pp. 325–332, June 2011.

[282] M. Krause, "Magnetic Fields and Star Formation in Spiral Galaxies," in *Revista Mexicana de Astronomia y Astrofisica Conference Series*, vol. 36 of *Revista Mexicana de Astronomia y Astrofisica Conference Series*, pp. 25–29, Aug. 2009.

[283] M. S. Pshirkov, P. G. Tinyakov, P. P. Kronberg, and K. J. Newton-McGee, "Deriving global structure of the Galactic Magnetic Field from Faraday Rotation Measures of extragalactic sources," *Astrophys. J.*, vol. 738, p. 192, 2011.

[284] M. Wood, R. Caputo, E. Charles, M. Di Mauro, J. Magill, and J. Perkins, “Proc. 35th int. cosm. ray conf., vol. 301, fermipy: An open-source python package for analysis of fermi-lat data,” 2017.

[285] S. S. Wilks, “The Large-Sample Distribution of the Likelihood Ratio for Testing Composite Hypotheses,” *Annals Math. Statist.*, vol. 9, no. 1, pp. 60–62, 1938.

[286] A. Dobrynina, A. Kartavtsev, and G. Raffelt, “Photon-photon dispersion of tev gamma rays and its role for photon-alp conversion,” *Physical Review D*, vol. 91, no. 8, p. 083003, 2015.

[287] P. M. Chadwick, K. Lyons, T. J. L. McComb, S. McQueen, K. J. Orford, J. L. Osborne, S. M. Rayner, S. E. Shaw, K. E. Turver, and G. J. Wieczorek, “Pks 2155-304 - a source of vhe gamma-rays,” *Astropart. Phys.*, vol. 11, no. 1-2, pp. 145–148, 1999.

[288] A. Abramowski *et al.*, “VHE gamma-ray emission of PKS 2155-304: spectral and temporal variability,” *Astron. Astrophys.*, vol. 520, p. A83, 2010.

[289] P. Brun and D. Wouters, “Constraints on axion-like particles with H.E.S.S. from observations of PKS 2155-304,” in *33rd International Cosmic Ray Conference*, p. 0949, 7 2013.

[290] F. Aharonian *et al.*, “Multi-wavelength observations of PKS 2155-304 with H.E.S.S,” *Astron. Astrophys.*, vol. 442, p. 895, 2005.

[291] H. Abdalla *et al.*, “Gamma-ray blazar spectra with H.E.S.S. II mono analysis: The case of PKS 2155$-$304 and PG 1553+113,” *Astron. Astrophys.*, vol. 600, p. A89, 2017.

[292] R. Falomo, J. E. Pesce, and A. Treves, “The Environment of the BL Lac object PKS 2155-304,” *Astrophys. J. Lett.*, vol. 411, p. L63, 1993.

[293] P. Bruel, T. H. Burnett, S. W. Digel, G. Johannesson, N. Omodei, and M. Wood, “Fermi-LAT improved Pass˜8 event selection,” in *8th International Fermi Symposium: Celebrating 10 Year of Fermi*, 10 2018.

[294] M. Punch *et al.*, “Detection of TeV photons from the active galaxy Markarian 421,” *Nature*, vol. 358, pp. 477–478, 1992.

[295] A. A. Abdo *et al.*, “Fermi large area telescope observations of Markarian 421: The missing piece of its spectral energy distribution,” *Astrophys. J.*, vol. 736, p. 131, 2011.

[296] A. Franceschini, G. Rodighiero, and M. Vaccari, "Extragalactic optical-infrared background radiation, its time evolution and the cosmic photon-photon opacity," *Astronomy & Astrophysics*, vol. 487, no. 3, pp. 837–852, 2008.

[297] L. Dirson and D. Horns, "Phenomenological modelling of the Crab Nebula's broadband energy spectrum and its apparent extension," *Astron. Astrophys.*, vol. 671, p. A67, 2023.

[298] R. Davies, R. Genzel, L. Tacconi, F. M. Sanchez, and A. Sternberg, "Star Formation and Molecular Gas in AGN," in *Symposium on Mapping the Galaxy and Nearby Galaxies*, pp. 144–149, 10 2006.

[299] F. Marinacci *et al.*, "First results from the IllustrisTNG simulations: radio haloes and magnetic fields," *Mon. Not. Roy. Astron. Soc.*, vol. 480, no. 4, pp. 5113–5139, 2018.

[300] V. Springel *et al.*, "First results from the IllustrisTNG simulations: matter and galaxy clustering," *Mon. Not. Roy. Astron. Soc.*, vol. 475, no. 1, pp. 676–698, 2018.

[301] K. T. Kim, P. P. Kronberg, P. E. Dewdney, and T. L. Landecker, "The Halo and Magnetic Field of the Coma Cluster of Galaxies," *Astrophys. J.*, vol. 355, p. 29, May 1990.

[302] V. Heesen, S. P. O'Sullivan, M. Brüggen, A. Basu, R. Beck, A. Seta, E. Carretti, M. G. H. Krause, M. Haverkorn, S. Hutschenreuter, A. Bracco, M. Stein, D. J. Bomans, R. J. Dettmar, K. T. Chyży, G. H. Heald, R. Paladino, and C. Horellou, "Detection of magnetic fields in the circumgalactic medium of nearby galaxies using Faraday rotation," *Astron. Astrophys.*, vol. 670, p. L23, Feb. 2023.

[303] F. Yusef-Zadeh, J. W. Hewitt, M. Wardle, V. Tatischeff, D. A. Roberts, W. Cotton, H. Uchiyama, M. Nobukawa, T. G. Tsuru, C. Heinke, and M. Royster, "Interacting Cosmic Rays with Molecular Clouds: A Bremsstrahlung Origin of Diffuse High-energy Emission from the Inner $2^\circ\times1^\circ$ of the Galactic Center," *"Astrophys. J."*, vol. 762, p. 33, Jan. 2013.

[304] A. Nikishov, "Absorption of high energy photons in the universe," *Zhur. Eksptl'. i Teoret. Fiz.*, vol. 41, 1961.

[305] R. J. Gould and G. Schréder, "Opacity of the universe to high-energy photons," *Physical Review Letters*, vol. 16, no. 6, p. 252, 1966.

[306] J. Abraham, P. Abreu, M. Aglietta, E. Ahn, D. Allard, J. Allen, J. Alvarez-Muniz, M. Ambrosio, L. Anchordoqui, S. Andringa, *et al.*, "Measurement of the energy

spectrum of cosmic rays above 1018 ev using the pierre auger observatory," *Physics Letters B*, vol. 685, no. 4-5, pp. 239–246, 2010.

[307] A. A. Abdo, M. Ackermann, M. Ajello, A. Allafort, W. B. Atwood, L. Baldini, J. Ballet, G. Barbiellini, M. G. Baring, D. Bastieri, *et al.*, "Fermi large area telescope constraints on the gamma-ray opacity of the universe," *The Astrophysical Journal*, vol. 723, no. 2, p. 1082, 2010.

[308] M. G. Hauser and E. Dwek, "The cosmic infrared background: measurements and implications," *Annual Review of Astronomy and Astrophysics*, vol. 39, no. 1, pp. 249–307, 2001.

[309] P. Madau and L. Pozzetti, "Deep galaxy counts, extragalactic background light and the stellar baryon budget," *Monthly Notices of the Royal Astronomical Society*, vol. 312, no. 2, pp. L9–L15, 2000.

[310] F. Aharonian, A. Akhperjanian, A. Bazer-Bachi, M. Beilicke, W. Benbow, D. Berge, K. Bernlöhr, C. Boisson, O. Bolz, V. Borrel, *et al.*, "A low level of extragalactic background light as revealed by γ-rays from blazars," *Nature*, vol. 440, no. 7087, pp. 1018–1021, 2006.

[311] J. Albert, E. Aliu, H. Anderhub, P. Antoranz, A. Armada, M. Asensio, C. Baixeras, J. Barrio, M. Bartelt, H. Bartko, *et al.*, "Discovery of very high energy gamma rays from 1es 1218+ 30.4," *The Astrophysical Journal*, vol. 642, no. 2, p. L119, 2006.

[312] E. Dwek and F. Krennrich, "The extragalactic background light and the gamma-ray opacity of the universe," *Astroparticle Physics*, vol. 43, pp. 112–133, 2013.

[313] T. M. Kneiske and H. Dole, "A lower-limit flux for the extragalactic background light," *Astronomy & Astrophysics*, vol. 515, p. A19, 2010.

[314] J. D. Finke, S. Razzaque, and C. D. Dermer, "Modeling the extragalactic background light from stars and dust," *The Astrophysical Journal*, vol. 712, no. 1, p. 238, 2010.

[315] R. C. Gilmore, R. S. Somerville, J. R. Primack, and A. Domínguez, "Semi-analytic modelling of the extragalactic background light and consequences for extragalactic gamma-ray spectra," *Monthly Notices of the Royal Astronomical Society*, vol. 422, no. 4, pp. 3189–3207, 2012.

[316] J. Abraham *et al.*, "Correlation of the highest energy cosmic rays with nearby extragalactic objects," *Science*, vol. 318, pp. 938–943, 2007.

[317] K. Greisen, "End to the cosmic ray spectrum?," *Phys. Rev. Lett.*, vol. 16, pp. 748–750, 1966.

[318] G. T. Zatsepin and V. A. Kuzmin, "Upper limit of the spectrum of cosmic rays," *JETP Lett.*, vol. 4, pp. 78–80, 1966.

[319] H.-S. Zechlin, A. Cuoco, F. Donato, N. Fornengo, and A. Vittino, "Unveiling the Gamma-ray Source Count Distribution Below the Fermi Detection Limit with Photon Statistics," *Astrophys. J. Suppl.*, vol. 225, no. 2, p. 18, 2016.

[320] A. Amerio, A. Cuoco, and N. Fornengo, "Extracting the gamma-ray source-count distribution below the Fermi-LAT detection limit with deep learning," 2 2023.

[321] M. Su, T. R. Slatyer, and D. P. Finkbeiner, "Giant Gamma-ray Bubbles from Fermi-LAT: AGN Activity or Bipolar Galactic Wind?," *Astrophys. J.*, vol. 724, pp. 1044–1082, 2010.

[322] G. Sigl, M. Lemoine, and P. Biermann, "Ultrahigh-energy cosmic ray propagation in the local supercluster," *Astropart. Phys.*, vol. 10, pp. 141–156, 1999.

[323] A. M. Hillas, "The Origin of Ultrahigh-Energy Cosmic Rays," *Ann. Rev. Astron. Astrophys.*, vol. 22, pp. 425–444, 1984.

[324] C. A. Norman, D. B. Melrose, and A. Achterberg, "The Origin of Cosmic Rays above 10 18.5 eV," *Astrophys. J.*, vol. 454, p. 60, Nov. 1995.

[325] S. Inoue, "Origin of ultra-high energy cosmic rays in the era of Auger and Telescope Array," *J. Phys. Conf. Ser.*, vol. 120, p. 062001, 2008.

[326] V. N. Zirakashvili and V. S. Ptuskin, "Cosmic ray acceleration in accretion flows of galaxy clusters," *J. Phys. Conf. Ser.*, vol. 1181, no. 1, p. 012033, 2019.

Acknowledgements

There have been many people in the past four years who has helped me, guided me, and created relaxing atmosphere around me.

First of all, I would like to express my greatest gratitude to my supervisor, Prof. Dr. Dieter Horns, for his unwavering support and patient guidance throughout my entire doctoral journey. I will always be indebted to him for his patience, encouragement and the countless hours poured into so many times of good discussions and writing together. I still remember for the first presentation I did about my project in front of a large audience on QU day in early 2020, when I made a mistake for using the wrong plot, and Prof. Dr. Dieter Horns immediately approached me and helped me go through the plot and the outline of my project right after the presentation. He has always been kindly guiding me whenever I need it, and I am always more than happier to receive the positive feedback he had about my progresses. Most importantly, his enthusiasm and strict attitude toward physics inspire me greatly and have shown me how to become a great physicist. I am also deeply appreciating when he helped me in the last duration of my PhD pursuit and offered me a potential opportunity to continue the research on this exciting topic.

Second of all, I would like to thank my co-supervisor Prof. Dr. Günter Sigl for co-refereeing my thesis and examining my defense, as well as his valuable comments and suggests in my PhD panel meeting. I would also like to express my heartful thanks to the rest of my examination committee members: Prof. Dr. Michael Potthoff, Prof. Dr. Manuel Meyer, and Prof. Dr. Marcus Brüggen, for their kind acceptance to be the part of the defense committee. I am again indebted to Prof. Dr. Dieter Horns for his valuable comments and suggestions for the writing of my thesis.

I want to express my big gratitude to my parents and my sister, who have always provided me with great support no matter what. I am also grateful to my grandparents, who have always believed in me, supported me, and been proud of who I have become.

I also want to express my deepest appreciation to the funding agency of China scholarship Council for providing me such an opportunity to pursue my PhD study overseas. The thanks also goes to the Quantum Universe of Hamburg University for supporting me to attend many workshops, conferences and outreach activities to improve myself.

My big thanks goes to the entire group members for their endless support, in both life and research. I send my earliest thanks to Dr. Marios Maroudas, Josep Maria Batllori Berenguer, Matías Sotomayor, Zhongyue Zhang, Ali Baktash, Sara Porras and Leonie Schwert, for proof reading my thesis and give me valuable comments and suggestions. I also thank Dr. Martin Tluczykont and Dr. Le Hoang Nguyen for their helpful discussion with some physics problems. A special thanks goes to Michael Blank for the helping me out with the doctoral proceedings and and the most amazing carrot cake I had in my life. I would also like to thank Yikun Gu, Ludmilla Dirson and Haritha Retnakaran for their companionship in the hardest time of COVID-19. I thank my fellow office mates, Dr. Alaa Awad, Haritha Retnakaran and other office mates for creating such a nice working environment. I also want to thank our lunch group memebers, Josep, Delia, Sara, Rebecca, Marios, Rahul and others for all the chit-chat we had. Another thanks goes to the previous members, Francesca and Julian, who had worked on the same topic as me, and helped me with many discussions.

Last but not least, I would like to thank my best friend, my teammate, my life partner, my girlfriend, Valeria Bregovec, who has always been there for me, taking care of me, giving me endless support and love. This thanks is also given to my boy and my off-work supervisor, Grischa, who has warmed my heart and given me great amount of comfort whenever I need. This journey could not be completed without you guys. I also thank my family in Münster who have made me feel at home for the whole period of time.

Eidesstattliche Versicherung

Declaration on oath

Hiermit erklare ich an Eides statt, dass ich die vorliegende Dissertationsschrift selbst verfasst und keine anderen als die angegebenen Quellen und Hilfsmittel benutzt habe.

I hereby declare, on oath, that I have written the present dissertation by my own and have not used other than the acknowledged resources and aids.

Hamburg
September 20th, 2023
Signature of the doctoral student ______________